Ocean response and feedback to tropical cyclones in the South Pacific: processes and climatology

Swen Jullien

▶ **To cite this version:**

Swen Jullien. Ocean response and feedback to tropical cyclones in the South Pacific: processes and climatology. Ocean, Atmosphere. Université Paul Sabatier - Toulouse III, 2013. English. ⟨NNT : ⟩. ⟨tel-00943495⟩

HAL Id: tel-00943495

https://theses.hal.science/tel-00943495v1

Submitted on 7 Feb 2014

HAL is a multi-disciplinary open access archive for the deposit and dissemination of scientific research documents, whether they are published or not. The documents may come from teaching and research institutions in France or abroad, or from public or private research centers.

L'archive ouverte pluridisciplinaire **HAL**, est destinée au dépôt et à la diffusion de documents scientifiques de niveau recherche, publiés ou non, émanant des établissements d'enseignement et de recherche français ou étrangers, des laboratoires publics ou privés.

HAL Authorization

Université de Toulouse

THÈSE

En vue de l'obtention du

DOCTORAT DE L'UNIVERSITÉ DE TOULOUSE

Délivré par : *l'Université Toulouse 3 Paul Sabatier (UT3 Paul Sabatier)*

Présentée et soutenue le *28/11/2013* **par :**

Swen JULLIEN

Interactions océan-atmosphère au sein des cyclones tropicaux du Pacifique Sud : processus et climatologie

---

JURY

Franck ROUX	Professeur d'Université	Président du Jury
Pascale BRACONNOT	Directrice de Recherche	Rapporteur
Bernard BARNIER	Directeur de Recherche	Rapporteur
Fabrice CHAUVIN	Ingénieur Météo-France	Examinateur
Patrick MARCHESIELLO	Directeur de Recherche	Directeur de thèse
Christophe MENKES	Chargé de Recherche	Co-directeur de thèse
Nicholas HALL	Professeur d'Université	Invité

École doctorale et spécialité :
SDU2E : Dynamique de l'océan et de l'atmosphère

Unité de Recherche :
Laboratoire d'Etudes en Géophysique et Océanographie Spatiale (UMR 5566)

Directeur(s) de Thèse :
Patrick MARCHESIELLO et *Christophe MENKES*

Rapporteurs :
Pascale BRACONNOT et *Bernard BARNIER*

Ocean response and feedback to tropical cyclones in the South Pacific: processes and climatology

Swen Jullien

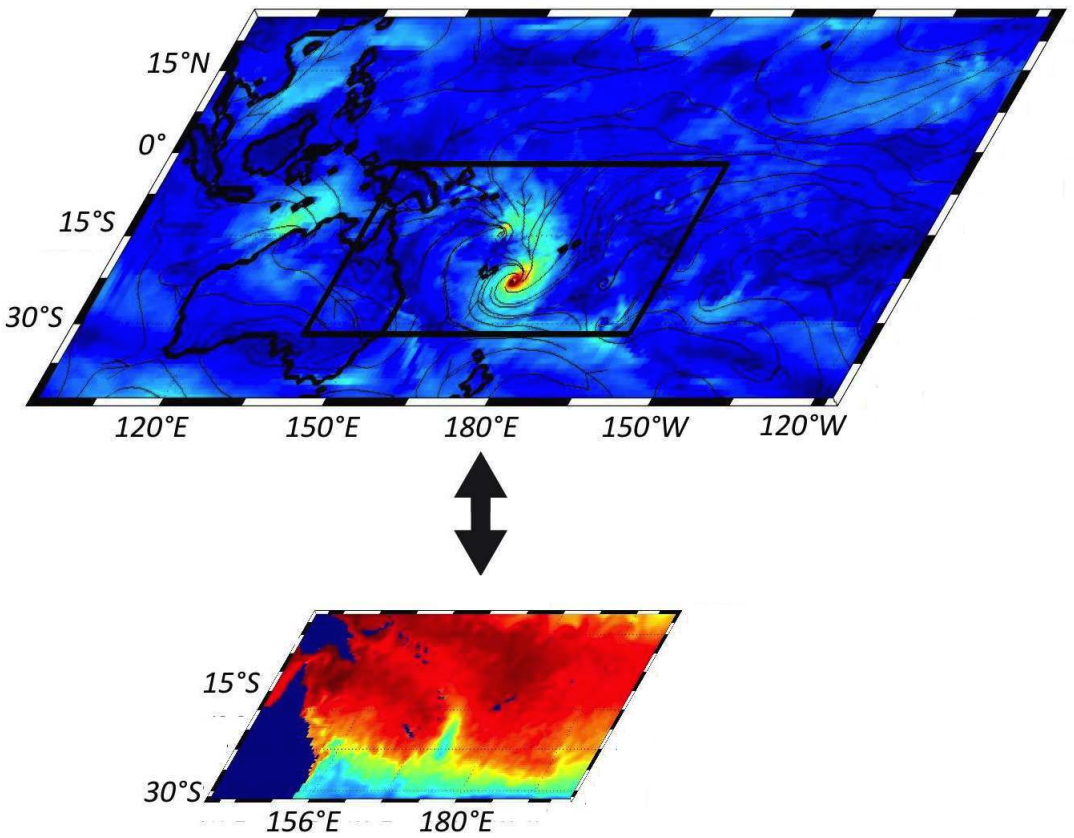

Université Toulouse III Paul Sabatier

Remerciements

Mes remerciements vont tout d'abord à Patrick et Christophe qui m'ont permis de réaliser cette thèse avec un encadrement scientifique et humain exceptionnel. Je mesure toute la valeur d'avoir eu des directeurs disponibles, impliqués et compétents sur mon sujet, mais également amicaux et qui ont accepté mon caractère quelque peu têtu et franc parfois... Je te remercie aussi Patrick, avec le recul, pour l'auto-apprentissage que tu m'as forcé à faire au début (même si ça me faisait parfois râler) et tes réponses que je garderai en mémoire : "t'as cherché sur google?". Je suis finalement devenue une vraie "n3rd" comme disent tes filles. Bien sûr je n'oublierai pas non plus les discussions cinématographiques entre frenchies de la conférence à Kos. Christophe, merci de m'avoir donné le goût de la modélisation, parce que finalement ça me plaît bien, et des discussions scientifiques au café sur le CYGP ou le changement climatique mais aussi de m'avoir permis de partir en campagne en mer entre mon stage et ma thèse. Et puis surtout, après mes séjours à Nouméa, je ne peux que me remémorer avec nostalgie les pique-niques à l'île aux canards et les cafés philosophiques dans le patio avec Andres et les filles. J'en profite donc pour un remerciement aux copines de Calédo Laury, Christelle, Mag, Marion, Steph et JB (désolée tu es passé chez les copines). Merci aussi à Flog de m'avoir donné les contacts nouméens et surtout celui d'un chercheur aux drôles de cheveux bouclés qui fume la pipe.

Un énorme merci à Jérôme pour son aide sans faille sur tout type de fichier log même à 10h de décalage horaire et 17 288 km de distance, et pour son calme impressionnant face à un ordinateur. Sans parler de ses prouesses en planche à voile et des miennes...

Je tiens aussi à remercier toute l'équipe cyclone pour son soutien scientifique et particulièrement Nico pour ses programmes shell/fortran et sa liqueur de papaye, Matthieu pour la "cellule psychologique" et son rire, Guillaume pour avoir partager les fameuses discussions WRF avec moi, Ariane pour sa motivation, son enthousiasme et pour la mission Indomix, Margot pour les discussions SPCZ, changement climatique et les dessins de Christophe.

Je remercie également les membres de mon jury de thèse pour leur temps accordé à la lecture de mon manuscrit (en anglais...) et à la soutenance. Un remerciement spécial pour Nick, qui m'a suivi tout au long de mon parcours en météo et océanographie à la fac puis au labo et surtout qui a crée CHEVRE pour qu'on puisse enfin faire des réunions scientifiques et pas administratives !

Un remerciement particulier à toute l'équipe de gestion du LEGOS, Martine, Nadine, Brigitte et Agathe, pour leur aide précieuse pour les missions, leur soutien et leur convivialité. Le LEGOS a de la chance d'avoir des perles comme elles !

Pour mes débuts dans le monde de la recherche et de l'océanographie de terrain avec les missions à la lagune de Lapalme et pour des parties de baby mémorables sur le Marion Dufresne, merci à Pieter et Marc. Sans oublier François qui est le témoin de notre victoire et qui a des supers poissons dans son bureau.

Enfin, tout ce début de chemin parcouru dans les couloirs du LEGOS et sur le terrain aurait vraiment manqué de potins et de discussions de filles sans Marie et Sabine et je suis vraiment contente d'avoir partagé ce temps avec elles.

Merci à Nathan et Robin, copains du midi (on attend toujours cette bouteille de rouge d'ailleurs Robin !) et de la pétanque.

Bien sûr cette thèse n'aurait pas été aussi agréable sans la compagnie et le soutien de Yves et Clément qui ont supporté mes questions geek et mes vociférations informatiques et avec qui j'ai pu partager des cafés, des croissants, des mojitos/parties de belote et encore bien des choses. Yves, merci aussi d'avoir écouté ma présentation de soutenance quelque chose comme au moins 5 fois ! Je pense que tu aurais finalement pu la faire à ma place.

Pour terminer, plus que des remerciements pour Marc qui a partagé mes moments de motivation qui impliquaient de discuter de pondération de moyenne le soir, comme mes moments de stress (et ceux qui me connaissent savent que je ne suis pas de la plus grande douceur dans ces moments...). Merci aussi de m'avoir laissé partir en Nouvelle-Calédonie et surtout de m'avoir toujours soutenue et de le faire encore.

Contents

Introduction générale 1

Chapter 1 Introduction 3
1.1 Generalities on tropical cyclones . . . 4
1.1.1 Observations . . . 4
1.1.2 General characteristics . . . 6
1.1.3 The South Pacific . . . 7
1.2 TC formation and intensification . . . 8
1.3 Ocean response to TCs . . . 12
1.3.1 Cold wake formation . . . 12
1.3.2 Mixing and upwelling mechanisms . . . 12
1.3.3 The role of ocean structure and dynamics . . . 14
1.3.4 Impact on the ocean climate . . . 15
1.4 Ocean feedback to tropical cyclones . . . 16
1.5 State of the art modeling of tropical cyclones . . . 18
1.5.1 Climate models . . . 20
1.5.2 Simple coupled models . . . 20
1.5.3 Realistic coupled models . . . 21
1.5.4 Long-term regional simulations . . . 21
1.6 Manuscript outline . . . 22

Chapter 2 Development of a coupled model for the South Pacific 25
2.1 Models . . . 26
2.1.1 Atmospheric model: WRF . . . 26
2.1.2 Ocean model: ROMS . . . 29
2.1.3 Coupler . . . 31
2.1.3.1 Coupling methodology . . . 31
2.1.3.2 Computational performances . . . 34
2.1.3.3 Note on OASIS coupler . . . 35
2.2 Sensitivity tests . . . 35
2.2.1 Convection . . . 35

2.2.2 Planetary boundary layer (PBL) . . . 37
2.2.3 Cloud microphysics . . . 38
2.2.4 Shortwave radiation . . . 38
2.2.5 Surface drag . . . 39
2.2.6 Skin SST . . . 41
2.2.7 Land surface model . . . 42
2.2.8 Sponge layers . . . 43
2.2.9 Sensitivity to vertical resolution . . . 43
2.3 Methodology . . . 43
2.3.1 TC tracking and SPEArTC database . . . 43
2.3.2 Forced model: cold track filtering technique . . . 47
2.3.3 Statistics and error bars . . . 49
2.3.3.1 Interannual variability . . . 49
2.3.3.2 Seasonal or intensity variability . . . 51
2.3.3.3 Similarity of forced and coupled models distributions . . . 52
2.3.4 Compositing methodology . . . 53
2.4 Summary of the experiments . . . 54

Chapter 3 Climatology of the South Pacific and model validation **57**
3.1 Validation datasets . . . 58
3.1.1 Ocean properties . . . 58
Pathfinder SST . . . 58
CARS climatology . . . 58
Montegut et al. [2004] MLD climatology . . . 58
3.1.2 Precipitation . . . 58
TRMM . . . 58
GPCP . . . 60
CMAP . . . 60
3.1.3 Air-Sea Fluxes . . . 60
TropFlux . . . 60
OAFlux . . . 60
COADS . . . 60
NOC1 . . . 61
3.1.4 Wind . . . 61
QuickSCAT . . . 61
3.1.5 NCEP-2 Reanalysis . . . 61
3.2 Oceanic circulation . . . 62
3.2.1 Large-scale circulation and zonal jets . . . 62
3.2.2 Mesoscale activity . . . 63
3.2.3 Surface properties . . . 64
3.2.4 Vertical structure . . . 66
3.3 Atmospheric circulation . . . 66
3.3.1 SPCZ dynamics . . . 66
3.3.2 Vertical structure: the Hadley cell . . . 69
3.3.3 Seasonal cycle and air-sea fluxes . . . 72

3.4 TC distributions . . . 75
3.4.1 Environmental conditions of cyclogenesis . . . 75
3.4.2 Seasonal distribution . . . 76
3.4.3 Interannual variability . . . 78
3.4.4 ENSO . . . 79
3.4.5 Environmental *vs.* stochastic forcing of cyclogenesis . . . 81

Chapter 4 Impact of Tropical Cyclones on the Heat Budget of the South Pacific Ocean 85
4.1 Introduction . . . 87
4.2 Materials and methods . . . 89
4.2.1 The regional ocean model . . . 89
4.2.2 TC forcing in twin ocean experiments . . . 90
4.2.3 Temperature equation and tendencies . . . 92
4.3 Validation of the ocean model with WRF forcing . . . 93
4.4 Results . . . 96
4.4.1 Case studies . . . 96
4.4.2 Composite analysis of TC wakes . . . 100
4.4.2.1 Composite anomalies under the cyclone . . . 101
4.4.2.2 Surface composites in the cyclone wake . . . 102
Cyclone wake evolution . . . 103
Cross-track pattern . . . 103
4.4.2.3 Subsurface waters . . . 106
Cyclone wake evolution . . . 106
Cross-track pattern . . . 106
4.4.2.4 Integrated effect in the cyclone wake . . . 108
4.4.3 TC impacts on the ocean climate . . . 110
4.4.3.1 Surface temperature . . . 110
4.4.3.2 Vertical structure . . . 112
4.4.3.3 Interannual variability . . . 115
4.5 Conclusions and discussion . . . 116
Acknowledgments . . . 118
4.6 Appendix: KPP . . . 118
4.6.1 Interior mixing . . . 119
4.6.2 Boundary layer mixing . . . 119
4.6.2.1 Boundary layer thickness h_{bl} . . . 119
4.6.2.2 Turbulent velocity scale . . . 120
4.6.2.3 K profile . . . 120

Chapter 5 Ocean feedback to tropical cyclones: climatology and processes 121
5.1 Introduction . . . 123
5.2 Models and Methods . . . 124
5.2.1 Atmospheric model . . . 124
5.2.2 Ocean model . . . 126
5.2.3 Coupling procedure . . . 127

5.2.4 Forced simulation setup . . . 128
5.2.5 Tracking methodology . . . 129
5.2.6 Compositing methodology . . . 130
5.3 Environmental conditions . . . 131
5.3.1 The ocean-atmosphere interface . . . 131
5.3.2 SPCZ and cyclogenesis index . . . 133
5.4 TC structure . . . 134
5.5 Coupling effect on cyclonic activity . . . 138
5.5.1 Cyclogenesis geography . . . 138
5.5.2 Intensity distribution . . . 139
5.6 Coupling effect on air-sea fluxes . . . 140
5.6.1 SST cooling . . . 140
5.6.2 Specific humidity . . . 142
5.6.3 Air-sea fluxes . . . 142
5.7 The role of ocean dynamics . . . 143
5.7.1 Geography of storm-induced cooling . . . 143
5.7.2 Storm sensitivity to SST . . . 144
5.7.3 Mixed layer depth . . . 145
5.7.4 Barrier layers . . . 146
5.7.5 Ocean eddies . . . 147
5.8 TC intensification . . . 149
5.9 Summary and Discussion . . . 153
Ackowledgments . . . 156

Chapter 6 Conclusions and Perspectives **157**
6.1 Conclusions . . . 158
6.1.1 Development of a mesoscale resolution regional coupled model . . . 159
6.1.2 Oceanic response to TCs . . . 160
6.1.3 Ocean feedback effect on tropical cyclones . . . 162
6.2 Directions for future work . . . 164
6.2.1 Increasing resolution . . . 164
6.2.2 Improving the air-sea interface . . . 165
6.2.3 Short and long-term variability of cyclonic activity . . . 168
6.2.3.1 Intra-seasonal MJO variability . . . 168
6.2.3.2 Climate change . . . 168
6.2.4 Marine ecosystems and coastal impacts . . . 169
6.2.4.1 Marine ecosystems . . . 169
6.2.4.2 Island vulnerability . . . 170

Conclusion générale **171**

Bibliography **173**

A Description of WRF namelist variables **185**

B WRF namelist used for coupled and forced experiments 199

C Statistical tables 203

Extended summary 213

Introduction générale

Les cyclones tropicaux sont les phénomènes les plus puissants de l'atmosphère tropicale (puissance instantanée de 10^{12} W). Ce sont des dépressions de plus de 1000 km de diamètre qui se développent sur les océans chauds du globe. Nommés ouragans dans l'Atlantique nord et le nord-est du Pacifique, typhons dans le nord-ouest du Pacifique ou cyclones tropicaux dans l'océan Indien et l'océan Pacifique Sud, ils représentent tous le même phénomène : un système de nuages organisés, en rotation et couplé avec l'océan. Ils sont surtout connus pour leur potentiel destructeur causant des victimes et des dégâts matériels aux populations côtières. N'ayant pour le moment pas de solution pour contrôler ou utiliser leur puissance, nous ne pouvons qu'améliorer la prévention des dommages qu'ils engendrent. Les australiens ont par exemple récemment développé des éoliennes qui peuvent être repliées au sol pour éviter qu'elles ne soient détruites par les vents violents des cyclones.

En tant que chercheurs, nous pouvons travailler à une meilleure compréhension des mécanismes d'intensification et d'évolution des cyclones tropicaux dans le but d'améliorer leur prévision. Au cours des dernières années, l'augmentation de la puissance de calcul et l'amélioration des capacités de modélisation et d'observation ont permis d'améliorer les prévisions de la trajectoire des cyclones. En revanche, leur intensité est encore mal prédite. Ceci est probablement dû à une mauvaise prise en compte de la structure et de la dynamique océanique dans les prévisions opérationnelles. Les travaux présentés dans ce manuscrit aspirent donc à améliorer notre connaissance des interactions entre les cyclones et l'océan.

Les interactions des cyclones tropicaux avec l'océan sont essentielles à leur formation et leur évolution. La chaleur contenue dans les couches superficielles de l'océan est la source d'énergie des cyclones. En retour, les vents extrêmes des cyclones injectent de l'énergie mécanique dans l'océan et modifient sa structure. On observe la plupart du temps un refroidissement de surface sur la trace des cyclones. Ce sillage froid peut alors potentiellement exercer une rétroaction négative sur l'intensité des cyclones eux-mêmes. Les principaux objectifs de cette thèse sont de fournir une climatologie de la réponse océanique aux cyclones et de sa rétroaction sur leur intensité et d'en comprendre les mécanismes. Pour cela, un modèle régional couplé du Pacifique sud-ouest a été développé permettant de réaliser des simulations longues du climat présent avec une résolution méso-échelle. Cette approche a alors permis d'obtenir des expériences statistiquement robustes manquant dans la littérature actuelle entre études climatiques à basse résolution et cas d'études.

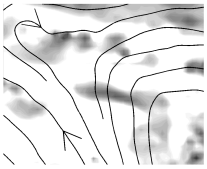

Chapter 1

Introduction

Contents

1.1 Generalities on tropical cyclones 4
1.1.1 Observations 4
1.1.2 General characteristics 6
1.1.3 The South Pacific 7
1.2 TC formation and intensification 8
1.3 Ocean response to TCs 12
1.3.1 Cold wake formation 12
1.3.2 Mixing and upwelling mechanisms 12
1.3.3 The role of ocean structure and dynamics 14
1.3.4 Impact on the ocean climate 15
1.4 Ocean feedback to tropical cyclones 16
1.5 State of the art modeling of tropical cyclones 18
1.5.1 Climate models 20
1.5.2 Simple coupled models 20
1.5.3 Realistic coupled models 21
1.5.4 Long-term regional simulations 21
1.6 Manuscript outline 22

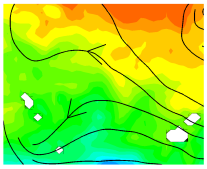

Tropical cyclones (TCs) are the most powerful phenomena of the tropical atmosphere (instantaneous power of 10^{12} W). They are low-pressure tropical disturbances of more than 1000 km diameter that develop over warm tropical oceans (Fig. 1.1). *Hurricanes* in the north Atlantic and northeastern Pacific, *typhoons* in the northwestern Pacific or *tropical cyclones* in the Indian and south Pacific oceans all refer to the same phenomenon: a rotating, organized system of clouds coupled with the ocean. They are popularly known for their destructiveness causing casualties and material damages to coastal populations. Waiting for solutions to control and use their power, we are left to find solutions to prevent the damages. For example, Australians or Caledonians (Aerowatt company) recently developed wind turbines that can be folded on the ground to prevent their destruction by extreme winds.

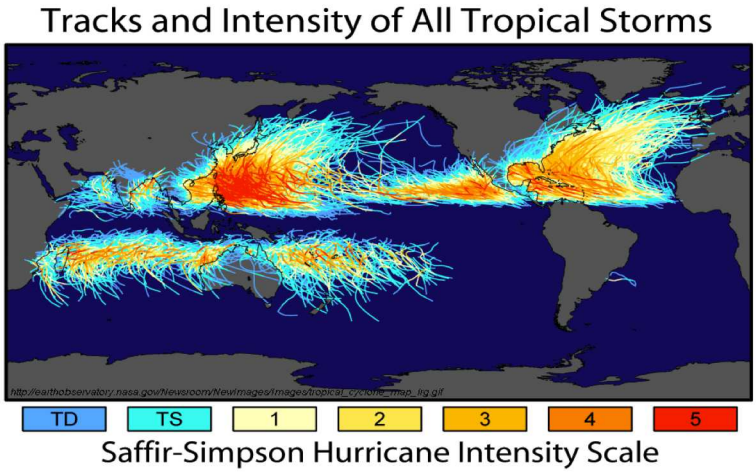

Figure 1.1 - Glopbal map of tropical cyclone tracks. Figure from NASA.

As researchers, we can work at a better understanding of the mechanisms of intensification and evolution of tropical cyclones in order to improve their forecast. In recent years, increasing computing power, modeling and observational skills have sustained improvements in the forecast of TC tracks. By contrast, their intensity is still poorly predicted. A probable source of failure is the poor account of ocean structure and dynamics in operational forecasts. The work presented in this manuscript aspire to advance our knowledge of interactions between tropical cyclones and the ocean.

1.1 Generalities on tropical cyclones

1.1.1 Observations

Tropical cyclone observation has been carried out over the past couple of centuries in various ways. Before the satellite era, it was essentially performed by unfortunate commercial ships crossing storms. Since World War II, reconnaissance

aircrafts called hurricane hunters have been flying out to sea to find tropical cyclones. Nowadays, they provide the most detailed measurements. They use dropwindsondes that are deployed from the aircraft and drift down on a parachute measuring vertical profiles of pressure, temperature, humidity and wind as they fall. However, aircraft deployments are very expensive and only operational in the North Atlantic and North Pacific by American and Japan governments. Since the 1970's, satellites allow us to observe TCs from space with an increasing space and time coverage. Visible and infrared measurements provides images of the cloud structure and temperature at upper levels, which are representative of the cyclonic circulation, cyclone eye and deep convection. Micro-wave measurements give information on the ocean surface. Scatterometers retrieve the wind direction and intensity and altimeters significant wave height. Satellite and coastal radars provide precipitation rates and patterns. Measurements of oceanic fields and air-sea fluxes can also be retrieved by moorings, Argo autonomous profilers, expendable current profilers or bathythermographs released for a particular event study (for example during the CBLAST, Coupled Boundary Layer Air-Sea Transfer, experiment; Fig. 1.2, Black et al., 2007).

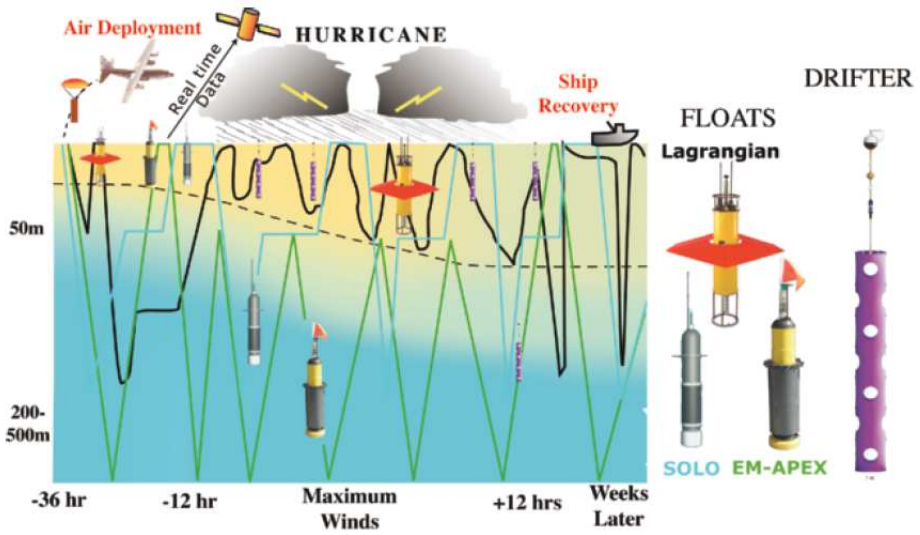

Figure 1.2 - Schematic picture of the instruments deployed into hurricane Frances (2004) during the CBLAST experiment. Figure from Black et al. [2007].

Observations have been very valuable to our understanding of tropical cyclones and are still required, but they are either impracticable or limited. Satellite observations have a good space and time coverage that is very useful for detecting and tracking TCs. However, with a bi-dimensional space coverage, they largely miss the TC structure and only cover the ocean surface. *In situ* observations on the other hand have insufficient space and time coverage. In the absence of a continuous three-dimensional dataset, modeling offers a good alternative to advance our knowledge of tropical cyclones and underlying mechanisms.

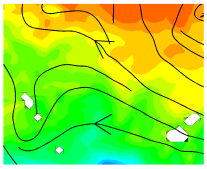

1.1.2 General characteristics

Tropical cyclones are deep warm-core structures characterized by organized convection, rotating winds, humidity convergence at low-levels and divergence in the upper troposphere (Fig. 1.3). They are maintained by the extraction of heat energy from the warm ocean and are thus part of the marine system; landfall is the end of the cyclone life. Obviously, cyclonic winds inflict a lot of damages to coastal populations before they die as their outer winds can sweep the coast before the eye makes landfall (damages also arise from heavy rain, storm surge and wave set-up and run-up). They can sometimes survive after crossing an island if they are strong and fast enough. Another decaying process is the progression over colder waters and across jet-streams in the subtropics. This is usual as TC trajectory is mainly driven by the mean tropospheric flow that is generally poleward.

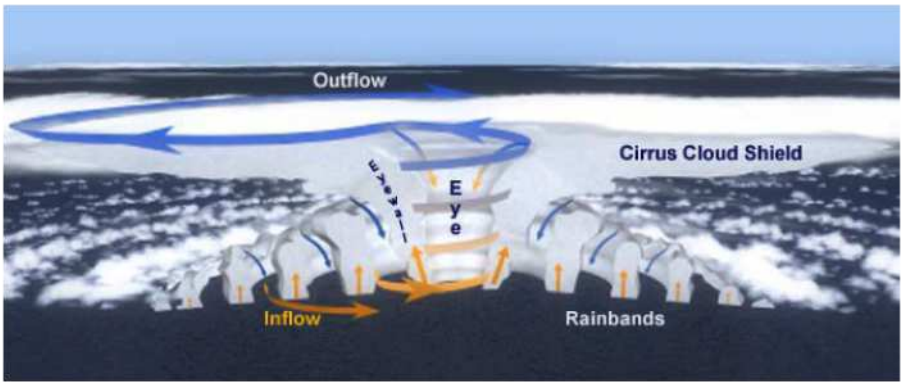

Figure 1.3 - Schematic vertical section of TC circulation. Figure from Gray and Emanuel [2010].

Tropical cyclones need specific environmental conditions to develop and maintain [Gray, 1968]:

- oceanic temperature above 26°C over the first 60 m of the ocean, to fuel the heat engine of the tropical cyclone
- sufficient environmental lapse rate for conditional instability
- high relative humidity at mid troposphere sustaining deep convection
- cyclonic absolute vorticity at low level
- weak vertical wind shear preventing vortex disruption and upper dry air intrusion

These conditions are met in tropical convergence zones (Fig. 1.1) where about 80 TCs develop each year. Interestingly, there are no tropical cyclones in the South Atlantic because of strong wind shear and possibly lack of weather disturbances favorable for tropical cyclone initialization [Gray, 1968].

1.1.3 The South Pacific

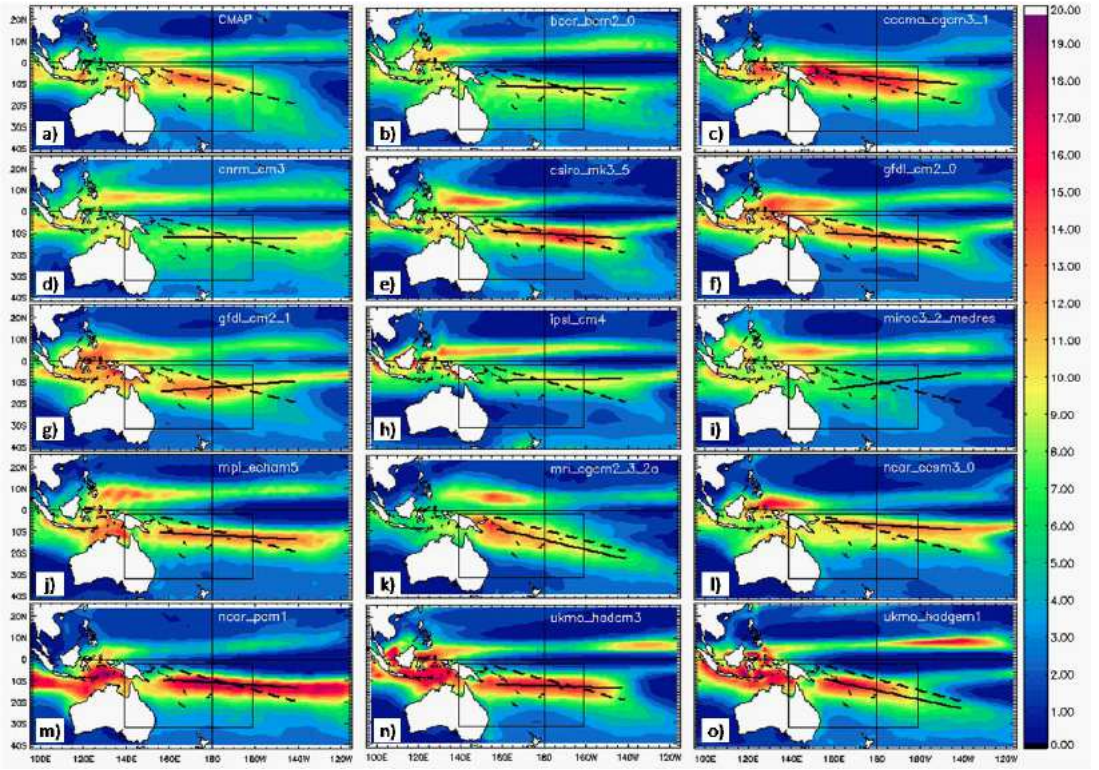

Figure 1.4 - Austral summer (January-March) mean precipitation in (a) CMAP observations and (b-o) a selection of best CMIP3 climate models in the South Pacific region. The black solid lines represent the SPCZ position in each model. The black dashed line represents the SPCZ position in CMAP observations. Figure from Bador et al. [2012].

The South Pacific region was chosen for this study in continuation of the work of Jourdain et al. [2011] as part of long-term projects of the IRD (Institut de Recherche pour le Développement). The South Pacific is composed by numerous poor islands that are particularly vulnerable to TC activity. It is also largely impacted by the El Niño Southern Oscillation (ENSO) phenomenon. The South Pacific Convergence Zone (SPCZ), which is the only convergence zone of the southern hemisphere that is present all year long, is submitted to significant interannual variations due to ENSO with consequences on cyclogenesis. The SPCZ is one of the most poorly simulated convergence zone in climate models (Fig. 1.4) and few studies are dedicated to its understanding. However, the IRD established in Noumea (New Caledonia) for nearly 70 years has dedicated numerous research in the South Pacific (sharing that with Australians) and this thesis is part of the effort.

TC activity in the South Pacific is measured with a different intensity scale than the well-known Saffir-Simpson intensity scale mainly used in the North Atlantic. These scales are reported in Table 1.1. TC intensity is usually represented by

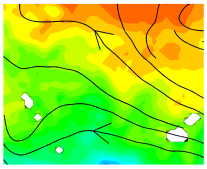

the TC central pressure. The relationship between maximum winds and central pressure for observed TCs in the South Pacific is illustrated in Figure 1.5.

Table 1.1 - South Pacific and Saffir-Simpson intensity scales for tropical cyclones. TS is used for Tropical Storm.

Wind speed	South Pacific scale	Saffir-Simpson scale
17-24 m/s	cat. 1	TS
24-33 m/s	cat. 2	TS
33-44 m/s	cat. 3	cat. 1
44-55 m/s	cat. 4	cat. 2-3
55-70 m/s	cat. 5	cat. 3-4
>70 m/s	cat. 5	cat. 5

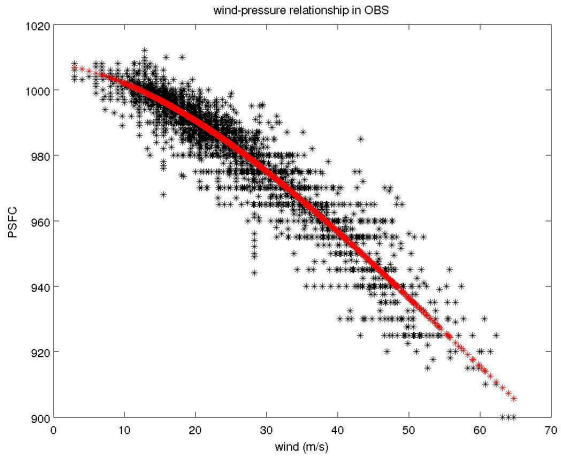

Figure 1.5 - Wind-pressure relationship for observed TCs in the South Pacific (SPEArTC data from 1979 to 1999).

1.2 TC FORMATION AND INTENSIFICATION

The genesis and intensification of tropical cyclones has been investigated for decades. Gray [1998] reviewed the processes of tropical cyclone formation. Here, we give a quick summary. Tropical convection forms a variety of mesoscale systems (cloud clusters, mesoscale convective systems: MCSs) with generally short life span. A strong convective system can develop a mesoscale convective vortex (MCV) that may persist 1 to 3 days after the MCSs die. This residual cyclonic circulation is only about 150-km wide and 5-km deep (Fig. 1.6a) but it has a warm-core with a structure analogous to that of a tropical cyclone and can serve as the nucleus for its formation.

The cyclonic flow associated with the low-pressure center can help organize new areas of convection, but a second external forcing is required to trigger extreme convection (EC; Fig. 1.6a). External forcing can be exerted by wind surges that encounter a convergence line in trade winds or monsoon flow (Fig. 1.7), easterly waves (particularly in the North Atlantic), or other forms of disturbances.

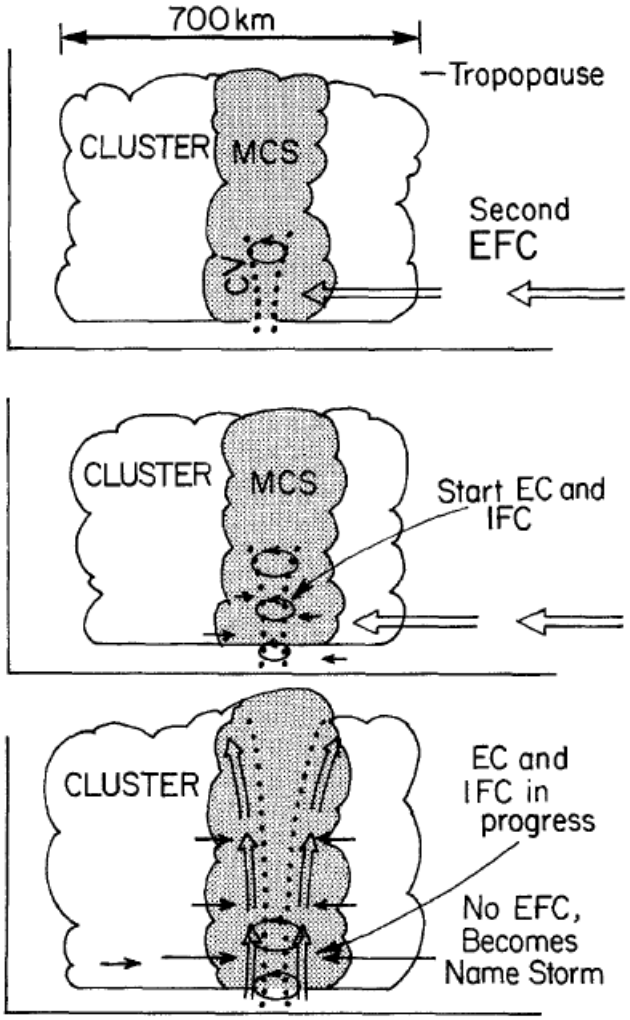

Figure 1.6 - Cross-section view of the steps describing how an externally forced convergence (EFC) acts to initiate an area of extreme convection (EC) and the activation of an internally forced convection (IFC), which after a short time of intensification becomes a named storm. Figure from Gray [1998].

The external forced convergence (EFC) must produce an increase in humidity of 20-25% and force the development of extreme convection (EC) in the MCS. It is strong enough to drive air parcels to near saturation and suppress strong downdrafts (1.6b). A larger scale, self-sustained secondary circulation, named internally forced convection (IFC) by Gray [1998], takes place (1.6c). The IFC increases the mass inflow at low-levels from the surrounding environment. At this stage, a tropical cyclone can form. Pressure starts to drop rapidly (5-10 hPa/day)

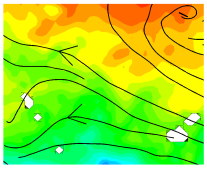

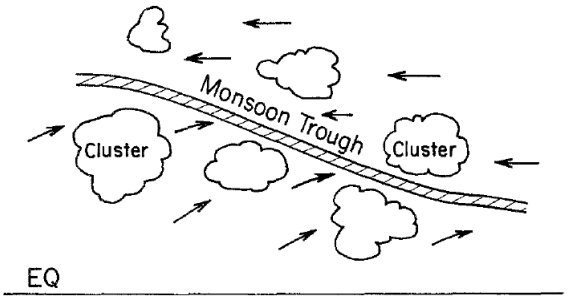

Figure 1.7 - Schematic picture of the typical organization of cloud clusters in the south-westerly monsoon or trade wind flow. Figure from Gray [1998].

accompanied by a rapid wind spin-up in the inner region. A gradient wind balance between the cloudy area and its environment is established. The pressure gradient towards the storm center maintains the convergence and the TC evolves independently from its environment. One important aspect of this conceptual model is that the development of tropical disturbance must first concentrate on a small inner area with an in-up-and-out radial circulation that allows for a rapid intensification. Then tangential winds out of the core can intensify. An anticyclonic flow at upper-levels promotes the tangential wind increase out of the core. The intensification also results in strong inertial stability that in turn inhibits the transverse circulation to the core and slows down the intensification.

The conceptual model of Gray [1998] is in essence similar to the Conditional Instability of the Second Kind [CISK; Charney and Eliassen, 1964]. CISK describes the unstable growth of a group of convective clouds which differs by size and time scale from the instability of the first kind that describes the unstable growth of individual cumulus clouds. Charney and Eliassen [1964] suggested that this linear instability process occurs over a 400-500 km area and is initiated by frictionally forced convergence akin to the internally forced convection of Gray [1998]. Frictional convergence is analogous to Ekman pumping, *i.e.*, the process of inducing vertical motions by boundary layer friction. As friction increases with wind speed, frictional convergence is maximum near the radius of maximum winds in the eyewall. Gray [1998] agrees with the concept of CISK but argue that unstable growth can only occur on smaller scales.

Other theories were proposed by Emanuel [1986] and Rotunno and Emanuel [1987] following the idea of a thermodynamical rather than mechanical trigger for deep convection. They suggest that different thermodynamical states exist between disturbances that develop or not into TCs: the developing systems would present higher values of temperature and/or humidity at low-levels. Gray [1998] objects that rawindsonde observations does not indicate systematic differences in temperature and humidity between developing or non-developing disturbances. The Wind-Induced Surface Heat Exchange theory [WISHE; Emanuel et al., 1994]

is a theory of linear instability involving thermodynamical arguments. WISHE is based on the assumption that convection is self-fueling in a coupling process between surface fluxes and winds within the convective system. The TC growth rate is restricted by the magnitude of surface heat and moisture fluxes rather than the frictional convergence mechanism as in CISK [Craig and Gray, 1996]. WISHE has achieved widespread acceptance in the current literature but recent modeling studies have questioned its validity or completeness [Montgomery et al., 2009]. Our work goes along this latter line of research.

A last important aspect of research, of growing interest, is the role of mesoscale interactions in TC formation. The merging of two mesoscale vortices producing a full grown cyclone is relatively rare but has been observed [Kuo et al., 2000] and modeled [Fig. 1.8, Jourdain et al., 2011]. More generally, vortex interaction, from elastic interaction to straining and merger, are ubiquitous aspect of TC formation that should be accounted for [Dritschel, 1995; Guinn and Schubert, 1993].
Obviously, the formation and intensification processes of tropical cyclones are still a matter of research and debate. Tropical disturbances such as wind surges or vortex interaction are difficult to forecast because of their chaotic nature. Forecasting generally starts only after the initialization process. The difficulty of forecasting TC intensity is certainly related to the flaw of understanding of intensification processes.

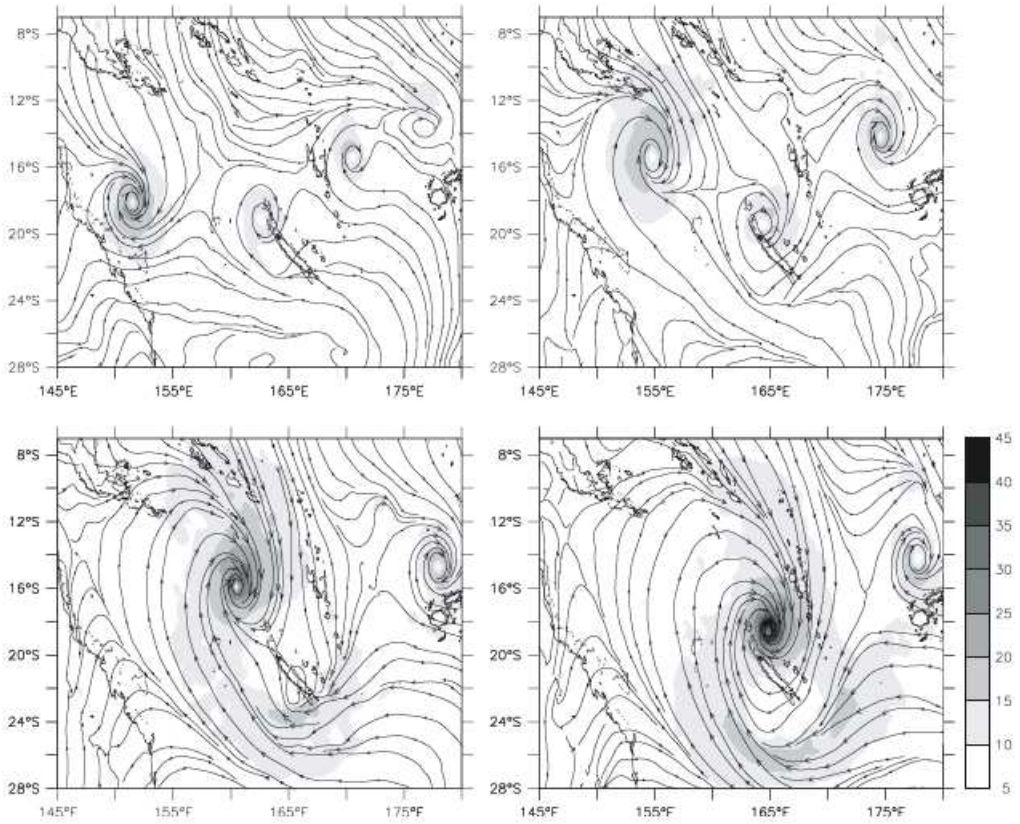

Figure 1.8 - Simulated TC formation by vortex merging. Low-level wind (at 925 hPa) is shown as streamlines and colors ($m.s^{-1}$). Figure from Jourdain et al. [2011].

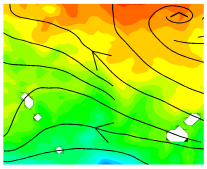

1.3 Ocean response to TCs

1.3.1 Cold wake formation

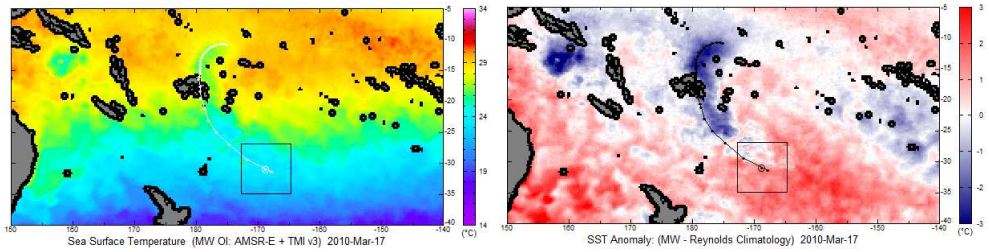

Figure 1.9 - SST field and cooling anomaly after the passage of TCs Tomas (black track) and Ului (next to Papua-New-Guinea) in March 2010 retrieve by TMI-AMSR-E satellite data.

The most reported effect of TCs on the ocean is the surface water cooling observed from satellites where it appears as TC *cold wake* (Fig. 1.9). The surface cold wake expresses various storm-induced processes: heat loss to the atmosphere, mixing with subsurface water, upwelling of deep water by Ekman pumping (Fig. 1.11). SST cooling is usually asymmetric because of asymmetric wind forcing. We define the TC *strong side* as the side of strongest cooling. On the strong side, tangential winds and translation speed are added (right-hand side in the Northern Hemisphere and left hand side in the Southern Hemisphere). It is the opposite on the weak side. Asymmetry in winds induces asymmetry in turbulent mixing. In addition, resonance between ocean currents and winds leads to another asymmetric increase in mixing. Translation speed thus has the effect of shifting SST cooling away from the cyclone track [Price, 1981; Samson et al., 2009]. Concurrently, fast translation speed weakens SST cooling (Fig. 1.10). We will show in this thesis that this is largely an effect of supercritical translation speed (with reference to near-inertial phase speed) that weakens the upwelling effect relative to mixing. More detail on the known mechanisms are given below.

1.3.2 Mixing and upwelling mechanisms

Extreme winds in cyclones produce strong mixing of warm surface waters with colder subsurface waters. Mixing is due to both mixed layer entrainment and shear instability associated with near-inertial oscillations, a transitory response to a moving storm [Chang and Anthes, 1978; Shay et al., 1989; Jaimes and Shay, 2009]. Near-inertial motions are characterized by oscillating horizontal and vertical velocities associated with *inertial pumping* (Figs. 1.12, 1.13a). Cyclonic rotating winds also induce an Ekman pumping that is particularly strong for slow or static storms. It is characterized by a very strong upwelling of cold deep water under the cyclone track with weaker and more widespread downwelling on the sides (Fig. 1.13b). In the linear theory, upwelling velocity from Ekman pumping is maximum at the base of the surface boundary layer then decreases linearly [*e.g.*,

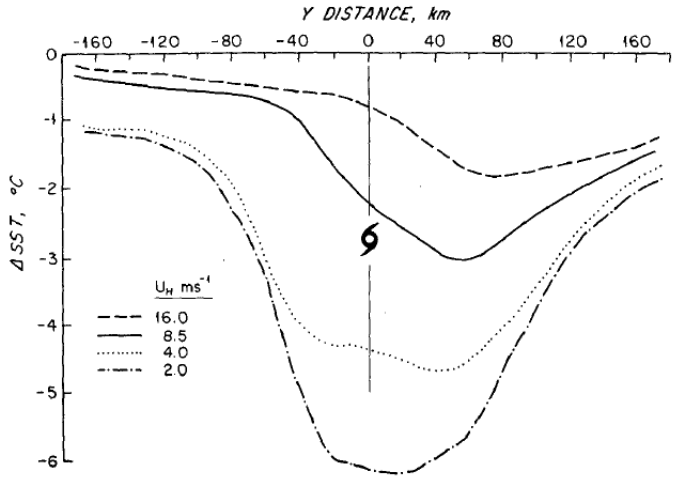

Figure 1.10 - Cross-track section profile of SST cooling for different hurricane translation speeds. Figure from Price [1981].

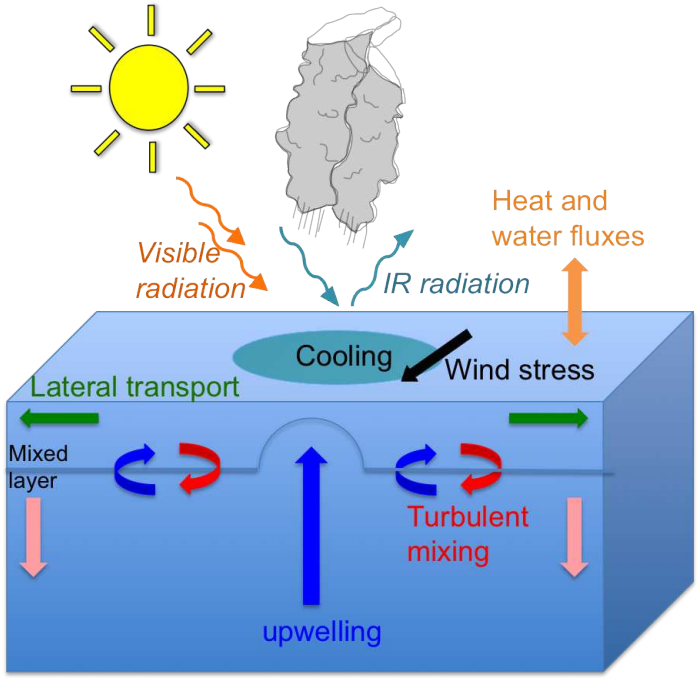

Figure 1.11 - Schematic picture of ocean-atmosphere interactions under a tropical cyclone.

McWilliams, 2006]. Therefore, it strongly participates in the surface thermal response by uplifting the thermocline [Price, 1981; Shay et al., 2000]. Yet, Ekman pumping is generally neglected in conceptual models, at the benefit of the mixing process, as it requires a three-dimensional approach. We will see in this thesis work that Ekman pumping is major player in the cold wake formation.

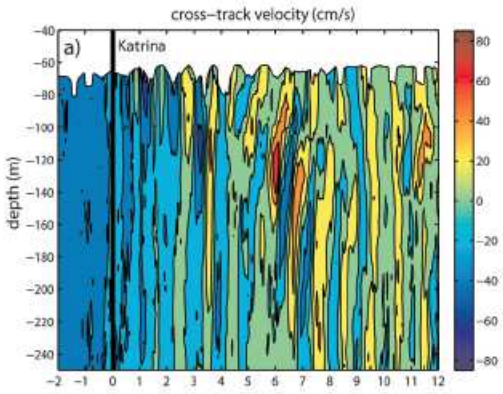

Figure 1.12 - Cross-track velocity response at a mooring site during hurricane Katrina. Figure from Jaimes and Shay [2009].

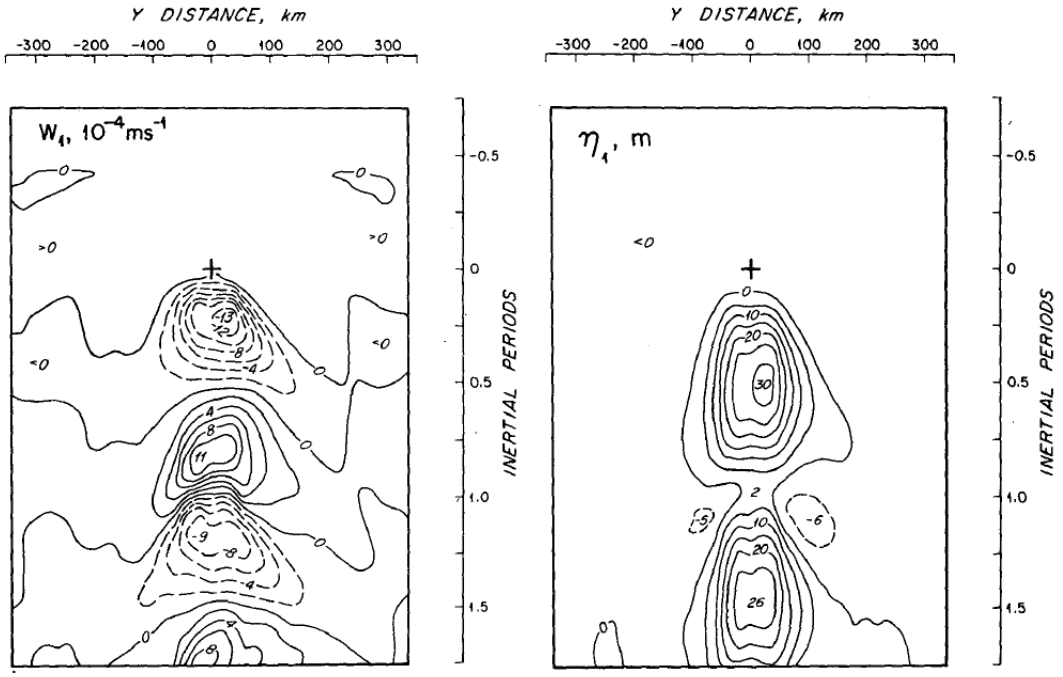

Figure 1.13 - TC-induced (a) inertial pumping ($10^{-4} m.s^{-1}$) and (b) upwelling just below the base of the mixed layer (m) for hurricane Eloise case. Negative values in (a) indicate upward motion, which tends to reduce the mixed layer depth. Figure from Price [1981].

1.3.3 The role of ocean structure and dynamics

Ocean heat transports associated with mixing and upwelling are dependent on upper ocean stratification, which is modulated by surface ocean dynamics. The ocean is structured at different and interacting scales: large-scale, regional scale, mesoscale and submesoscale. Mesoscale activity, *i.e.*, the formation and evolution of cyclonic and anticyclonic ocean eddies on the scale of baroclinic deformation radius, shapes the upper thermocline: shallower (deeper) mixed layer is observed for cyclonic (anticyclonic) eddies. The ocean response to TCs over mesoscale

structures were investigated mainly in the Gulf of Mexico [*e.g.*, Bao et al., 2000; Jaimes and Shay, 2009] where the Loop Current (LC) releases large anticyclonic warm core eddies (WCEs) with positive sea level anomaly and deep mixed layer, *i.e.*, higher heat content. In this case, it is noticed that mixing produced by extreme winds is less efficient as a surface cooling process (Fig. 1.14a). On the contrary, a cold core cyclonic eddy (CCE) tends to enhance surface cooling (Fig. 1.14b). Mesoscale eddies are also known for their effect on the efficiency of vertical radiation of near-inertial motions, as their frequency is shifted by the background relative vorticity [Kunze, 1985]. They may even be trapped in the eddy field, enhancing mixing depending on the sign of vorticity [Jaimes and Shay, 2010]. Obviously, upwelling and mixing are complex and interactive processes at multiple scales. Our approach using long-term simulations with realistic models will permit to bring together all this complexity and provide more realistic estimates of their effects.

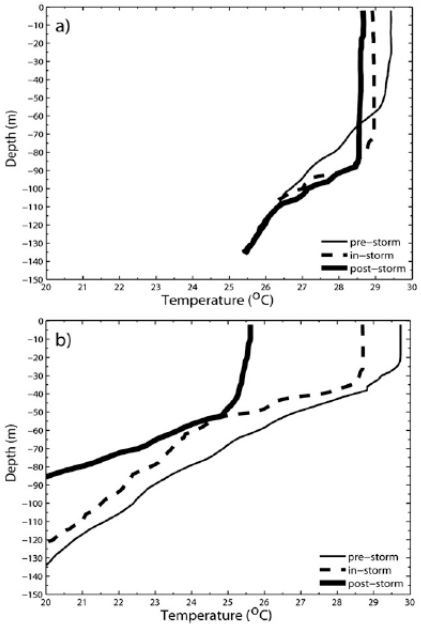

Figure 1.14 - Upper-ocean temperature profile changes induced by hurricane Rita: (a) in the Loop Current (LC) bulge and (b) in the cyclonic circulation of a growing cold core eddy from airborne profiler clustered data. Figure from Jaimes and Shay [2009].

1.3.4 Impact on the ocean climate

Upwelling is generally considered as a reversible process that has no lasting effect. Yet, vertical advection is a non-linear process interacting with the background flow and may affect the heat and salt budgets over considerable distances. We will see in this thesis that its long-term impact has also been underestimated and misunderstood in previous studies. By contrast, mixing, an irreversible process, was emphasized for injecting heat below the surface. This process called *ocean heat uptake* is assumed to exactly balance sea surface cooling (Fig. 1.15; Emanuel,

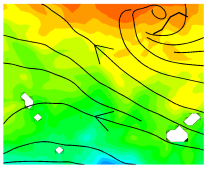

2001; Sriver and Huber, 2007). The heat uptake is then assumed available for poleward transport by the meridional overturning circulation [Emanuel, 2001]. Based on this idea, TC-induced meridional heat transport was estimated by generally applying an *ad-hoc* mixing coefficient [Manucharyan et al., 2011] and resulted in TC contribution to heat transport of 10 to 20%. However, several mechanisms are misconceived in this approach, which we believe largely overestimates the importance of TCs on the climatic scale (see also Vincent et al. [2012c]). First, mixing is a nonlinear process that cannot be simply modeled using scale analysis. Second, ocean heat uptake does not balance SST cooling because of the interaction between mixing and upwelling and because a large amount of this uptake is released back to the atmosphere in winter. These mechanisms and their quantitative effects are analyzed in this work.

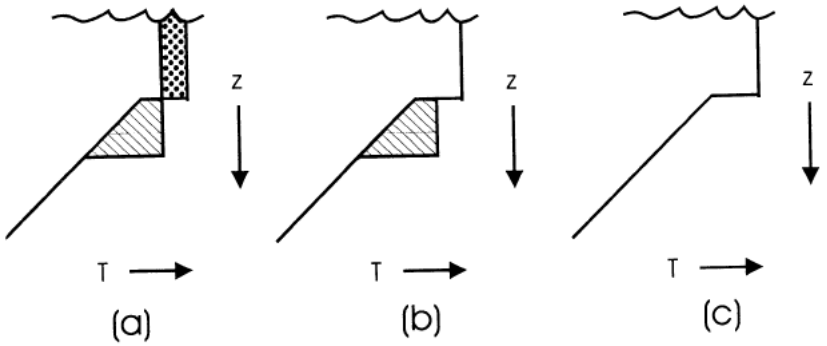

Figure 1.15 - Schematic picture of the steps of Emanuel's hypothesis on TC-induced ocean heat uptake. (a) Strong mixing deepens the mixed layer, creating a cold anomaly at hte top (dotted) and a compensating warm anomaly below (striped). (b) The cold anomaly is removed by net surface enthalpy fluxes. (c) The warm anomaly is removed advectively by buoyancy adjustement to the surrounding ocean. Figure from Emanuel [2001].

1.4 Ocean feedback to tropical cyclones

TC-ocean interactions are essential for cyclone formation and evolution. Ocean heat content is the fuel of TCs. In return, extreme winds inject mechanical energy into the ocean and modify its structure. Modifying the surface ocean heat content, the cold wake has the potential effect of negative feedback on TC intensity (*e.g.*, Bender et al., 1993; Holland, 1997; Schade and Emanuel, 1999; Figs. 1.16 and 1.17). Stronger TCs induce stronger cooling that in turn would produce stronger feedback. The question is on the quantification of SST feedback to storm intensity. The thermodynamical theory [Emanuel et al., 1994; Holland, 1997] appears to overestimate the feedback effect compared with observations and realistic modeling case studies. The discrepancy may be related to the assumed intensification process. The WISHE concept implies a large feedback of SST cooling (Emanuel [1999] suggests that a 2.5°C cooling could totally shut down energy supply) while the CISK concept puts much weaker emphasis on surface

fluxes (more on storm-scale humidity convergence) and implies a weaker feedback effect [*e.g.*, Chang and Anthes, 1979; Sutyrin, 1979]. A better understanding and quantification of ocean-cyclone interactions is therefore required. Our work will provide valuable insights.

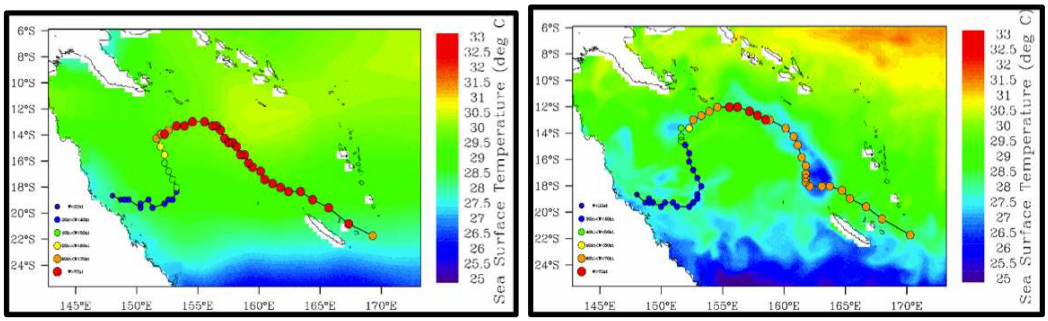

Figure 1.16 - SST field and intensity of TC Erica (2003) along its track simulated in (a) forced and (b) coupled ROMS-WRF models. Figure from Lemarié [2008].

Air-sea fluxes are poorly known in general and in particular for extreme events where measurements are impractical. Their evaluation thus remains challenging. Radiative fluxes are better known than turbulent fluxes as they are provided by remote satellite measurements. Usually, turbulent air-sea fluxes are computed using bulk formula that have parameterized exchange coefficients between the ocean and atmosphere for heat, humidity and momentum. The transfer coefficients known as surface drag coefficient, C_D, and enthalpy exchange coefficient, C_K, are the subject of much research [Charnock, 1955; Powell et al., 2003; Donelan et al., 2004]. The idea is generally to find the best fit to *in situ* observations for all situations. However, the variety of sea states and the large range of wind speed make this task difficult. The transfer coefficients for mature swell are generally consensual, but limited fetch young waves and extreme wind conditions can have various and opposite effects. Large and slow (young) waves increase surface roughness and thus the exchange of heat and momentum with negative feedback on wind speed [Doyle, 2002]. On the other hand, sea-spray, *i.e.*, droplets torn by extreme winds or produced by breaking waves, promote heat and humidity exchanges as they easily evaporate, leading to increased heat supply to TCs. This represents a positive feedback to cyclonic winds [Bao et al., 2000]. Finally, foam layers act as slipping layers that limit heat and momentum exchanges. As all these processes arise concurrently, the parameterization of exchange coefficients under extreme wind speed conditions is problematic (see also Chapter 6 Section 6.2.2).

On the issue of transfer coefficients, we will use a conservative approach (with the Charnock relation) and leave the wave interface coupling for further research. Our objective is focused on the feedback effect of storm-induced SST cooling. This effect is thought as the primary source of interaction between tropical cyclones and the ocean.

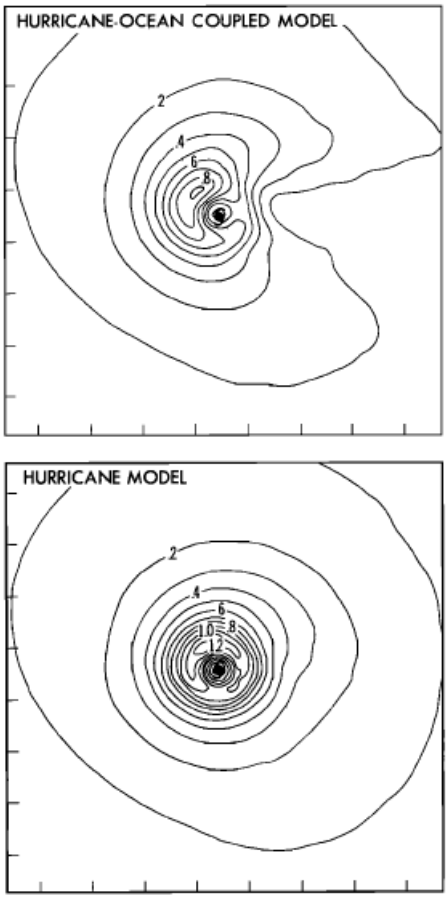

Figure 1.17 - Total surface heat flux ($kW.m^{-2}$ (positive value directed upward into the atmosphere) averaged over 72 hours from idealized model experiments (top) with air-sea coupling and (bottom) whithout coupling. Tick marks are 1° intervals. Figure from Bender et al. [1993].

1.5 State of the art modeling of tropical cyclones

Tropical cyclone modeling has gradually improved with increasing computing power, more sophisticated models and data assimilation techniques. The large range of scales and processes involved in the tropical cyclone formation and evolution and their interaction with the ocean would suggest to use mesoscale or cloud-scale coupled models rather than climate models. However, high-resolution models are complex and still computationally expensive. Until now, only few attempts have been made and they were all based on case studies. Other investigations have used simpler models based on a certain number of assumptions.

The resolution needed to resolve the TC dynamics and its small scale processes such as convection, vortex Rossby waves and mesovortices is very high. Figures 1.18 and 1.19 show precipitation and vertical velocity fields that can be obtained with different resolution and model configurations. At 35 km resolution, even though small-scale convective processes are parameterized, the overall TC struc-

ture is captured, showing eye and eyewall, intense precipitation and rain bands that spirals around. The structure of the vertical velocity field with a tilted eyewall is also correctly represented. The main issue at such mesoscale resolution is that vertical velocities are under-estimated, thus preventing the formation of the most extreme TCs [Gentry and Lackmann, 2009].

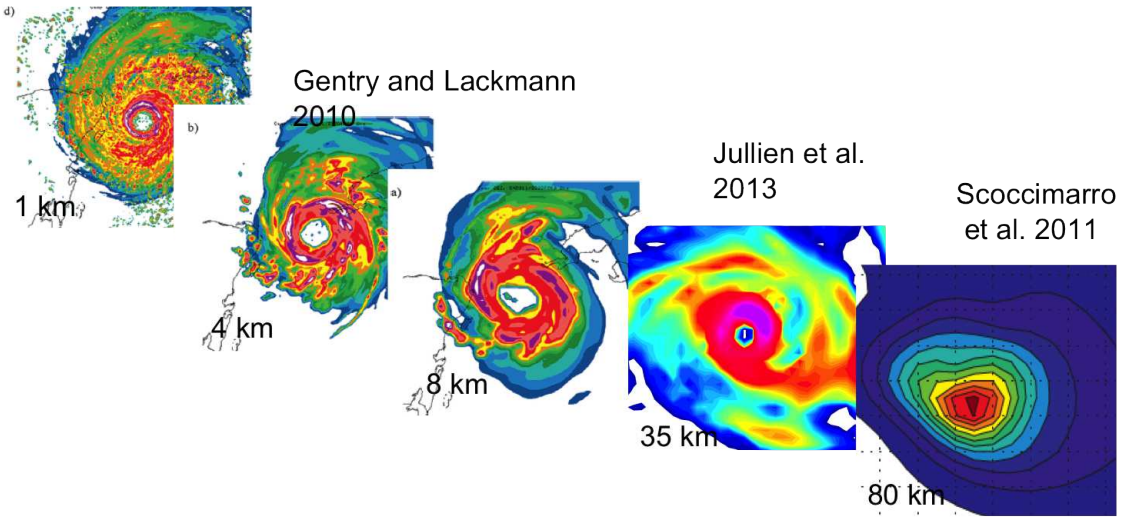

Figure 1.18 - Instantaneous precipitation field from Gentry and Lackmann [2009] at 1, 4, 8 km resolution in WRF, from our study at 35 km resolution in coupled WRF-ROMS and in Scoccimarro et al. [2011] at 80 km resolution in a CGCM.

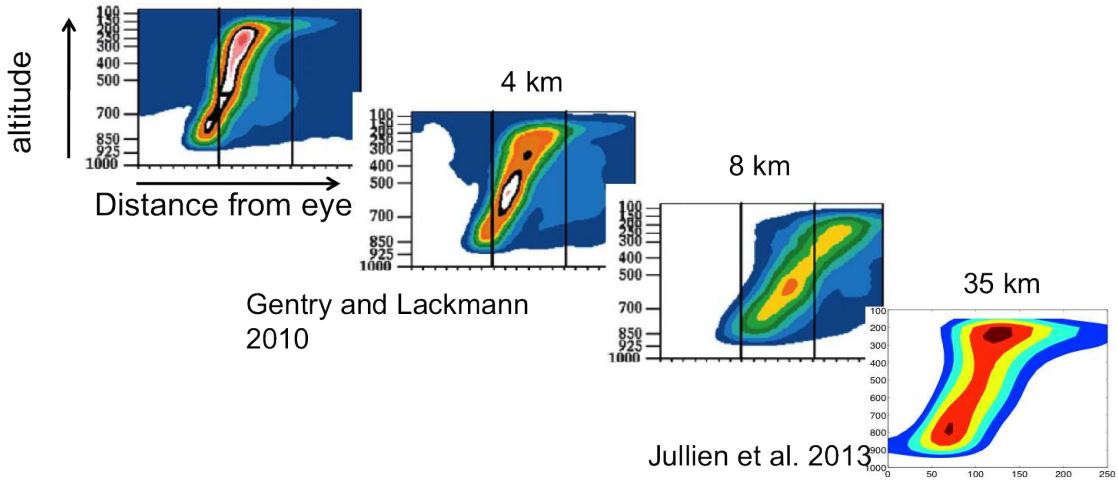

Figure 1.19 - Vertical velocity section composite from Gentry and Lackmann [2009] at 1, 4, 8 km resolution in WRF and from our study at 35 km resolution in coupled WRF-ROMS.

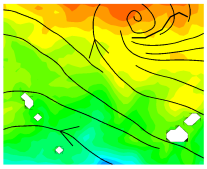

1.5.1 Climate models

The recent attention given to climate change has stimulated the use of global climate models to study changes of tropical cyclone activity in future scenarii. Yet, global climate models still have insufficient resolution (1° or 2°) to correctly represent TCs and fail also in some regions to accurately represent the favorable environmental conditions for tropical cyclogenesis. At coarse resolution, models only produce *cyclone-like* vortices, which are vortices presenting some characteristics of tropical cyclones but much lower intensities [*e.g.*, Sugi et al., 2002; Camargo et al., 2005; Scoccimarro et al., 2011]. Their relevance to TC activity remains difficult to assess [Gray, 1998; Camargo et al., 2007]. Increased resolution at 0.5° in more recent global models appears to improve the representation of cyclones [*e.g.*, Chauvin et al., 2006; Zhao et al., 2009] but the computational cost of these models limit the number of possible experiments that are needed for tuning the model and for exploring its parameter sensitivity. In addition, the goal of global models is to compute the best global solution at the expense of regional ones. In particular, global models generally fail in representing the South Pacific climate [Zhao et al., 2009; Bador et al., 2012].

To investigate the ocean response to TCs, coarse atmospheric solutions are of poor interest because their underestimated wind magnitude have a corresponding low response in the ocean through mixing and upwelling processes. Pasquero and Emanuel [2008] used the Massachusetts Institute of Technology global ocean model with 4° horizontal resolution and 20 vertical levels. They forced the ocean model with coarse fluxes but added a temperature perturbation over the regions of strong TC activity to simulate their mixing effect. A similarly rough technique was employed by Manucharyan et al. [2011]. The approach is crude, relying on a single process (mixing) that is largely misconceived.

1.5.2 Simple coupled models

Earlier coupled experiments used axisymmetric TC models coupled with a simple slab ocean mixed layer [*e.g.*, Chang and Anthes, 1979; Sutyrin, 1979]. In a slab model, the ocean response is controlled by a balance between surface fluxes and entrainment of deep water of pre-defined temperature. Their is no representation here of Ekman pumping or shear instability associated with near-inertial motions. In the TC model, the energy growth rate is balanced by horizontal diffusion and surface friction while the balance of water vapor is achieved by evaporation, horizontal advection and precipitation. Emanuel [1995] designed another type of axisymmetric hurricane model that assumes gradient-wind and hydrostatic balance. This strongly constrains the vortex structure. Moist convection is represented by a one-dimensional plume whose mass flux is specified to ensure the entropy equilibrium of the boundary layer. This model has the advantage of thermodynamic consistency for assessing the effect of surface heat fluxes on the TC intensity but has oversimplified dynamics for the ocean and atmosphere. An improvement was proposed by [Schade and Emanuel, 1999] using a 3-layer ocean model (mixed layer, thermocline, deep ocean) that allowed internal-wave

dynamics. Before that, Price [1981] also used a 3-layer ocean model but included a representation of Ekman pumping.

1.5.3 Realistic coupled models

Three-dimensional primitive equation ocean models, assuming hydrostatic balance and incompressibility, allow a full description of the ocean heat budget affected by TCs [Price et al., 1994; Huang et al., 2009]. Until now, their use was limited to the study of TC events and focused mostly on surface processes. In chapter 4 of this manuscript we propose a full description of the ocean response to TCs using a similar model but on a great number of events ($\sim$ 200) produced by a 25-year long simulation.

Realistic coupled experiments with 3D ocean and atmosphere models started quite recently. Bender et al. [1993] originally used a simple 3-layer ocean model coupled with the NOAA-GFDL multiply nested movable mesh (1°-1/3°-1/6°). They conducted various idealized simulations comparing the feedback effect of SST cooling. More recently, Bender and Ginis [2000] coupled the same atmospheric model with the primitive equations Princeton Ocean Model. They performed 163 nowcasts during the 95-98 North Atlantic cyclonic seasons and showed that the mean absolute forecast error of central pressure could be reduced by about 26% with the coupled model compared with the operation GFDL model.

The effect of waves in realistic coupled models was investigated by Bao et al. [2000]. They coupled the PSU/NCAR mesoscale atmospheric model MM5 (with 45-15km resolution) with the WAve prediction Model (WAM) and the Colorado University Ocean Model (CUPOM, at 1/5° resolution). They conducted idealized experiments over the Gulf of Mexico including the effect of sea spray evaporation and wave age. Sandery et al. [2010] coupled the Bureau of Meteorology's Tropical Cyclone Limited area Prediction System (TC-LAPS; at 0.15° resolution and 29 sigma levels) and the Ocean Forecasting Australia Model (OFAM; at 1/10° resolution and 47 vertical levels) with the OASIS-3.1 coupler. In this case, momentum coupling relies on a so-called inertial relation of surface bulk formulations in the atmosphere and ocean (rather than a transfer of the atmospheric momentum to the ocean). This relation accounts for the waves as a moving reference, not for its effects on the surface drag, which is a weakness of the method. The model was applied on real events of the Australian region.

1.5.4 Long-term regional simulations

Regional models represent a cost-effective alternative for simulating multiple seasons of TC activity. They also benefit from a geographical focus that allows better adjustments of parametrizations, and from the opportunity of controlling lateral inputs. Despite these advantages, few attempts were made at running long-term regional TC simulations.

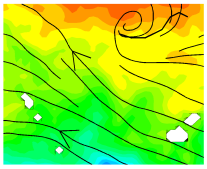

Long-term regional studies of the South Pacific at mesoscale resolution (30-35 km) were conducted in the South Pacific by Walsh [2004] using the CSIRO Division of Atmospheric Research Limited area Model (DARLAM) and by Jourdain et al. [2011] using the Weather Research and Forecast model (WRF). These models generate intense TCs, with structures that are often in good agreement with dropsonde data. Spatial and temporal TC distributions are also realistic (at seasonal and interannual timescales). The intensity distribution is good but miss the strongest cyclones (cloud-scale models with resolution of 1-2 km are required for that; see Gentry and Lackmann, 2009), but those are very rare events. Mesoscale configurations have thus the advantage of covering a large range of space and time scales.

Nevertheless, there usage was limited until now to the atmospheric circulation, neglecting interactions with the ocean, *i.e.*, the feedback from storm-induced SST cooling. To respond to the challenge, we updated the model configuration of Jourdain et al. [2011] and coupled it to the Regional Ocean Modeling System (ROMS). In doing so, we filled a gap between case studies and coarse resolution climate models.

1.6 Manuscript outline

The objective of the present work is to investigate the coupled mechanisms at play in tropical cyclones. First the oceanic response to TCs, then the ocean feedback are assessed. Contrasting with previous studies of individual events, our analysis is for the first time applied on 20-year realistic simulation of TC activity computed from a regional coupled model of the South Pacific.

Chapter 2 describes in details the coupled model and its configuration, the choice of parametrization and parameter sensitivity experiments. The design of twin coupled and forced simulations that reveals the coupling effects in the analysis is presented, with also the methodology developed to treat the great number (150-200) of simulated TCs.

Chapter 3 presents the South Pacific dynamics and model performances for the regional climate and TC climatology. The seasonal and interannual variability of the South Pacific Convergence Zone and cyclogenesis are assessed and the respective parts of forced and stochastic variability are evaluated.

The impact of TCs on the full 3D ocean heat budget is detailed in Chapter 4. It shows a complete description of the ocean structure changes induced by TC occurrence. The oceanic response is first addressed at the cyclone scale before assessing its lasting effect on the ocean climatology. The use of a composite method representing the average of all simulated TCs highlights the most robust features of their effect.

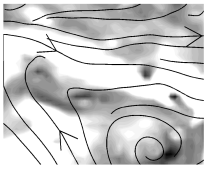

The ocean feedback on TCs is finally studied in Chapter 5. It presents the modification of air-sea fluxes by SST cooling and associated reduction of the TC heat supply. The role of the oceanic structure and dynamics in modulating the ocean feedback to TCs is examined. Regional patterns of coupling sensitivity are deducted. Finally, TC intensification theories are discussed in the view of our results.

Chapter 6 summarizes the conclusions and novel results of the thesis. We then propose future directions for the continuation and application of this work.

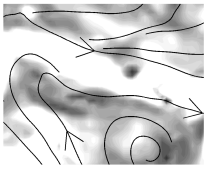

Chapter 2

Development of a coupled model for the South Pacific

Contents

2.1 Models 26
2.1.1 Atmospheric model: WRF 26
2.1.2 Ocean model: ROMS 29
2.1.3 Coupler 31
2.2 Sensitivity tests 35
2.2.1 Convection 35
2.2.2 Planetary boundary layer (PBL) 37
2.2.3 Cloud microphysics 38
2.2.4 Shortwave radiation 38
2.2.5 Surface drag 39
2.2.6 Skin SST 41
2.2.7 Land surface model 42
2.2.8 Sponge layers 43
2.2.9 Sensitivity to vertical resolution 43
2.3 Methodology 43
2.3.1 TC tracking and SPEArTC database 43
2.3.2 Forced model: cold track filtering technique 47
2.3.3 Statistics and error bars 49
2.3.4 Compositing methodology 53
2.4 Summary of the experiments 54

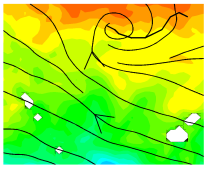

Our objective is to analyze the ocean-atmosphere coupling processes that influence tropical cyclonic activity and the ocean response to this activity. We propose a statistically robust approach using long-term simulations of the South Pacific present climate that produce a great number of tropical cyclones (150-200 TCs). This requires a coupled model of the South Pacific region with good capabilities in simulating the present climate at large scale and at cyclone scale. To that end, we developed a coupled framework that was submitted to numerous sensitivity tests to select the best set of parameters and parameterizations for the representation of the regional climate and cyclonic activity. The coupled system and sensitivity experiments are described in this chapter. Some statistical methods to assess error bars in our model solutions will also be presented.

2.1 Models

2.1.1 Atmospheric model: WRF

The regional Weather Research and Forecast model (WRF) was chosen for this study in continuation to the work of Jourdain et al. [2011]. It is a three-dimensional regional community model that resolves compressible, non-hydrostatic Euler equations. We use the Advanced Research WRF (ARW) dynamic solver [Skamarock and Klemp, 2008] as it was specially designed with high-order numerical schemes to enhance the model's effective resolution of mesoscale dynamics [Skamarock, 2004] which is the point of our study. WRF also includes a large set of parameterizations that can be selected and adjusted for a given problem. It is widely used all over the world as it provides, in addition to state-of-the-art methods, great support from developers and the whole users community. New releases of the model are regularly (almost every year) proposed. We chose the version 3.3.1 as it was the latest release available at the beginning of my work, but updated from the version 2.2 used in Jourdain et al. [2011]. As parametrization schemes can change from one release to another, it was necessary to test again the chosen set of parameterizations and eventually adjust some parameters to correctly represent the regional dynamics.

The WRF simulation of Jourdain et al. [2011] were analyzed to present the climatology and interannual variability of South Pacific TC distribution (this simulation will be used to force our ocean model in the first part of the results of the thesis). They evaluated the effective resolution of the model for a 35-km grid resolution. The effective resolution of a model can be defined as the scale at which the model kinetic energy spectrum decays relative to the expected spectrum [Errico, 1985; Skamarock, 2004] which is the $k^{-5/3}$ Kolmogorov scaling law describing motions at scales below 1000 km. Figure 2.1 shows that the model effective resolution is 155 km (break in the slope) that is 5 times the grid resolution. This is finer than most of mesoscale convective systems ($\sim$ 250 km) from which tropical cyclones form [Gray, 1998].

At the boundaries of the regional model, forcing from the 6-hourly National Centers for Environmental Prediction Reanalysis 2 [NCEP-2 reanalysis; Kanamitsu et al., 2002] is applied. Figure 2.1 shows also that NCEP-2 effective resolution is 1250 km and that the NCEP2 forcing conditions are properly passed down to WRF since the spectra obtained for WRF and NCEP-2 are very similar for scales larger than 3000 km.

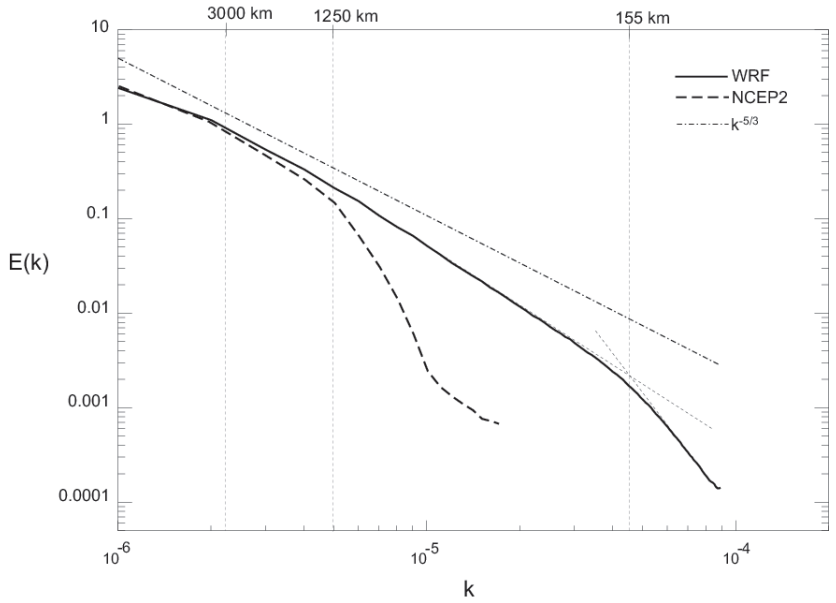

Figure 2.1 - 1981 summer (January-March) wavenumber spectra of surface kinetic energy for WRF model (solid bold curve), NCEP2 reanalysis (dashed bold curve) and theoric Kolmogorov law (dotted-dashed curve). The kinetic energy E is in Joules, the wavenumber k in m^{-1}. Figure from Jourdain et al. [2011]

The regional domain of simulation encompasses the Indo-Pacific region (89.83°E-240.18°E/41.21°S-21.62°N) in order to properly resolve mesoscale activity around the convergence zones (Inter Tropical convergence Zone, ITCZ, and South Pacific Convergence Zone, SPCZ). Our experience is that boundary forcing located too close to these zones introduces strong biases. A two-way nesting is used to refine the resolution in the region of interest (southwest Pacific) and limit the computational cost. The parent domain has a 105-km resolution and the child domain (139.62°E-200.02°E/31.40°S-1.62°S) 35-km resolution (Fig. 2.2). This 3:1 ratio is generally recommended for nesting as it avoids sharp changes of scales and dynamic regimes across embedded grids. Two-way nesting consists in (at each model time step of 300 s): computation of the parent solution; interpolation of parent solution on the lateral boundaries of the child domain; advancing the child solution for 3 time steps (100 s each); providing a feedback of the child solution to the parent grid (*i.e.*, interpolated at the parent domain resolution) for the next computational time step of the parent domain.
The model uses a C-grid (Fig. 2.3) with 31 terrain-following vertical levels with refinement in the planetary boundary layer (PBL) and in the upper troposphere

(Fig. 2.3). Other vertical resolutions and refinements have been tested and are presented in section 2.2.

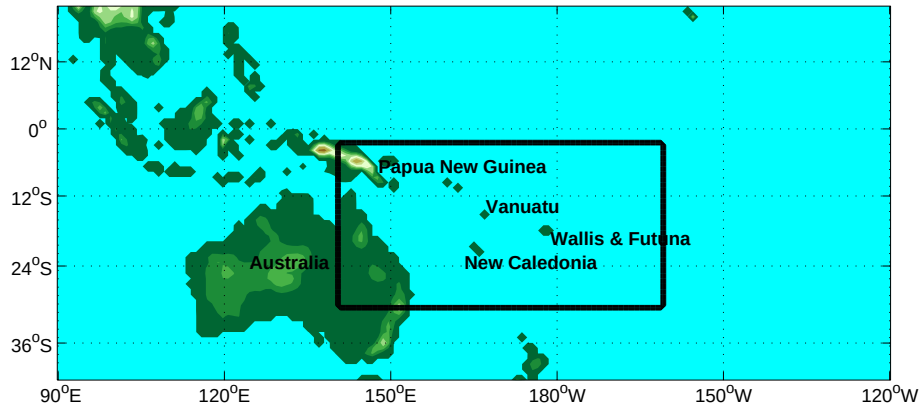

Figure 2.2 - Simulation domain. Shading represents the terrain height. The rectangle black box represents the limits of the child domain.

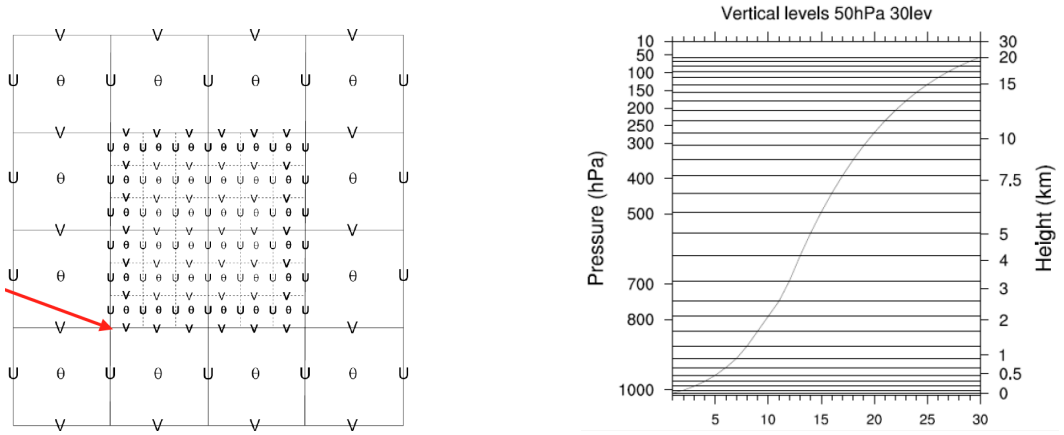

Figure 2.3 - (a) C-grid of the WRF model with nesting. The red arrow points to the (i, j) position of the nest in the parent domain. (b) Distribution of the 31 vertical levels in our WRF configuration.

The configuration and choice of parametrization is very similar to that of Jourdain et al. [2011] and was selected to realistically represent the large-scale environment and related tropical cyclone activity in the Southwest Pacific. The details of the whole set of parameterizations used can be found in the model namelist and parameterization short description (see Appendices A and B). Physical parametrizations include the Betts-Miller-Janjic (BMJ) convective scheme; the Yonsei University (YSU) planetary boundary layer (PBL) with Monin-Obukhov surface layer parameterization; the WRF single-moment three-class microphysics scheme (WSM3); the Dudhia shortwave radiation scheme; and the Rapid Radiation Transfer Model (RRTM) for longwave radiation. The surface drag coefficient

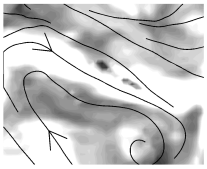

is given by the classical Charnock relation. Sensitivity tests on these parameterizations are presented in section 2.2 as some of the schemes (*e.g.*, BMJ) were significantly updated since version 2.2.

2.1.2 Ocean model: ROMS

The ocean model used is the Regional Oceanic Modeling System [ROMS; Shchepetkin and McWilliams, 2005]. ROMS solves the primitive equations in an Earth-centered rotating environment, based on the Boussinesq approximation and hydrostatic vertical momentum balance. In this study, we use the ROMS-AGRIF version of the model that has two-way nesting capability (not used here) and a compact package for implementation of realistic configurations [Debreu et al., 2012]. It is a split-explicit, free-surface ocean model, discretized in coastline- and terrain-following curvilinear coordinates using high-order numerical methods for reduction of small-scale numerical dispersion and diffusion errors. Associated with a 3rd-order time stepping, a 3rd-order, upstream-biased advection scheme allows the generation of steep gradients, enhancing the model's effective resolution [Marchesiello et al., 2011]. Because of the implicit diffusion in the advection scheme, explicit lateral viscosity is unnecessary, except in sponge layers near the open boundaries where it increases smoothly close to the lateral open boundaries. For tracers, a 3rd-order upstream-biased advection scheme is also implemented but the diffusion part of this scheme is rotated along isopycnal surfaces to avoid spurious diapycnal mixing and loss of water masses [Marchesiello et al., 2009; Lemarie et al., 2012].

The turbulent vertical mixing parameterization is based on the scheme proposed by Large et al. [1994], featuring a K-profile parameterization (KPP) for the planetary boundary layer connected to an interior mixing scheme (see section 4.6 for details). The boundary layer depth (h) varies with surface momentum and buoyancy forcing and is determined by comparing a bulk Richardson number to a critical value. The surface layer above the oceanic boundary layer obeys the similarity theory of turbulence. At the base of the boundary layer, both diffusivity and its gradient are forced to match the interior values. Below the boundary layer, vertical mixing is regarded as the superposition of three processes: vertical shear, internal wave breaking, and convective adjustment. The KPP model has been shown to accurately simulate processes such as convective boundary layer deepening, diurnal cycling, and storm forcing: it is widely used in ocean modeling [*e.g.*, Halliwell et al., 2011]. The model has also shown a reasonable level of accuracy in modeling TC-induced mixing [Jacob and Shay, 2003]. Some processes are nevertheless missing in this parameterization: for example, mixed layer instabilities that would further help the restratification process in the TC wake [Boccaletti et al., 2007] are neither resolved in our 1/3° resolution model nor parameterized [for tropical applications, see also Marchesiello et al., 2011].

Open boundary conditions are treated using a mixed active/passive scheme [Marchesiello et al., 2001] that forces large-scale information from the Nucleus for

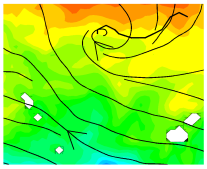

European Modeling of the Ocean (NEMO) global model while allowing anomalies to radiate out of the domain. The use of similar ROMS configurations in the south-west tropical Pacific region is largely validated through studies demonstrating skills in simulating both the surface [Marchesiello et al., 2010b] and subsurface ocean circulation [Couvelard et al., 2008].

Two different configurations of the ocean model are used along this thesis. The first one was used to study the ocean response to TC forcing. It is a 25-year (1979-2003) forced ocean simulation with NEMO 1/2° simulation forcing at the boundaries [described in Couvelard et al., 2008] and 41 terrain-following vertical levels with 2-5-m vertical resolution in the first 50 m of the surface and then 10-20-m resolution in the thermocline and 200-1000-m resolution in the deep ocean. The horizontal resolution is 1/3°, and the baroclinic time step is 1 h; hourly outputs are stored for a case study and 1-day- averaged outputs are stored for long-term analysis. In this first configuration The modeled domain is quite the same as the child domain of the atmospheric model (140°E-190°E/30°S-8°S, Fig. 2.4).
The second configuration is 20-year long simulation (1979-1998) coupled with WRF to study the feedback effect of storm-induced SST. It has 51 terrain-following vertical levels with 2-5 m resolution in the first 50 m, 10-20 m resolution in the thermocline and 50-250 m in the deep ocean. The oceanic domain is the same as the inner atmospheric domain (139.62°E -200.02°E /31.40°S -1.62°S) with the exact same grid and same 35-km horizontal resolution (no interpolation is needed to transfer data between the ocean and atmosphere). The interannual oceanic forcing is from the ORCA025 (NEMO 1/4°) global oceanic model simulation [Barnier et al., 2006] and applied at open boundaries with the mixed active/passive conditions described above.

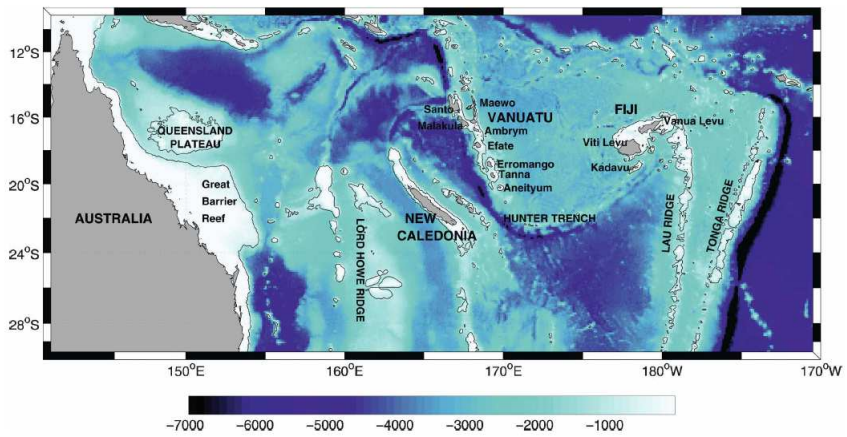

Figure 2.4 - Oceanic geography of the southwest Pacific. Shading is the ocean depth. Figure from Couvelard et al. [2008].

2.1.3 Coupler

2.1.3.1 Coupling methodology

The procedure of ocean-atmosphere coupling is not straightforward as it requires to ensure a continuity of heat and momentum fluxes at the air-sea interface. Two usual coupling approaches can be found. For global configurations [Bryan et al., 1998], it is based on the exchange of averaged-in-time fluxes on a given time window (between 1 hour and 1 day depending on the application and the need to resolve the diurnal cycle; Fig. 2.5). Over this time window, both models are forced by exactly the same mean fluxes which ensures strict conservation of the quantities. However, the models are not in exact balance as the modification of the ocean state does not feed the atmosphere model on the proper time window but only on the next one. This is thus only an approximation of the mathematical coupling problem and suffers from synchronization issues that may lead to a form of numerical instability [Lemarié, 2008; Lemarie et al., 2013].

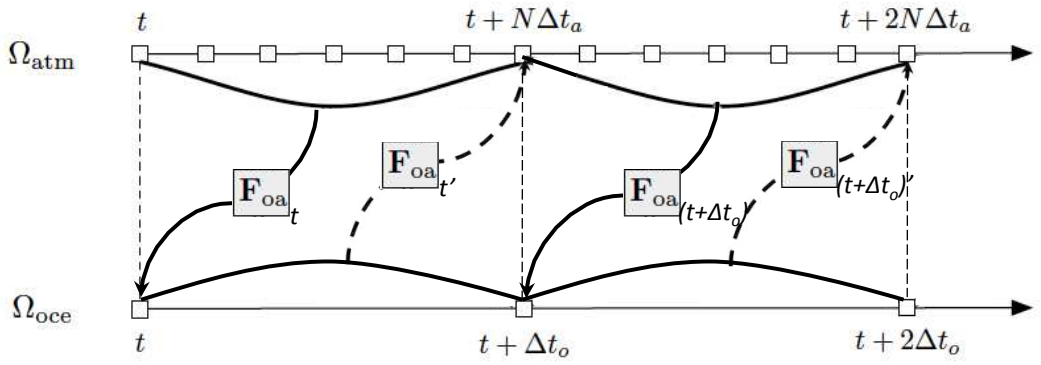

Figure 2.5 - Schematic picture of the coupling by time window.

For regional configurations using high-resolution grids [Perlin et al., 2007; Bao et al., 2000], the coupling is usually achieved by the exchange of instantaneous fluxes on the larger model time step (usually the ocean model time step, Fig. 2.6a). It is also possible to exchange integrated atmospheric fluxes over the coupling time step (Fig. 2.6b). This method has less synchronization issues (this method is sometimes referred to as synchronous) but may raise some conservation problems [Lemarie et al., 2013]. More importantly perhaps, the method is mathematically sound only if the coupling time step is small enough to represent the continuous exchange of fluxes between the ocean and the atmosphere. However, the sign of turbulent fluxes, involved in the computation of air-sea fluxes, can be uncertain on time scales less than 10 minutes and hourly fluxes are more relevant [Large, 2006]. This is explained by the lack of accurate knowledge and direct observations of fine-scale air-sea fluxes. Moreover, the empirical transfer coefficients involved in bulk formulations are calibrated through mean hourly measurements. To partly alleviate this problem, additional physical processes can be implemented in bulk formulations that are relevant to high-frequency coupling or extreme conditions.

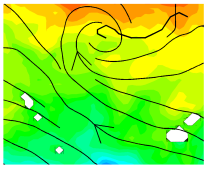

For tropical cyclones, relevant processes involves sea-spray contributions and wave age factors to turbulent exchanges in the wavy boundary layer [Bao et al., 2000]. In this case, it can be assumed that uncertainties in bulk fluxes are reduced and instantaneous fluxes may become more relevant. However, more research is needed in this direction.

Lemarié [2008] has proposed a compromising approach for synchronous coupling based on the time window framework. The method uses a global in time Schwarz method that consists in iterating the coupling procedure at each time step until flux computation converges. More specifically, the coupling algorithm, schematized in Figure 2.7, consists in the following steps:

1 Advancing the atmospheric solution on a given time window (coupling frequency), using the ocean model SST of the last time window (or the initial SST field at initialization).

2 Computing averaged surface momentum, heat and fresh water fluxes over the time window

3 Advancing the ocean model for the same time window using surface fluxes computed at step 2 for model forcing.

4 Advancing again the atmospheric model on the same time window using the ocean model SST computed at step 3 and computing again the averaged surface momentum, heat and fresh water fluxes over the time window

5 Comparing the fluxes computed at step 2 and 4 to evaluate the convergence (convergence is reached when the difference between computed fluxes is lower than a given threshold).

This algorithm ensures synchronization and a strict conservation between models. On the other hand, the iterative procedure considerably increases the computational cost of the coupling, especially when the convergence is slow. Lemarie et al. [2013] evaluates the performance of the coupling algorithm on the Erica tropical cyclone case in the South Pacific. They found that 3 iterations of the coupling algorithm was enough for convergence and to get rid of the numerical instability arising from synchronization lost. In our study, the need of long-term simulations prevents the use of an iterative process that multiplies by 3 our computational cost (see section 2.1.3.2). However, a compromise was found by reducing the coupling time window to 3 hours, which put us in a middle ground between synchronous and asynchronous methods. We performed sensitivity tests that compared the number of coupling iterations (1 *vs.*3 iterations) and found no particular improvement with the 3-iteration experiment. We conclude that the time window is small enough to prevent the numerical instability described by Lemarie et al. [2013], at least most of the time.

As a result of our experiments, we choose to use the coupler of Lemarié [2008] with only one iteration. This is equivalent to use the global-in-time coupling

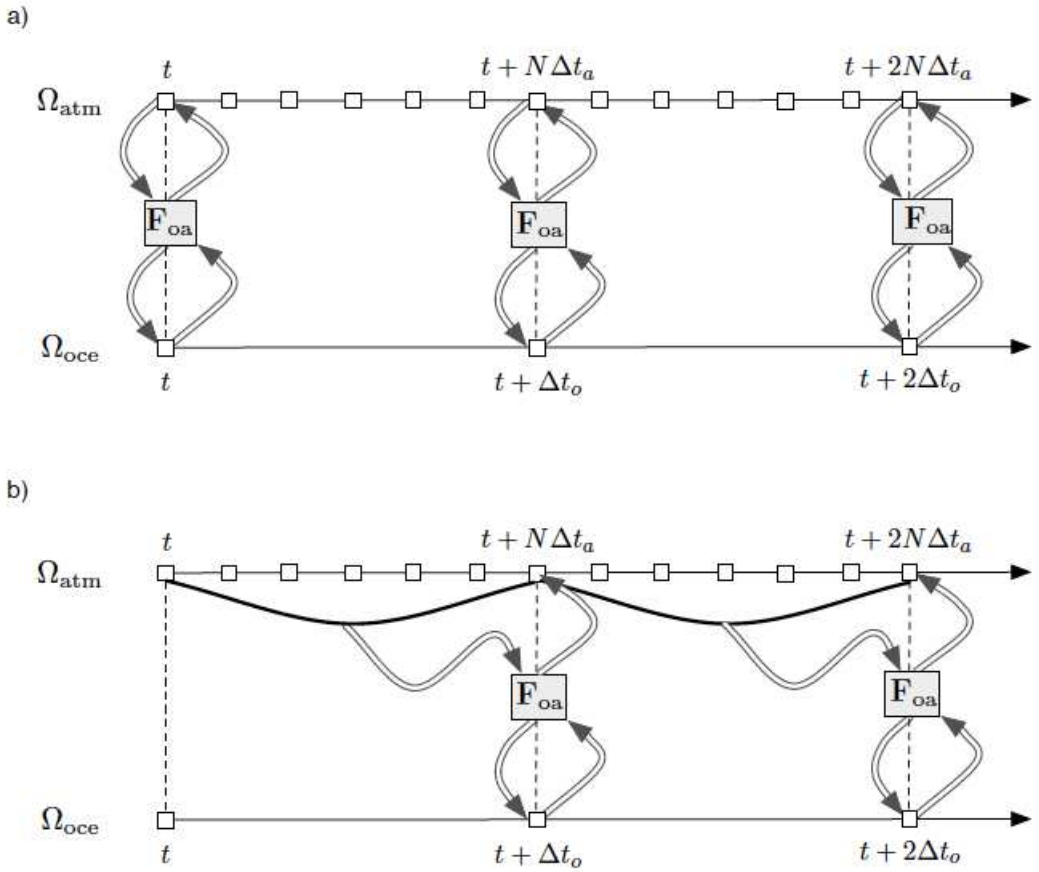

Figure 2.6 - Example of two coupling strategies at the time step level. t_o and t_a denote the (baroclinic) time steps respectively of the ocean and the atmosphere model, with $t_o = N t_a$ ($N = 6$ here). The arrows represent an exchange of information with the surface layer parameterization function F_{oa}. For the atmospheric component, this exchange is based on instantaneous values in algorithm a) and on time-integrated values in b). From Lemarie et al. [2013].

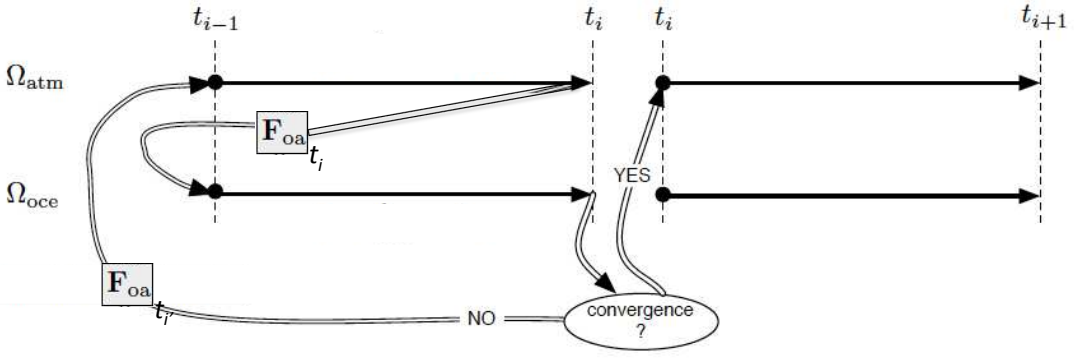

Figure 2.7 - Schematic picture of the iteration process to evaluate convergence in the Schwarz algorithm. Figure from Lemarie et al. [2013].

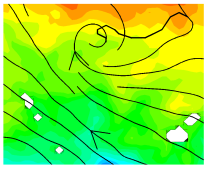

method first described above, but with small time windows of 3 hours. In this case, the OASIS coupler could be used with similar result (see section 2.1.3.3). At this coupling frequency, the diurnal cycle and storm displacement are also properly resolved. The coupling is performed in the high-resolution SPCZ domain (139.6-200.0°E / 31.4-1.6°S), *i.e.*, on the 35-km grid shared by both oceanic and atmospheric models. Figure 2.8 shows that with our choice of coupler and parameterizations, the coupled solution appears to have a balanced interface and does not drift away from the observed present climate, which is a usual problem of coupled models even in regional configurations.

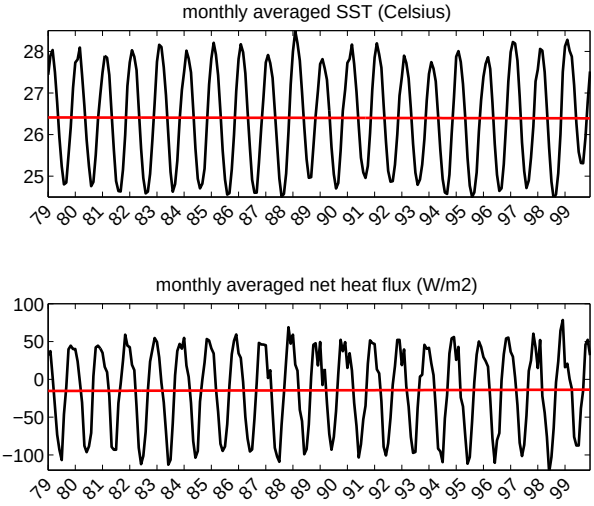

Figure 2.8 - 1979-1998 timeserie of the coupled model monthly mean values of (a) SST (°C) and (b) net heat flux ($W.m^{-2}$).

2.1.3.2 Computational performances

A coupled model configuration is complex and onerous, especially when long-term simulations are involved. Both atmosphere and ocean models are efficiently parallelized for distributed memory, message-passing architectures, and make good use of large PC clusters such as that proposed by the Computing Center of Region Midi-Pyrénées (CALMIP, Toulouse, France). However, our fortran coupler is not parallelized and more importantly, it is based on a large amount of additional input/output processing (at each coupling time window of 3 hours) that generates large runtime overhead. Both WRF and ROMS offers solutions to deal with parallel I/Os. WRF uses an I/O server that dedicates CPUs to the I/O process. ROMS parallelizes the I/O processes and distributes the load over the CPUs. Nevertheless, the relatively small size of the computational grids limits the number of processors that can be used and our tests indicated an optimal choice of 16 CPUs, which permitted to run one month of simulation in 6 hours wall-time, *i.e.*, 2 months wall-time for the whole 20 years of simulation.

2.1.3.3 Note on OASIS coupler

The OASIS coupler is widely used in the European ocean-atmosphere community, particularly in climate models. It operates via the Message-Passing Interface (MPI), thus avoiding any I/O implication. OASIS proposes various interpolation methods that enable the choice of different model grid resolution for the ocean and the atmosphere. It has also recently been parallelized (through its combination with the U.S. coupler MCT in OASIS3-MCT). However, OASIS only follows a synchronous-type algorithm (Fig. 2.6b) and does not enable neither iterative procedures to improve flux convergence nor conservative integral of fluxes over time windows. Finally, OASIS is more intrusive than our coupler (even though it is less so than many other couplers of the same type) and its implementation in the coupled system requires building interfaces for each models. In comparison, our simple Fortran coupler is totally external to the models. The work of OASIS implementation was in progress during my thesis and I took part in this development. It is now fully operational and available to the ROMS-AGRIF community.

2.2 Sensitivity tests

Numerous sensitivity experiments were conducted to select the optimal choice of configuration for the study of present-climate tropical cyclones in the South Pacific. WRF proposes many physical parameterizations. We partly relied on the work of Jourdain et al. [2011] but tested some updates between our versions and concentrated more effort to physics relevant to air-sea exchanges: the surface drag; shortwave radiation; SST skin; cloud microphysics and planetary boundary layer (PBL). Other aspects, such as the land surface model or the sponge layers at the model boundaries have also been investigated for improving the regional climatology and numerical model stability.

2.2.1 Convection

The convection scheme was thoroughly tested by Jourdain et al. [2011] in a similar WRF configuration and by Samson et al. [2013] in an Indian basin configuration (at 25km resolution coupled with NEMO) with similar results. These experiments essentially compared the Kain-Fritsch mass-flux formulation [KF; Kain, 2004] and relaxation scheme of Betts-Miller-Janjic [BMJ; Janjić, 1994] in their ability to sustain realistic representation of the regional climate and cyclonic activity. These comparisons are seldom conducted in long-term simulations and the results can be quite different. BMJ was shown to provide the best results, with a much better representation of South Pacific Convergence Zone (SPCZ). The simulated SPCZ using KF extends too far south (by 5-10°) and has a zonal orientation east of 170°E rather than the classical northwest-southeast tilt (Fig. 2.9).

BMJ is a convective adjustment scheme that had been initially developed for tropical regions and successfully tested in TC simulations [Baik et al., 1990]. Its success owes to realistic heating and moistening in the vertical due to a simple relaxation to observation-based reference profiles. Mass-flux schemes attempt

at representing entrainment/detrainment processes and updrafts/downdrafts as a kind of upscaling process between subgrid-scale convection and storm-scale circulation. These where initially developed to improve precipitation forecasts of synoptic events. For long-term simulations, the performances of KF (as well as the Grell-Devenyi scheme (GD); Grell and Devenyi, 2002) were disapointing.

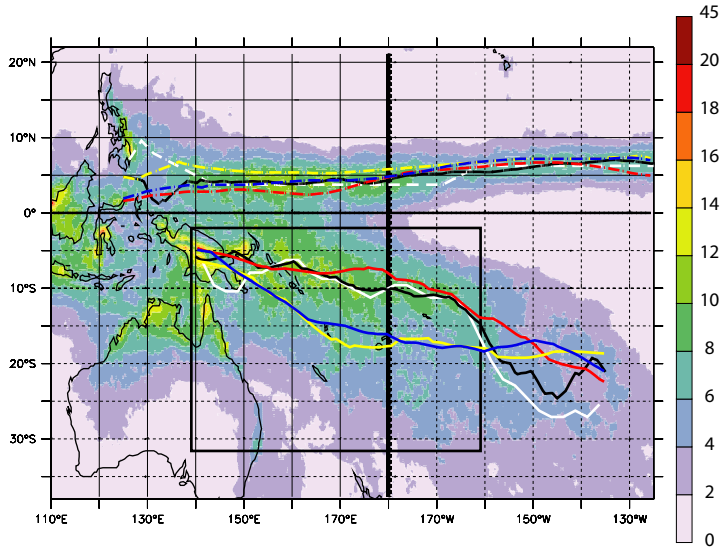

Figure 2.9 - Mean TRMM data JFM precipitation from 2000 to 2004 ($mm.day^{-1}$) with position of ITCZ (dashed) and SPCZ from: TRMM (black), GPCP (white), BMJ (red), KF (dark blue) and GD (yellow). The inner domain of integration is delimited by the black box. The lines representing the SPCZ are defined as maxima of the meridionally smoothed precipitation field. Figure from Jourdain et al. [2011]

The difference between convection schemes was even greater for TC activity. BMJ provides a realistic number of TCs in the South Pacific while KF produces three times the observed TCs (Jourdain et al., 2011; twice in the Indian ocean according to Samson et al., 2013). The impressive result from the mass-flux scheme maybe related to parameter tuning or more generically to the interplay between subgrid-scale and grid-scale convection. Our understanding is that KF tends to accelerate the initialization phase of cyclogenesis by the parametrization of strong updraft. If BMJ offers better TC counts, it only produces moderate TCs (with winds at a maximum of about 45 $m.s^{-1}$), while KF produces more intense TCs. This limitation in TC category is due to the limited horizontal resolution of 35 km. Here, we find useful the remark of Gray [1998] that the most recent convective schemes are probably too preoccupied with catching the full intensity of TC properties in the later formation stages, as it represents the essential task for event forecasters who bypass the earlier stages using data assimilation, than to realistically represent the whole cyclogenesis process and effective number of cyclones. Following Jourdain et al. [2011] and Gray [1998] remark, we choose BMJ as the best scheme for regional climate and cyclonic activity of the southwest Pacific.

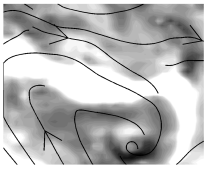

Important note: In the BMJ scheme, a cloud efficiency parameter (EFI between 0 and 1) was introduced to improve the original Betts-Miller scheme. This allowed a modulation of the timescale of convective adjustment (between 1 and 2 hours) by acting on the efficiency of precipitation for a given change of the *environment*. Smaller is the cloud efficiency, longer is the timescale and smaller is convective precipitation. By setting a set of environmental parameters controlling cloud efficiency, Janjić [1994] could improve the convective response to various climatic regimes (without relaying on a set of convective timescale for each of these regimes). Different values for these parameters are found in various WRF releases (giving higher values of EFI in the 3.3 than in the 2.2 release), which explains the difference of precipitation rates obtained in our study compared with Jourdain et al. [2011]. We found that changing EFI parameters of WRF 3.3 to lower cloud efficiency gave more realistic precipitation climatology for the Southwest Pacific. This requires for example modifying the following line in module_cu_bmj.F :

& ,DTTOP=0.,EFIFC=5.0,EFIMN=0.20,EFMNT=0.70 &
by
& ,DTTOP=0.,EFIFC=5.0,EFIMN=0.10,EFMNT=0.20 &

Since there are no indications in the WRF tutorial and forum that this important set of parameters can be tuned, it is probably a valuable piece of information to other WRF users in regional climate studies.

2.2.2 Planetary boundary layer (PBL)

The Yonsei University Planetary Boundary Layer [YSU; Noh et al., 2003] with Monin-Obukhov surface layer parametrization was chosen. It is a non-local K-profile closure scheme with explicit entrainment layer and parabolic K profile in unstable mixed layer that has been proved to correctly represent mixing under storms conditions. We also tested a one-dimensional prognostic turbulent kinetic energy (TKE)scheme, the widely used Mellor-Yamada-Janjic (MYJ) scheme. We found it to strongly limit convection and therefore the formation of TCs, which is of course a significant problem for our study. This is consistent with the known disadvantage of TKE-closure, *i.e.*, weak non-local turbulence aspects with poor entrainment at the PBL top as a result (TKE schemes are also known to require higher vertical resolution to function optimally). MYJ is more often used with success in the stable regime of PBL. For example, a study evaluating WRF parameterization on some events over southwest Australia found that the weak convection shown by the combination of BMJ and MYJ was an advantage in their study [Evans et al., 2012]. Interestingly, we tried more successfully another TKE-closure formulation recently implemented in WRF: the University of Washington scheme [UW; Bretherton and Park, 2009].The results of this test showed no appreciable differences in climatology between UW and YSU, which we would attribute to some efforts devoted to the entrainment processes in UW compared to MYJ. Nevertheless, our preference remains to YSU as in Jourdain et al. [2011]. It is relatively simple and cost effective with good performances in

the convective regime [see also Hill and Lackmann, 2009].

2.2.3 Cloud microphysics

The choice of cloud microphysics parameterization was also investigated. We tried the single-moment 3- and 6-class schemes (WSM-3 and WSM-6). WSM-3 is a simple but robust and cost-effective model with 3 hydrometeors (including ice). It provided more realistic rain and wind conditions in our mesoscale resolution than WSM-6. The latter produced excessive rain (Fig. 2.10) and overly fast vertical motions, although it provided a more realistic representation of clouds, compensating for underestimation by BMJ convection. WSM-3 remained our choice as in Jourdain et al. [2011].

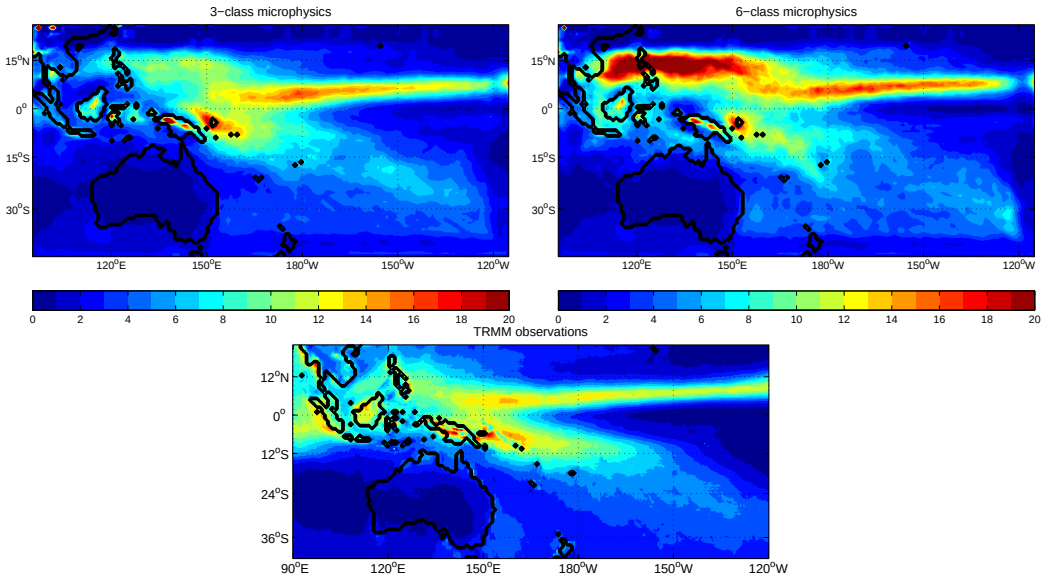

Figure 2.10 - Yearly averaged precipitation fields generated from two WRF simulations differing by their microphysics parameterization: (a) the WSM 3-class simple-ice scheme and (b) the WSM 6-class graupel scheme.

2.2.4 Shortwave radiation

WRF includes several shortwave radiation schemes. The simplest is the Dudhia scheme [Dudhia, 1989]; it consists in a simple downward integration allowing efficiently for clouds and clear-sky absorption and scattering. The clear-sky absorption and scattering represents the effect of aerosols not explicitly represented in this scheme and can be modified by changing the value of a "scattering parameter". The default value of this parameter is fixed to 1 which is equivalent to 1.e-5 $m^2.kg^{-1}$ that is 10% of scattering; when the value is greater than 1, it increases the scattering (2 increases the scattering to 20%) and therefore decreases the downward shortwave radiation at the surface (Fig. 2.11). We found that modifying this parameter has a significant impact on SST, precipitations and heat and momentum surface fluxes and has to be correctly tuned.

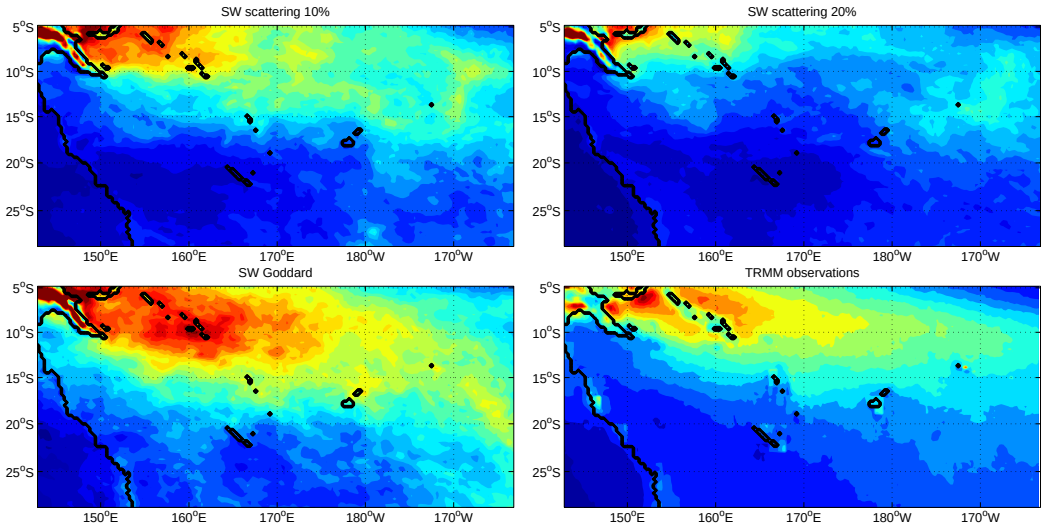

Figure 2.11 - Yearly mean precipitation fields in 3 WRF-ROMS experiments differing by their shortwave radiation parameterization: (a) the Dudhia scheme with 10% scattering, (b) the Dudhia scheme with 20% scattering and (c) the Goddard scheme. (d) represents the TRMM observed precipitation field.

The Goddard shortwave scheme was also tested. It is a slightly more complex scheme that consists in a two-stream multi-band scheme with ozone from climatology and cloud effects. In our simulations, the downward shortwave radiation at the surface was too strong with this scheme and induced warm SST bias and strong latent heat flux to balance the excessive incoming radiation. The warm bias also showed a dynamical influence, modifying the convergence patterns and precipitation in the SPCZ (Fig. 2.11). This strong sensitivity to shortwave radiation could thus affect heat and momentum exchanges at the air-sea interface with widespread consequences. We conclude that the radiation scheme is probably the most sensitive aspect of parametrization in a coupled model. Here again, we retain the Dudhia radiation scheme as in Jourdain et al. [2011] with the same default scattering parameter.

2.2.5 Surface drag

The parameterization of surface drag coefficient (C_D) is a key feature of the ocean-wave-atmosphere interface and thus of coupled models. Waves generated by TCs can reach more than 10-m height and have a feedback effect on winds as they modify surface roughness, which in turn affect ocean currents and mixing. The classical Charnock parameterization [Charnock, 1955] has been recurrently validated for typical moderate wind intensities (say 5-20 m/s) and mature seas [Garratt, 1977]. However under extreme wind conditions, recent *in situ* measurements [Donelan et al., 2004; Powell et al., 2003] and numerical simulations with wave-atmosphere coupled models [Moon et al., 2004] indicate a different behavior. Young seas are high frequency waves that travel at lower speed than well developed swell (owing to the deep water dispersion relation $C_P = g/\omega$). Their slow

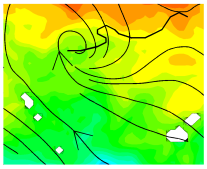

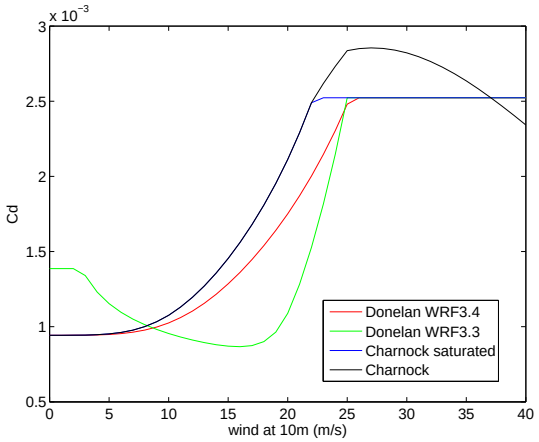

Figure 2.12 - Drag coefficient as a function of 10m wind speed for various parameterizations.

speed induce a wave form drag that increase the ocean surface roughness [Doyle, 2002]. On the contrary, the foam layer created by extreme winds produce a slipping layer [Powell et al., 2003]. We also note the effect of sea-spray that tends to intensify air-sea exchanges of heat and moisture [Bao et al., 2000]. In usual empirical formulations, C_D is only a function of the wind speed. More elaborate formulations enter the wave age factors, which can only be assessed through wave models. Nevertheless, some simple parametrization are proposed for the observed saturation of C_D at high wind speed. In WRF, the Donelan parameterization [Donelan et al., 2004] was recently implemented in various forms in the different releases. This scheme assumes a drag saturation at high wind speed but also reduces the drag coefficient values at moderate wind speeds (Fig. 2.12).

In our sensitivity experiments, this last feature induces a general increase of regional SST, wind speed (Fig. 2.13) and precipitation and a decrease of atmospheric humidity, all of which tend to disagree with observations. There is also a negative impact on cyclogenesis since a slight change with the Donelan scheme of wind convergence patterns near Papua New Guinea induced a spurious concentration of cyclogenesis in the Coral Sea region. For all these reasons, we decided to retain the Charnock parameterization. Besides, with 35-km grid resolution, maximum wind speed rarely exceeds 35 $m.s^{-1}$, which roughly remains in the range of validity of Charnock parameterization. In any case, more investigations of the drag coefficient at high wind speed are needed. For example, considering surface drag saturation as a sole function of wind speed may be totally misleading (B. Chapron, personal communication) as TC satellite observations may suggest a more complex behavior with C_D powering in some parts of the storm due to wave age factors and saturating elsewhere, presumably due to the presence of foam layer or wave-atmosphere coupling processes (as in Moon et al., 2004). The role of ocean currents in the coupled TC system also need thorough investigation.

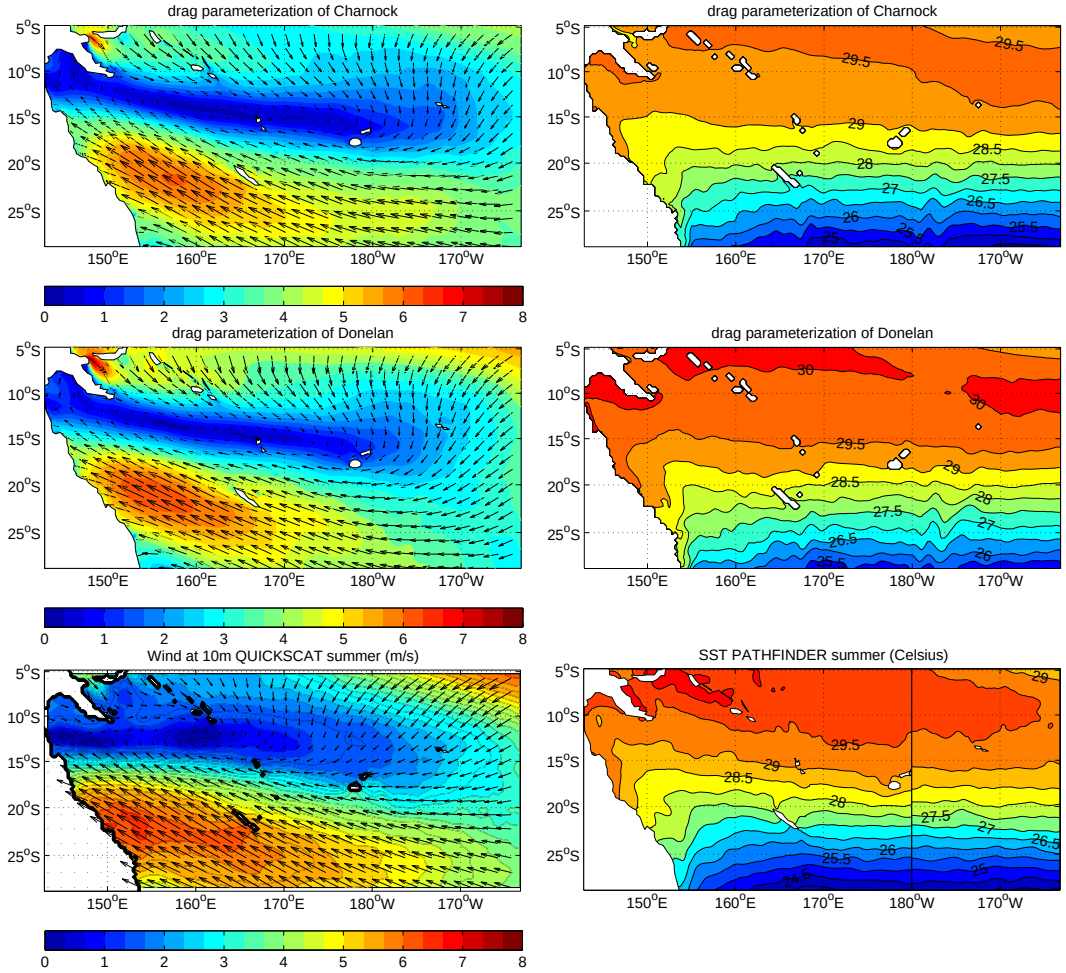

Figure 2.13 - Summer 10-m wind speed and SST (°C) for two WRF-ROMS coupled simulations differing by their surface drag parameterization: (a) the Charnock parameterization and (b) the Donelan parameterization.

2.2.6 Skin SST

In our coupled model, surface bulk formulations are computed in the atmospheric model as a function of SST, which is provided by the ocean model. However, the ocean model computes a bulk rather than skin SST that requires very fine surface resolution. The skin SST has a larger diurnal variability (particularly in the Pacific warm pool area) that directly impact air-sea fluxes. For more realism in the estimation of these fluxes in WRF, a sea surface skin temperature is computed from the scheme of Zeng and Beljaars [2005]. It consists of prognostic, one-dimensional heat transfer equations for the molecular sublayer (cool skin) and diurnal layer (warm skin) of the ocean (Fig. 2.14). It provides the difference of temperature between the skin temperature at the top of the cool skin and the bulk temperature (given by the model SST) at the bottom of the warm layer. The ocean model bulk SST is here taken at 10 m depth for consistency with the scheme of Zeng and Beljaars [2005].
Our model results show a mean difference between ROMS SST and skin SST of

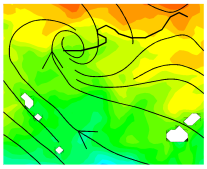

about 0.25°C (Fig. 2.15). The skin SST is colder on average due to heat loss in the cool skin by long-wave radiation. There is a small impact on heat and moisture fluxes that are slightly weaker because of the cool skin. On the other hand, there is a realistic diurnal cycle of 0.5-2°C in the skin SST, that contrasts with the ocean model SST. Overall, the impact on regional climate and cyclonic activity is not tremendous as indicated by a comparison of the standard run with an equivalent one using ROMS SST rather than skin SST (not shown).

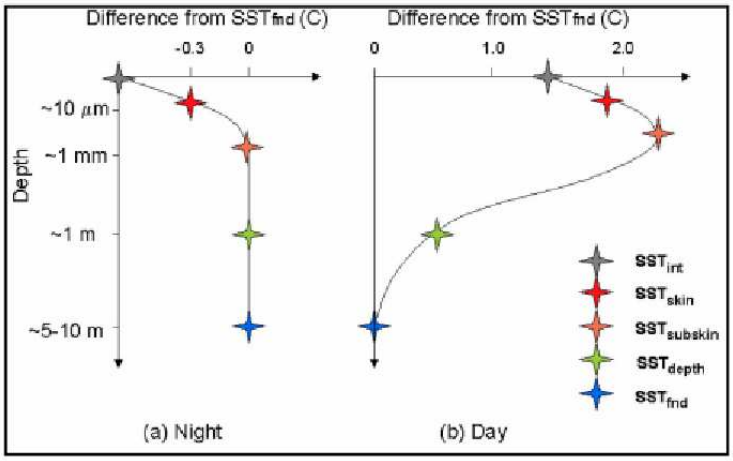

Figure 2.14 - Schematic view of near-surface vertical temperature profiles at (a) nighttime, (b) daytime. Figure from Donlon and the GHRSST-PP Science Team (2005).

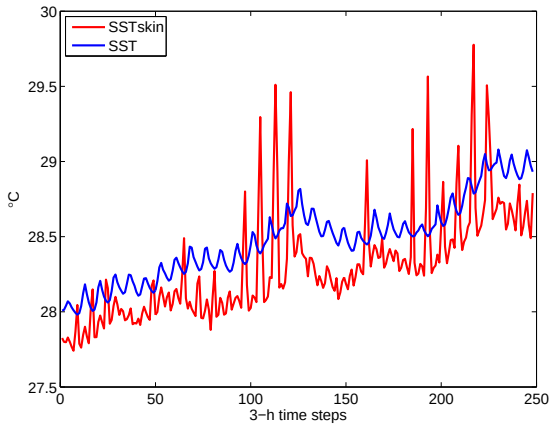

Figure 2.15 - ROMS-WRF time series of SST and skin SST computed with the scheme of Zeng and Beljaars [2005]. The station location is in the middle of the child domain and the time period is December.

2.2.7 Land surface model

The land surface model is one-dimensional computation of the heat and moisture budgets at the land-atmosphere interface involving some ecosystem processes. Numerous schemes of different complexity are available in WRF. The simplest

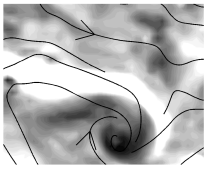

approach is given by a 5-layer thermal diffusion scheme that only simulates soil temperature using 5 levels above ground. A more common option inherited from MM5 is the Noah Land Surface Model, which is used operationally at NCEP. Noah remains fairly simple. It simulates soil temperature and moisture in four layers, fractional snow cover and frozen soil physics. In our study, the ocean surface has obviously a dominant impact on TC activity but a correct simulation of soil temperature and moisture fluxes over land is needed for proper representation of large-scale dynamics and precipitation patterns. For example, the Noah Land Surface Model gives a better solution for the minimum precipitation observed over Australia compared with the 5-layer thermal diffusion scheme.

2.2.8 Sponge layers

In addition to surface fluxes, regional models have the characteristic of being also forced through the lateral boundaries. WRF lateral forcing is specified with NCEP-2 reanalysis at the lateral boundaries of the parent domain. The most external points are directly specified with NCEP-2 data. Then, in a relaxation zone of a given number of points, the specification of NCEP-2 data is weighted against the model solution using an interpolation scheme. The width of the relaxation zone and the profile of interpolation weights (linear ramp or exponential decay) can be specified. We found that an exponential decay over 10 relaxation points allows a better transparency of sensitive fields like precipitation, which suggest a better damping of perturbations accessing the boundaries.

2.2.9 Sensitivity to vertical resolution

Various vertical resolutions were tested: 30 or 50 levels with automatic WRF stretching or manual stretching. Neither the 50 level experiments nor manual refinement in the lower troposphere showed any real improvement compared with the 30 level experiment used in Jourdain et al. [2011]. We thus retain the same vertical resolution with a 50 hPa top level pressure for its advantageous computational cost.

2.3 Methodology

2.3.1 TC tracking and SPEArTC database

The analysis of tropical cyclones first requires their identification and tracking. Several agencies and research groups devote their time to observations and tracking techniques that are extremely useful for forecasters as for constructing TC climatologies. The Regional Specialized Meteorological Centers (RSMCs) in Miami, Honolulu, Tokyo, New Delhi, La Réunion, Nadi and the Tropical Cyclones Warning Centers (TCWCs) in Perth, Darwin, Brisbane, Wellington are part of the World Meteorological Organization (WMO) and have regional responsibilities in providing advisories and bulletins of tropical cyclone activity (Fig. 2.16). The Joint Typhoon Warning Center (JTWC), China Meteorological Administration (CMA)

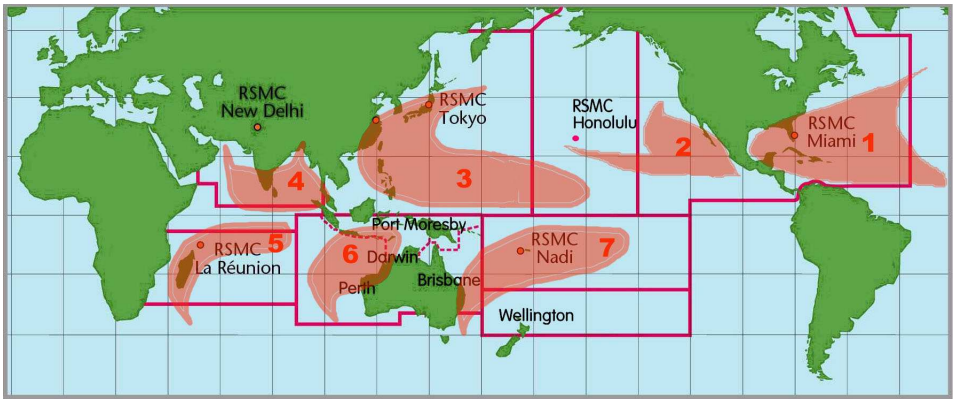

Figure 2.16 - RSMC responsability regions. Figure from NOAA.

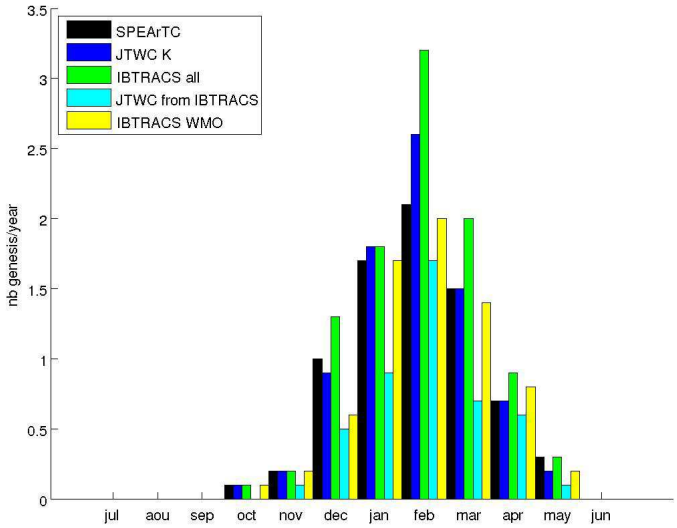

Figure 2.17 - Seasonal distribution of yearly cyclogenesis number in the southwest Pacific from 1979 to 1988 for different observational datasets: SPEArTC dataset (black), Kerry Emanuel dataset based on JTWC data (blue), IBTrACS dataset from all centers (green), JTWC data extracted from IBTrACS dataset (cyan) and IBTrACS-WMO dataset (yellow).

Shanghai Typhoon Institute, Hong-Kong Observatory, National Climatic Data Center (NCDC) Global Consolidated Tropical Cyclone Data (DSI-9636) and the University Corporation for Atmospheric Research (UCAR) data (ds824.1) also provide tropical cyclone track informations. All these data are centralized in the International Best Tracks Archive for Climate Stewardship (IBTrACS) which has two versions: one using the informations from all centers and the IBTrACS-WMO version that only use the informations from the RSMC and TCWC centers.

SPEArTC is new dataset recently developed for the southwest Pacific region by Diamond et al. [2012]. It uses IBTrACS data along with historical archives from the regional Pacific Island National Meteorological Services (PINMS), improving

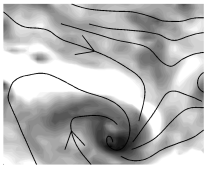

spatial coverage and extending the time-period of the record. In addition, a strict quality control of the tracks was applied to find the best track record and avoid multiple detections of the same storm or erroneous tracks (*e.g.*, some problems at the International Date Line). We naturally chose this dataset for comparisons with the model results. Figure 2.17 shows the seasonal distribution of yearly cyclogenesis number in the southwest Pacific given by various observational datasets. The dispersion between observations is important but SPEArTC gives values than sits in the middle range, which is consistent with it being in principle the best dataset.

In numerical models, the detection of tropical cyclones is done by a specific tracking algorithm. We used the algorithm developed by Chauvin et al. [2006] and applied in Jourdain et al. [2011] with few modifications. Several algorithms can be found in the literature [*e.g.*, Bengtsson et al., 1995; Walsh and Watterson, 1997; Sugi et al., 2002] and are usually based on similar criteria:

- Mean sea level pressure is a local minimum
- 850 hPa vorticity > VOR
- maximum 850 hPa wind speed > WT
- Mean 700-300 hPa temperature anomaly > TT
- 300 hPa temperature anomaly > 850 hPa temperature anomaly
- 850 hPa tangential wind > 300 hPa tangential wind

VOR, WT and TT are threshold parameters that have to be specified. Anomalies are defined as the difference between the system and its environment (both areas defined using the radius of maximum radial pressure gradient; see Chauvin et al., 2006). The first two criteria detect low pressure vorticies. The other criteria are requested to differentiate tropical cyclones from mid-latitude depressions. The radical difference between a tropical and extratropical cyclone is that one is a warm-core and the other cold-core eddy. The vortex circulation must also be stronger in the lower than upper troposphere. Once the locations where the data match all these criteria are identified, they are linked together with an iterative process, thus defining tracks. Finally, all criteria except the one on vorticity are relaxed to complete the tracks backward and forward to avoid multiple detections of the same TC that could intensify, decay and intensify again. For the relaxation phase, we can keep the vorticity criterion at the standard detection value or lower it. In addition, as the South Pacific cyclonic season extends from October to May, we defined *austral years* from the months of July to June (of the next year) to avoid splitting a TC life cycle between December and January. The choice of threshold parameters is empirical and depends on the model resolution [Walsh et al., 2007]. In our case, we tried different sets of thresholds while checking that the detected systems were actual tropical cyclones and comparing the statistics of TC distributions with observations. Figure 2.18 shows the results of our sensitivity experiments on tracking thresholds. In these tests, VOR is set to 20.10^{-5} s^{-1} as lower values (10.10^{-5} s^{-1}) detected unrealistic tracks (not shown) while higher

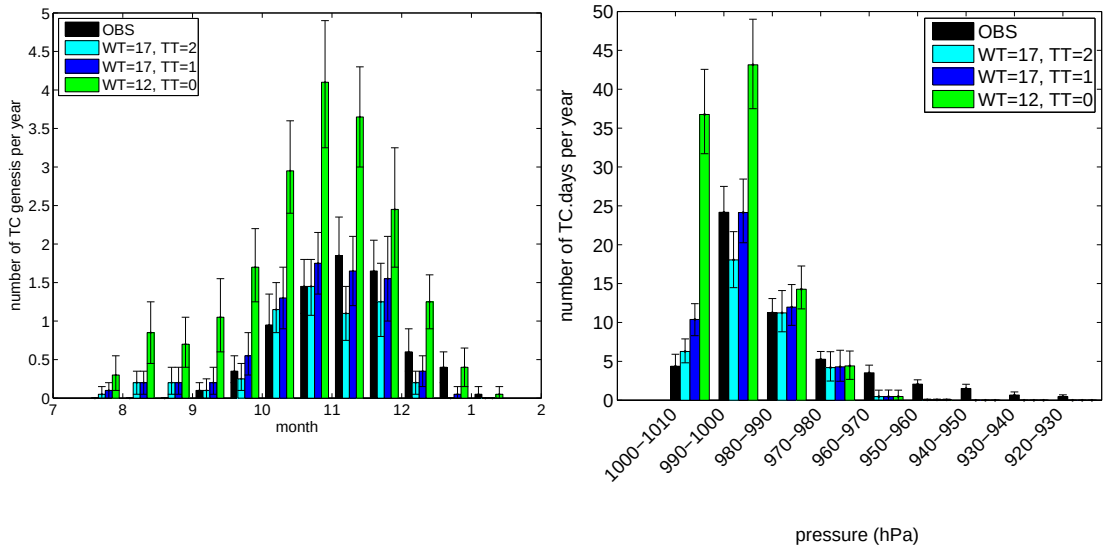

Figure 2.18 - (a) Seasonal distribution of the number of cyclogenesis per year and (b) central pressure distribution of TC occurences per year in the southwest Pacific from 1979 to 1988 for different WT and TT tracking criteria for the coupled run and for SPEArTC observations. The VOR criteria is keep to 20 s^{-1}.

values (30.10^{-5} s^{-1}) detected too few cyclones. Not surprisingly, it also appears in our results that the warm-core criterion is requested (TT=0 produces too many storms of mixed origin), but should not be set too high. We finally retained the following thresholds:

$$\text{VOR}=20.10^{-5}\ s^{-1}\ ,\ \text{WT}=17\ m.s^{-1}\ \text{and TT}=1\ K.$$

All observed and simulated TC tracks are represented in Figure 2.19.

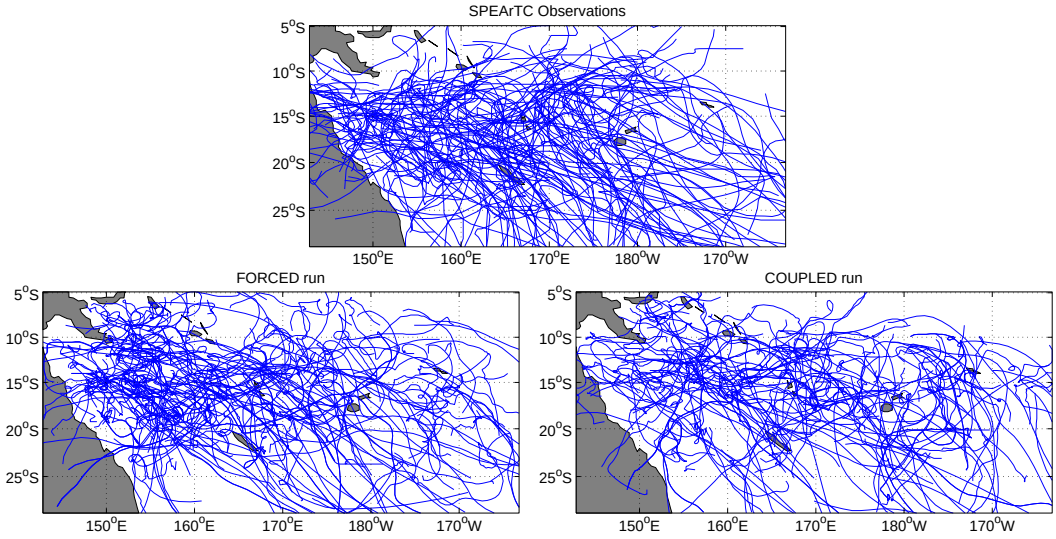

Figure 2.19 - 1979-1998 TC tracks for the observations, the forced run and the coupled run with chosen tracking criteria (VOR=20.10^{-5} s^{-1} , WT=17 $m.s^{-1}$ and TT=1 K).

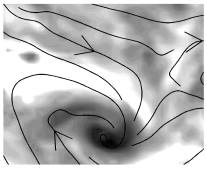

2.3.2 Forced model: cold track filtering technique

To assess the impact of coupling in tropical cyclones, we built an atmospheric forced simulation, *i.e.*, uncoupled with the ocean. The way to proceed was to remove the effect of TCs in the SST of the coupled run and feed the atmospheric model with the the filtered SST. Without filtering, a forced simulation can still be set by perturbing the initial conditions of the simulation. The chaotic nature of atmosphere dynamics suffice to modify the timing of cyclogenesis and cyclone tracks so that the probability of crossing a storm-induced cold wake (produced in the coupled model) is very small. Actually, the filtering procedure has the double advantage of removing the cold wake (albeit in an imperfect way) and modifying in the same time the chaotic course of the atmosphere, including its storm activity. Therefore, there is virtually no chance of the forced cyclones being affected by a remnant feedback effect of SST cooling.

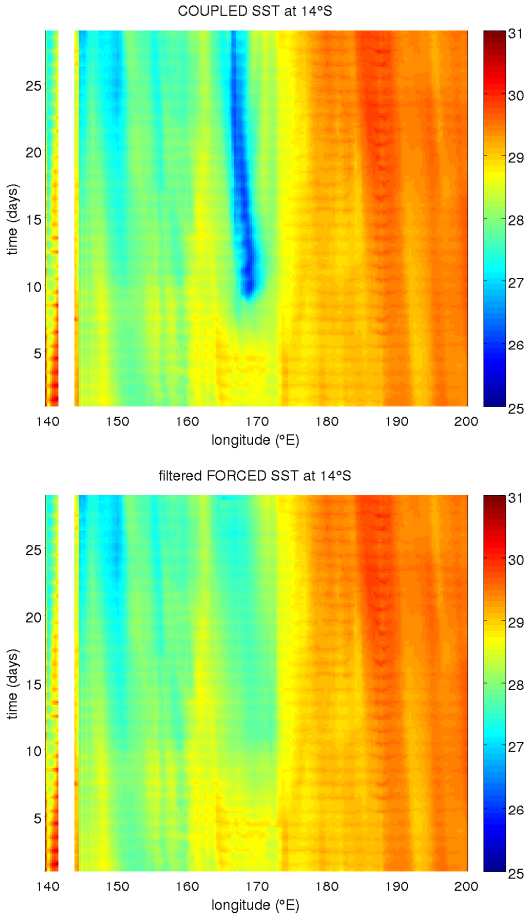

Figure 2.20 - Time evolution of the SST field at 14°S as a function of longitude for the example of Fig. 2.21 (a) for the original coupled SST field and (b) for the filtered SST field (using the 90-day FFT low-pass filter over 20 days after TC passage).

The cold wake filtering procedure has a few parameters that were evaluated for best results. The general approach is:

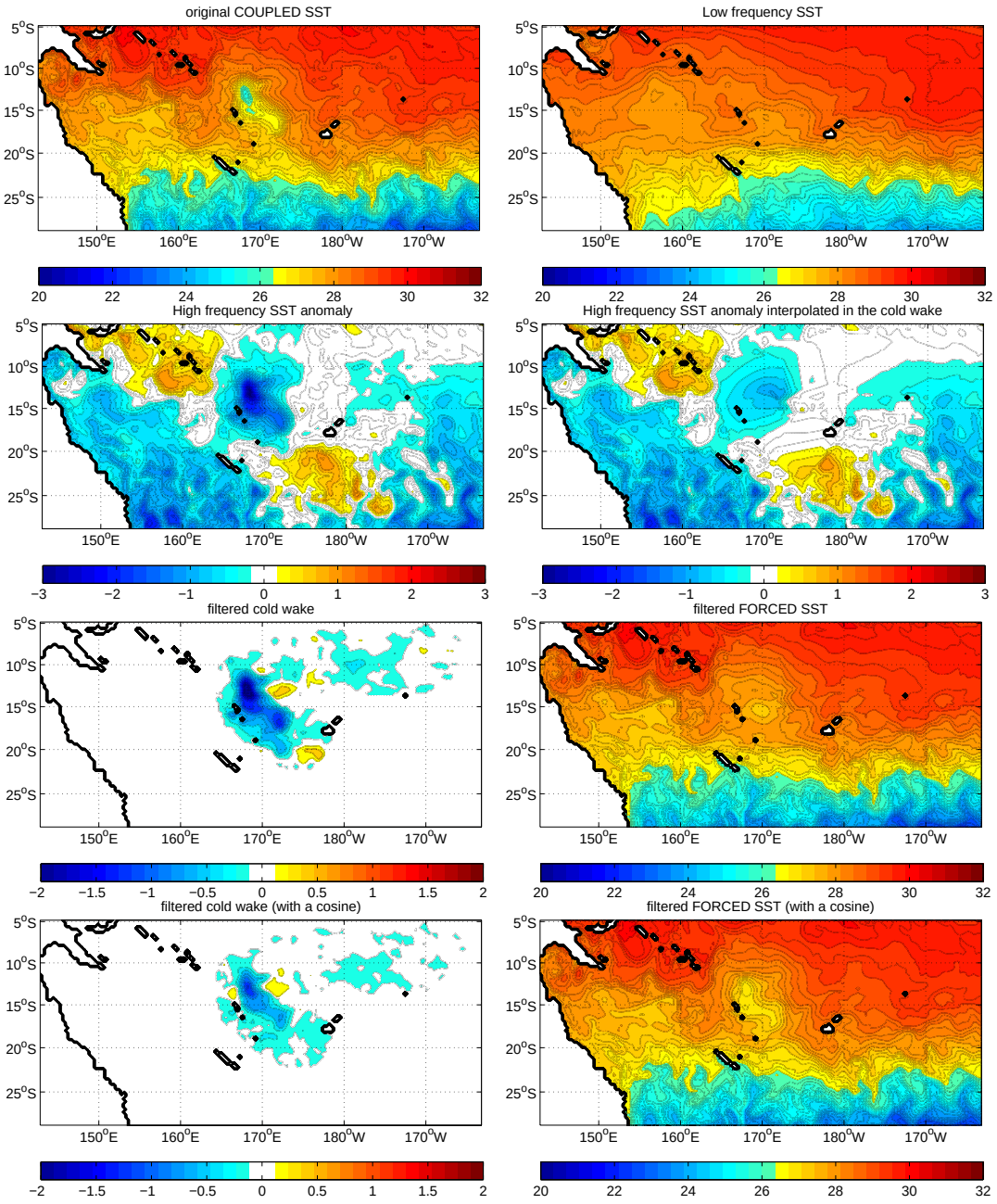

Figure 2.21 - SST fields (°C) in the different steps of cold wake filtering procedure: (a) original coupled model SST during a particular TC event; (b) low-frequency SST filtered with a 90-day FFT low-pass filter; (c) high-frequency SST anomaly computed as the difference between SST and low-frequency SST; (d) high-frequency SST anomaly in which the cold wake was removed and the surrounding HF SST anomaly interpolated; (e) the filtered cold wake, (f) the final SST field used as forcing for the forced atmospheric model. (g) and (h) are similar to (f) and (g) but using a 90-day cosine filter.

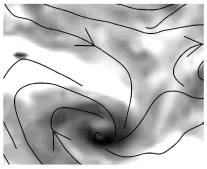

- computing the low-frequency (LF) SST signal using a low-pass filter in time (Fig. 2.21b)
- computing the high-frequency (HF) SST signal as the difference between SST and its low-frequency part (Fig. 2.21c)
- removing HF SST in the cyclone wake over a given radius and for a given time period
- spatially interpolating surrounding HF SST in the cyclone wake (Fig. 2.21d)
- reconstructing a new SST field by adding LF SST and new interpolated HF SST (Fig. 2.21f)

Figure 2.21e-h shows the result of two different filters: a cosine filter on a 90-day time window; and a Fast Fourier Transform (FFT) that filters out frequencies higher than 90 days in the spectrum. We retained the FFT filter which appeared more efficient. The filter is applied at each point of the TC tracks for a certain time. Because the cold wake remains long after the TC passage (Fig. 2.20), we needed to test the time needed to totally remove the cold wake signal. We obtain best results with a period of 20 days after the TC passage. We also applied the filter one day before TC passage because of the TC large size that affects a given location before the TC core reaches it. The radius of filtering was fixed to 3°around the TC core as it encompasses the area of even strong TC-induced cooling.

2.3.3 Statistics and error bars

2.3.3.1 Interannual variability

We performed several 20-year (25-year) long simulations of the South Pacific, producing 150-200 simulated TCs, to assess the most robust effects of ocean-atmosphere coupling in tropical cyclones. The long-term simulations are analyzed as statistical distributions with error bars and statistical tests. For interannual variability of TC number over N years of simulation, we have N independent values of annual anomaly, which can be processed as follows:

- computing the standard deviation σ of the N values
- computing percentiles on the N values
- computing the confidence interval around the mean value using:
  - the student distribution formula:

$$CI = m \pm \Phi^{-1}_{1-\frac{\alpha}{2}} \frac{\sigma}{\sqrt{N}} = m \pm \Phi^{-1}_{1-\frac{\alpha}{2}} \sqrt{\frac{\sum_{i=1}^{N}(x_i - m)^2}{N(N-1)}} \tag{2.1}$$

where m is the mean value and x_i the annual values, $\Phi^{-1}_{1-\frac{\alpha}{2}}$ is the value of the inverse of the repartition function of the law for a significance at

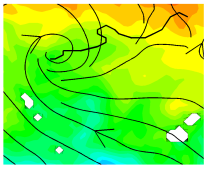

$1-\alpha$. For a normal law and $\alpha = 0.05$, $\Phi^{-1} = 1.96$ (for $\alpha = 0.1$, that is a 5-95% confidence interval, $\Phi^{-1} = 1.64$). For the case of small samples (N<30) which is our case, we have to use a student law (the student law is a flatter normal law). In this case, for $\alpha = 0.05$ and $N = 10$ (that is $N - 1 = 9$ degrees of freedom), $\Phi^{-1} = 2.26$ and for $\alpha = 0.1$ and $N = 10$, $\Phi^{-1} = 1.83$ (see Appendice C).

– or a bootstrap resampling and taking the 5-95% of the distribution. The bootstrap resampling consists in a random sampling with replacement of the annual TC number series among N possible values. This is done X times (we choose X=1000) provide a histogram of X bootstrap means. Finally, an error bar is given by the 5-95 percentiles of the X bootstrap means.

All these computations are illustrated in Figure 2.22 for the interannual variability of monthly cyclogenesis. The standard deviation and confidence intervals provide various estimates. They are not always relevant as they can reach negative TC numbers, which is obviously irrealistic. The 5-95 percentile bar also largely overestimates variability, compared with student test and bootstrap resampling. We will use the latter method in the following.

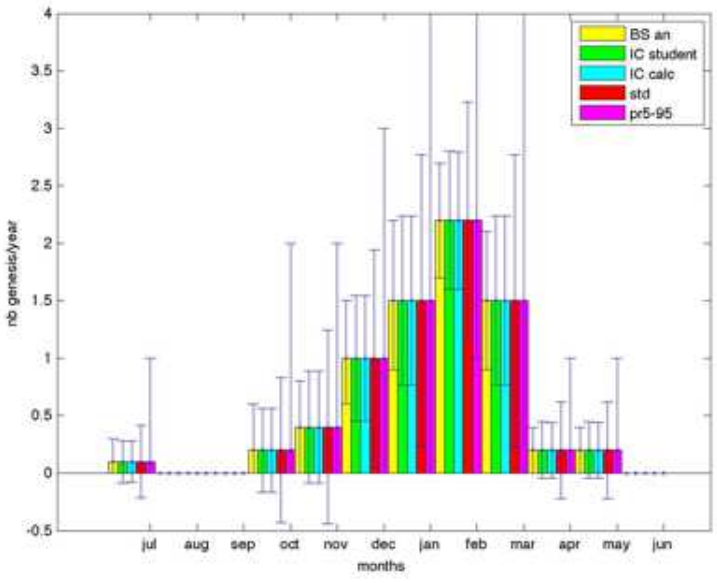

Figure 2.22 - Seasonal distribution of yearly cyclogenesis in a 10-year coupled simulation. The different colors represent the histogrammes with different computation of interannual variability: bootstrap resampling (yellow), Student CI computed by a matlab existing function (green), Student CI computed following equation 2.1 (cyan), the standard deviation (red) and the 5-95 percentiles (magenta).

2.3.3.2 Seasonal or intensity variability

Next, we evaluated the chances that cyclonic events fall within a particular month or intensity category, *i.e.*, we draw the error bars on seasonal and intensity distributions. To increase the number of events and reduce uncertainties, we considered the possibility that TCs could be accounted as multiple random events. However, analyzing all TC tracks, we found that the decorrelation time of a TC intensity along its track is very close to the mean TC lifetime. Therefore, TC events cannot be considered as separate events. The steps for evaluating the statistical confidence of seasonal and intensity TC distributions are as follows (Fig. 2.23):

- computing the confidence interval around the percentage of each month or category:

$$CI_i = p_i \pm \Phi^{-1}_{1-\frac{\alpha}{2}} \sqrt{\frac{p_i(1-p_i)}{N_{TC}-1}} \tag{2.2}$$

  where p_i is the percentage of the considered category and N_{TC} is the total number of TC events. In our case, the percentage of each month or category is computed as follows:

  $p_i = \frac{n_i}{\sum_i n_i}$

  where n_i is the number of TCs in a given month/category. Then the confidence interval is computed and multiplied by $\sum_i n_i$ as the histograms represent the $n_i = p_i . \sum_i n_i$ distribution. This formula is only valid for p above 0.5 or for large N_{TC}. In our case, for 10 years of simulation, $N_{TC} \sim 70$, which is a large number. However, the formula is not valid for $p < 0.1$ which is a problem for categories where there is too few TCs. In such cases, the bootstrap method below should be considered.

- taking the 5-95% of a bootstrap distribution of all N_{TC} events of the simulations. At each event is assigned a value corresponding to the month of genesis or intensity category. A sampling with replacement is done X times and provide X histograms of the months of genesis or TC categories. Finally, in each month or category, the 5-95 percentile of histogram values provide the error bars.

- taking the 5-95% of a bootstrap distribution computed on all time steps of a given month. For example, a time series is created of all January months and the genesis number is counted at each time step (0 or 1 most of the time). X random sampling with replacement of the time series are computed along with the 5-95 percentiles of the resamples. Note that this method is similar to the previous one except that all time steps of a given month are considered, implying that there are more possible combinations in the

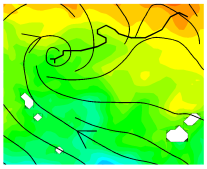

resamples. This gives a more accurate bootstrap distribution (*i.e.*, with more categories).

2.3.3.3 Similarity of forced and coupled models distributions

To evaluate the similarity of statistical estimations (means, variances and distributions) between the forced and coupled models, we can use a variety of statistical tests. For means and variances, we used:

- A student test to compare the mean of 2 samples.
- A Mann-Whitney (or Wilcoxon rank) test to compare the median of 2 samples.
- A Fisher test to compare the variance of 2 samples.

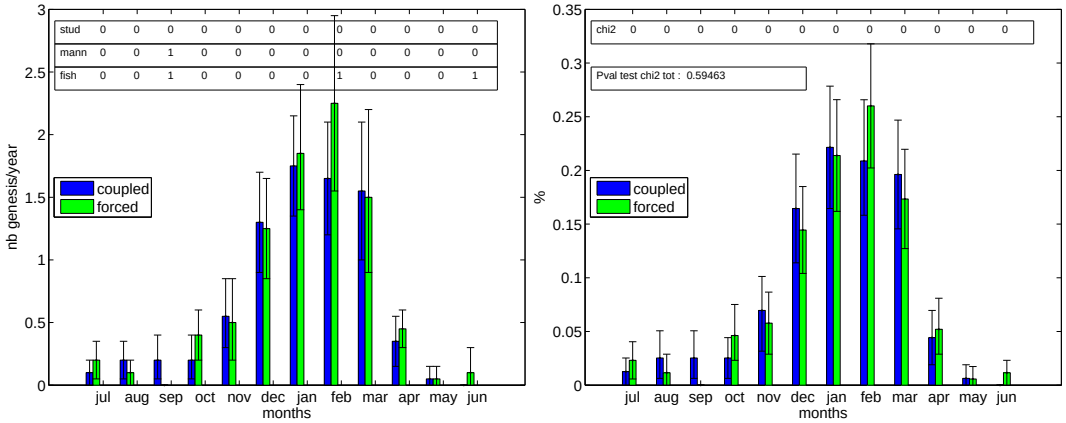

Figure 2.23 - Seasonal distribution of yearly cyclogenesis in (a) yearly TC number, (b) percentage of TCs in each month (1 is 100%) for coupled (blue) and forced (green) simulations (1979-1998). Error bars are computed with a bootstrap resampling. The table summarizes the similarity tests between coupled and forced simulations in each TC category: 0 means statistically similar distributions (at the 90% confidence level), 1 means statistically different distributions for (a) *stud* the Student test, *mann* the Mann-Whitney test, *fish* the Fisher test and (b) *chi2* the χ^2 test. The *Pval test chi2 tot* is the probability value of having the same distributions in the forced and coupled models.

The χ^2 test was used to test the alignment between TC distributions in the forced and coupled model. It assumes independent events (the number of monthly genesis or the number of storms reaching a given wind category in our case). The χ^2 test evaluates the difference between observed values O_{ij} and the expected values E_{ij}. We create tables of these values with 2 columns (simulations) and 2 rows (categories). The expected values are estimated as:

$$E_{ij} = \frac{\sum_j O_{ij} \sum_i O_{ij}}{N} = \frac{(row\ total) \times (column\ total)}{N} \tag{2.3}$$

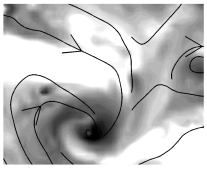

where N is the total number of cyclones (adding N_{TC} from the coupled and forced models). The χ^2 value is then given by:

$$\chi^2 = \sum_{ij} \frac{(O_{ij} - E_{ij})^2}{E_{ij}} \tag{2.4}$$

The result must be compared with a critical value given in a Chi Square table (see Appendice C) to determine whether the comparison shows significance. The critical value is a function of the degree of freedom, which is equal to $(number\ of\ rows - 1) * (number\ of\ columns - 1)$. The test is valid only under certain conditions: the 1954 Cochran criterion is usually used, it specifies that all i and j classes must have a non-zero expected value ($E_{ij} \geq 1$) and that 80% of classes must have an expected value greater or equal to 5. These conditions are met in our case except for categories with no cyclones.
An example of χ^2 test for two TC categories: relatively weak TCs (wind speed of 17-22 $m.s^{-1}$) and stronger TCs (wind speed > 22 $m.s^{-1}$) over 10 years of simulation is given. The following tables are computed :

Table 2.1 - Observations O_{ij}

TC category	Coupled run	Forced run	Total
17-22 m/s	9	14	23
other	64	55	119
Total	73	69	142

Table 2.2 - Expectations E_{ij}

TC category	Coupled run	Forced run	Total
17-22 m/s	23*73/142=11.8	23*69/142=11.2	23
other	119*73/142=61.2	119*69/142=57.8	119
Total	73	69	142

$\chi^2 = (9-11.8)^2/11.8+(14-11.2)^2/11.2+(64-61.2)^2/61.2+(55-57.8)^2/57.8 = 1.7$
For a degree of freedom of 1 (only 2 TC categories in our example), the critical value given in the Chi Square table is 2.70 for a 90% significance. Since χ^2=1.7<2.70, the distribution of weak TCs in the coupled and forced simulations are statistically similar.

2.3.4 Compositing methodology

To asses the most robust processes operating at the cyclone-scale, we opted for a compositing approach, synthesizing the fate and effects of 150-200 cyclones. The composite methodology consists in averaging all TCs or a part of them (*e.g.*,

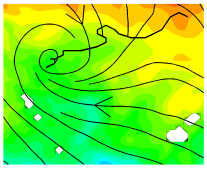

strong events reaching 27 $m.s^{-1}$). Various TC characteristics can be so described: cross-track and vertical structure, TC life-cycle, storm-induced cold ocean wake. Three types of composites are needed. They rely on the tracking of all TC locations where the variables of interest are extracted on a 12°([-6°; +6°]) cross track section and from 10 days before TC passage to 30 days after. A TC database is thus produced of a set of variables at all TC locations, varying as a function of time from TC passage, distance from track and vertical position (for 3D atmospheric and oceanic fields).

A *cross-track composite* is created by averaging values at all TC locations at a given time (usually the TC passage time or else the time of maximum impact on the ocean). This cross-track composite therefore describe the most robust (permanent) features of the cross-track structure of TCs or their oceanic response. Cross-track composites are also useful for exposing the spatial distribution of storm induced SST cooling. To that end, all TC cross-tracks are projected on a regional map. If two tracks overlap, the maximum or mean value of SST cooling is retained.

A *lag composite* or *Eulerian composite* is built by averaging values of all TC locations over a 4° ([-2°; +2°]) cross-track section at any given time of the storm event. It results in a composited TC wake evolution as a function of time from TC passage and possibly vertical position. It represents an Eulerian view of events at any given location.

Finally, an *along-track composite* or *Lagrangian composite* is built by first considering individual TC tracks, with spatially-averaged quantities over a 4° ([-2°;+2°]) cross-track section. Then, each individual TC track is rescaled on a standard 8-day duration. Finally quantities of all tracks are averaged, providing a composite track with a Lagrangian view of a composited TC life cycle: intensification, mature phase and decay.

2.4 Summary of the experiments

Different model configurations are used in the next chapters and are summarized in Table 2.4.

Table 2.3 - Summary of the different numerical experiments characteristics

Experiments	Models	Domain	Resolution	Time period	Surface forcing	Boundary forcing
Forced ocean model CYCLONE exp.	ROMS	140°E-190°E 30°S-8°S	1/3° horizontal 41 vertical levels	1979-2003	Jourdain et al. [2011] WRF2.2 simulation	NEMO 1/2° climatology
NOCYCLONE exp.					Jourdain et al. [2011] WRF2.2 simulation with TCs removed	
Ocean-Atmosphere (OA) Coupled model	WRF-ROMS Fortran Coupler	D1: 89.83°E-240.18°E 41.21°S-21.62°N D2: 139.62°E -200.02°E 31.40°S -1.62°S	D1: 105 km D2: 35 km A: 30 vertical levels O: 51 vertical levels	1979-1999		A: NCEP-2 reanalysis O: NEMO (1/4°) interannual simulation
Forced atmospheric model	WRF	D1: 89.83°E-240.18°E /41.21°S-21.62°N D2: 139.62°E -200.02°E 31.40°S -1.62°S	D1: 105 km D2: 35 km 30 vertical levels	1979-1999	coupled model SST with cold wakes removed	NCEP-2 reanalysis

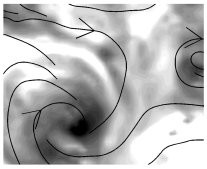

Chapter 3

Climatology of the South Pacific and model validation

Contents

3.1 Validation datasets **58**
3.1.1 Ocean properties 58
3.1.2 Precipitation 58
3.1.3 Air-Sea Fluxes 60
3.1.4 Wind 61
3.1.5 NCEP-2 Reanalysis 61
3.2 Oceanic circulation **62**
3.2.1 Large-scale circulation and zonal jets 62
3.2.2 Mesoscale activity 63
3.2.3 Surface properties 64
3.2.4 Vertical structure 66
3.3 Atmospheric circulation **66**
3.3.1 SPCZ dynamics 66
3.3.2 Vertical structure: the Hadley cell 69
3.3.3 Seasonal cycle and air-sea fluxes 72
3.4 TC distributions **75**
3.4.1 Environmental conditions of cyclogenesis 75
3.4.2 Seasonal distribution 76
3.4.3 Interannual variability 78
3.4.4 ENSO 79
3.4.5 Environmental *vs.* stochastic forcing of cyclogenesis . . 81

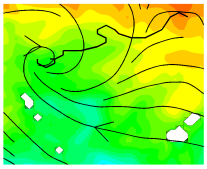

3.1 Validation datasets

3.1.1 Ocean properties

Pathfinder SST The Pathfinder SST climatology is a dataset developed by the NASA Physical Oceanography Distributed Active Archive Center (PO.DAAC) and the NOAA National Oceanographic Data Center (NODC). It is based on satellite observations (NOAA-9,11,14,16,17,18 satellites) and uses multi-channel measurements from 1985 to 2009. It is given on a 4-km grid.

CARS climatology The CSIRO (Commonwealth Scientific and Industrial Research Organisation) Atlas of Regional Seas (CARS) in its 2009 version (http://www.marine.csiro.au/~dunn/cars2009/) is used to validate the temperature and salinity structures of our ocean model. CARS2009 dataset provides climatological fields and seasonal cycles. It was built on the basis of the last 50-year observational data from research vessels and autonomous profilers. Because the data is too sparse to provide a monthly information on every specific year, it is averaged over all 50 years only keeping the seasonal cycle. A correction of the interannual signal is applied in the Western Equatorial Pacific and the main bias in the dataset is the large increase in the number of data with years.

Montegut et al. [2004] MLD climatology The Montegut et al. [2004] ocean mixed layer depth (MLD) climatology from observations (http://www.locean-ipsl.upmc.fr/~cdblod/mld.html) is used as reference to validate our ocean model MLD. The dataset uses more than 5 million individual profiles obtained from the National Oceanographic Data Center (NODC), from the World Ocean Circulation Experiment (WOCE) database, and from the ARGO program. They include all available data with high vertical resolution from 1941 to 2008, *i.e.*, observations made from mechanical bathythermograph (MBT), expendable bathythermograph (XBT), conductivity-temperature-depth probes (CTD), and profiling floats (PFL). From each profile, an estimation of MLD is given by the depth where the change in temperature or density compared with the 10-m value reaches a given threshold (0.2 °C for temperature; 0.03 $kg.m^{-3}$ for density). A linear interpolation between data levels is used to refine the mixed layer position. The final MLD product is gridded on 2° by 2°. Smoothing is applied to account for irregular sampling and missing data are evaluated with an ordinary kriging method on a 1000-km radius disk (Fig. 3.1). The number of profiles per grid box used for MLD estimation in the South Pacific is mapped in Figure 3.2. It is important to note that few profiles are available in the region (less than 5 in many areas), indicating that the observational map of MLD must be used with caution in the validation process.

3.1.2 Precipitation

TRMM The highest resolution dataset available for precipitation is the satellite 3B-42 Tropical Rainfall Measuring Mission (TRMM) product at 1/4° resolution. This product is a merge of infra-red data from various satellites (GMS, GOES-E,

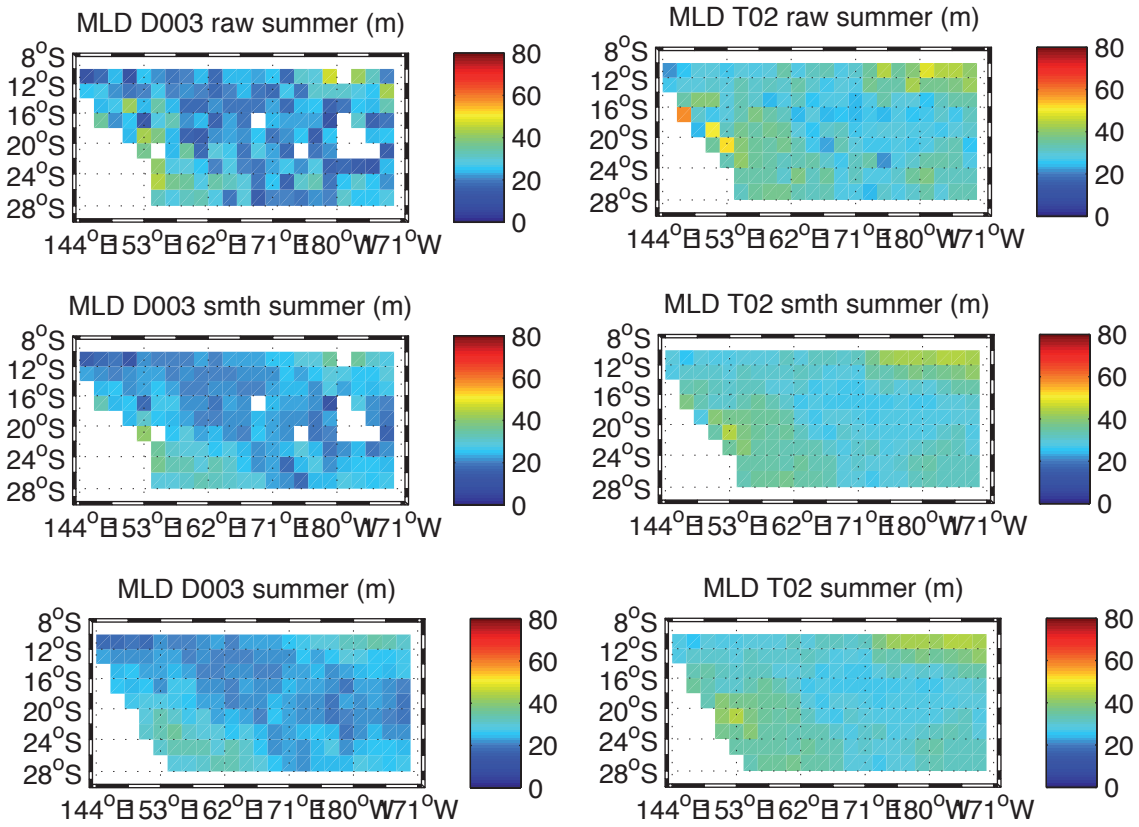

Figure 3.1 - Climatological summer MLD from Montegut et al. [2004] dataset computed with (left) density criterion ($\rho - \rho_{10m} > 0.03 kg.m^{-3}$), (right) temperature criterion ($T - T_{10m} < -0.2°C$). (a-b) are the raw estimates (median value in each grid box), (c-d) are the estimates with smoothing by weighted neighboring profiles and (e-f) are the final estimate after smoothing and kriging.

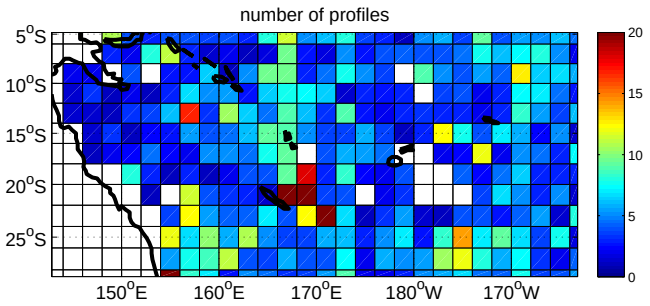

Figure 3.2 - Number of profiles in each grid box used for the estimation of the Montegut et al. [2004] MLD climatology.

GOES-W, Meteosat-7, Meteosat-5 and NOAA-12) that are adjusted. It is only available from 2001 to 2011, which is outside the simulation period (1979-1999). Nevertheless, we use this product for climatological comparisons, aware of possible mismatch due in part to multidecadal variability.

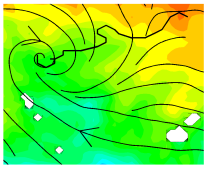

GPCP Global Precipitation Climatology Project [GPCP; Huffman, 1997] dataset merges measurements from over 6,000 rain gauge stations, and satellite geostationnary and low-orbit infra-red, passive microwave and sounding observations. It is gridded at a 2.5°x2.5° resolution and covers the 1979-to-present period. This is more representative of a present climate estimation and more comparable with our 1979-1999 simulations. A usual flaw in observational rainfall over oceanic areas is the over-representation of island data. Nevertheless, comparing independent measurements of precipitation rates in west Pacific atolls to TRMM and GPCP products, Adler et al. [2003] found a negative bias of approximately 10% for both datasets. They also noted a sensitivity of the TRMM estimation to retrieval algorithms that can reach 30% in heavy precipitation areas of the SPCZ.

CMAP The CPC Merged Analysis of Precipitation dataset [CMAP; Xie and Arkin, 1997] is another product of global monthly precipitation reconstructed from infra-red and microwave satellite data (GPI, OPI, SSM/I scattering, SSM/I emission and MSU). The grid resolution is relatively coarse: 2.5°x2.5°, but the data extends from 1979 to 2011 and provide a more comparable climatology to our simulations than TRMM. We preferentially use CMAP over GPCP because the latter appears similar but more patchy in the SPCZ region (not shown).

3.1.3 Air-Sea Fluxes

TropFlux Tropflux (http://www.locean-ipsl.upmc.fr/~tropflux/data) is a product of air-sea heat and momentum fluxes for tropical oceans (30°S-30°N). It presents daily fluxes from 1979 to 2011 on a 1°x1° grid. The surface fluxes are essentially computed from ERA-Interim reanalysis data [Dee et al., 2011] but short-wave radiation is from satellite measurements of the International Satellite Cloud Climatology Project (ISCCP). Turbulent fluxes and wind-stress are computed using COARE v3.0 bulk algorithm [Fairall et al., 2003]. In addition, a series of corrections based on the global tropical moored buoy array is applied [Kumar et al., 2012].

OAFlux The Objectively Analyzed air-sea Fluxes (OAFlux, http://oaflux.whoi.edu) dataset from 1958 to present is constructed applying an objective analysis that seeks optimal synthesis of satellite and Numerical Weather prediction (NWP) data sources [Yu and Rienecker, 2008]. The resolution is 1°x1°. The turbulent latent and sensible heat fluxes are estimated from the objectively analyzed surface meteorological variables by using the COARE v3.0 bulk flux algorithm [Fairall et al., 2003]. The net heat flux computation includes short-wave and long-wave radiation fluxes from ISCCP and is unbalanced (residual of O(30 $W.m^{-2}$) when averaged over the global ocean).

COADS The previous two datasets are derived from models with data assimilation and additional corrections from observations. The two following datasets are constructed from observations only. The Comprehensive Ocean-Atmosphere Data Set [COADS; Slutz et al., 1985] has produced various monthly climatology derived

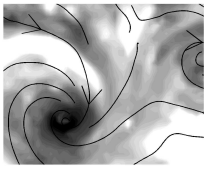

from global marine data (air and sea surface temperatures, wind, pressure, humidity, and cloudiness) observed during 1854-1997, primarily by ships-of-opportunity. The surface flux dataset used in this study is a half-degree resolution product presented by da Silva et al. [1994], including specific algorithms and procedures.

NOC1 The National Oceanography Centre (NOC) dataset (http://www.noc.soton.ac.uk/science-technology/earth-ocean-system/atmosphere-ocean/) version 1.1 is constructed from the fields derived from COADS-1a (1980-1993) enhanced with additional metadata from the WMO47 list of ships, that is *in situ* observations. Consequently, the quality of the fields depends on the region: the North Atlantic and North Pacific are well sampled while the Southern Hemisphere have less observations.

3.1.4 Wind

QuickSCAT The ocean surface wind vectors observational product used here is the QuickSCAT dataset. It is based on the NASA/JPL's Sea Winds Scatterometer and is given on a 1/4° grid. A scatterometer is a microwave radar sensor that measures the speed and direction of surface wind. It is able to measure across the clouds but can be contaminated by moderate to heavy rainfalls. The dataset used for our comparisons is a climatology of QuickSCAT data from 2000 to 2009.

3.1.5 NCEP-2 Reanalysis

NCEP-2 reanalysis is used as boundary conditions for our regional atmospheric model. It is also important to compare our simulations with this dataset in order to diagnose the dynamical downscaling procedure and eventually understand some of the model biases or tendencies. It is important to note that reanalyses are model-interpolated observations that have their own errors due to model numerics and parametrizations or to the data assimilation procedure. For example, a known rain-rate assimilation problem was reported to produce excessive tropical rainfall in ERA-40 [Andersson et al., 2005] [1]. Nevertheless, they are the best available global gridded compilation of data (from radiosondes, balloons, aircraft, buoys and satellites) and have the advantage of physical balance guaranteed by the model's equations. NCEP-2 is provided as 6 hourly product on a 2.5°x2.5° grid since 1979.

[1] Because humidity is a major ingredient of cyclone formation and potential intensity, the excess of tropical humidity seen in ERA-40 and also in most climate models (associated with an overly strong Hadley cell; see Caballero, 2008) has an explosive effect on cyclogenesis when these large-scale product are used to force regional models [Codron and Marchesiello, 2011].

3.2 Oceanic circulation

3.2.1 Large-scale circulation and zonal jets

The Southwest Pacific circulation (Fig. 3.3) is embedded in the subtropical anticyclonic gyre whose northern branch is the South Equatorial Current (SEC). This is a large westward current driven by trade winds in the eastern Pacific but branches between numerous islands as it enters the southwest Pacific, forming a more complex zonal circulation system [Couvelard et al., 2008] . Further west, the resulting jets reach the Australian coast and split, forming two western boundary currents: the East Australian Current (EAC) and the Northward Queensland Current (NQS). South Pacific zonal jets where first evidenced by Webb [2000].

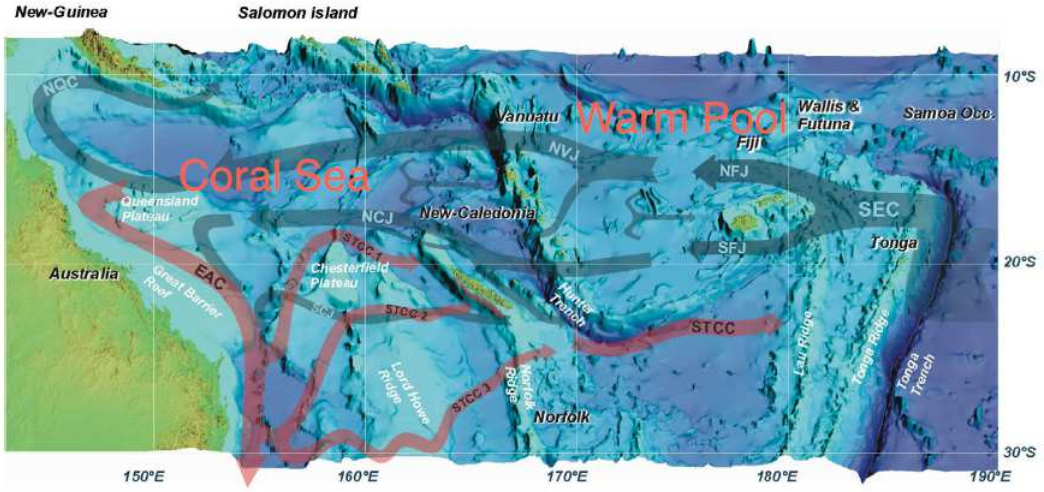

Figure 3.3 - Schematic picture of the main currents and topography of the southwest Pacific. Blue arrows indicate the various branches of the SEC system, which are essentially barotropic with maximum intensity around 200 m. Red arrows represent the EAC and STCC branches that are on contrary strongly baroclinic, surface enhanced currents. From Marchesiello et al. [2010b].

Using ROMS at 1/12° resolution, Couvelard et al. [2008] studied the influence of topographic effects and nonlinear advection on the formation of these jets. They show that the island rule based on the Sverdrup balance, which assumes infinite depth, is very marginally valid in the southwest Pacific. The rugged ocean topography of the region is mostly meridionally oriented and drives a general equatorward deflection of the jets, which is beneficial to the North Fiji, North Vanuatu and North Caledonian jets (NFJ, NVJ, NCJ) at the expense of the South Fiji and South Caledonian jets (SFJ, SCJ). Couvelard et al. [2008] confirmed their numerical results with new glider measurements. Linear advection plays an important role in balancing some of the topographic constraint and promoting zonal flow.
Finally, Couvelard et al. [2008] show that mesoscale eddies generated by barotropic instabilities (nonlinear advection effect) drive observed counter-currents (especially between the NVJ and NCJ in the Coral Sea) along eddy-mixed potential

vorticity surfaces.
The SEC and its branches are subsurface flow. Surface waters are characterized by different dynamical regimes. They are largely composed of Ekman drifts forced by trade winds and subtropical westerlies. South of New Caledonia, geostrophic adjustment to strong surface density gradient resulting from the convergence of tropical and subtropical waters produces a surface eastward flow: the SubTropical Counter Current (STCC) in the Southern part of the domain (connecting with the EAC off Australia). As the STCC flows in an opposite direction to the SCJ, the subtropical zone is characterized by strong vertical shears. It produces baroclinic instabilities from the conversion of potential energy and an intense mesoscale activity that is observed through satellite altimetry [Qiu et al., 2008].

3.2.2 Mesoscale activity

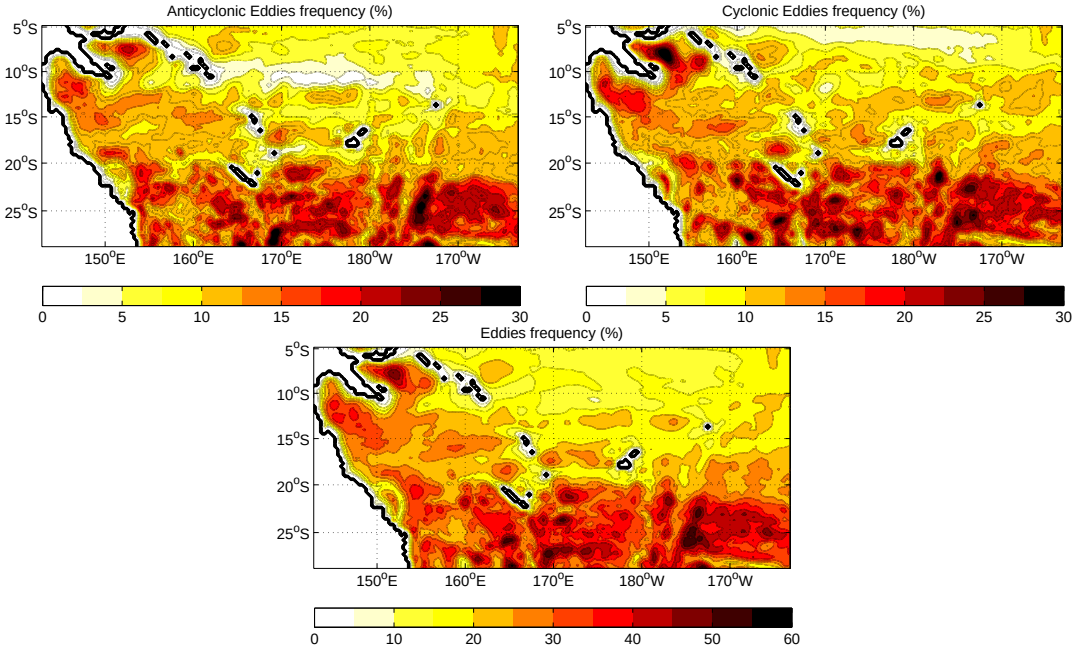

Figure 3.4 - Eddy frequency as a percentage of eddy presence during the cyclonic season (October-May) in the 1979-1998 coupled model for (a) anticyclonic eddies, (b) cyclonic eddies and (c) all eddies together.

Consistently with satellite-derived estimate of Qiu et al. [2008] and high-resolution model calculation of Couvelard et al. [2008], the eddy distribution in the present coupled model shows a markedly greater eddy activity south of 20°S (Fig. 3.4) due to the baroclinicity of the STCC region. However, mesoscale activity is also present in the Coral Sea region resulting from barotropic instability of tropical zonal jets. Cyclonic and anticyclonic eddies have a similar frequency, albeit with a small advantage to cyclonic eddies in the Coral Sea region and generally above 20°S. Eddies in the region have radii between 25 and 300 km with a peak distribution around 75 km (Fig. 3.5). Their amplitude varies between 2 and 16 cm with a greater amount of weak eddies having 2 to 5 cm amplitude (Fig.

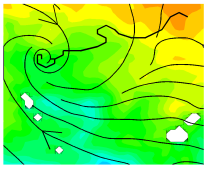

3.5) in agreement with Chelton et al. [2011]. Note that the most intense eddies are also of larger radii and are thus better resolved by our medium-resolution model. Nevertheless, mesoscale eddy kinetic energy is similarly distributed but slightly weaker in our 1/3° than in the 1/12° resolution model of Couvelard et al. [2008]. Therefore, the amplitude of eddies in our coupled model is generally underestimated and we should expect that their effect on tropical cyclones is also slightly underestimated.

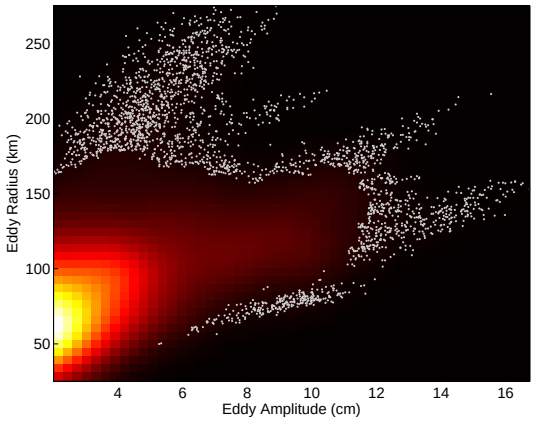

Figure 3.5 - Density plot of eddy radius (km) *vs.* eddy amplitude (cm) for all eddies in the 1979-1998 coupled simulation during the cyclonic season (October-May).

3.2.3 Surface properties

Sea surface temperature (SST) and salinity (SSS) are presented in Figure 3.6a-d. The warm pool region is characterized by warm and fresh waters. The fresh water tongue stretches under the South Pacific Convergence Zone (SPCZ), a location of heavy rainfall described in section 3.3.1. Below 15°S, the SST and SSS fields present a strong gradient between tropical and subtropical colder and saltier waters. Both patterns are well represented by the model, albeit with lower salinity values in the warm pool produced by excessive rainfall (see Fig. 3.8).

The mixed layer depth (Fig. 3.6e-f) shows good agreement with *in situ* observations [Montegut et al., 2004] except on the Queensland Plateau where there is no *in situ* observations at all (see Fig. 3.2). A striking feature of this map is the contrast between the warm pool characterized by a deep mixed layer and the Coral Sea by a shallow mixed layer.

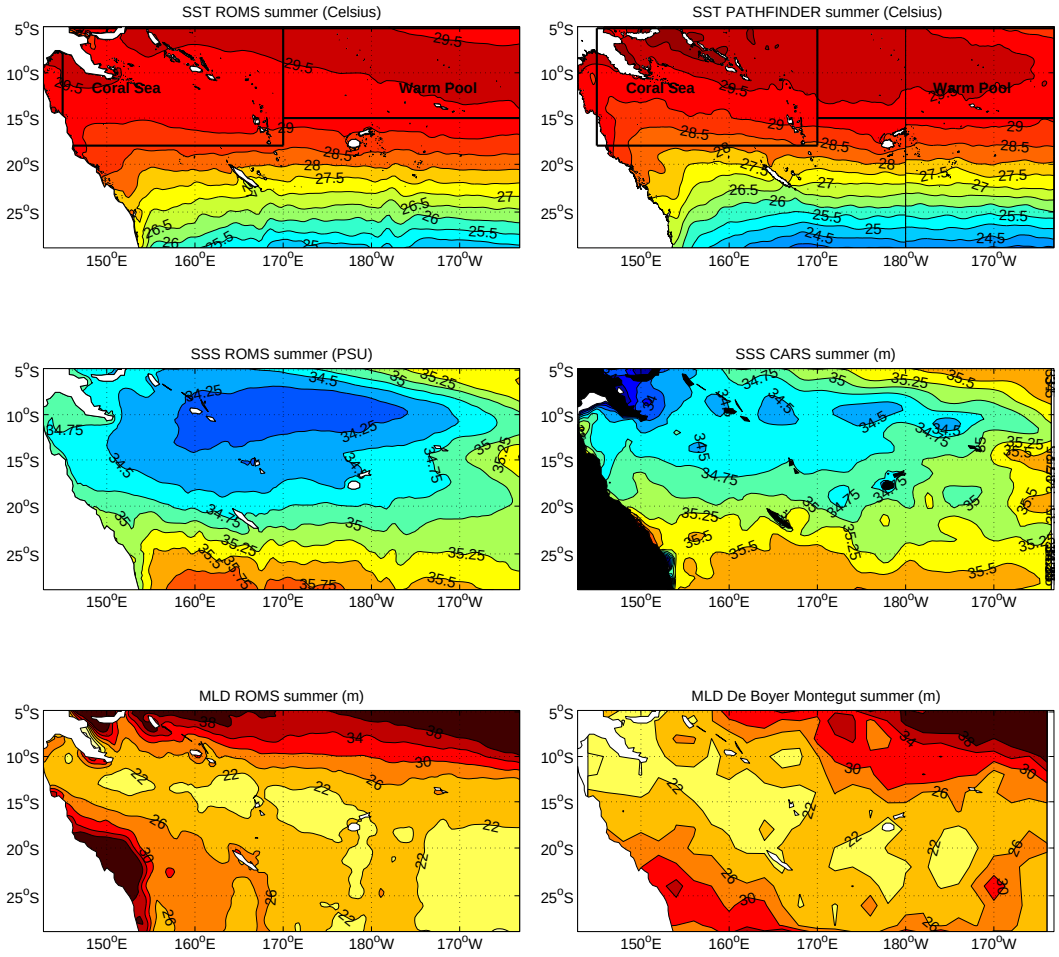

Figure 3.6 - Austral summer (January-March) averaged (a-b) SST (°C), (c-d) SSS (PSU) and (e-f) MLD (m) for the 1979-1998 coupled model (left) and for the observational datasets (right): Pathfinder for the SST, CARS for the SSS and Montegut et al. [2004] climatology for the MLD.

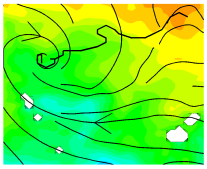

3.2.4 Vertical structure

The vertical structure of the ocean is illustrated by sections of the zonal mean temperature and salinity (Fig. 3.7a-d). The temperature and salinity stratifications are very well reproduced by the model; the salinity section presents a deep maximum around 150 m, which characterizes the SEC and its various branches. The overestimated surface salinity minimum in the SPCZ that was previously noticed is again apparent here. The temperature section clearly illustrates the fundamental stratification difference between the warm pool and Coral Sea. The strong surface stratification of the Coral Sea is more amenable to cooling than the warm pool under extreme atmospheric forcing as will be seen in the next chapters. This is even amplified by the salinity barrier formed by heavy rainfall in the warm pool, which tends to isolate cold subsurface waters even more in this region.

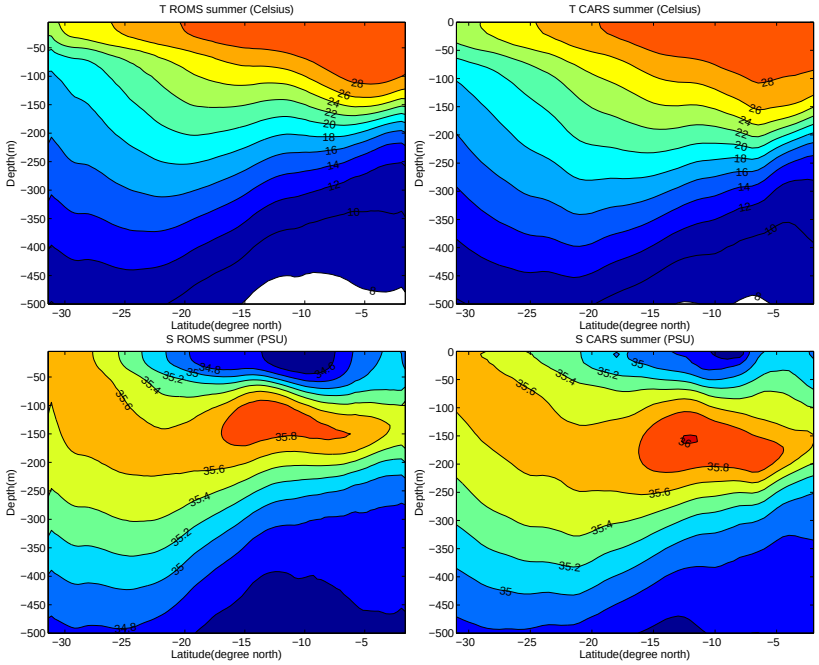

Figure 3.7 - Austral summer (January-March) time-averaged vertical sections of (a-b) mean zonal temperature (°C) and (c-d) mean zonal salinity (PSU) in the upper ocean for the 1979-1998 coupled model (left) and for CARS observations (right).

3.3 Atmospheric circulation

3.3.1 SPCZ dynamics

The South Pacific Convergence Zone is one of the most important convective zone of the tropical regions. It is the only convergence zone of the Southern Hemisphere present throughout the year even if it is particularly active during austral summer. The SPCZ is the location of both maximum precipitation and cyclogenesis. The numerous poor and vulnerable islands of the South Pacific are very sensitive to

severe storm events, *i.e.*, extreme winds and waves and heavy rainfall that cause extensive damages.
The SPCZ dynamics and its large interannual variability, essentially associated with El Niño Southern Oscillation (ENSO) phenomenon will be presented in this section. A more detailed study is presented in Vincent et al. [2011] based on ERA-40 reanalysis and observations. Here, the dominant features are highlighted, in particular those pertaining to cyclogenesis since TC variability is strongly associated with that of the SPCZ. Our focus is naturally on the cyclonic season: austral summer.

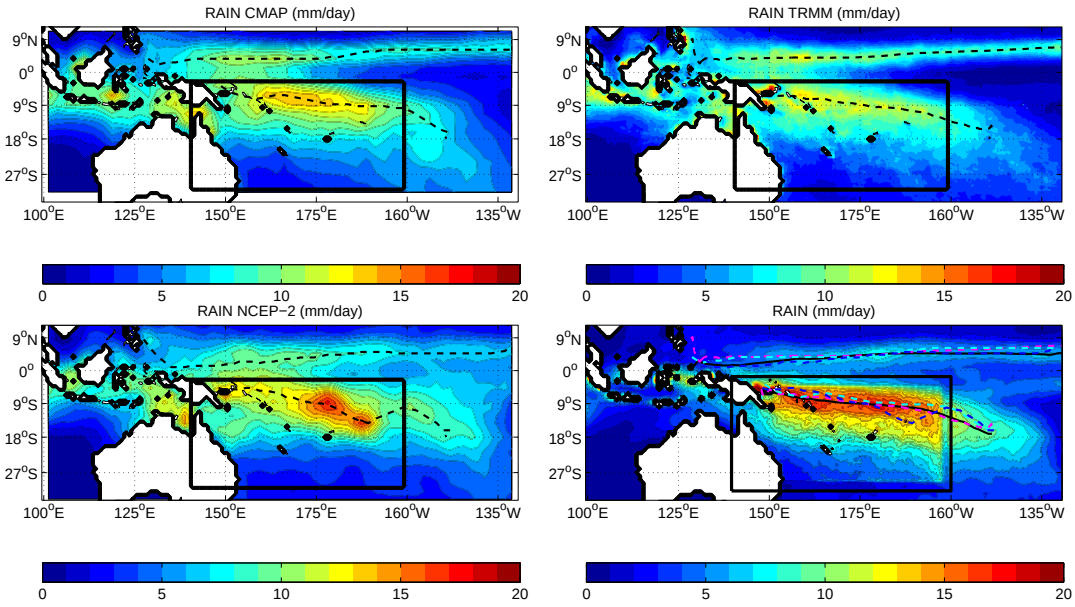

Figure 3.8 - Austral summer (January-March) precipitation (mm/day) climatology (1979-1998 average) for (a) CMAP observations, (b) TRMM observations, (c) NCEP-2 reanalysis and (d) the coupled model. Black lines denote the maximum precipitation in the ITCZ and SPCZ. In (d) ITCZ and SPCZ lines from CMAP (cyan), TRMM (magenta) and NCEP-2 (blue) are presented in addition to the black model lines.

The SPCZ can be defined as a line of maximum precipitation in the South Pacific tropical zone (Fig. 3.8). Its equivalent system in the northern hemisphere is the Inter Tropical Convergence Zone (ITCZ) that is also encompassed in our model parent domain. Both the SPCZ and the ITCZ positions are very well represented in the model compared to observations (Fig. 3.8), albeit with overestimated rainfall in the SPCZ (maximum value of 18 mm/day in the model and 12-15 mm/day in the observations) and underestimated rainfall in the ITCZ (maximum value of 8 mm/day in the model and 12 mm/day in the observations). Recall that observations are believed to underestimate precipitation rates by 10% compared with atolls observations [Adler et al., 2000]. NCEP-2 reanalysis show a larger rainfall amount.

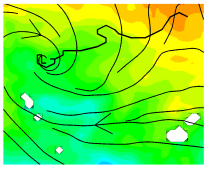

In addition, excess precipitation in the model can be attributed to high cloud efficiency in the BMJ convection scheme of WRF3.1, which was discussed previously. During the course of the study we corrected this parameter and lowered the rainfall amount in the SPCZ but the simulations presented here did not include this improvement. The slightly larger monsoon winds and wind convergence in the SPCZ (described below) can also feedback to convection through humidity convergence. Nevertheless, the differences between the two simulations are mild and, we believe, unimportant to our study; the effect of precipitation bias is mostly a decrease of surface salinity minimum in the warm pool (described earlier). Note also that precipitation in the Indonesian and north Australian regions is underestimated in the model over the ocean as it is concentrated over land (not shown). This is probably due to a poor representation of orographic effects over land because of low resolution in the parent domain. Overall and more importantly, our coupled model provides a net improvement of SPCZ representation compared with usual simulations from non-assimilated global and regional models [Walsh et al., 2004]. The general organization of winds and their divergence (Fig. 3.9) is very similar

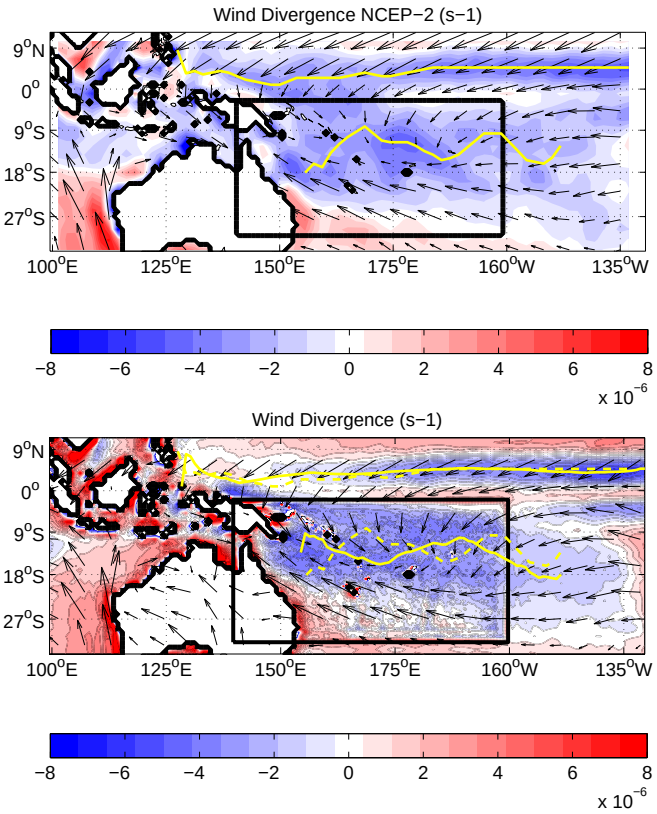

Figure 3.9 - Austral summer (January-March) 10-m wind divergence (s^{-1}) and wind vectors climatology (1979-1998 average) for (a) NCEP-2 reanalysis and (b) the coupled model. Yellow solid lines denote wind convergence lines in each map. in (b) dashed yellow lines denote NCEP-2 wind convergence lines.

in the model and NCEP-2 reanalysis. It shows the rotation of monsoon winds flowing towards the southern hemisphere and across the equator converging with the trade winds. The SPCZ and ITCZ are convergence zones (negative divergence)

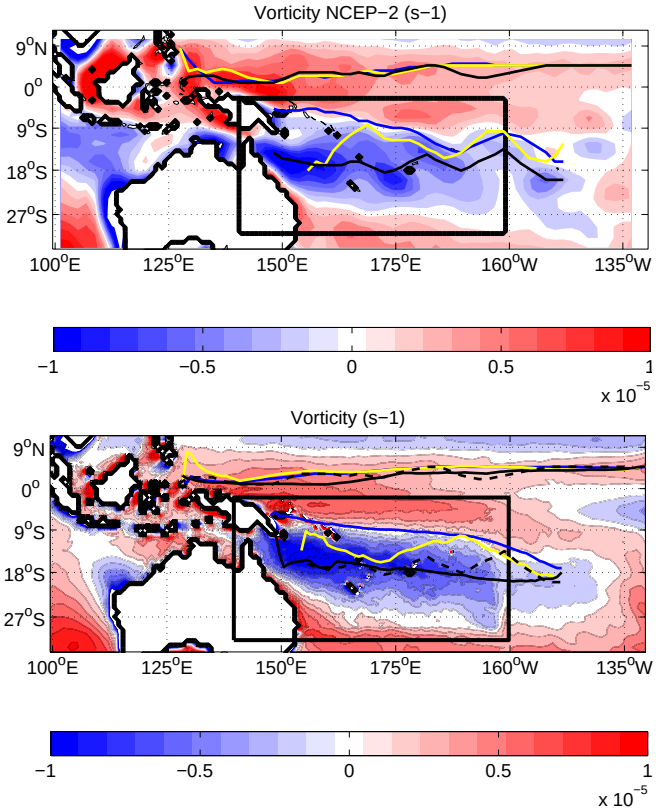

Figure 3.10 - Austral summer (January-March) 10-m wind vorticity (s^{-1}) climatology (1979-1998) for (a) NCEP-2 reanalysis and (b) the coupled model. Cyclonic vorticity is negative in the southern hemisphere and positive in the northern hemisphere. Black solid lines denote maximum cyclonic vorticity lines in each map, yellow lines the wind convergence lines and blue lines the ITCZ/SPCZ lines. In (b) the dashed black lines denote NCEP-2 maximum cyclonic vorticity.

for momentum and humidity, which feeds deep convection and rainfall. We note again a bias in wind divergence over Indonesian and north Australian regions that seems to be associated with mesoscale processes.
The horizontal wind shear between trade winds and monsoon winds creates a region of cyclonic vorticity (Fig. 3.10) whose northern limit is the SPCZ line and whose maximum is located 5-10° further south. The model again accurately reproduce the vorticity field compared with the reanalysis. In both case, the SPCZ is collocated with the zero relative vorticity line at low levels. The reason for the separation between precipitation and vorticity lines in the SPCZ is debated (the ITCZ is clearly different in this respect). One possibility is that the vorticity is a residual artifact of the numerous mesoscale vortices generated along the SPCZ line but moving south, where some of them become tropical cyclones.

3.3.2 Vertical structure: the Hadley cell

The SPCZ harbors the tropical ascendant branch of Hadley-Walker circulation (Fig. 3.11a-b) with a maximum ascendant velocity located between 5 and 10°S. It corre-

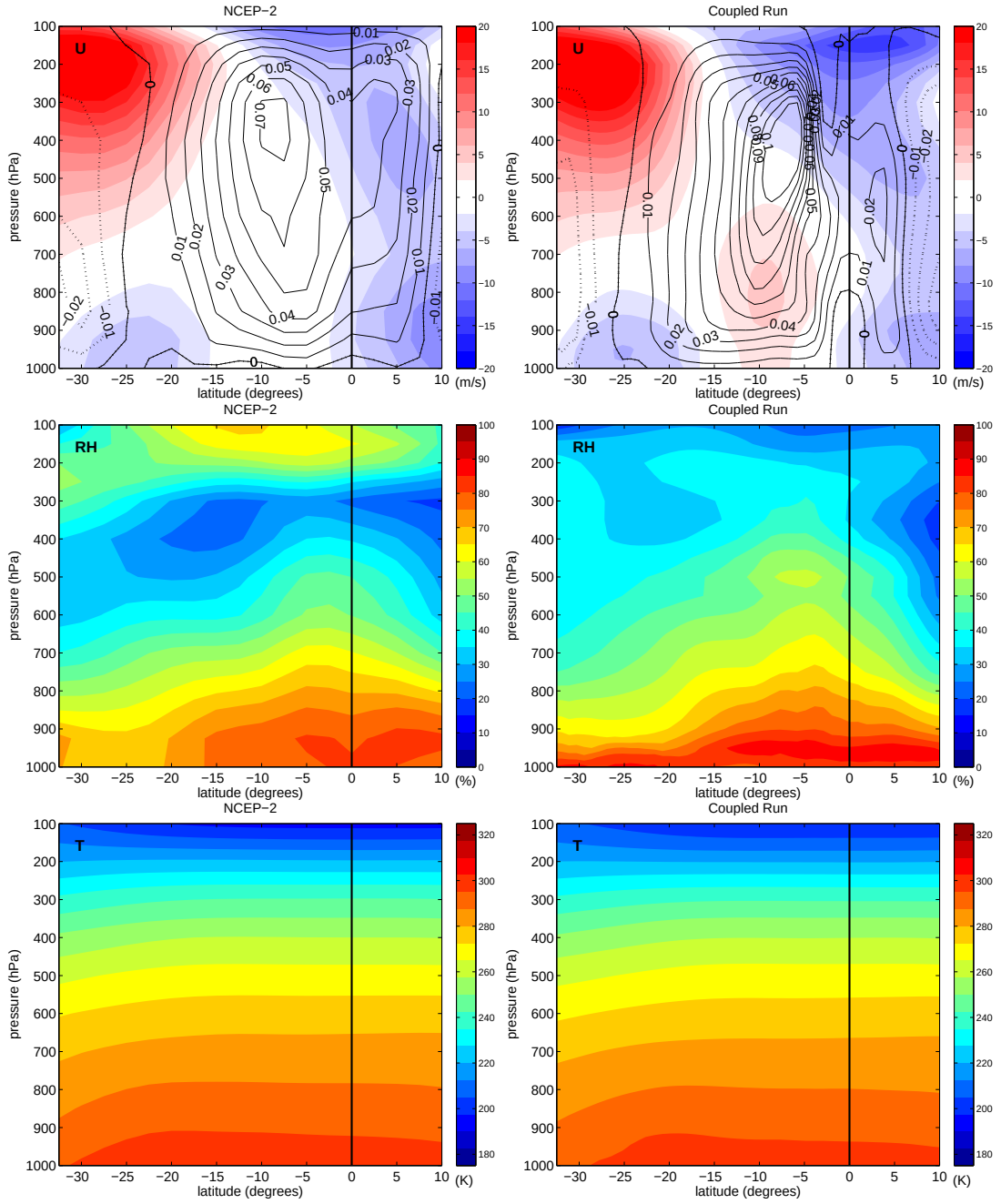

Figure 3.11 - Vertical sections in austral summer (January-March) of (a-b) zonal winds (m/s) and contours of vertical velocity (Pa/s; dashed for downward velocities), (c-d) relative humidity (%), (e-f) temperature (K) for (left) NCEP-2 reanalysis and (right) the coupled model. The fields are zonal means except for vertical velocity taken at 170°E.

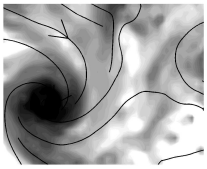

sponds to a maximum in tropospheric humidity (Fig. 3.11c-d) and a minimum in vertical wind shear (Fig. 3.11a-b). The Hadley cell is more active in the southern hemisphere (in austral summer) but is also present in the northern hemisphere with ascendance around 5°N (ITCZ region). The subtropical subsiding branch of the cell is also well reproduced around 30°S. The model and NCEP-2 reanalysis are thus in general good agreement. However, the modeled Hadley cell appears stronger than in NCEP-2. This can be associated with the previously noticed excess in rainfall but it remains in the low range of estimations compared with most global models [Caballero, 2008]. Caballero [2008] attributes the overestimation of southern hemisphere Hadley circulation in coarse global models to wrong representation of Reynolds stresses due to large extratropical eddies [2].
The zonal component of the flow in WRF and NCEP-2 similarly shows the trade winds in the lower troposphere that reach their maximum between the ascendance and subsidence zones at 25°S (10°N in the northern hemisphere). We also note aloft the presence of the westerly subtropical jet stream centered at 30°S and about 200hPa. The jet stream position and its variability are of great interest to cyclogenesis for their strong wind shear conditions that preclude any deep convection.

The temperature sections (Fig. 3.11e-f) are similar in WRF and NCEP2. The modeled relative humidity (RH, Fig. 3.11c-d) is also comparable with some differences. Positive anomalies in tropical mid-troposhere corresponds to the ascendant branch of the Hadley cell. The anomaly is larger in the model consistently with stronger vertical velocities (Fig. 3.11a-b). Here, we should point out to the still large uncertainties of climatological tropical humidity profiles, especially at altitudes above the 500 hPa pressure level [Gutzler, 1993; Paltridge et al., 2009]. It is significant in this respect that the difference of humidity profiles between NCEP-2 and ERA-40 (not shown) are larger than that between NCEP-2 and our simulations (partly due to a data-assimilation problem in ERA-40 as mentioned earlier). The mid-tropospheric decrease of humidity with height and minimum seen at 10-20°S and 5-10°N are nevertheless present in both WRF and NCEP-2. However, the upper troposphere increase of relative humidity in NCEP-2 is not represented in our simulation, although it is not well established either in the climatology from direct observations [Luo et al., 2007]. If it is confirmed, a common explanation is that the upper levels correspond to the convective detrainment layer, where there is an ejection of saturated air. The lower levels, on the other hand, are subjected to subsidence drying (at constant specific humidity, relative humidity keeps decreasing with subsidence because of temperature increase). This process seems at work in our model but has weaker effect than in NCEP-2. It can be due to multiple causes: the convection may not be deep enough in the model;

[2] They base their argumentation on the zonal- and climatological-mean zonal momentum balance of the subtropical upper troposphere: $fv \sim R_{st}$. This is a balance between the Coriolis force acting on the upper branch of the Hadley cell and the stationary and transient eddy stresses R_{st} (divergence of eddy momentum fluxes $-\partial\overline{u'v'}/\partial y$) associated with perturbations of the jet stream. Their computations show that transient eddies play the largest role in the southern hemisphere (the opposite in the northern hemisphere). See similar arguments in the presentation of the zonally averaged circulation in the book of Holton [2004].

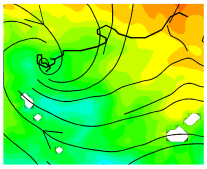

detrainment processes may be too weak; NCEP-2 may overestimate the upper-level increase of RH...

3.3.3 Seasonal cycle and air-sea fluxes

The seasonal cycle of atmospheric state variables and air-sea fluxes, averaged in the SPCZ domain, are presented in this section for various observational datasets and for both the coupled and forced models. We will show that the model climatology is very similar in the forced and coupled model, which we expected because the only difference between the simulations is the removing of storm-induced cold-wakes. The similarity of environmental conditions will confirm that we can isolate the ocean-TC interaction effect by comparing the forced and model solutions.

The SST seasonal cycle (Fig. 3.12a) is well represented in the model with warmer water (about 28°C) during austral summer (January-March) and colder water (about 25°C) during austral winter (July-September). The observational range is relatively narrow with the larger cycle given by Pathfinder data and smaller one by COADS. One interesting feature is the seasonal skin SST that is regularly lower than bulk SST by about 0.2° (an effect of the cool skin layer; see section 2.2.6). Skin SST is closer to SST observations than bulk SST, which thus presents a warm bias of about 0.2°. Yet, *in-situ* SST observations provide bulk SSTs (representative of the first few meters of the surface) and satellite observations are calibrated using observed bulk SSTs. We conclude that the model presents a slight warm bias but the use of skin SST reduces the propagation of errors in the air-sea flux computation (compared to the more conventional usage of ocean model SST). The model mean wind speed and seasonal cycle is similar to QuikSCAT estimates with stronger winds during winter and weaker winds during summer (Fig. 3.12b). The seasonal cycle of precipitation (Fig. 3.12c) is also correct but its intensity is overestimated. This bias, already noticed above, impacts the E-P (evaporation minus precipitation) intensity but the seasonal cycle is correct (Fig. 3.12d). 2-m specific humidity (Fig. 3.12f) is in very good agreement with OAflux and TropFlux datasets. The difference between 2-m air temperature and SST in the model is closer to OAflux than TropFlux in winter but lies in between in summer (Fig. 3.12e). Using skin SST instead of SST in the model (not shown), the model values are a bit higher than OAFlux but the observational products are based on bulk formulations that uses bulk, not skin SST.

The seasonal evolution of air-sea fluxes is presented in Figure 3.13. The seasonal cycle of all fluxes is well captured by the model which is not surprising as state variables are well represented. We also note the particular wide range of observations on flux measurements. The model is within this range for the sensible flux, short and long-wave fluxes but the latent heat flux appears overestimated. The bias in latent heat flux is in part reminiscent of the small warm bias noted for the bulk SST. It is also due to the high value of bulk transfer coefficient for latent heat flux in WRF (it equals the momentum coefficient in the default configuration). The net heat flux is thus close to observations but in the lower range.

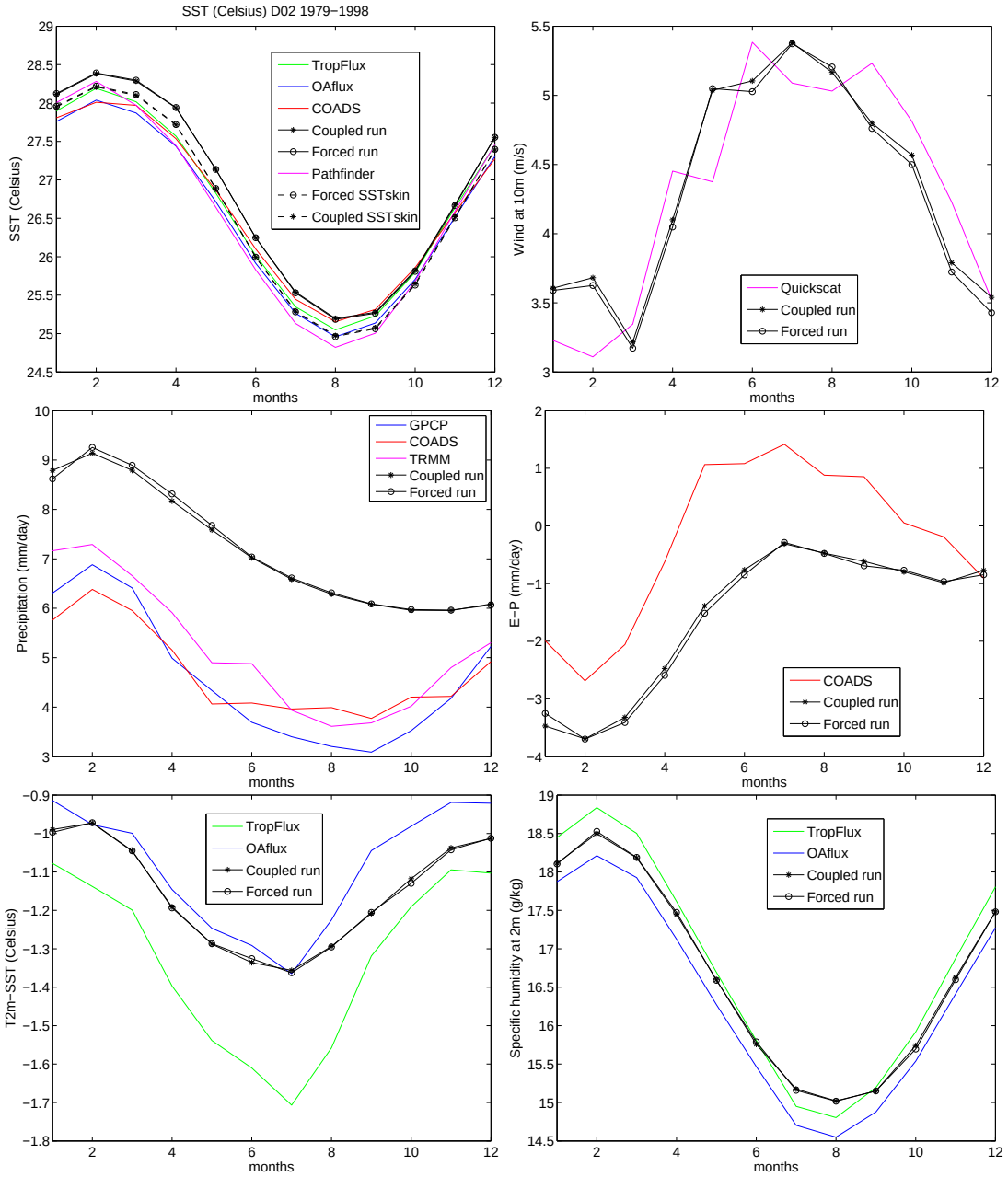

Figure 3.12 - Climatological seasonal cycle (1979-1988 monthly means) of (a) SST (°C) , (b) 10-m wind speed (m/s), (c) precipitation (mm/day), (d) evaporation minus precipitation (mm/day), (e) 2-m temperature minus SST (°C) and (f) 2-m specific humidity for the coupled model (black solid line with stars), the forced model (black solid line with circles) and various observational datasets. Tropflux is in green, OAflux in blue, COADS in red, Pathfinder in purple (for SST), QuikSCAT in purple (for wind), TRMM in purple (for precipitation) and GPCP in blue (for precipitation). The dashed black lines in (a) represent the skin SST for the coupled (stars) and forced (circles) simulations.

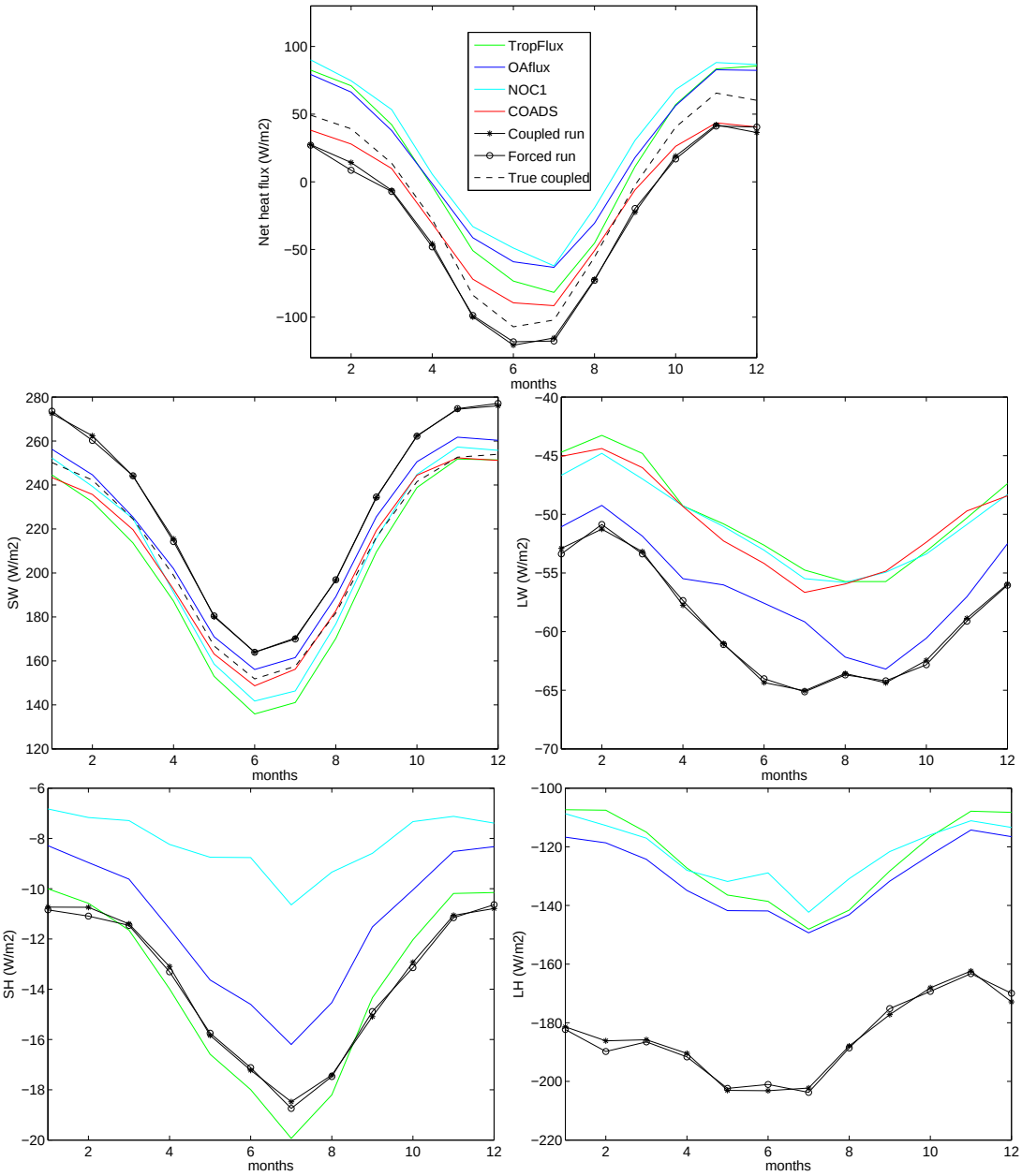

Figure 3.13 - Climatological seasonal cycle (1979-1988 monthly means) of surface heat fluxes (in $W.m^{-2}$): (a) net heat flux , (b) short-wave radiation, (c) long-wave radiation, (d) sensible heat flux, and (e) latent heat flux for the coupled model (black solid line with stars), the forced model (black solid line with circles) and various observational datasets. Tropflux is in green, OAflux in blue, COADS in red and NOC1 in cyan. The dashed black line in (a) and (b) represents the "true" mean flux computed by the coupler from 30-min instantaneous outputs while the solid black lines is made with 3-h instantaneous model outputs.

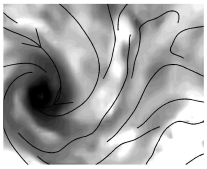

Interestingly, the computation of mean fluxes based on a subsample of instantaneous WRF fluxes (3-hour sampling period; solid black lines with markers in Fig. 3.13) produce a noticeable bias on the short-wave radiation that propagates into the net heat flux. There is also a bias in the other fluxes but we could not estimate it as we only accessed subsampled fields for these fluxes. Anyway, this is a warning against the use of instantaneous fluxes to evaluate daily mean solar radiation at ground level (considering the high frequency effect of clouds), and to force ocean models with it.

3.4 TC DISTRIBUTIONS

3.4.1 Environmental conditions of cyclogenesis

Cyclogenesis requires a series of environmental conditions: low vertical wind shear, high relative humidity at mid-troposphere, high SST and cyclonic relative vorticity [Gray, 1968]. All these conditions are regularly present in the SPCZ region during austral summer as previously shown. The SPCZ is thus home to 10-15% of the world cyclogenesis. Numerous indices of cyclogenesis that combine favorable environmental conditions were developed to propose predictions at interannual and climate scales. Menkes et al. [2012b] compare these indices and evaluate their ability to reproduce the observed cyclogenesis and its interannual variability. All indices fail in representing the observed amplitude of cyclogenesis variability. However, they show some skills in representing the in-phase relationship between cyclogenesis and El Niño Southern Oscillation (ENSO). The Convective Yearly Potential Index (CYGP) shows the best skills for spatial and temporal variability in the South Pacific and is used by Vincent et al. [2011] to evaluate the relation between SPCZ position and cyclogenesis at interannual timescales. Jourdain et al. [2011] show that CYGP is also a very good index for evaluating the environmental conditions of cyclogenesis in a forced atmospheric model. We follow their steps but will show in the course of this study that CYGP underestimate the air-sea coupling effect on cyclogenesis.

The CYGP index is computed as follows:

$$CYGP = \underbrace{|f| I_\xi}_{vorticity} \underbrace{I_S}_{\substack{wind \\ shear}} \underbrace{k(P_C - P_0)}_{thermal} \tag{3.1}$$

where f is the Coriolis parameter in $10^{-5}\mathrm{s}^{-1}$, $I_\xi = \xi_r \frac{f}{|f|} + 5$ with ξ_r the relative vorticity at 925 hPa in $10^{-6}s^{-1}$, $I_S = (|\frac{\delta V}{\delta P}| + 3)^{-1}$ with $\frac{\delta V}{\delta P}$ the vertical shear of the horizontal wind between 925 and 200 hPa in $m.s^{-1}/755hPa$, k is an arbitrary constant adjusted to produce the right number of cyclones, P_C is the convective precipitation in $mm.day^{-1}$ and P_0 is a threshold below which the convective potential is set to zero to avoid spurious cyclogenesis off the tropics. We chose to use this cyclogenesis index with $P_0 = 3$ in agreement with Menkes et al. [2012b] as it

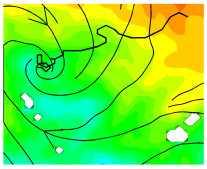

better represents interannual variability of cyclogenesis in the South Pacific. CYGP (Fig. 3.14) shows favorable conditions of cyclogenesis slightly south of the SPCZ position, *i.e.*, near the maximum of vorticity. The region of highest potential cyclogenesis given by CYGP is the Coral Sea where the vorticity part of the index is also maximum. The thermal and shear components show greater potential in the warm pool region but approaching the equator the low absolute vorticity is a barrier to cyclogenesis. Therefore, only the southern part of the warm pool around 10°S is favorable to cyclogenesis. In more subtropical regions (south of about 15°S), thermal and wind-shear conditions are become unfavorable.

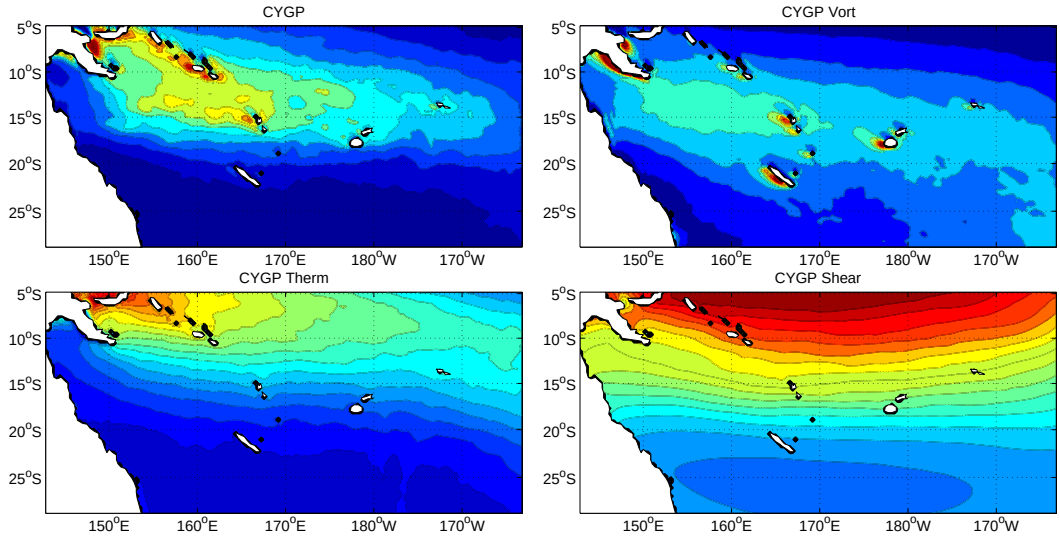

Figure 3.14 - (a) Mean yearly CYGP index for the coupled model and its (b) vorticity, (c) thermal and (d) shear components. No colorbar are provided as the index has to be normalized to the observed or modeled number of genesis. These maps are presented to describe the pattern of this index and components.

From the SPEArTC database, the density of observed cyclogenesis (Fig. 3.15) presents maxima located between 10°S and 15°S, consistently with the environmental index. The coupled model presents a very similar distribution, although the maxima are not exactly collocated, presumably due to the stochastic nature of TC genesis (this will be detailed in the following). Interestingly, the observed cyclogenesis pattern presents some difference with CYGP. In particular, the maximum concentration of favorable conditions in the Coral Sea according to CYGP is not seen reflected in the cyclone data. In this respect, model and data are closer. This observation will be understood later in the manuscript as an effect of coupling on cyclogenesis distribution (see chapter 5).

3.4.2 Seasonal distribution

The seasonal distribution of cyclogenesis and cyclone occurrence are given in Figure 3.16. Both forced and coupled models correctly represent the seasonal cycle of TC genesis and occurrence with more than one TC produced each month between December and March. A χ^2 statistical test (see section 2.3.3.3) indicates

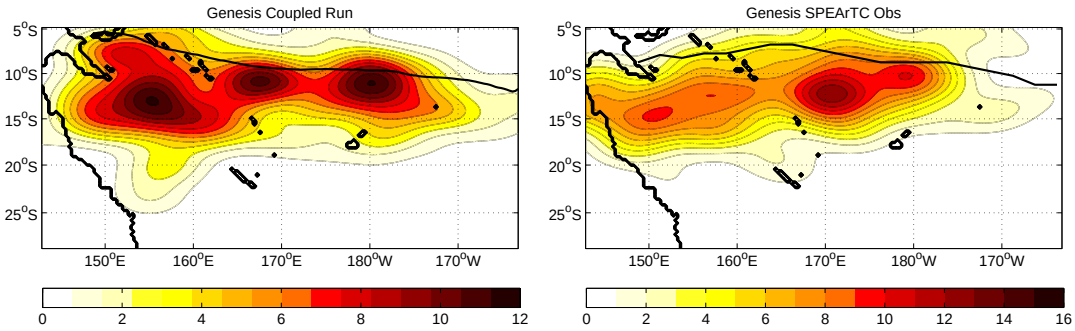

Figure 3.15 - PDF of cyclogenesis (in number of TCs per 5° and per 20 years) for (a) the coupled model and (b) SPEArTC observational dataset. Black lines represent the averaged SPCZ position in (a) the coupled model and (b) CMAP observations.

that the forced and coupled seasonal distribution are similar (at 60%). As in Jourdain et al. [2011], a few cyclones are produced during particularly warm winters (July-September), which is a bias or our model. However, these are rare and short-lived events, confined in the warm pool area. Interestingly, the production of TCs during warm winter seasons are not precluded by the cyclogenesis index (Fig. 3.16), suggesting that the model may be overly responsive to favorable large-scale conditions; something to relate to the trigger function or other parameters of the convection scheme (see section 2.2.1). Besides these winter events, the CYGP index shows a realistic seasonal cycle but with weaker amplitude in the peak months. The index is of poor utility for intraseasonal predictions. The occurrence distribution shows that the number of cyclone days is lower in the coupled than in the forced model indicating that coupled cyclones have a shorter life. Indeed the average life time of TCs in the coupled model is 7 days while it is 8 days in the forced model.

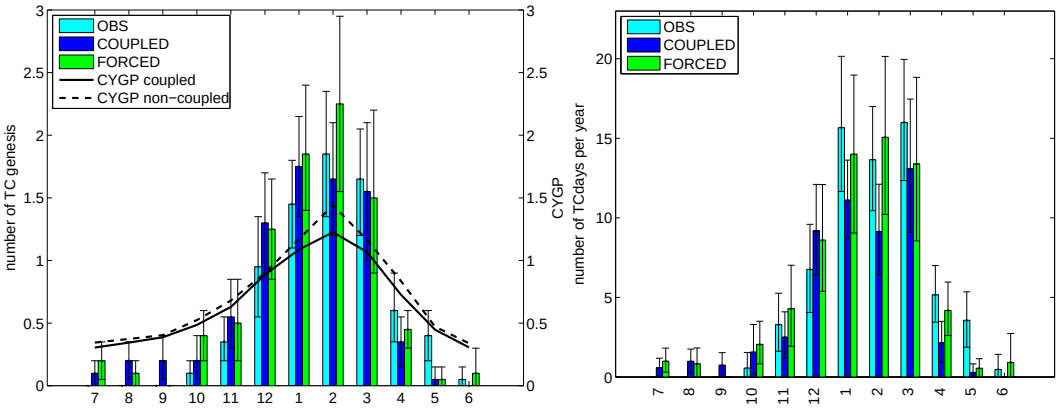

Figure 3.16 - Seasonal distribution of yearly averaged (a) TC genesis and (b) TC occurrence (in number of cyclone days per year) for SPEArTC observational data (in cyan), the coupled model (in blue) and the forced model (in green). Error bars are computed using a bootstrap sampling on interannual variability. In (a) the black bold curves represent the yearly mean CYGP index associated with the coupled (solid) and forced (dashed) simulations (it is normalized to produce the yearly number of genesis in each simulation).

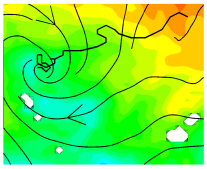

3.4.3 Interannual variability

The total number of TCs per year is 7.9 for the coupled model, 8.7 for the forced model and 7.4 for the observations. The coupled model is thus closer to observations. A student test indicates that the difference of mean TC counts between the forced and coupled model is significant at 62%. In addition, a Fisher test on the variance of TC number at interannual timescale indicates 92% chances of getting a different variance between the two runs. Therefore, the ocean feedback modifies both the mean TC count and its interannual variability.

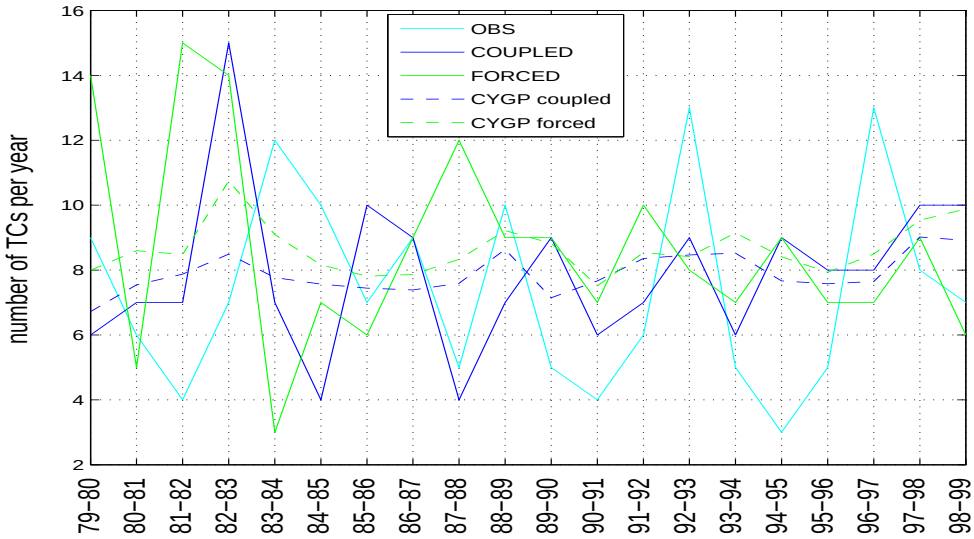

Figure 3.17 - Time series of yearly cyclogenesis number for SPEArTC observational data (in cyan), the coupled model (in blue) and the forced model (in green). Dashed lines represent the CYGP index for the environmental conditions of the coupled (blue) and forced (green) models.

The time series of yearly cyclogenesis number is presented in Figure 3.17. It shows that interannual variability is strong in both forced and coupled models and in the observations. The CYGP index variability is much weaker, similarly to computations based on reanalysis data [Menkes et al., 2012b]. Note that the model interannual variability (both forced and coupled) seems to decrease with time from initialization, which is not seen in the observations. We rule out the possibility of a model drift because it is not apparent in the environmental conditions. We believe that this apparent trend is not significant and would disappear in longer simulations (as in Jourdain et al. [2011]).
The correlation of yearly genesis between model and observations are very low and even negative for the forced model with a low degree of confidence. The correlations with CYGP predictions are also low in both models but slightly higher in the coupled model (0.35 *vs.* 0.12). However, the correlation between forced and coupled CYGP is 0.69 with 99.9% confidence. This means that the environmental conditions of cyclogenesis are very similar in both runs but do not control the variability of yearly cyclogenesis for the South Pacific as a whole. In

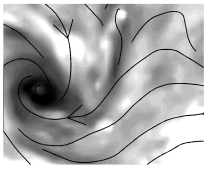

the next section, we will see that El Niño Southern Oscillation (ENSO) has some control on the spatial distribution of interannual variability. Next, the problem of stochasticity will be addressed.

3.4.4 ENSO

El Niño Southern Oscillation is the main mode of interannual variability in the tropical South Pacific. This phenomenon modifies the environmental conditions of cyclogenesis through its strong control of the SPCZ [Vincent et al., 2011]. Many studies have investigated ENSO-related variability using various classifications of ENSO events [*e.g.*, Vincent et al., 2011; Chand et al., 2013]. We use here the classification of ENSO years by the Niño3.4 index (Table 3.1).

Table 3.1 - Classification of ENSO years from the Niño3.4 index. In bold are the years when the SPCZ has a zonal position, corresponding to major El Niño events.

Neutral years	1980/1981 - 1981/1982 - 1985/1986 - 1989/1990 1990/1991 - 1992/1993 - 1993/1994 - 1996/1997
Niño years	1979/1980 - **1982/1983** - 1986/1987 - 1987/1988 **1991/1992** - 1994/1995 - **1997/1998**
Niña years	1983/1984 - 1984/1985 - 1988/1989 - 1995/1996 1998/1999

ENSO is an ocean-atmosphere coupled variability mode that is roughly characterized by two phases: El Niño and La Niña phases. During El Niño, the trade winds weaken and the warm pool eastern edge is shifted to the East leading to an increase of central and eastern Pacific SSTs and a decrease of western Pacific SSTs. The Walker cell is displaced towards the East with increased rainfalls on the Peru-Chile region and increased droughts over Australia. During La Niña phase, the trade winds strengthen and the warm pool eastern edge is shifted to the West leading to warmer SSTs in the western Pacific and cooler SSTs in the central Pacific. The Walker cell is confined to the western Pacific with increased rainfalls over northern Australia and Indonesia.

The SPCZ position is controlled by surface wind convergence, which itself responds to local evaporation and humidity convergence, hence to surface temperature gradients. It is shown [Ramsay et al., 2008] that SPCZ variations are particularly well correlated to temperature variations in the central Pacific, making the Niño 3.4 index a good predictor of SPCZ position. Through SPCZ variations, environmental conditions of cyclogenesis in the South Pacific are also impacted by ENSO. Kuleshov et al. [2009] and Vincent et al. [2011] find a major role played by vorticity and humidity changes, then vertical wind shear and SST. Note that because the SPCZ is usually badly represented in global models, the interannual variability of cyclogenesis is also generally wrong (wether inferred from environmental indices or direct TC counts). Our regional model, consistently with

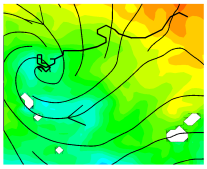

Jourdain et al. [2011] shows a clear improvement in comparison.

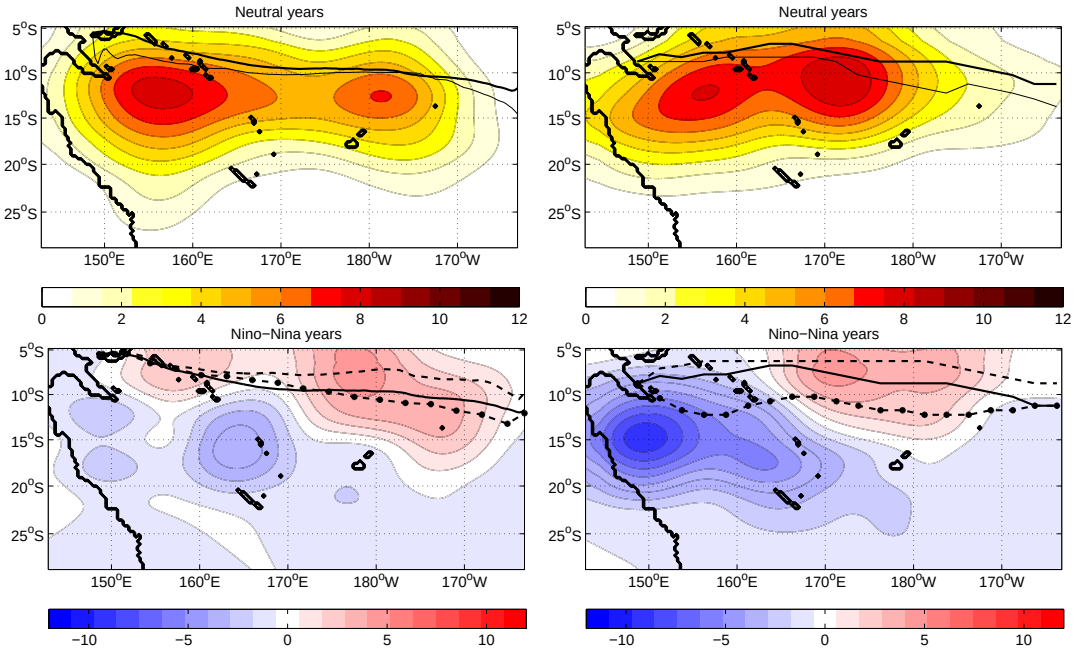

Figure 3.18 - Probability density functions of the number of TC genesis (per 5° and per 20 years with smoothing) for the coupled run (left) and SPEArTC observational dataset (right) for different years: (a-b) neutral seasons (see Table 3.1); and (c-d) Niño minus Niña. The black bold line represents the mean 1979-1998 SPCZ position in the coupled model (left) and GPCP observations (right); the black thin line represents the neutral SPCZ position; the black dashed line represents El Niño SPCZ position; and the dotted-dashed line represents La Niña SPCZ position.

Figure 3.18 shows the probability density functions of cyclogenesis and the SPCZ position for different ENSO phases in the coupled model and in the observations. In agreement with Vincent et al. [2011], we find that during El Niño years the SPCZ is shifted to the North by about 3°, taking a zonal orientation. The cyclogenesis is coherently shifted to the northeast with an increase of the number of TCs in the warm pool region and a decrease in the Coral Sea and near the coast of Australia [Evans and Allan, 1992]. During these years, eastern regions, starting from Fidji are particularly affected [Chand and Walsh, 2009]. TCs can form as far as French Polynesia with important damages on theses islands that are normally spared from TC occurrence.
During La Niña years, the SPCZ is shifted to the south by a few degrees. In the coupled model, the usual slanting of the SPCZ is further increased (as opposed to Niño years), which appears in some observational datasets [Jourdain et al., 2011]. Note that there are only 5 La Niña years during the simulation period and our analysis may lack robustness on these events. The cyclogenesis PDF for Niña years has more TCs in the Coral Sea and less in the warm pool, a reverse pattern from Niño years. As a result the difference between Niño and Niña years (Fig. 3.18c-d) presents a slantwise dipole pattern in both model and observations. Jourdain et al.

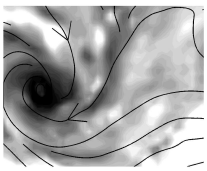

[2011] showed that this pattern is detrimental to ENSO-based seasonal forecasting except in the extreme parts of the cyclogenesis area (*i.e.*, French Polynesia in the east and the Australian coast in the west). For sure, the variations of the total count of cyclogenesis tends to cancel out when positive and negative values are added. This is consistent with the findings of the previous paragraph.

Lower frequency variability like the interdecadal Pacific oscillation (15-30 year cycles) and its effect on SPCZ position have been investigated [Folland et al., 2002]. Our own study is limited here by the 20-year duration of the simulations. On the other end of the spectrum, intraseasonal variability is important in the tropics as well and is generally organized as a Madden-Julian oscillation, which drives convection on a 30-90 day timescale. Previous studies [Leroy and Wheeler, 2008; Camargo et al., 2009] have looked at cyclonic activity modulation by MJO and offer interesting perspectives for intraseasonal forecasting (at the scale of a few weeks). We did not focus on this issue that would require a larger tropical pacific domain covering the Indian Ocean (a tropical channel would be best).

3.4.5 Environmental *vs.* stochastic forcing of cyclogenesis

Previously, we have confirmed after Jourdain et al. [2011] that the interannual variability of total yearly cyclogenesis is poorly correlated between model and observations, despite locally strong ENSO forcing. In addition, the environmental conditions of cyclogenesis (from CYGP) have much lower interannual variability than observed cyclogenesis. All this points to a different forcing than large-scale conditions for the interannual variability of TCs in the South Pacific. Zhao et al. [2009] found correlations between the number of observed and simulated cyclones higher than 0.8 in the North Atlantic cyclonic region while their correlations are only 0.3 in the South Pacific, consistent with Jourdain et al. [2011] and our results. This suggests again that the predictability of TCs in the South Pacific is low due to the lack of correlation with environmental forcing.

Jourdain et al. [2011] assume that a great part of TC variability is stochastic, *i.e.*, linked to intrinsic variability produced by non-linear mesoscale interactions. They evaluate the forced *vs.* stochastic parts of TC variability by considering the yearly number of cyclogenesis as a product of forced and stochastic processes where the forced processes are represented by the cyclogenesis index. This gives the system:

$$\begin{cases} N_{TC}(t) = N_{CYGP}(t).\Phi_{stoch}(t) \\ \langle N_{TC}(t) \rangle = \langle N_{CYGP}(t) \rangle \end{cases} \tag{3.2}$$

where N_{TC} is the total number of TCs per year, N_{CYGP} is the number of TCs per year given by the CYGP (normalized and spatially integrated) and Φ_{stoch} is a stochastic function. $\langle . \rangle$ represents a time average over all simulated years.

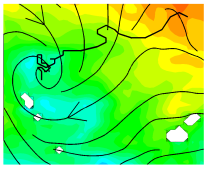

Assuming that N_{CYGP} and Φ_{stoch} are uncorrelated variables, the rules of uncertainty propagation then suggest the following statistical relation between forced and stochastic variability:

$$\left(\frac{\sigma_{N_{TC}}}{\langle N_{TC}(t)\rangle}\right)^2 \simeq \left(\frac{\sigma_{CYGP}}{\langle N_{CYGP}(t)\rangle}\right)^2 + \left(\frac{\sigma_{stoch}}{\langle \Phi_{stoch}(t)\rangle}\right)^2 \tag{3.3}$$

where $\sigma_{N_{TC}}$, σ_{CYGP} and σ_{stoch} are the standard deviations of the genesis number, genesis index, and stochastic distribution respectively. It is a direct relation between the variance of genesis number and mean genesis numbers $\langle N_{TC}(t)\rangle$.

Using the relation 3.2, we compute the stochastic function and analyze its distribution. As in Jourdain et al. [2011], we find a log-normal law (Fig. 3.19), *i.e.*, the logarithm of the stochastic function follows a normal law:

$$f(x) = \frac{1}{\sigma\sqrt{2\pi}} \exp -\left(\frac{x-\mu}{2\sigma}\right)^2 \tag{3.4}$$

where σ is the standard deviation of x and μ the mean of x. In our case:

$$\begin{cases} x = ln(\Phi_{stoch}) & \\ \mu = \langle ln(\Phi_{stoch})\rangle & \mu = -0.04 \text{ for the coupled run and } \mu = -0.06 \text{ for the forced run} \\ \sigma = \sigma_{ln(\Phi_{stoch})} & \sigma = 0.29 \text{ for the coupled run and } \sigma = 0.39 \text{ for the forced run} \end{cases}$$

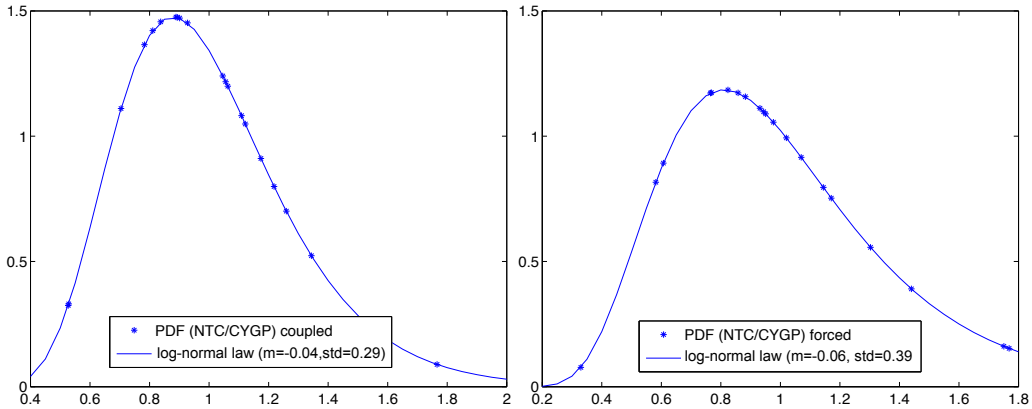

Figure 3.19 - Distributions of the stochastic function from the coupled (a) and forced (b) models (stars) and fitting with of a log-normal law (solid line).

Using equations 3.2 and 3.3, we compute the forced and stochastic variability of cyclogenesis in both the forced and coupled simulations (Table 3.2). We find that the environmental forced variability is lower than that estimated in Jourdain et al. [2011]: $\sigma_{CYGP} = 1.8$. The forced variability accounts for only about 6% of total variability in our case while Jourdain et al. [2011] found about 30%. The difference could be due to multiple factors. First, the number of simulated years (20 years) may still be insufficient for accurately separating forced and stochastic interannual

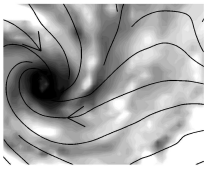

variability. Second, large scale variability is slightly different in our simulation. It is so in particular for correlations between ENSO and cyclogenesis distribution. Note that the correlations are spatially strong but averaged over the whole domain they almost vanish (pointing back to the first point). Finally, another difference concerns the SST field. In our case, SST is computed by the ocean model and has mesoscale structures whereas in Jourdain et al. [2011], the SST field is from NCEP2 and is very smoothed. Mesoscale interactions may add stochasticity to the problem. This could be checked in further studies. However, despite uncertainties in the exact amount of stochasticity, both studies confirm that the major part of interannual variability in TC number is stochastic. Interestingly, the stochastic variability is lower in the coupled than in the forced model, albeit within the range of uncertainty of equation 3.3. As noticed by Jourdain et al. [2011], stochasticity may be overestimated because CYGP is not an exact measure of environmental conditions, as will be confirmed in chapter 5. Overall, large stochasticity indicates poor predictability of cyclogenesis in the South Pacific as a whole. Nevertheless, predictability can be locally much higher due to ENSO forcing (Sec. 3.4.4).

Table 3.2 - Statistics of the 1979-1998 mean TC numbers in the coupled and forced models and in SPEArTC observations, including forced and stochastic variability.

	$\langle N_{TC}(t)\rangle$	$\sigma_{N_{TC}}$	σ_{CYGP}	σ_{stoch}	$\left(\frac{\sigma_{N_{TC}}}{\langle N_{TC}(t)\rangle}\right)^2$	$\left(\frac{\sigma_{CYGP}}{\langle N_{CYGP}(t)\rangle}\right)^2$	$\left(\frac{\sigma_{stoch}}{\langle \Phi_{stoch}(t)\rangle}\right)^2$
Obs.	7.4	3.0			0.166		
Coupled	7.9	2.4	0.61	0.29	0.096	0.006	0.083
Forced	8.7	3.1	0.78	0.36	0.130	0.008	0.128

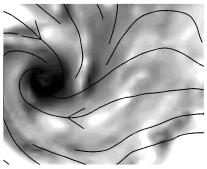

Chapter 4

Impact of Tropical Cyclones on the Heat Budget of the South Pacific Ocean

Contents

4.1 Introduction **87**
4.2 Materials and methods **89**
4.2.1 The regional ocean model 89
4.2.2 TC forcing in twin ocean experiments 90
4.2.3 Temperature equation and tendencies 92
4.3 Validation of the ocean model with WRF forcing **93**
4.4 Results **96**
4.4.1 Case studies 96
4.4.2 Composite analysis of TC wakes 100
4.4.3 TC impacts on the ocean climate 110
4.5 Conclusions and discussion **116**
4.6 Appendix: KPP **118**
4.6.1 Interior mixing 119
4.6.2 Boundary layer mixing 119

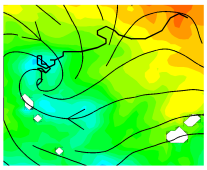

Abstract

The present study investigates the integrated ocean response to tropical cyclones (TCs) in the South Pacific convergence zone through a complete ocean heat budget. The TC impact analysis is based on the comparison between two long-term (1979-2003) oceanic simulations forced by a mesoscale atmospheric model solution in which extreme winds associated with cyclones are either maintained or filtered. The simulations provide a statistically robust experiment that fills a gap in the current modeling literature between coarse-resolution and short-term studies. The authors' results show a significant thermal response of the ocean to at least 500-m depth, driven by competing mixing and upwelling mechanisms. As suggested in previous studies, vertical mixing largely explains surface cooling induced by TCs. However, TC-induced upwelling of deeper waters plays an unexpected role as it partly balances the warming of subsurface waters induced by vertical mixing. Below 100 m, vertical advection results in cooling that persists long after the storm passes and has a signature in the ocean climatology. The heat lost through TC-induced vertical advection is exported outside the cyclogenesis area with strong interannual variability. In addition, 60% of the heat input below the surface during the cyclone season is released back to the oceanic mixed layer through winter entrainment and then to the atmosphere. Therefore, seasonal modulation reduces the mean surface heat flux due to TCs to about $3.10^{-3} PW$ in this region exposed to 10%-15% of the world's cyclones. The resulting climatological anomaly is a warming of about 0.1°C in the subsurface layer and cooling below the thermocline (less than 0.1°C).

Published in *Journal of Physical Oceanography* Volume 42

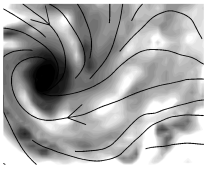

4.1 Introduction

Tropical cyclones (TCs) are among the most powerful extreme events of atmospheric circulation. While numerous studies have been devoted to the dynamics of TCs, comparatively few have investigated their oceanic impact. When cyclones occur, they generally induce strong oceanic surface cooling [Leipper, 1967; Withee and Johnson, 1976; Pudov, 1979; McPhaden et al., 2009], which feeds back to them, moderating their intensity [Schade and Emanuel, 1999; D'Asaro et al., 2007]. Understanding the surface heat balance associated with TCs is thus of major relevance to our understanding and predictive skills regarding these extreme events.

Previous studies have suggested various mechanisms affecting the ocean surface during and after a cyclone passage. From event studies using Lagrangian floats [D'Asaro et al., 2007], expendable airborne instruments [Jacob et al., 2000], or simple ocean models [Price, 1981], 70%-85% of sea surface temperature (SST) cooling is estimated to result from extreme wind mixing of surface waters with deeper, colder ocean layers. Several case studies [*e.g.*, Shay et al., 2000; Jaimes and Shay, 2009; Shay and Uhlhorn, 2008] show that vertical mixing in the TC wake is mainly driven by shear instability of near-inertial oscillations (NIOs) that have maximum impact 3-5 days after the TC passage. A rightward SST cooling asymmetry (in the Northern Hemisphere) is often observed [*e.g.*, Pudov, 1979; McPhaden et al., 2009; Shay et al., 1992] and has been largely attributed to two phenomena. First, the wind stress asymmetry associated with TC translation speed can inject more mechanical energy into the ocean on the right side of the track [Northern Hemisphere; Shay et al., 1989; Chang and Anthes, 1978]. Second, mixing can be further increased because of resonance between wind and inertial currents on the same side [Price, 1981; Price et al., 1994; Sanford et al., 2007; Samson et al., 2009].

Satellites provide both local and global observation of surface cooling in the cyclone wake and an estimation of the time needed to restore the surface to its prestorm conditions [Price et al., 2008]. Yet, satellite observations cannot be used to acquire a complete surface heat budget that requires subsurface data. Ocean subsurface observations during cyclone occurrence indicate that subsurface oceanic background conditions may have a large control on the TC surface signature [Jacob et al., 2000; Lloyd and Vecchi, 2011]. The exact processes involved are difficult to assess from observations alone. Nevertheless, a few analyses conducted for specific events revealed that TC-induced upwelling may dominate the subsurface heat budget under the cyclone eye [Price et al., 1994; Huang et al., 2009] and that lateral advection may be important as a redistribution process [D'Asaro, 2003; Huang et al., 2009; Price, 1981; Greatbatch, 1983; Vincent et al., 2012a]. In addition to subsurface processes, it appears that latent heat fluxes from evaporation may also be of importance to the heat budget [Price, 1981; Bender et al., 1993; Huang et al., 2009]. However, assessing the robustness of these processes in a statistical sense and their long-term oceanic impact has remained challenging.

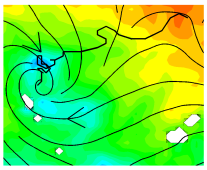

Quantifying subsurface warming through extreme wind mixing is another matter of debate. In the TC-induced mixing process, the heat lost near the surface is transferred down below the mixed layer. However, it is unclear to what extent other processes modulate this subsurface heat input. In particular, cooling through vertical advection may compete with mixing-induced warming [*e.g.*, Price et al., 1994] and the heat anomaly may be redistributed away from its generation area. This raises the issue of residual effect of tropical cyclones on the regional and global ocean climate. Assuming that TC-induced surface cooling results in a permanent heat transport below the mixed layer, Emanuel [2001] estimates a relatively large heat input of $\sim 1.4 \pm 0.7PW$ below the surface. He thus suggests that TCs have an important role in the global ocean diapycnal mixing that regulates the meridional overturning circulation and, in turn, the climate system. Based on similar assumptions and dimensional analysis of vertical mixing, Sriver and Huber [2007] give a lower estimate of $0.26PW$ of heat input due to cyclones [Sriver et al. [2008] update this value to 0.35-0.60 PW]. More recently, Jansen et al. [2010] have argued that TC-induced heat input below the surface is overestimated since part of the heat injected in the seasonal thermocline during the summer cyclonic season is injected back through winter entrainment to the ocean surface and then to the atmosphere. Therefore, while there is general agreement that some heat is permanently injected below the mixed layer, the few attempts at quantification are very sensitive to the data used and processes accounted for in the estimation.

In the absence of a global high-resolution ocean dataset, ocean models remain the best alternative to advance our knowledge of the oceanic response to cyclones. There is still a gap between modeling case studies, which detail the oceanic response to a given or idealized event, and long-term, statistically reliable ocean climate modeling. Studies of the second type usually use low-resolution grids and idealized mixing processes [*e.g.*, Pasquero and Emanuel, 2008; Sriver, 2010]. Global low-resolution models provide reasonable estimates of heat transport in the ocean, but they cannot represent the complexity of TC-induced processes. Specifying realistic TC distributions on a low-resolution grid is a major challenge in itself. Therefore, regional high-resolution studies would offer a good alternative. To our knowledge, this has not yet been attempted.

Using a state of the art, primitive equations, regional oceanic model, the present study investigates the various processes by which extreme winds associated with cyclones influence the oceanic heat budget and impose their residual effect. The study area is located in the southwest Pacific and encompasses the South Pacific convergence zone [SPCZ; Vincent et al., 2012a]. The SPCZ is one of the most intense atmospheric convergence zones of the world and a major cyclogenesis area: 10%-15% of global cyclogenesis occurs in this region. To account for the extreme winds that must force the ocean model, we use a 25-yr simulation with a regional mesoscale atmospheric model that realistically simulates TC distributions in the South Pacific [Jourdain et al., 2011]. The adopted methodology consists of comparing twin oceanic experiments that are distinct by the presence or absence of extreme wind forcing in TCs. Using heat budget equations and analyzing the

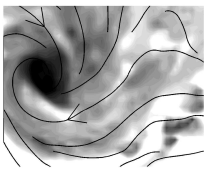

three-dimensional (3D) tendencies that explain TC-induced temperature changes, we provide an exhaustive quantification of physical processes responsible for oceanic heat changes along each cyclone track and over the whole region. After detailing the methodology and the model validation at event and climatological scales (sections 4.2 and 4.3), we examine the ocean heat budget associated with a composite of all cyclones and finally expand to the ocean climatology of the South Pacific (section 4.4).

4.2 Materials and methods

4.2.1 The regional ocean model

The ocean model configuration uses the Regional Oceanic Modeling System [ROMS; Shchepetkin and McWilliams, 2005] in its nested version [Penven et al., 2006] over the southwest Pacific region (8-30°S, 140-170°W). It has 41 terrain-following vertical levels with 2-5-m vertical resolution in the first 50 m of the surface and then 10-20-m resolution in the thermocline and 200-1000-m resolution in the deep ocean. The horizontal resolution is 1/3°, and the baroclinic time step is 1 h; hourly outputs are stored for a case study and 1-day- averaged outputs are stored for long-term analysis.

The turbulent vertical mixing parameterization is based on the scheme proposed by Large et al. [1994], featuring a K-profile parameterization (KPP) for the planetary boundary layer connected to an interior mixing scheme (see 4.6 for details). The boundary layer depth (h) varies with surface momentum and buoyancy forcing and is determined by comparing a bulk Richardson number to a critical value. The surface layer above the oceanic boundary layer obeys the similarity theory of turbulence. At the base of the boundary layer, both diffusivity and its gradient are forced to match the interior values. Below the boundary layer, vertical mixing is regarded as the superposition of three processes: vertical shear, internal wave breaking, and convective adjustment. The KPP model has been shown to accurately simulate processes such as convective boundary layer deepening, diurnal cycling, and storm forcing: it is widely used in ocean modeling [*e.g.*, Halliwell et al., 2011]. The model has also shown a reasonable level of accuracy in modeling TC-induced mixing [Jacob and Shay, 2003]. Some processes are nevertheless missing in this parameterization: for example, mixed layer instabilities that would further help the restratification process in the TC wake [Boccaletti et al., 2007] are neither resolved in our 1/3° resolution model nor parameterized [for tropical applications, see also Marchesiello et al., 2011].

Open boundary conditions are treated using a mixed active/passive scheme [Marchesiello et al., 2001] that forces large-scale information from the Nucleus for European Modeling of the Ocean (NEMO) 1/2° global model simulation [described in Couvelard et al., 2008] while allowing anomalies to radiate out of the domain. The use of similar ROMS configurations in the southwest tropical Pacific region is largely validated through studies demonstrating skills in simulating both the

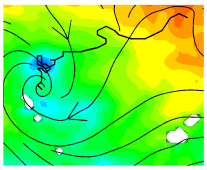

surface [Marchesiello et al., 2010b] and subsurface ocean circulation [Couvelard et al., 2008].

4.2.2 TC forcing in twin ocean experiments

The present oceanic configuration mainly differs from Marchesiello et al. [2010b] by the atmospheric forcing. To compute the momentum fluxes, we use the 1979-2003 6-hourly outputs of atmospheric fields from a Weather Research and Forecasting model (WRF) simulation of the South Pacific climate [Jourdain et al., 2011]. The simulation uses a two-way nested configuration forced at the lateral boundaries by the National Centers for Environmental Prediction/Department of Energy Global Reanalysis 2 [NCEP-2; Kanamitsu et al., 2002]. The parent domain at 105-km resolution spans the Indo-Pacific region (42°S-25°N, 95°E-115°W), and the child domain at 35-km resolution fully encompasses the SPCZ region (2-32°S, 139°E-161°W). The modeled large-scale environment and TC activity are validated and analyzed in detail in Jourdain et al. [2011]. The large-scale SPCZ behavior, including both seasonal and interannual variability, and the statistical distribution of TC activity (genesis and occurrence) are in good agreement with observations. Jourdain et al. [2011] noted, however, a shift of TC intensity distribution toward more frequent occurrence of weaker cyclones (a known bias of medium-resolution models). All modeled TCs are identified via a cyclone tracker, which will be used again in the present study. Over the 1979-2003 period, our atmospheric simulation presents 235 TCs (10-m wind speed reaching 17 $m.s^{-1}$ in 6-hourly outputs) including 55 TCs reaching at least 33 $m.s^{-1}$. The most extreme cyclones are absent from this model solution, but they do represent a small fraction of the total number. More importantly perhaps, the model provides a coherent set of TC events with a realistic development process (genesis and intensification stages). In addition, the large number of simulated cyclones in the atmospheric forcing allows a statistically robust representation of the oceanic response.

We purposely choose to focus here on the oceanic response to TC momentum forcing, which is assumed to be of primary importance. A more complete acknowledgment of TC forcing would require a representation of coupling processes involving the feedback of ocean temperatures [*e.g.*, Lloyd and Vecchi, 2011], wind waves, and sea spray [Bao et al., 2000] to TC formation and development. This will be explored in further studies. The 6-hourly momentum forcing of the ocean model is computed using wind fields from the WRF simulation; it is converted into stresses using the drag formulation of Powell et al. [2003] that parameterizes the drag reduction observed under extreme wind conditions. Surface freshwater and heat fluxes are computed using bulk formulations [Marchesiello et al., 2010b] with large-scale air temperature, wind speed, and relative humidity from NCEP-2 data. TC winds do not enter the formulation of turbulent fluxes at the air-sea interface and TC forcing can only proceed by mechanical action of the wind stress (and its curl). Yet, negative feedbacks of SST perturbation on latent and sensible heat fluxes are permitted, but not on the outward longwave radiation (NCEP-2 SST values are used in this case). These choices underestimate the negative feedback

of the ocean to TC-induced forcing: that is, one that would minimize the oceanic response to TCs. However, our results will show that only the strongest TC events appear to overestimate the oceanic response and that these events only weakly affect the overall cyclone effect. The simulation that includes TC wind forcing is referred to as the cyclone experiment in the following.

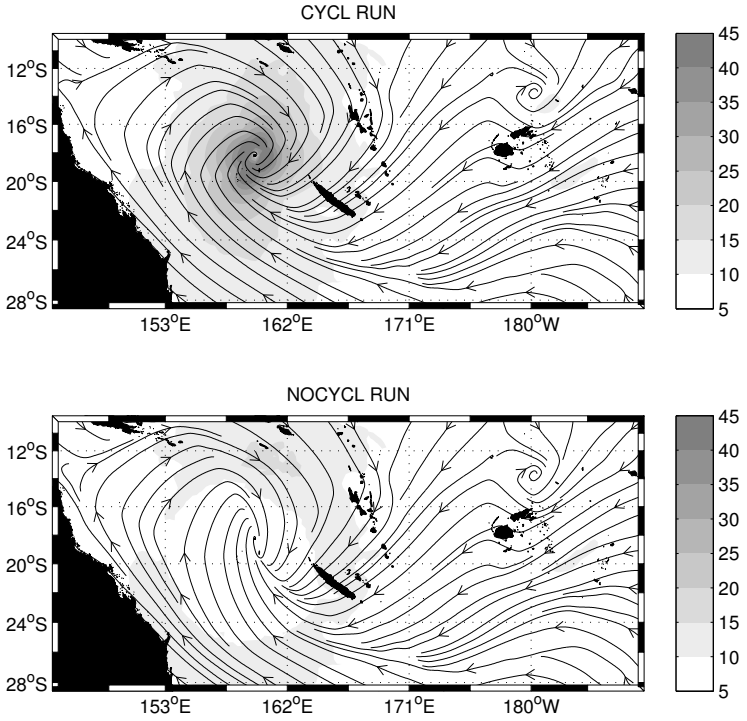

Figure 4.1 - Snapshots of WRF surface wind intensity (shading; $m.s^{-1}$) and streamlines. (a) A typical cyclone used as forcing for the reference ROMS ocean simulation (the cyclone experiment). (b) Extreme wind speeds are removed from the TC winds and the remaining field is used as forcing for the ocean simulation (the no-cyclone experiment). A wind stress threshold of 0.1 $N.m^{-2}$ is used to clip extreme winds within a 6° disk radius of the cyclone center.

To assess the oceanic impact of extreme winds associated with cyclones, a twin simulation with "cyclone free" atmospheric forcing is designed (the no-cyclone experiment). Note that the term "cyclone free" does not indicate here the absence of cyclones but the absence of the extreme winds associated with them. The cyclone-free forcing field is computed by saturating wind stress intensity at 0.1 $N.m^{-2}$ (which corresponds to a maximum surface wind speed of about 13 $m.s^{-1}$) while preserving wind stress directions, within a 6° radius disk around each point of the cyclone tracks. The value of 0.1 $N.m^{-2}$ was chosen as the maximum climatological wind stress during summer in that region. It seemed reasonable to assume that such a threshold would prevent any major effect of cyclones while preserving their large-scale environment. Note that the TC removal procedure does not affect any other high wind event that can escape the cyclone tracker. Figure 4.1 shows an example of the resulting wind forcing in the cyclone and no-cyclone experiments

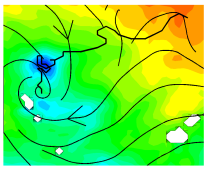

for a strong TC. Only the extreme winds are removed, but the large-scale wind pattern remains unchanged. It may be questioned whether the weak large-scale cyclonic vortex that remains around the cyclone core should also be removed. Our understanding is that they participate in low numbers to the activity of numerous tropical storms that populate the cyclogenesis area. It is also consistent with the virtual reality of a cyclone-free world where storms do not get to become cyclones. In the following, TC-induced oceanic anomalies are assessed by analyzing the differences between the twin ocean experiments.

4.2.3 Temperature equation and tendencies

To characterize the processes responsible for temperature anomalies, the heat budget is computed. The full three-dimensional temperature equation of the interior ocean is

$$\underbrace{\delta_t T}_{RATE} = \underbrace{-u\delta_x T - v\delta_y T}_{HADV} \underbrace{-w\delta_z T}_{VADV} + \underbrace{D_l(T)}_{HMIX} + \underbrace{D_z(T)}_{VMIX} + \underbrace{I(z)}_{FORC} \tag{4.1}$$

with the following surface boundary condition:

$$(k_z \delta_z T)_{z=0} = \frac{Q* + Q_S}{\rho_0 C_p}$$

where T is the model potential temperature; (u, y, w) are the components of ocean currents; $D_l(T)$ is the lateral diffusion operator; $D_z(T) = \delta_z(k_z \delta_z T)$ is the vertical diffusion operator with k_z being the vertical diffusion coefficient; and $I(z) = (Q_S/\rho_0 C_p)\delta_z f(z)$ is the heating rate due to the penetrative solar heat flux with Q_S being the net surface solar heat flux and $f(z)$ being the attenuation factor that determines the fraction of solar radiation that reaches depth z. Here, $Q*$ contains the other surface heat flux terms: longwave radiation and latent and sensible heat fluxes ($Q*$ and Q_S are positive when directed downward: *i.e.*, warming the ocean). A proxy for the SST equation is derived by averaging Eq. 4.1 over the time-varying mixed layer depth h [Menkes et al., 2006],

$$\underbrace{\delta_t SST}_{RATE} = \underbrace{-\langle u\delta_x T + v\delta_y T\rangle}_{HADV} \underbrace{-\langle w\delta_z T\rangle}_{VADV} + \underbrace{\langle D_l(T)\rangle}_{HMIX} + \underbrace{\frac{Q* + Q_S[1 - f(z=h)]}{\rho_0 C_p h}}_{FORC}$$
$$\underbrace{- \frac{(k_z\delta_z T)(z=-h)}{h} - \frac{1}{h}\delta_t h[SST - T(z=-h)]}_{VMIX} \tag{4.2}$$

Brackets denote the vertical average over the mixed layer depth h (with our notation, h is positive): $hxi50(1/h)2hxdz$. Here, RATE is the rate of change (or temporal tendency) of SST; HADV is lateral advection; VADV is vertical advection; HMIX is lateral diffusion; FORC is the heat input by surface forcing in the mixed layer with $Q*$ the nonsolar heat flux; and VMIX is the heat input through the mixed layer base by vertical mixing [we define here vertical mixing as the combination of

entrainment/detrainment and local (downgradient) vertical diffusion at the mixed layer base]. The mixed layer depth is calculated as the depth at which density is 0.01 $kg.m^{-3}$ greater than surface density, as in Menkes et al. [2006]. This criterion is in the range of those reported in the literature [for a detailed discussion, see Montegut et al., 2004]. SST is used interchangeably with mixed layer temperature in the following. The various SST budget terms, as well as all model state variables, are 1-day averaged. Three layers are defined in the following: the surface layer from the surface to the mixed layer (~0-30 m); the subsurface layer below the mixed layer (~30-100 m); and the deep layer (below 100 m).

4.3 Validation of the ocean model with WRF forcing

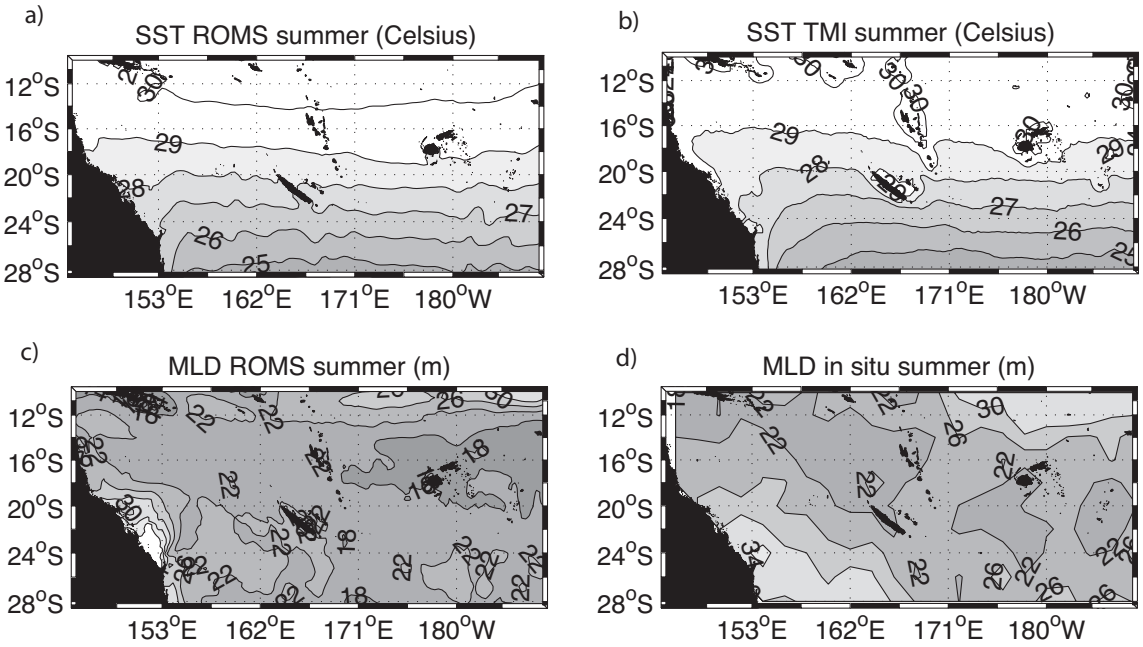

Figure 4.2 - (top) Mean austral summer [January-March (JFM)] SST (°C) from (a) the 1979-2003 ROMS control run and (b) the TMI-AMSR-E 1998-2009 data (http://www.ssmi.com/sst). (bottom) Mean summer (JFM) mixed layer depth from (c) 1979-2003 ROMS control run and (d) climatology from Montegut et al. [2004].

The climatological ocean circulation and its validation are detailed in Couvelard et al. [2008] and Marchesiello et al. [2010b]. Here, we focus on temperature during the austral summer, which is the cyclone season. The SST pattern agrees well with observations (Figs. 4.2a,b) having a realistic north-south gradient, although a 1°C warm model bias is apparent in the warm pool region. Coastal cooling associated with the East Australian Current is also not properly resolved [Couvelard et al., 2008]. The mixed layer depth (Figs. 4.2c,d) shows good agreement with in situ observations [Montegut et al., 2004] in the TC occurrence region. The vertical structure of summer temperature is illustrated in Fig. 4.3; it is also close to observations, despite the already mentioned warm bias in the surface

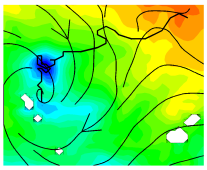

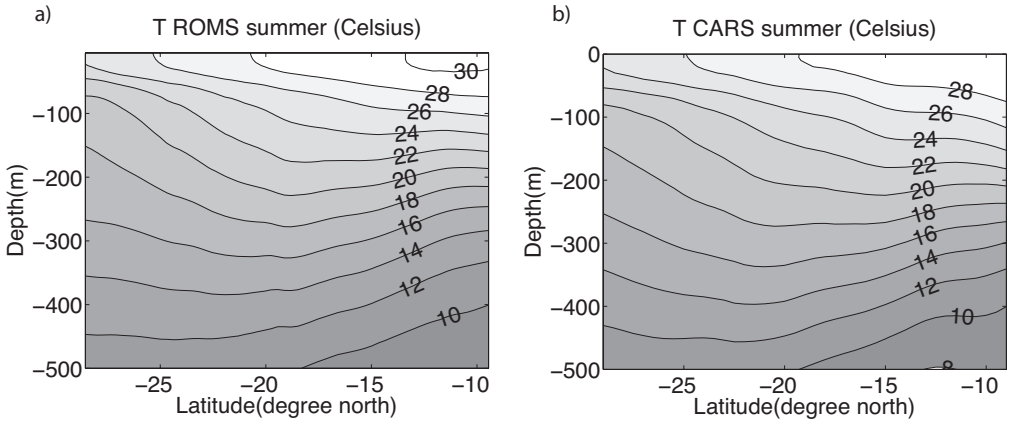

Figure 4.3 - Zonally averaged vertical section of JFM temperature (°C) from (a) the 1979-2003 ROMS control run and (b) Commonwealth Scientific and Industrial Research Organisation (CSIRO) Atlas of Regional Seas (CARS) data (http://www.marine.csiro.au/ dunn/cars2006).

warm pool, but this area is rarely impacted by TCs. These brief validations indicate that the WRF atmospheric wind forcing leads to a relevant representation of the mean ocean structure.

More importantly, the modeled ocean response to TC forcing is validated in Fig. 4.4. It is performed by extracting SST from the cyclone experiment along all cyclone tracks from 10 days before to 30 days after the cyclone passage. A similar extraction is performed in the Tropical Rainfall Measuring Mission (TRMM) Microwave Imager (TMI)-Advanced Microwave Scanning Radiometer for Earth Observing System (EOS) (AMSR-E) dataset (http://www.ssmi.com/sst) from 1998 to 2007 along the observed cyclone tracks from IbTrack dataset (http://www.ncdc.noaa.gov/oa/ibtracs). For both the model and the observations, the seasonal cycle is removed by subtracting the daily climatology. To illustrate the effect of TCs, we first estimate the prestorm SST value at each point of a cyclone track by taking the averaged SST between days -10 and -2. Then, we calculate for each cyclone and at each point along the track the difference between the SST at any given time between days 210 and 130 and its prestorm value. This procedure provides SST anomalies for both the model and the observations.

The timing of the modeled SST response to TCs is in excellent agreement with observations, but the intensity of the response is weaker in the model by about 50% (Fig. 4.4a). Nevertheless, the SST spread around the mean value is similar in the model and observations, suggesting that the model is able to capture the diversity of oceanic response. A separation using the southwest Pacific TC intensity scale[1] (Fig. 4.4c) shows that the model SST anomaly (bold curve) is largely dominated

[1]The southwest Pacific TC intensity scale (the same as the Australian TC intensity scale) measures tropical cyclones using a five-category system for winds in the ranges of 17-24 $m.s^{-}1$; 24-33 $m.s^{-}1$; 33-44 $m.s^{-}1$; and 44-55 $m.s^{-}1$, respectively. Categories 3-5 are hurricanes in the Saffir-Simpson scale.

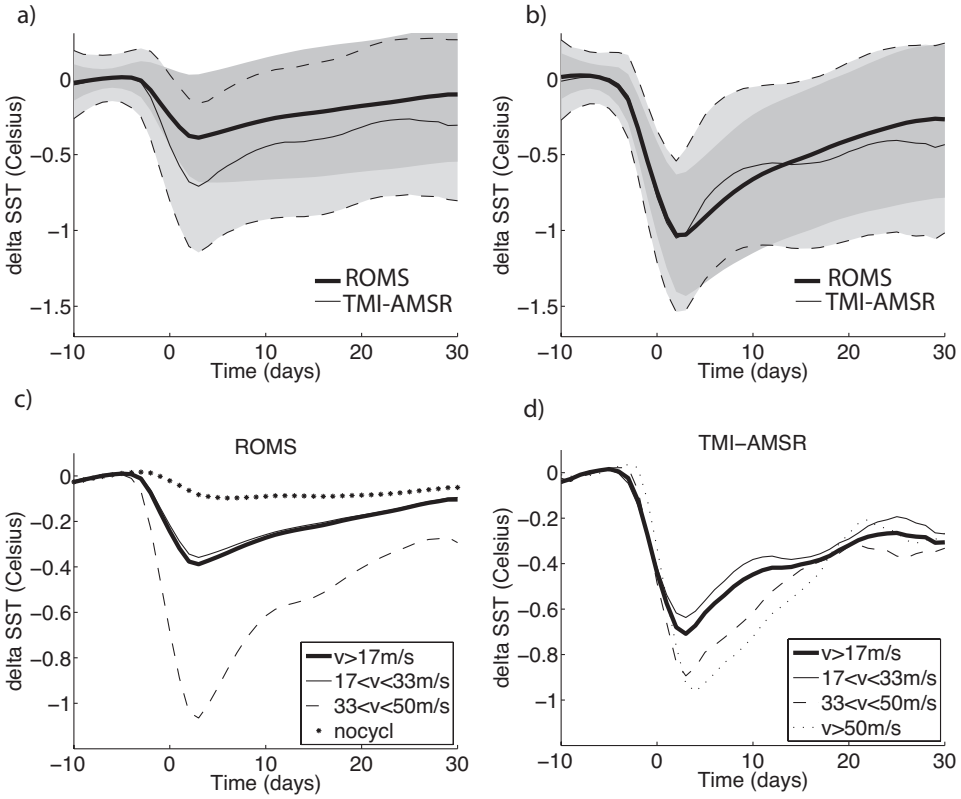

Figure 4.4 - (a),(b) The SST cooling anomaly (°C) of a composited cyclone wake (over 2° radius) as a function of time relative to cyclone occurrence in the 1979-2003 model simulation (black bold line) and in the TMI-AMSR-E 1998-2007 data (black thin line). The SST anomaly is calculated as the difference between the SST at time t and its prestorm value (average over the period from day -10 to day -2). In (a) all cyclones are considered and in (b) only those producing a cooling lower than -0.5°C at day 2 are considered. The dark gray shading (light gray with dashed lines) represents the limits of the upper and lower quartiles of the ROMS (TMI-AMSR-E) SST distribution. (c) The 1979-2003 model simulation and (d) the TMI-AMSR-E dataset SST cooling anomaly (°C) for various TC categories: all TC winds stronger than 17 $m.s^{-1}$ (bold solid line), TC winds between 17 and 33 $m.s^{-1}$ (thin solid line), TC winds between 33 and 50 $m.s^{-1}$ (dashed line), and TC winds stronger than 50 $m.s^{-1}$ (dotted line). Stars in (c) represent the residual SST anomaly of the cyclone-free experiment (i.e., an error estimate of our method for computing TC-induced thermal anomalies).

by the numerous weaker TCs (categories 1-2: wind speed between 17 and 33 $m.s^{-}1$; thin curve). In comparison with the TMI-AMSR-E dataset (Fig. 4.4d), the model seems to underestimate the cooling produced by those weaker cyclones (thin curve). Our understanding is that cooling underestimation is due to the use of large-scale (NCEP-2) atmospheric data to compute surface fluxes, which misses TC-induced latent heat fluxes. However, the model response seems to improve when only considering cyclones that are strong enough to produce significant cooling (anomalies lower than -0.5°C at day 2; see Fig. 4.4b). In this case, the match with observations becomes very good, suggesting that cyclones with the largest effect are properly represented in the model. Interestingly, further in the

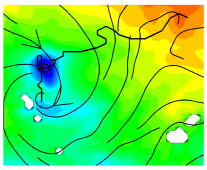

intensity scale we see that cooling by the model's strongest cyclones (categories 3-4: 33-50 $m.s^{-}1$; dashed curve in Fig. 4.4c) is overestimated. Their cooling effect is even larger than observed with category-5 TCs (Fig. 4.4d; wind speed greater than 50 $m.s^{-}1$: not represented in the model). However, it appears that strong cyclones are too rare to produce any significant impact on the composited SST. Nevertheless, the reason for overestimating their individual effect may be associated with air-sea coupling. The latter should provide significant negative feedback to the strong TCs (much less in weaker ones). It can thus be expected that a forced simulation would overestimate the lifetime of stronger TCs and therefore their SST cooling effect. However, for now we can only advance this as conjecture, pending coupled simulations to check its validity. Note, finally, that the bias associated with wind filtering method in the no-cyclone experiment is evaluated in Fig. 4.4c and appears to be very small. Overall, these comparisons give us confidence in the model's ability to simulate a statistically robust oceanic response to cyclones.

4.4 Results

4.4.1 Case studies

Table 4.1 - Parameters of three simulated TCs: TC wind speed W ($m.s^{-1}$); TC translation speed U_h ($m.s^{-1}$); velocity of the first baroclinic mode of NIOs c_1 ($m.s^{-1}$); Froude number ($Fr = U_h/c_1$); IP (h); and the wavelength L (given as U_hIP; km). Average and extreme values over the tracks are given.

	W ($m.s^{-1}$)	U_h ($m.s^{-1}$)	c_1 ($m.s^{-1}$)	Fr	IP (h)	L (km)
TC1 average	26.5	4.5	1.8	2.6	51.9	805
TC1 extrema	17.6-37.2	1.1-8.7	0.9-2.2	0.6-7.5	24.4-173.3	193-2363
TC2 average	30.7	3.9	1.9	2.1	53.0	653
TC2 extrema	17.1-44.1	1.1-8.0	0.9-2.3	0.5-4.0	26.8-96.4	158-1564
TC3 average	24.0	4.5	1.8	2.8	41.6	516
TC3 extrema	18.3-27.1	1.8-7.2	0.8-2.1	1.2-8.7	24.8-49.4	128-899

The oceanic response to three selected TC events of the WRF solution is illustrated in Fig. 4.5 and Table 4.1. The cyclones are labeled TC1 (January 1979), TC2 (western event during December 1981), and TC3 (eastern event during December 1981). Anomalies, calculated as differences between the cyclone and no-cyclone experiments, are composited along the cyclone track at each 6-h location over a 6°radius disk. If successive disks overlap, the largest anomalies between overlapping points are retained. TC-induced SST cooling appears usually much stronger at the track center and on its left side (with reference to the cyclone motion which is southward) than on its right side (Figs. 4.5a,b). In the following, the left (right) side is referred to as strong (weak) side. This asymmetry is well known and has been usually attributed to enhanced vertical mixing in the storm's strong side

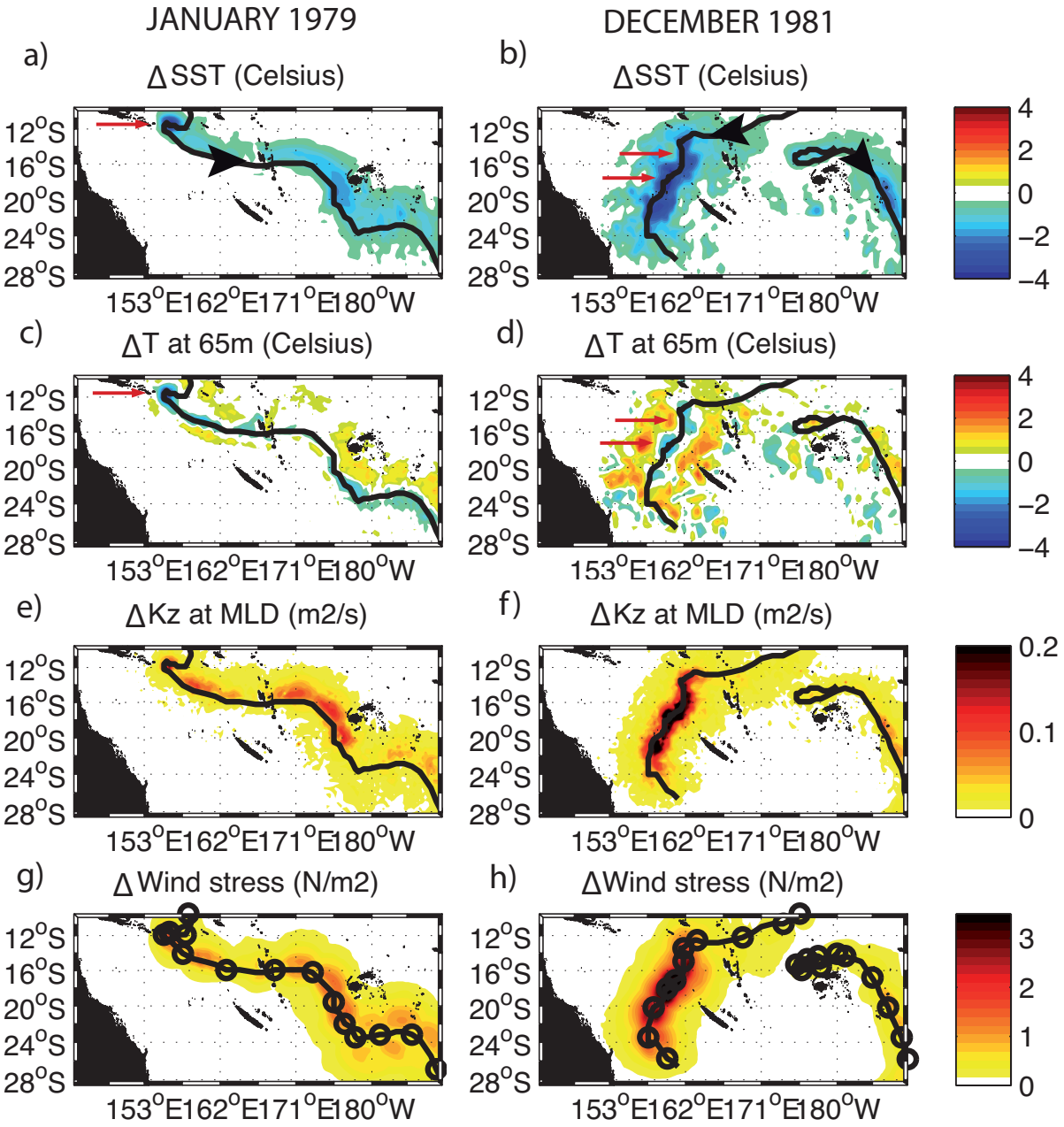

Figure 4.5 - TC-induced anomalies for three typical cyclones (tracks in black lines) in (left) January 1979 (TC1) and (right) December 1981 (TC2 and TC3). (a),(b) SST (°C); (c),(d) temperature at 65 m (°C); (e),(f) vertical diffusivity ($m^2.s^{-1}$); and (g),(h) wind stress ($N.m^{-2}$). Circles represent the daily position of cyclones. Black arrows represent the TC motion direction. At each track point, anomalies during the cyclone passage are shaded over a 6° radius. Red arrows point to locations where Froude numbers are less than unity (subcritical translation speed).

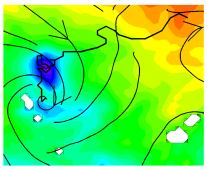

[Chang and Anthes, 1978; Pudov, 1979; Price, 1981; Sanford et al., 2007; Samson et al., 2009]. It partly results from enhanced wind speed on this particular side due to the translation speed of the storm (Figs. 4.5g,h); TC2 is the strongest of the three TCs and also the slowest one (see Table 4.1) moving at 1.75 $m.s^{-1}$ when it reaches category 4. These combined characteristics produce the strongest cooling, reaching -4°C, but with a rather modest bias on the strong side, consistent with the cyclone's slow motion (Fig. 4.5b). The two other TCs moving faster exhibit a larger leftward bias than TC2 because of their faster motions (Figs. 4.5a,b and Table 4.1). A confirmation of the role played by vertical mixing in the surface oceanic response is the good match between spatial patterns of surface cooling and vertical diffusivity K_z anomaly at the mixed layer base (*cf.*, Figs. 4.5a,b and *cf.*, Figs. 4.5e,f). Wind stress anomalies (Figs. 4.5g,h) also match extremely well the pattern and intensity of vertical mixing. The role played by near-inertial currents in shear-driven mixing has long been recognized [*e.g.*, Chang and Anthes, 1978]. Near-inertial motions are a nonstationary response to the moving storm and are promoted by strong, fast-moving storms: that is, with a smaller time scale than the inertial period [IP; Froude number greater than 1; Greatbatch, 1983]. Following Jaimes and Shay [2009], we computed the Froude number Fr as the ratio between the TC translation speed U_h and the phase speed of NIOs first baroclinic mode c_1,

$$Fr = \frac{U_h}{c_1} \quad \text{with} \quad c_1^2 = g(\frac{\rho_2 - \rho_1}{\rho 2})\frac{h_1 h_2}{h_1 + h_2},$$

where h_1 is the 20°C isotherm depth (proxy for the thermocline); h_2 is the thickness of the layer extending from h_1 down to 1000 m; and ρ_1 and ρ_2 are vertically averaged densities upon h_1 and h_2, respectively. Froude numbers exceeding unity are typically associated with a translation speed greater than 1-2 $m.s^{-1}$. These numbers for our three selected case studies are given in Table 4.1. In all cases, their average values are greater than 1, indicating a predominant near-inertial response. However, at some locations (pointed to by the red arrows in Fig. 4.5), TC1 and TC2 have subcritical translation speeds (Fr<1), suggesting a more dominant stationary signature of the wind stress curl, expressed as Ekman pumping[2] near the TC center (as opposed to nonstationary inertial pumping). To extend this discussion to the more general case, the probability density function (PDF) of Froude numbers based on all simulated events is given in Fig. 4.6. It shows that most cyclones along their tracks have supercritical translation speeds. This result confirms the ubiquity of near-inertial response in TC wakes, which are prone to vertical shear instability. However, as will be seen by examining the heat budget (following sections), it is not inconsistent with Ekman pumping being a major player in TC-induced temperature anomalies. Note that IPs and wavelengths L of TC-induced NIOs are also given in Table 4.1. With typical values of 1-2 days and 500 km, respectively, they are well resolved by the model whose temporal and spatial resolutions are 1 h and 35 km.

[2]In the linear theory, upwelling velocity from Ekman pumping is maximum at the base of the surface boundary layer then decreases linearly [*e.g.*, McWilliams, 2006]; thus, it strongly participates in the surface thermal response by uplifting the thermocline [*e.g.*, Price, 1981; Shay et al., 2000].

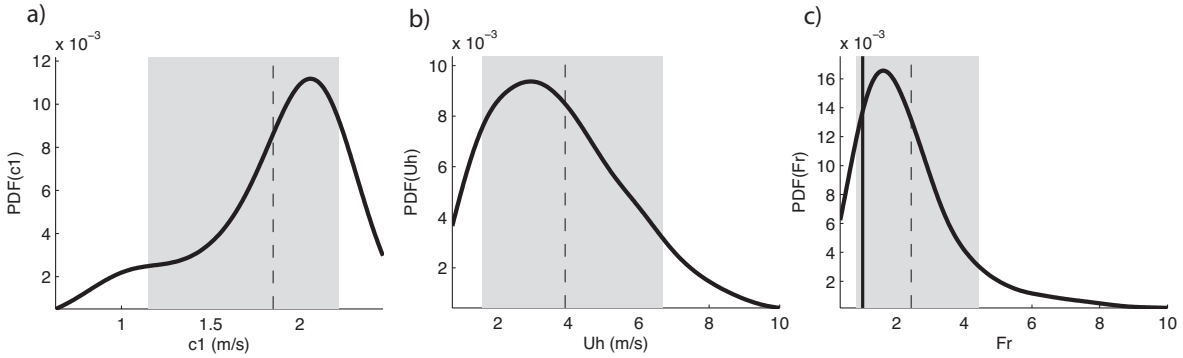

Figure 4.6 - PDFs over the whole cyclone simulation of the following parameters: (a) velocity of the first baroclinic mode of NIOs under TC tracks ($m.s^{-1}$), (b) TC translation speed ($m.s^{-1}$), and (c) TC Froude numbers. The shaded area represents the parameter distribution between the upper and lower 10^{th} percentile marks; the dashed vertical line represents the parameters mean values.

The subsurface thermal response (Figs. 4.5c,d) shows very different patterns compared with the surface, with both positive and negative anomalies for the three selected TCs. Consistent with its fast motion, TC1 induces a relatively weak negative anomaly of about -1°C around the track center (but reaching -4°C near Papua New Guinea, where it becomes subcritical; Fig. 4.5c, red arrow) and a weak positive anomaly on the left side, reaching +1°C at 300 km off its track. With its slow motion, TC2 shows stronger cooling under its track (particularly where Fr<1; Fig. 4.5d, red arrows) and stronger warming off its track, reaching +3°C and extending to 600 km on both sides. TC3 presents weaker anomalies again, consistent with weaker winds and fast motion. The difference between SST and subsurface temperature anomaly patterns confirms that mechanisms other than mixing (*e.g.*, upwelling) are significant as put forward by previous case studies. This is examined in the following sections using all events to provide statistical reliability.

The time evolution of subsurface ocean response to TC1 is illustrated in Fig. 4.7 at the location reached by the cyclone core on 13 January. Even before the passage of the cyclone's inner core, its outer winds can already inject mechanical energy into the ocean giving the effect of enhanced vertical mixing, a deepening of the mixed layer (Fig. 4.7a), and a slight warming of the ocean subsurface at 50-m depth (Fig. 4.7c). As the inner cyclone passes over the selected location, vertical mixing and mixed layer deepening reach their maxima (Fig. 4.7a). As the cyclone leaves the site, TC-induced upwelling associated with surface flow divergence (Ekman pumping) increases up to 80 $m.day^{-1}$ (Figs. 4.7b,d). It results in strong vertical advection of subsurface waters that lifts the mixed layer base (Figs. 4.7a,c,d). Following the TC-induced upwelling, the currents in the wake become more near inertial after the first half-inertial period; their transport converges toward the storm track, which forces downwelling of the isotherms (and a slight deepening of the mixed layer). A near-inertial cycle of upwelling and downwelling (inertial

pumping) then develops with speeds of 20-40 $m.day^{-1}$ in the thermocline (Figs. 4.7b,d). Once near-inertial motions are excited, their energy is radiated downward with an efficiency that depends on the geostrophic background flow [as their frequency is shifted by background relative vorticity; see Kunze, 1985]. They may even be trapped in the eddy field, enhancing surface or subsurface shear-driven mixing depending on the sign of background vorticity [Jaimes and Shay, 2010]. These typical features are similar to those described 30 yr ago by Price [1981] and more recently by Jaimes and Shay [2010]. They give us confidence in the model's ability to represent NIOs and shear-driven mixing, which are critical to reproducing the observed response to TCs.

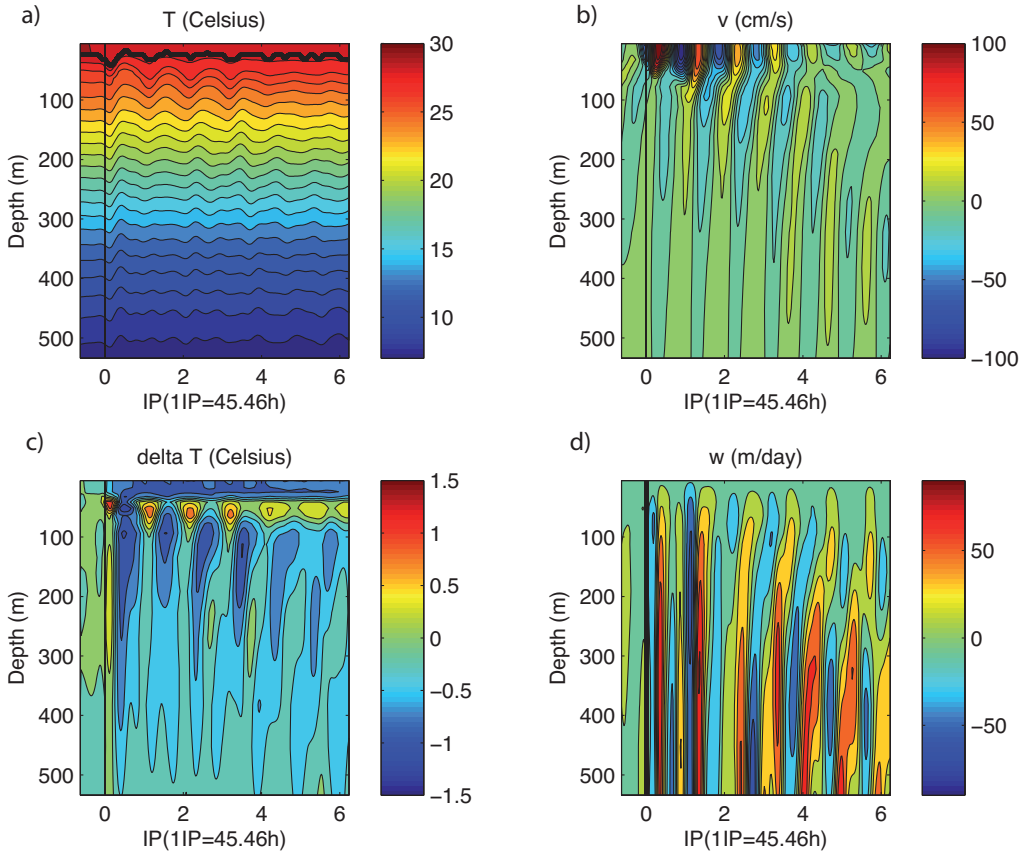

Figure 4.7 - Vertical profiles of fields extracted at the model time step (1 h) as a function of IP, at track location 15°S, 163°Eof cyclone TC1 (January 1979; Fig. 4.5). The vertical line denotes cyclone occurrence at the track location on 13 January. (a) Temperature (°C); (b) meridional velocity ($cm.s^{-1}$); (c) temperature anomaly (°C); and (d) vertical velocity ($m.day^{-1}$). Bold solid curve in (a) denotes the mixed layer depth.

4.4.2 Composite analysis of TC wakes

The previous section has illustrated the diversity of oceanic response to selected TC conditions and the time evolution of this response to a strong cyclone. The model is shown to reproduce observation of individual events. These validations allow us to turn to our main objective: an assessment of the mean balance of oceanic processes

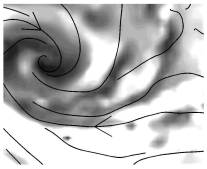

and regional climatic signature of tropical cyclones. To that end, we use 1-day averages of model variables and budget terms in which most near-inertial motions are filtered (NIOs are also filtered because of the compositing of many events in which their frequency varies according to background vorticity and latitude). In this section, a composite of all model TCs (235 cases) is presented. This will provide a generic oceanic response (only partially permitted by a selection of case studies) and present the cumulated effect of a realistic distribution of cyclones.

4.4.2.1 Composite anomalies under the cyclone

A spatial distribution of surface and subsurface effects during TC occurrence is presented for all events (Fig. 4.8). Figure 4.8 is thus an extension of Fig. 4.5 for all cyclones. TC-induced anomalies are computed over 6° radius disks at each 6-h TC location. The maximum value is retained if two successive disks of the same TC overlap. The full map is then computed by averaging all the resulting tracks over the 25-yr simulation.

As expected, the overall effect of cyclones at the ocean surface is cooling (Fig. 4.8a). The observed patchiness is due to remaining undersampling of a nonrandom collection of cyclone tracks and would be reduced by a longer simulation. Nevertheless, the pattern is coherent and shows a mean TC-induced cooling of about -1°C, within the range of published estimates [*e.g.*, Sriver and Huber, 2007; Sriver et al., 2008]. The spatial cooling pattern is strongly correlated with vertical diffusivity (Fig. 4.8c), with values as large as 0.035 $m^2.s^{-1}$ in intense cooling areas; diffusivity is itself strongly correlated with cyclone wind stress (Fig. 4.8d). Note that our modeled TC-induced diffusivities are about 50% stronger than those estimated in Sriver and Huber [2007][3].

At 65 m, which is below the mixed layer (Fig. 4.8b), the picture is quite different from that obtained with the assumption that subsurface anomalies are dominantly produced by wind-driven mixing [Sriver and Huber, 2007]. The same result can be seen in Fig. 4.5 for particular events with both positive and negative temperature anomalies along TC tracks. The composited subsurface pattern has a tendency to show slightly negative or near-zero anomalies north of 15°Sand a slight warming south of 15°S. This dipole pattern is also noticeable in Argo data and is linked to the competing vertical mixing and advection processes. Cooling by vertical advection has a deep signature and operates over the whole region, but vertical mixing is ineffective in the warm pool area (weak surface cooling and subsurface warming) because the thermocline is too deep for wind-driven mixing to reach there (see further in the text).

[3]Sriver and Huber [2007] estimate the annual-mean diffusivity attributable to TC mixing assuming that all mixing in a given year is achieved during the single largest cooling event calculated over a 24-h period. Thus, to compare with our Fig. 4.7c, we must multiply their diffusivity values by 365. In the South Pacific, their annual- mean value of 0.4 $cm^2.s^{-1}$ comes to 0.015 $cm^2.s^{-1}$ at event time scale.

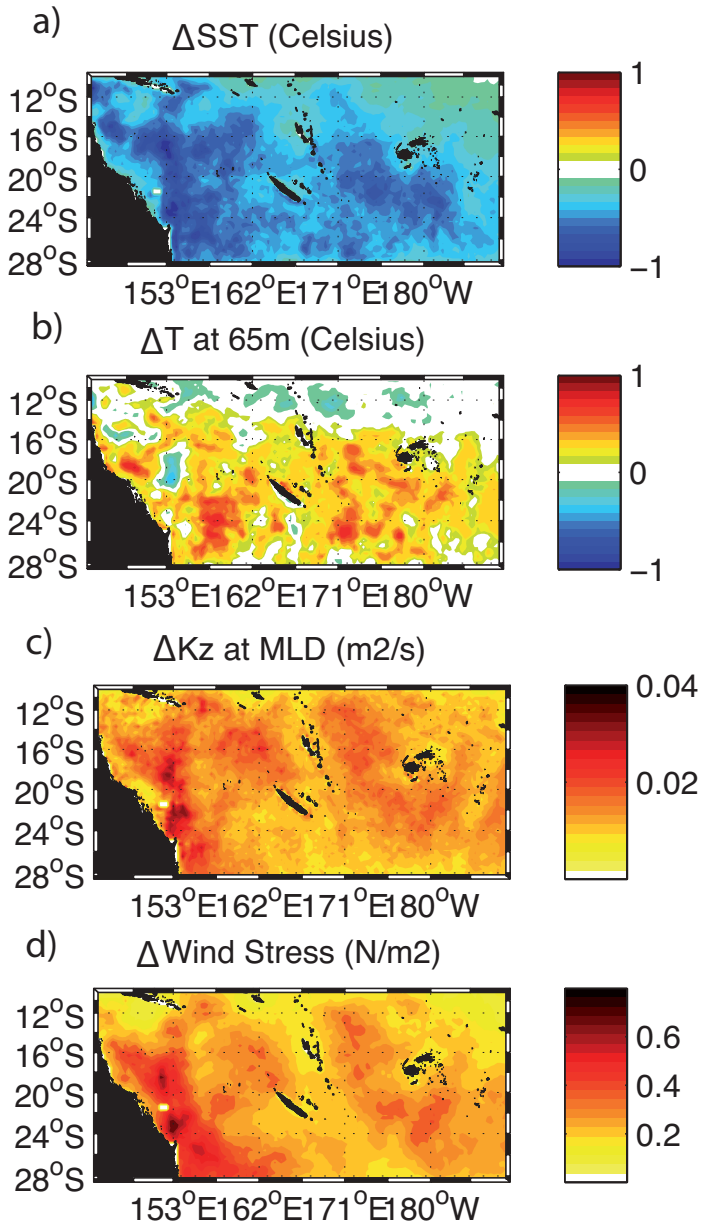

Figure 4.8 - Composite anomalies of all cyclone tracks (using a 6° radius) representing the model composited effect of cyclones within a day of their occurrence for (a) the SST (°C); (b) the temperature at 65 m (°C); (c) the vertical mixing coefficient ($m^2.s^{-1}$); and (d) the wind stress ($N.m^{-2}$).

4.4.2.2 Surface composites in the cyclone wake

In this and the following subsections, the most robust features are assessed by compositing temperature anomalies (difference between the cyclone and no-cyclone experiments) and their tendency terms along all cyclone tracks. The composite is constructed by averaging all the TC responses over the simulation period on a 12° cross-track section centered on the cyclone track at each TC passage point. To investigate the processes at work in the cyclone wake, the composite procedure is

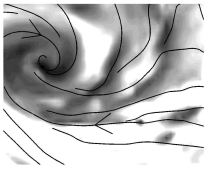

performed every day from 10 days before to 30 days after cyclone occurrence; day 0 represents the moment of occurrence of the cyclone inner core. This method provides a synthetic expression of the cyclone wake as a function of time, cross-track distance, and depth. Dispersion is calculated at each point by upper and lower quartiles (cuts off highest and lowest 25% of data, respectively) of that composited wake evolution. Because of the diversity of cyclones in terms of intensity, motion, location, and development, composited effects are necessarily weaker than the individual response to strong events, but it brings statistical reliability to the analysis.

Cyclone wake evolution The composited SST under the cyclone center (Fig. 4.9a) shows an averaged cooling of 0.8°C when all cyclones are considered (winds stronger than 17 $m.s^{-1}$; bold solid line) and an averaged cooling of 2.3°C for hurricanes (winds stronger than 33 $m.s^{-1}$; dashed line). Mixed layer deepening becomes significant a little prior to cyclone occurrence (Fig. 4.9b) because of wind stress intensification within the cyclone radius. The mixed layer reaches its maximum depth right at cyclone occurrence, ranging from 5- to 15-m deepening, depending on cyclone intensity (Fig. 4.9b). When the cyclone moves away, the mixed layer is progressively restored to its prestorm value and becomes even shallower 5 days after cyclone occurrence. The maximum cooling is reached in the cyclone wake 2 days after its occurrence (Fig. 4.9a). After 10 days, cooling is reduced by a factor of 2, but after 30 days the SST is not totally restored to its prestorm value, presenting a mean anomaly of -0.2°C (Fig. 4.9a). The dispersion of surface cooling illustrated by the upper and lower quartiles shows the response diversity.

The composited temperature budget in the mixed layer [see Eq. 4.2] shows that vertical mixing by entrainment and shear instability is the main process contributing to TC-induced surface cooling (Fig. 4.9c, black thin solid line). Its effect is mostly apparent during the storm's passage: that is, from 2 days before to 2-3 days after. This process remains active to a lesser extent until the mixed layer is restored to its prestorm value. The first stage of mixing can be attributed to a wind stirring process, whereas the second stage in the cyclone wake is induced by shear-generated turbulence associated with inertial currents. Vertical advection appears weak in this budget because its effect on the mixed layer is indirect. Ekman pumping acts in shallowing the mixed layer by uplifting the ther- mocline (see further in the text). Therefore, its contribution to surface cooling does not appear in the mixed layer budget but contributes to making vertical mixing more efficient. Later in the storm wake, lateral advection (Fig. 4.9c, dotted line) and atmospheric forcing (Fig. 4.9c, dashed line) balance shear-driven vertical mixing, re-heating the mixed layer. The surface forcing term shows a slight cooling during the cyclone passage and a strong restoring effect in its wake that contributes to the shallowing of the mixed layer (Fig. 4.9b). Lateral diffusion is negligible during cyclone event and will not be discussed further.

Cross-track pattern A composited cross-track section illustrates the asymmetry of surface cooling during the passage of cyclones (Fig. 4.10c). The mixed

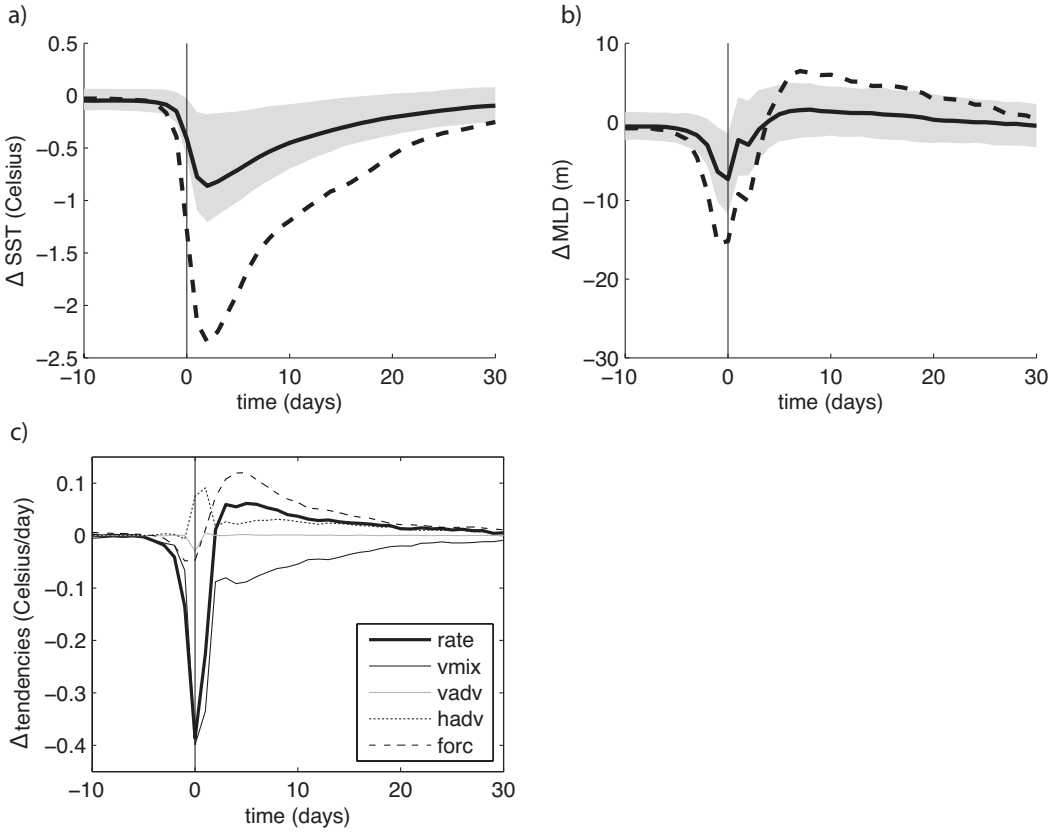

Figure 4.9 - Model composited cyclone wake anomalies in the storm-track center (over a 0.25° radius) as a function of time relative to occurrence (marked with a vertical solid line). (a) SST (°C); (b) mixed layer depth (m); and (c) mean temperature tendencies in the mixed layer (°C.day^{-1}). For (a),(b), the bold solid curve represents the mean effect of cyclones with wind speed reaching 17 $m.s^{-1}$. The upper and lower quartiles of SST and MLD distributions are shaded in gray. The bold dashed curve is the mean effect of hurricanes with wind speed reaching 33 $m.s^{-1}$. (c) Tendency terms of surface temperature anomaly budget in the composited cyclone wake; the black bold curve is rate of change, the black thin curve is vertical mixing, the gray curve is vertical advection, the dotted curve is horizontal advection, and the dashed curve is surface forcing.

layer deepening appears about 1.5 times larger on the strong side than at the storm center (Fig. 4.10d). A second maximum of mixed layer deepening is also located on the weak side resulting from relative shallowing at the center due to upwelling (Fig. 4.10d). The asymmetry of mixed layer deepening is consistent with an increase of vertical diffusivity on the strong side (Fig. 4.10b). Note that the cross-track structure of TC wind stress (Fig. 4.10a) is also asymmetric, as expected from the TC translation speed. The increase of vertical mixing on the strong side of the cyclone may thus be either directly induced by wind stirring asymmetry [*e.g.*, Chang and Anthes, 1978] or near-inertial oscillations that can be resonant with the wind forcing [*e.g.*, Price et al., 1994]. Separating out these effects is beyond the scope of this paper.

The budget analysis confirms that surface cooling is larger on the strong side

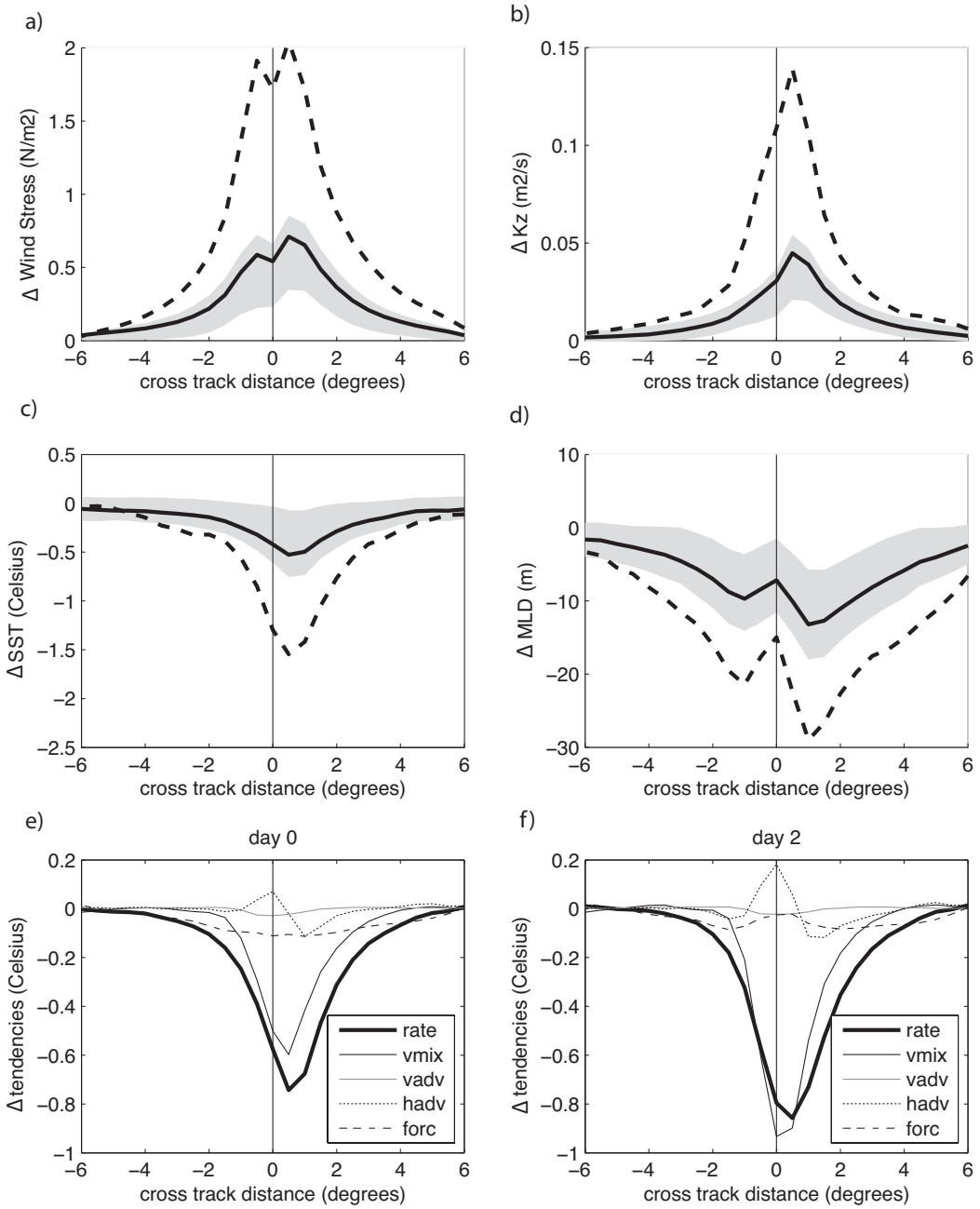

Figure 4.10 - Model composited anomalies at the time of TC center crossing as a function of cross-track distance to the cyclone center, where negative (positive) distances denote the cyclone's weak (strong) side. Shown are (a) the wind stress ($N.m^{-2}$); (b) the vertical mixing coefficient at the mixed layer base ($m^2.s^{-1}$); (c) SST (°C); and (d) mixed layer depth (m). The bold solid curve is the mean effect of cyclones with wind speed reaching 17 $m.s^{-1}$ (upper and lower quartiles are shaded in gray as in Fig. 4.9) and the bold dashed curve is the mean effect of hurricanes with wind speed reaching 33 $m.s^{-1}$. (bottom) Temperature budget terms in the mixed layer integrated (e) between days -2 and 0 (°C.day^{-1}) and (f) between days -2 and 2. The black bold curve is rate of change, the black thin curve is vertical mixing, the gray curve is vertical advection, the dotted curve is horizontal advection, and the dashed curve is surface forcing.

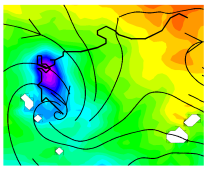

due to asymmetric vertical mixing (Fig. 4.10e, black bold and thin solid lines). Lateral advection also contributes to the asymmetry (Fig. 4.10e, dotted line), in agreement with previous studies [Price, 1981; D'Asaro, 2003; Huang et al., 2009; Vincent et al., 2012a], by cooling the strong side and warming the storm-track center. Surface cooling is greatest 2 days after TC occurrence (Fig. 4.10f, black bold solid line) and dominated by vertical mixing (Fig. 4.10f, black thin solid line), which is now stronger right under the TC center. This occurs in response to TC-induced upwelling in the track center, itself occurring between days 0 and 2, depending on the translation speed. As suggested in the previous section, upwelling helps the mixing process by uplifting cold water near the mixed layer base. Yet, the SST response is still asymmetric because the increased mixing at the center is largely balanced there by lateral advection. The latter also exerts cooling in the strong side (Fig. 4.10f, dotted line).

4.4.2.3 Subsurface waters

Cyclone wake evolution The evolution of heat budget at depth in the composited cyclone wake (in the wake center) is presented in Fig. 4.11 (see also the accumulated tendencies in Fig. 4.13). A few days before cyclone occurrence, vertical mixing at the mixed layer base increases, forced by the outer cyclone winds. This process moves heat from the mixed layer to the upper thermocline (Fig. 4.11b): that is, it warms subsurface waters. During the cyclone passage, Ekman pumping produces strong cooling by vertical advection of temperature (Fig. 4.11c), which overcomes the mixing-induced warming below the mixed layer (Figs. 4.11a,b) and cools the water column down to 1000 m (not shown). Such a deep impact of Ekman pumping is also noted in Scoccimarro et al. [2011]. After 2-3 days, these processes stop operating and slight oscillations are apparent because of the imperfectly smoothed NIOs. Interestingly, once the strong cooling by combined vertical advection and mixing has stopped, lateral advection becomes an active player and somewhat compensates for the subsurface cooling between the mixed layer base and 200 m. This lasts for a period of about 10 days after the cyclone passage (Figs. 4.11a-d). However, previous cooling by vertical advection is so intense that it persists long after cyclone occurrence (see Fig. 4.13a).

Cross-track pattern Figure 4.12 presents a cross section of the composited heat budget, integrated between days -2 and +5. It shows that vertical mixing (Fig. 4.12b) tends to warm the upper thermocline well off the track center, especially on the strong side (Figs. 4.12a,b). Yet, within 200 km of the center, the warming trend due to mixing is overwhelmed by cooling due to Ekman pumping that has a maximum effect near the mixed layer base (Fig. 4.12c). The vertical advection of temperature thus has the dual effect of cooling the water column and increasing the temperature gradient at the mixed layer base, as previously noted. In our model, because some cyclones reach the Australian coastline or the open boundaries, Ekman pumping in the composite storm center is not totally balanced by that of downwelling on the sides. More importantly, vertical advection is a nonlinear effect of Ekman pumping and has residual value in an open system that

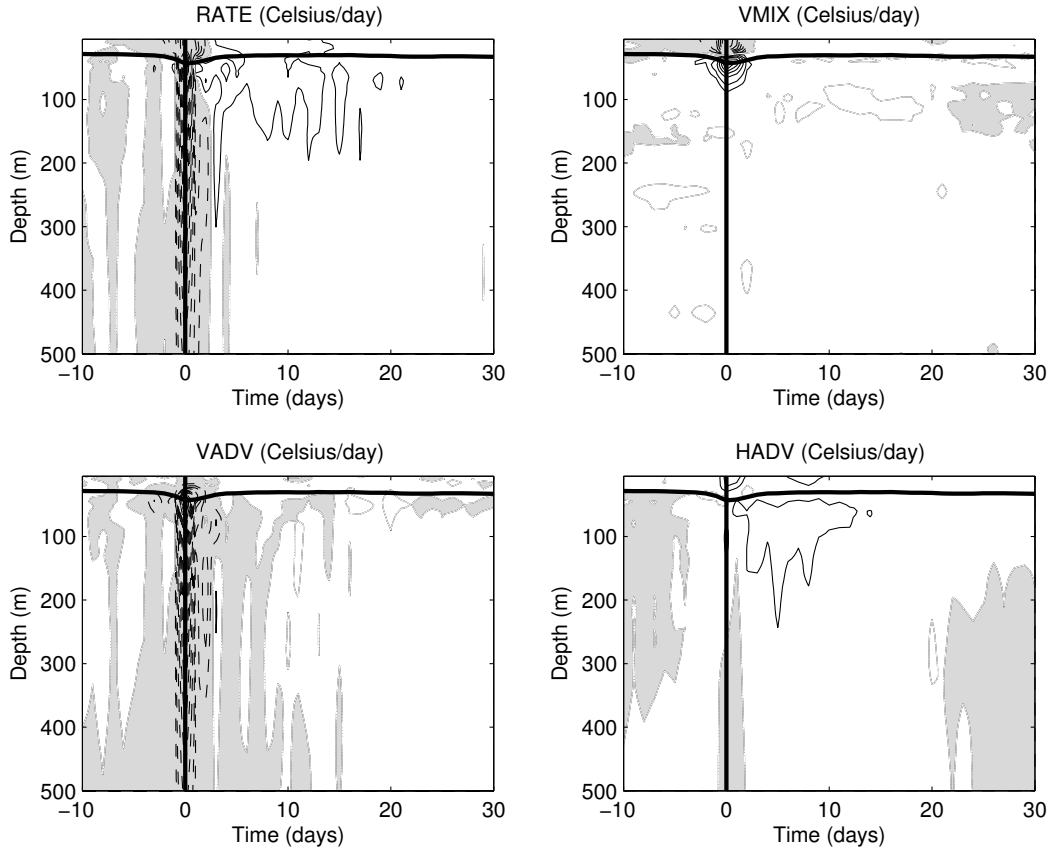

Figure 4.11 - Model composited anomalies of temperature tendencies (°C.day^{-1}) in the cyclone wake over the first 500 m in the storm-track center (averaged over 0.25° radius) as a function of time relative to occurrence. Shown are (a) rate of change, (b) vertical mixing, (c) vertical advection, and (d) horizontal advection. Dashed contours and gray areas are for negative values; solid contours and white areas are for positive values. The contour interval is 0.05°C.day^{-1} with additional 0.025 positive and negative contours. The bold solid line is the mixed layer.

can exchange energy through its boundaries (the cyclone's oceanic response is embedded within a background flow that can transport anomalies out of the TC footprint area). As a result, a weaker warming by advection occurs on the sides of the storm track compared to cooling in the center. It is mainly vertical mixing, not advection, that provides subsurface warming on the sides, particularly on the strong side of the storm track (Figs. 4.12a,b).

A synthetic picture of the integrated effect of the cyclone passage between days -2 and 5 averaged over the whole cross-track composite is given in Fig. 4.12e. The vertical distribution of the processes can be separated into roughly three layers: the surface layer (0-30 m), representative of SST variations under the composite cyclone; a subsurface layer (30-150 m) in the upper thermocline where vertical mixing and advection are the main players; and a deep layer (below 150 m) where vertical mixing shows poor activity. In the surface layer, vertical mixing controls most of the cooling under the cyclone passage, which results in an averaged

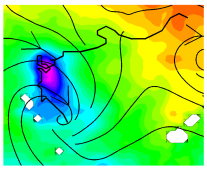

cooling of -0.2°C over the cross track. In the subsurface layer, warming is due to vertical mixing and lateral advection but vertical advection has a cooling effect. Therefore, only a fifth of the heat exchanged between the surface and subsurface layers results in subsurface warming. This suggests that estimates of subsurface warming based only on equiva- lent surface cooling [*e.g.*, in Emanuel, 2001] may be overestimated by 80%. The balance between advection and mixing results in a slight subsurface warming of 0.05°C in the cross-track composite. In the deep layer (below 150 m), vertical advection has a strong cooling effect partly balanced by lateral advection. In conclusion, the mean cyclone effect is to cool the ocean surface, moderately warm the subsurface, and moderately cool the deep ocean.

4.4.2.4 Integrated effect in the cyclone wake

We now assess the time-integrated effect of all these processes on the temperature changes between days -2 and 30 in order to highlight the persistent temperature changes due to cyclones. Except for the surface layer, the mean aspect of temperature tendencies averaged over the cross-track section is very similar to the one presented from day -2 to day 5 in the previous section (Figs. 4.12e,f), emphasizing the persistence of effects produced during the cyclone passage below the mixed layer. In the surface layer, once cooling has occurred, surface heat fluxes and lateral advection progressively tend to restore the background temperature, resulting in weaker cooling in the 30-day-long cyclone wake (*cf.*, Figs. 4.12e,f). In the subsurface and deep layers, the balance of processes described in the previous section remains valid in the longer term but with more prominent advection, particularly lateral advection. After the forced stage and up to four inertial periods, lateral advection is mostly driven by near-inertial motions (as shown in Fig. 4.7b). After a week and even more after a month, the effect of near-inertial currents begins to subside, whereas lateral advection remains high because of background currents that redistribute anomalies away from TC wakes.

Finally, Fig. 4.13 gives a mean picture of temperature evolution in the cyclone wake. The main effects occur in the storm-track center (Fig. 4.13a), except for the subsurface layer, which is significantly warmed on the sides (Fig. 4.13b). Therefore, the generic TC effect, 30 days after its passage, is qualitatively similar to its effect during occurrence: cooling in the surface and deep layers and warming in the subsurface. With particular reference to vertical mixing and vertical advection, the processes involved at the time of the cyclone passage (from day -2 to day 2), dominate the subsequent evolution of temperature. The only major difference appearing after the cyclone passage is associated with lateral advection, which increases with time: its role being to redistribute cyclone-induced anomalies across the region. Lateral advection in particular explains the smoothing with time of the differential response appearing between the storm-track center and its sides (*cf.*, Figs. 4.13a-c).

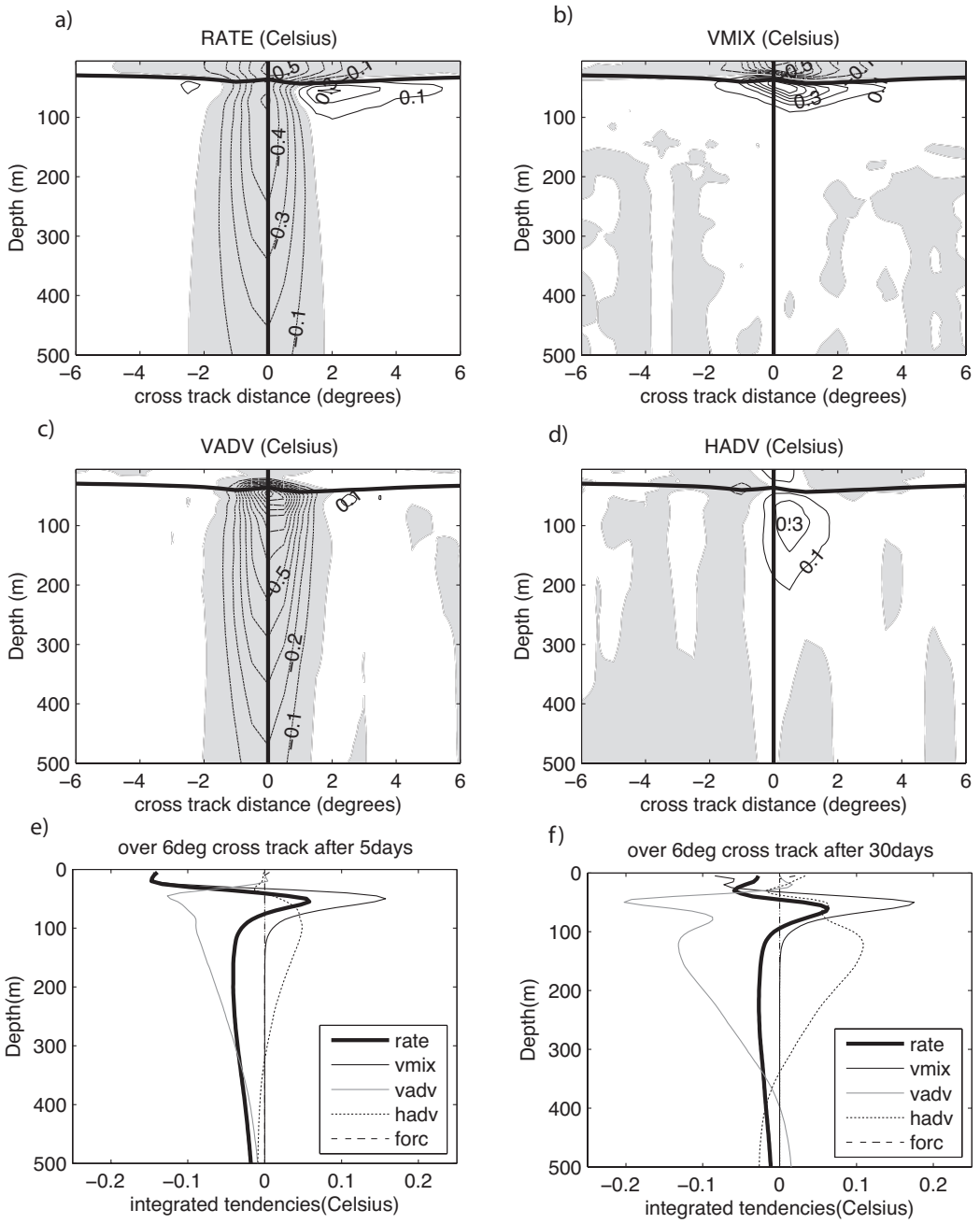

Figure 4.12 - Model composited anomalies of temperature tendencies (°C) integrated between days -2 and +5 on a cross-track section: (a) rate of change; (b) vertical mixing; (c) vertical advection; and (d) horizontal advection. Dotted contours and gray areas are for negative values; solid contours and white areas are for positive values. The contour interval is 0.1°C. The bold solid curve is the mixed layer depth and the vertical solid line is the track center. (e) Section-averaged composite anomalies integrated between days -2 and +5. (f) As in (e), but integrated between days -2 and 30. The black bold curve is the rate of change, the black thin curve is vertical mixing, the gray curve is vertical advection, the dotted curve is horizontal advection, and the dashed curve is surface forcing.

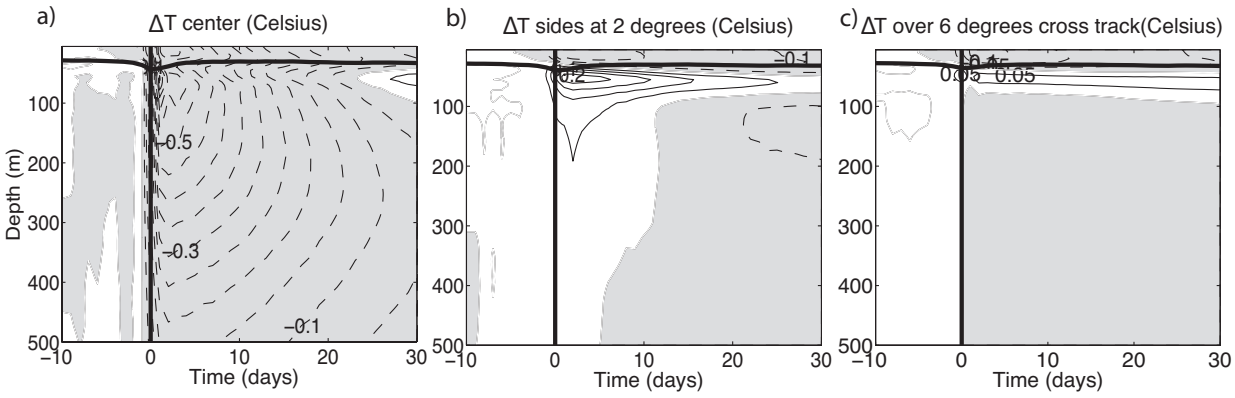

Figure 4.13 - Model composited anomalies of temperature (°C) as a function of time relative to cyclone occurrence (a) at the track center, (b) 28 off the center on both sides, and (c) averaged over a 6° radius cross-track section (see Fig. 4.12). Dashed contours and gray areas are for negative values; solid contours and white areas are for positive values. Contour interval is 0.05°C. The bold solid curve is the mixed layer depth and vertical solid line is the cyclone passage time.

4.4.3 TC impacts on the ocean climate

The remaining question — the climatological impact of cyclones — is a primary motivation for this study and will now be addressed. We address the problem by analyzing differences between the cyclone and no-cyclone experiment climatologies; for interpretation, we rely on the process study of the previous sections.

4.4.3.1 Surface temperature

The mean annual SST difference between the cyclone and no-cyclone experiments is presented in Fig. 4.14a. SST anomalies are weak but clearly organized in a regional pattern with cooling areas north of 15°Sand warming patches south of 15°S. Decomposing these SST patterns into the summer cyclonic season (Fig. 4.14b) and winter cyclone-free season (Fig. 4.14c) reveals interesting features. During the summer season, climatological SST anomalies are negative (~ -0.1°C) and in agreement with TC-induced surface cooling (see Fig. 4.8a). In contrast, winter climatological SST anomalies show a tendency toward positive values south of 15°S. This suggests that, during winter, some of the heat previously stored under the mixed layer reemerges in the surface layer. Winter surface heat fluxes south of 15°Sact to cool down SST and deepen the mixed layer through a negative buoyancy flux at the air-sea interface. As a result, winter entrainment transports back to the surface warm anomalies stored in the subsurface during summer. This reemergence process is in agreement with the observations of Jansen et al. [2010]. North of 15°S, summer TC-induced mixing is weak because of the deep warm pool thermocline that isolates cool subsurface waters from surface turbulence; there is little storage of warm anomalies in this case. Therefore, when adding the two seasons to evaluate the surface climatological effect of cyclones (Fig. 4.14a), the overall tendency is weak and differs south and north of 15°S.

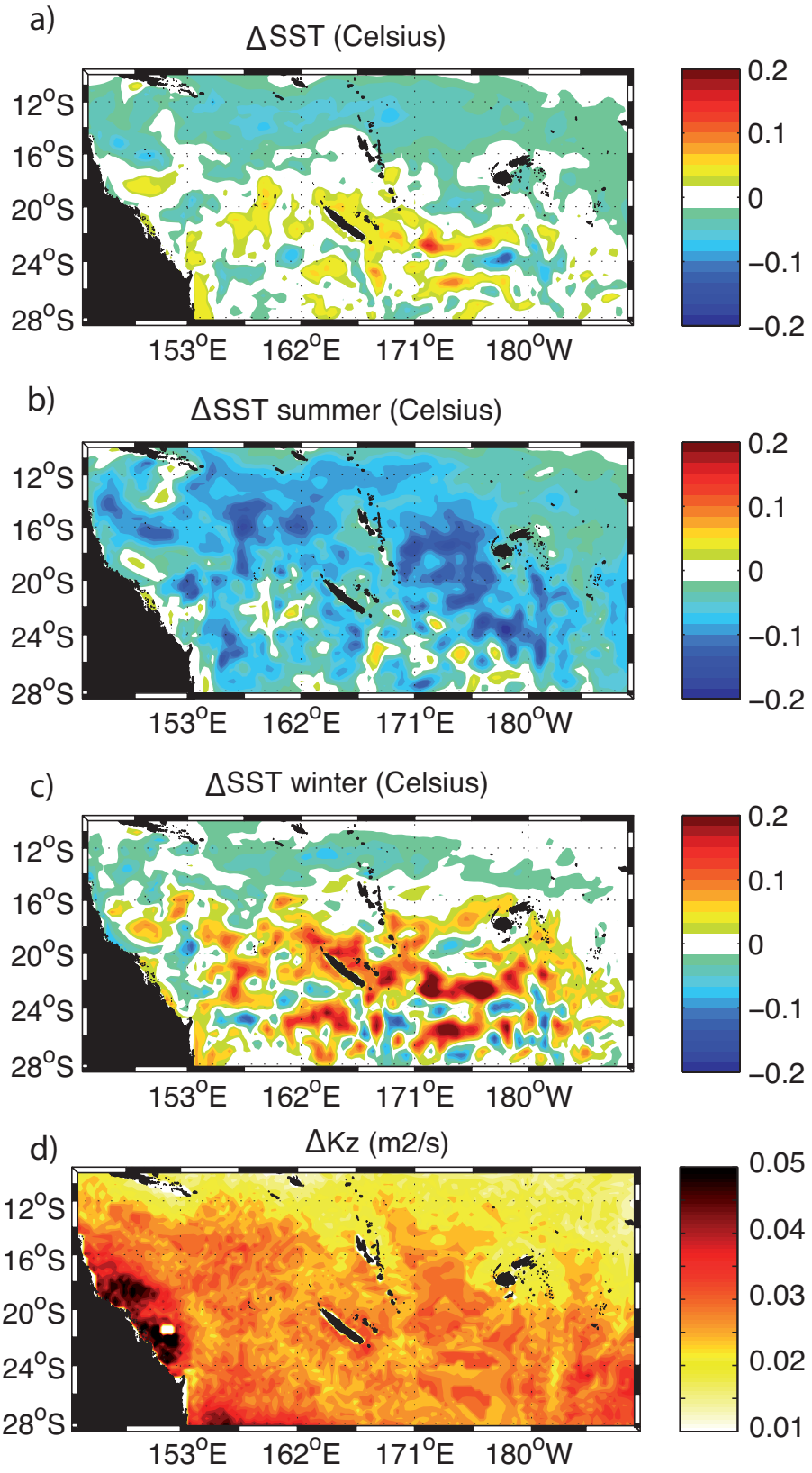

Figure 4.14 - Model-mean SST anomalies (°C) for (a) the whole period 1979-2003; (b) summer months (JFM) only; and (c) winter months [July-September (JAS)] only.

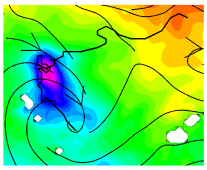

4.4.3.2 Vertical structure

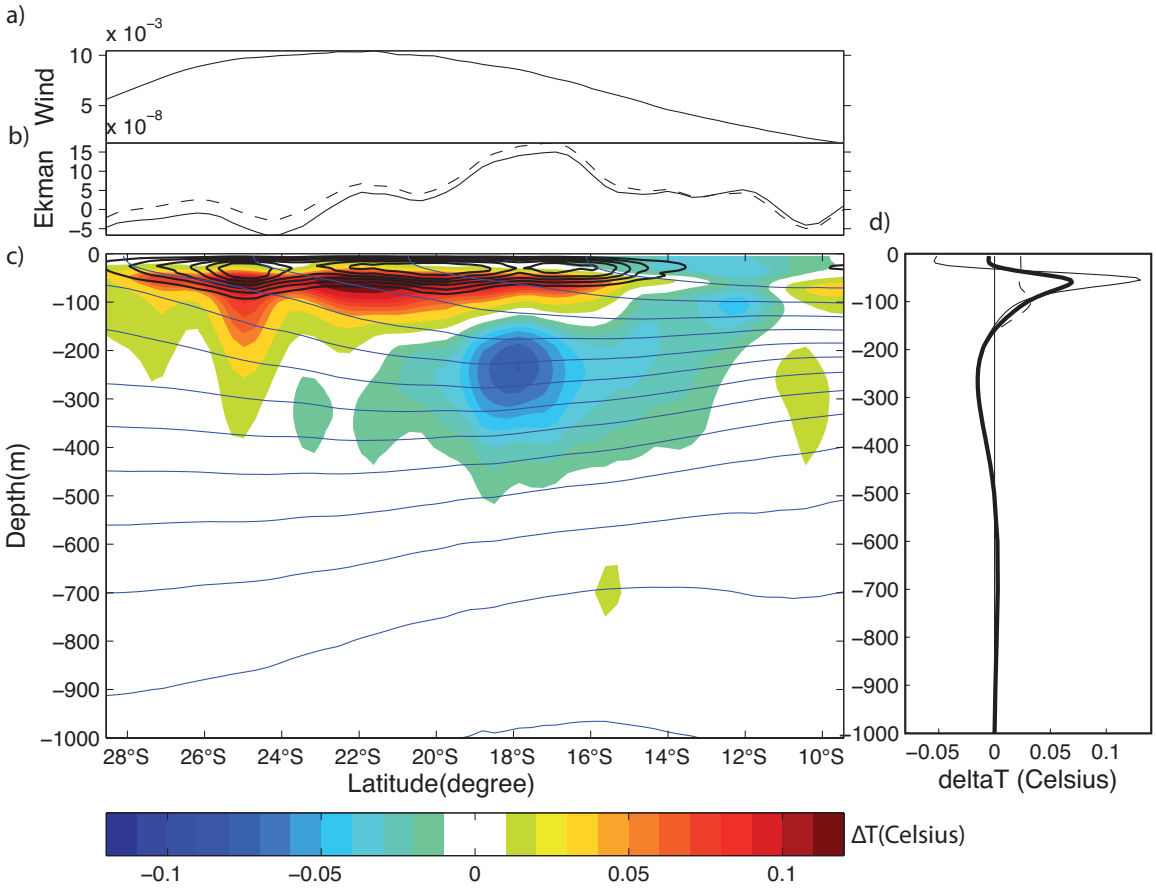

Figure 4.15 - Model zonal averages of various climatological field anomalies: (a) wind stress τ ($N.m^{-2}$); (b) Ekman pumping $w_E = curl(\tau/\rho f) = curl(\tau)/\rho f + \beta\tau_x/\rho f^2$, where τ_x is the zonal component of wind stress τ, ρ is the density of seawater, and β is the gradient of Coriolis frequency f (solid line) and the dashed line presents only the first component of Ekman pumping (i.e., Ekman pumping assuming no beta effect); and (c) temperature section (°C), where black contours represent vertical diffusivities ranging from 5 to 20 $cm^2.s^{-1}$ with a contour interval of 3 $cm^2.s^{-1}$ and blue curves show the stratification of the control run (isotherms with 2°C interval); (d) space- and time-averaged temperature profile for the annual mean (bold black curve), JFM months (thin solid curve), and JAS months (dashed curve).

We now turn to the vertical distribution of climatological temperature anomalies. The close similarity between the mean climatological anomaly profile (Fig. 4.15d, black bold curve) and the equivalent profile of integrated temperature changes in the composited cyclone wake (Fig. 4.12f, black bold curve) demonstrates that climatological effects can be understood from the study of composited cyclone wakes. Figure 4.15c shows a zonally averaged warm anomaly of up to 0.12°C in the subsurface layer, reaching down to 300 m in the southern region. This pattern is well correlated with vertical diffusivity anomalies (Fig. 4.15c, black contours) and wind stress anomalies (Fig. 4.15a) as expected from the TC-induced mixing process. A slight SST cooling in both surface and subsurface layers

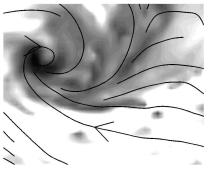

is apparent in the northern region as previously noticed and can be attributed to the warm pool deep thermocline (Fig. 4.15c, blue lines) that limits vertical mixing (a shallow process) more than it does vertical advection. This allows for neither important subsurface heat storage during the cyclonic season (Fig. 4.8b) nor reemergence of heat content in winter (Fig. 4.14c).

In the deep layer, the pattern is dominated by a cold anomaly of up to -0.08°C reaching down to 450 m with a maximum between 16 and 20°S. Deep warm anomalies surround this central pattern. This can be explained by the climatological distribution of TC-induced Ekman pumping. Vertical advection in TC wakes is characterized by strong upwelling in the TC core and weaker but more widely spread downwelling around the track. At climatological scale, the juxtaposition of TC tracks would have the apparent effect of moving the downwelling signal of each TC footprint toward the edges of TC distribution while maintaining upwelling in the center. Figure 4.15b displays the mean TC-induced Ekman pumping[4] [$w_E = curl(\tau/\rho_0 f) = curl(\tau)/\rho_0 f + \beta\tau_x/\rho_0 f^2$, where τ_x is the zonal component of wind stress τ, ρ_0 is the density of seawater, and β is the gradient of Coriolis frequency f]. It shows a very good correlation between latitudinal patterns of Ekman pumping and subsurface temperature anomalies (the correlation coefficient is 0.86 at 200 m). The minimum deep temperature anomaly around 18°Sis well collocated with the maximum Ekman pumping. North of 15°S, where vertical mixing is weaker, Ekman pumping can even affect the subsurface layer. On the other hand, Ekman downwelling impacts the meridional limits of TC distribution (north of 10°Sand south of 24°S) and is collocated with deep warm anomalies. The asymmetric effect of β in w_E is also of interest (*cf.*, solid and dashed lines in Fig. 4.15b), enhancing the southern downwelling signal. Note that total vertical advection resulting from extreme Ekman pumping in TC cores is not totally balanced by warming associated with downwelling on the sides. Integrated over TC footprints, total Ekman pumping would cancel if, according to the Kelvin-Stokes theorem, wind anomalies were zero along all footprint boundaries. However, this is not the case here because some cyclones reach the Australian coastline or the model open boundaries. Lateral advection of heat anomalies by the regional circulation and Rossby wave propagation are essentially zonal redistribution processes [Couvelard et al., 2008], but the presence of numerous islands and especially the Australian continent are responsible for meridional redistribution that must also be accounted for in the latitudinal anomaly pattern of Fig. 4.15.

The vertical distribution of climatological temperature anomalies is finally explained by the temperature box budget presented in Table 4.2. The rate of change term can be used as a measure of statistical reliability of our climatological budget over the 25 yr of seasonal TC forcing. It is on the order of $10^{11} W$; that is, only 1%-10% of the other terms. The balance of these terms appears similar here

[4]The effect of underlying currents in modulating Ekman pumping [see Jaimes and Shay, 2009, and references therein] results from interaction between wind stress and relative vorticity. This effect is not included here but should be investigated in further studies using higher-resolution simulations.

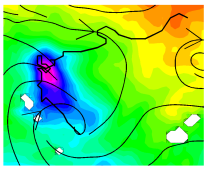

Table 4.2 - Box budget of climatological temperature anomalies between the cyclone and no-cyclone simulations. The budget is horizontally integrated over the entire domain and vertically integrated over three layers: the surface layer (0-30 m), the subsurface layer (30-150 m), and the deep layer (150 m to ocean bottom). The vertically integrated budget over the whole depth is also presented for the annual mean, the summer period (November-April) and the winter period (May-October). The term RATE is the rate of change of temperature anomalies (also a proxy for statistical error); HMIX is lateral diffusion; FORC is surface forcing, VMIX is vertical mixing; VADV is vertical advection; HADV is lateral advection; and ADV is total advection VADV+HADV (which equals the transport through the boxes).

Units: $10^{13}W$	RATE	HMIX	FORC	VMIX	VADV	HADV	ADV
0-30 m	-0.01	0.00	0.29	-0.63	0.08	0.25	0.33
30-150 m	0.04	-0.05	0.00	0.62	-1.88	1.35	-0.53
150 m-bottom	0.01	-0.03	0.00	0.01	-0.71	0.74	0.03
Total depth climatology	0.04	-0.08	0.29	0.00	-2.51	2.34	-0.17
Total depth summer	0.65	-0.10	1.48	0.00	-5.68	4.95	-0.73
Total depth winter	-0.56	-0.06	-0.91	0.00	0.66	-0.26	0.40

to the one presented for the composited cyclone wake. It confirms that the only cooling process at work below 30-m depth is vertical advection. Integrated over the whole water column, vertical and horizontal contributions to advection nearly balance and the remaining part equals lateral boundary fluxes. The result is a net heat input through the ocean surface (due to surface cooling by TC vertical mixing) compensated by heat transport through open boundaries (mostly by advection but with a weak contribution from turbulent diffusion).

Figure 4.15d presents annual, summer, and winter regional averages of temperature anomaly profiles and Table 4.2 (last three lines) the associated tendencies over the whole depth. It confirms that part of the subsurface warm anomaly stored during summer is fed back to the mixed layer (and to the atmosphere) during winter. Winter mixed layer deepening is clearly responsible for the smoothing of the summer temperature anomaly profile between 0 and 100 m. Heat anomaly[5] entering the ocean surface during the cyclonic season amounts to ~ 0.015 PW, and heat anomaly released back to the atmosphere during winter amounts to ~ 0.009 PW. Therefore, in a climatological sense, only $\sim 40\%$ of the heat input by cyclones in summer permanently modifies the ocean thermocline. The remaining regional anomaly is weak with a maximum of $\sim 0.07°C$ in the subsurface layer, which represents less than 10% of the seasonal variations. The deeper cold anomaly is also reduced during winter by transport through the open boundaries (advection in Table 4.2) and is only 70% of TC-induced cooling.

[5]Heat anomaly is calculated by integrating the surface heat flux over the computational domain and averaging the result over the season (November-April for cyclonic season and May-October for winter).

4.4.3.3 Interannual variability

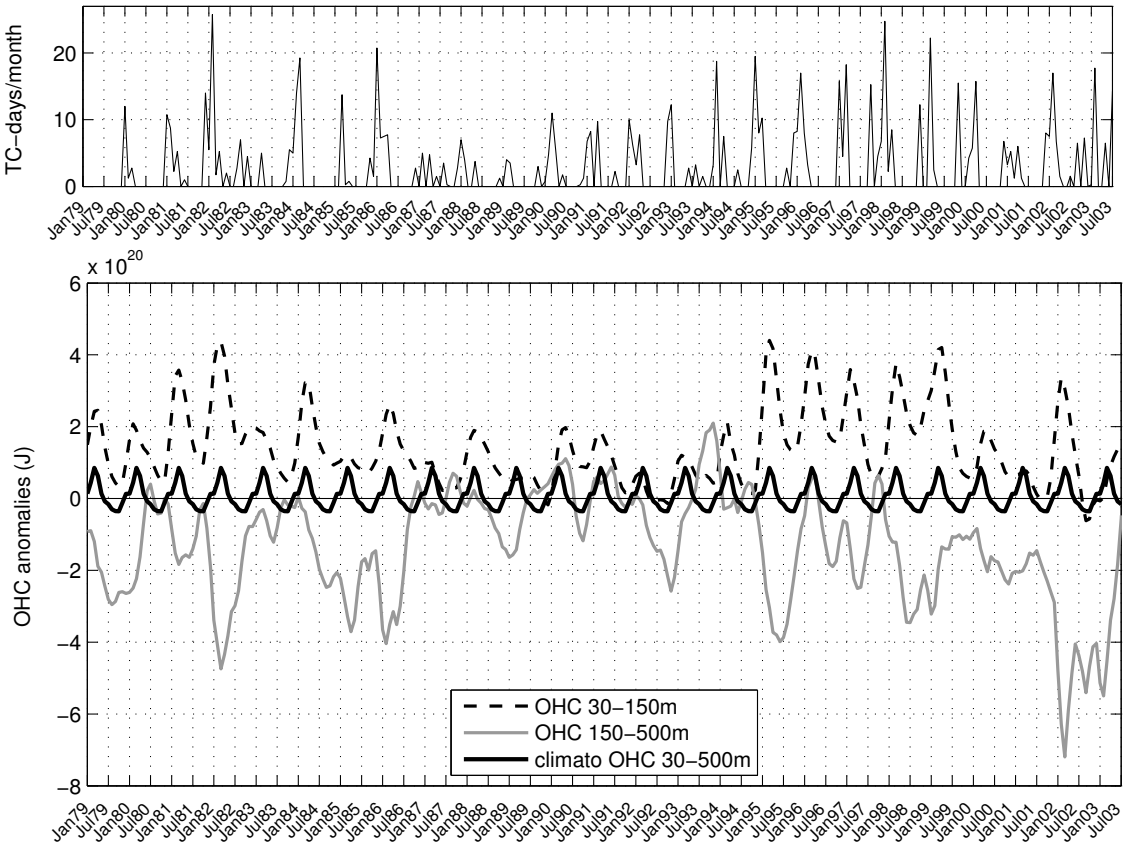

Figure 4.16 - Time series of (a) the number of simulated cyclone days per month (the first six months of 1979 are not represented) and (b) the integrated OHC anomaly (J) over 30-150-m depths (dashed line) and 150-500-m depths (gray solid line). The climatological heat content anomaly of the 30-500-m layer (black solid line) is repeated each year as a reference.

Time series of ocean heat content (OHC) anomalies induced by TCs [Fig. 4.16; $OHC = \rho_0 C_p \int_h \int_y \int_x (T_{CYCLONE} - T_{NOCYCLONE}) \delta_x \delta_y \delta_z$, where h is the depth of selected layer] confirm that the heat budget at depth is seasonally affected by TCs but with marked interannual variations (Fig. 4.16b, dashed and gray lines). In the 30-150-m subsurface layer where wind-driven mixing dominates, heat input is a robust feature of the summer period (Fig. 4.16b, dashed line). Interannual variability is equally strong in this layer and appears to match the variability of TC activity with a correlation coefficient of 0.8 (Fig. 4.16a). In the 150-500-m layer, the variability of OHC anomalies (Fig. 4.16b, gray line) has a lower correlation with TC activity of 0.5 (and 0.6 with 30-150-m OHC anomalies). Therefore, this deep interannual signal is driven by seasonal surface forcing during the cyclonic season and nonseasonal variability of the regional subsurface circulation at other times. These results confirm that a significant portion of heat input under the mixed layer is either systematically lost to the atmosphere at seasonal time scale (winter entrainment) or transported by the flow outside the cyclogenesis region

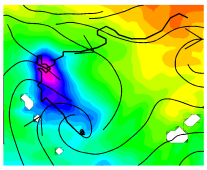

with in- terannual variability. In the long term (25 yr), there is no sign of heat accumulation due to cyclonic forcing.

4.5 Conclusions and discussion

In this study, we have detailed for the first time the long-term, three-dimensional ocean temperature response to cyclone forcing in the southwest Pacific. To that end, we used the surface wind stress of a 1/3° WRF regional atmospheric simulation over the period 1979-2003 [Jourdain et al., 2011]. This simulation contains realistic TC structure and distribution, albeit with fewer extreme cyclones than observed. However, such intense cyclones are rare in the southwest Pacific and are shown to have no statistical effect on the ocean response. The ocean impact of simulated TCs is assessed through the use of a regional 1/3° ROMS ocean model configuration. The model response to TCs is computed using differences between twin experiments: one with cyclone forcing (the cyclone experiment) and the other with cyclone-free forcing where extreme cyclone wind speeds are clipped (the no-cyclone experiment). The surface expression of TC-induced ocean wake is first compared with satellite data and shows a very good match. This successful validation and the model's capability to properly reproduce phenomena such as near-inertial oscillations leads us to believe that the model response is adequate to study the processes at work in nature. To evaluate the oceanic response to TC wind forcing, we then produce composites of all TC wakes to form a ge- neric cyclone wake. The respective contribution of each process in producing temperature anomalies in the com- posited cyclone wake is assessed using a 3D temperature heat budget. With the processes uncovered, we explore the climatological impact of TCs in the southwest Pacific.

The surface cooling bias on the strong side (left side in the Southern Hemisphere), observed in various events, is shown in our simulations to be robust and associated with various processes. During the cyclone passage, a cooling bias is driven by asymmetric vertical mixing: that is, wind stirring and shear-driven mixing from near-inertial currents. SST asymmetry is further reinforced by horizontal advection, cooling the strong side and warming the track center. Surface cooling is maximum 2 days after the cyclone passage and mostly driven by vertical mixing as suggested in previous studies. However, during the forced stage, vertical mixing acts also as a relay to another key process: TC-induced upwelling by Ekman pumping. As suggested by Price [1981], this relay process is most efficient at the storm-track center where upwelling is produced. The cooling bias is then shown to rely on asymmetric horizontal advection, as previously suggested from case studies [Price, 1981; D'Asaro, 2003; Huang et al., 2009]. In the cyclone wake (*i.e.*, after the passage of the cyclone), shear-driven mixing remains the only mixing process at work. Vertical advection has a lesser impact, and surface temperature is restored back to prestorm values by surface fluxes and lateral advec- tion. Yet, restoration is never fully achieved during the cyclone season and leaves a mean residual anomaly of -0.2°C.

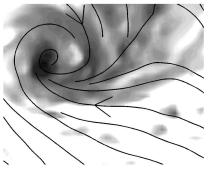

The subsurface layer experiences quite a different balance, with warming on both sides of the track and cooling at the track center during the cyclone passage. At the track center, a strong cooling that can reach down to 1000 m is driven by vertical advection from Ekman pumping within the TC core. Vertical advection then competes and overwhelms the warm anomaly set at depth by vertical mixing. On the sides, heat input by vertical mixing dominates, thus creating two warm lobes across the track center down to 100 m, with a larger effect on the strong side. Long after the cyclone passage, horizontal advection is also shown to produce warming at the track center, which eventually cancels out the initial cooling because of vertical advection. In the deep layer, below $\sim$ 150 m, there is a weak but widespread cold anomaly resulting from a balance between cooling by vertical advection and warming by lateral advection. On the sides, the role of advection is reversed because of horizontal transport and downwelling balancing the upwelling initiated at the center. Overall, within the cyclone area of influence, the residual TC effect after 30 days is a slight cooling in the top 30 m, warming in the subsurface layer, and cooling in deeper waters.

Temperature anomalies in the cyclones' wakes leave a residual signature in the model climatology, suggesting a persistent contribution of TCs on the ocean climate but of lower importance than previously claimed. The climatological effect of cyclones is mixing-induced warming of up to 0.12°C in the 20-300-m layer south of 20°Sand a cooling of up to 0.08°C in the 50-500 m associated with vertical advection north of 20°S. These anomalies are weak but significant compared to the model error associated with the forcing uncertainty and TC-extraction method (4.3) and to sampling error (the rate of change in the heat budget is less than 10% of the forcing term).

Our finding that vertical advection has a lasting effect in the southwest Pacific region is consistent with the recent results of Scoccimarro et al. [2011] but contrasts with those of Price [1981]. The latter describes upwelling and downwelling as compensating processes with no lasting effect. This is only exactly true for a closed system with no lateral exchange. In our simulations, there is substantial but not exact compensation by downwelling in the cyclone's footprint because of nonzero lateral transports. Therefore, the only relevant requirement is that the volume integral of heat advection equals the surface integral of heat fluxes at the system's boundaries (divergence theorem). Integrated over the whole region, we find that advection causes a net heat loss through the open boundaries, compensating for surface input. It produces a deep cooling in the center and weaker warming on the periphery of the cyclone distribution. In a statistical sense, the ocean responds to the cyclones' probability density function (PDF) with upwelling affecting high PDF zones and downwelling the periphery.

Sriver [2010] also show negative anomalies at 500-1500-m depths and suggest that they may be associated with vertical mixing. In our case, TC-induced vertical mixing has no impact at such depth, even though strong near-inertial oscillations

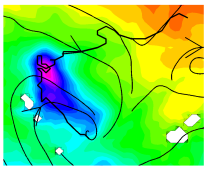

are seen to propagate to great depths. Because of the effect of advection, the heat content anomaly below the mixed layer is only about a fifth of that expected if vertical mixing were the only player. Consequently, previous studies based on the latter assumption [*e.g.*, Emanuel, 2001; Sriver and Huber, 2007; Pasquero and Emanuel, 2008] would produce an excessive amount of heat input from the atmosphere[6] and misconceive the process of heat storage and spreading across the ocean. More importantly, the seasonal cycle has a major impact on the amount of ocean heat storage as winter entrainment restores back to the surface 60% of the subsurface heat content anomaly. This is in agreement with suggestions by Jansen et al. [2010] from observations. Over the year, the surface flux anomaly is only $3.10^{-3} PW$ and a weak positive temperature anomaly (0.07°C in regional average) remains in the permanent thermocline. The deep cold anomaly (with a mean value of -0.02°C) also presents some seasonal modulation by surface forcing but is more affected by the interannual variability of oceanic circulation.

One limitation of our study is the too-large amount of TCs that are weaker than observed. This would impact the intensity of SST and possibly the 3D oceanic response, but we believe that the overall impact of cyclones would remain weak at the climatological scale. On the other hand, our method to remove extreme TC winds gives an uncertainty associated with the remaining filtered vortices. We estimated that these vortices have a residual thermal effect of less than 10%, indicating a possible underestimation of the ocean response. However, this residual effect is probably similar to that of tropical depressions, which are numerous in the region. Also, in our study, we focused on the cyclone momentum forcing; neither the thermal anomalous structure of the cyclone nor the complex air-sea coupling that would affect both their intensity and oceanic impact is accounted for. Considering these may affect the details of surface cooling in the cyclone wake, especially the restoring process, but the subsurface processes would be less affected. Nevertheless, it will be useful to readdress our questions in the context of high-resolution coupled ocean-atmosphere modeling.

Acknowledgments We appreciate financial support from the IRD. In particular, the PC cluster used for ROMS and WRF simulations was financed through IRD's scientific computing effort project SPIRALES. We also thank three anonymous reviewers who helped us to substantially improve our manuscript.

4.6 Appendix: KPP

The KPP scheme [Large et al., 1994] parameterizes the oceanic vertical turbulent fluxes of scalars and momentum in terms of K closure of turbulent fluxes $\overline{w'T'} =$

[6] Sriver and Huber [2007] estimate 0.26 PW of global heat input due to TCs. We find 3% of this number in the southwest Pacific (if winter reemergence is not considered), for about 10% of world TCs found in this region. That number thus amounts to a third of the estimation by Sriver and Huber [2007]. Further, accounting for winter reemergence, we only get about 10% of their 0.26 PW.

$-K_T(\delta T/\delta z - \gamma_T)$, where primes indicate turbulent quantities; w is the vertical velocity; T is temperature here but could be any scalar quantity or horizontal velocity component; and K_T is the vertical eddy diffusivity. The nonlocal transport term γ_T is nonzero only in the convective surface layer but is neglected here on the basis that turbulent fluxes induced by TCs are dominated by wind stirring and shear instabilities. The boundary layer K profile is computed as the product of the boundary layer thickness h_{bl}, a depth-dependent turbulent velocity scale w_s, and a nondimensional shape function G. Here, hbl is largely dependent on surface buoyancy and momentum forcing and is determined by equating a bulk Richardson number to a critical value. The shape function G is determined by matching the mixing coefficients and their first vertical derivatives to surface layer values (at the near-surface boundary) and to interior values (at the boundary layer depth). In the surface layer, K_T is formulated to agree with the similarity theory of turbulence. In the stratified interior, it is determined by the superposition of three processes: vertical shear instability, internal wave breaking, and convective adjustment (double diffusion is neglected here). The continuity imposed between boundary layer and interior mixing is an essential component of this formulation because it provides appropriate conditions for shear mixing by strong currents at the base of the boundary layer. This property is particularly important in the study of storm forcing where both wind stirring and shear mixing are active players. Details of the KPP formulation are given below.

4.6.1 Interior mixing

The mixing coefficient in the stratified interior is

$$K_T = \underbrace{10^{-3}}_{A} + \underbrace{5 * 10^{-3}[1 - (\underbrace{\frac{Ri}{0.7}}_{0\leq\ldots\leq 1})^2]^3}_{B} + \underbrace{0.1}_{C} \tag{4.3}$$

where Ri is the local Richardson number,

$$Ri = \frac{-\frac{g}{\rho_0}\frac{\delta\rho}{\delta z}}{(\frac{\delta u}{\delta z})^2 + (\frac{\delta v}{\delta z})^2},$$

with usual notations for density of seawater and horizontal component of current velocities. The terms A, B, and C represent the three mixing processes: internal wave breaking, vertical shear instability, and convective adjustment.

4.6.2 Boundary layer mixing

4.6.2.1 Boundary layer thickness h_{bl}

Here, h_{bl} is given by the minimum depth where the bulk Richardson number reaches its critical value ($Ri_c = 0.3$),

$$Ri_{bulk}(h_{bl}) = \frac{-g[\rho_{surf} - \rho(h_{bl})]h_{bl}}{\rho_0([u_{surf} - u(h_{bl})]^2 + [v_{surf} - v(h_{bl})]^2 + V_t^2(h_{bl}))} = Ri_c = 0.3,$$

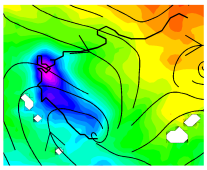

where V_t is the velocity scale of the turbulent shear,
$V_t^2(h_{bl} = \frac{C_v sqrt{-}\beta_T}{Ri_c \kappa^2} \sqrt{c_S \epsilon} h_{bl} N w_S)$.
The term $C_v = 1.8$ is the ratio of interior Brunt-Vaisala frequency to the Brunt-Vaisala frequency at the entrainment depth; $\beta_T = -0.2$ is the ratio of entrainment buoyancy flux to surface buoyancy flux; $\kappa = 0.4$ is von Karman's constant; $c_S = 98.96$ is a constant used in the calculation of the dimensionless flux profiles; $\epsilon = 0.1$ is the nondimensional extent of the surface layer; N is the Brunt-Vaisala frequency; and w_s is the turbulent velocity scale for scalars.
In case of stable buoyancy forcing ($B_f > 0$), h_{bl} is taken as the minimum of the h_{bl} value computed above and the Ekman depth $h_e = 0.7u*/f$, where $u* = |\tau_0|/\rho_0$ is the friction velocity.
Buoyancy forcing is computed as $B_f = g[\alpha Q_{total} - \beta(E-P)S - (\alpha I h_{bl}/\rho C_p)]$, where α is the thermal expansion coefficient and β is the saline contraction coefficient.

4.6.2.2 Turbulent velocity scale

Here,

$$w_S = \begin{cases} \kappa sqrt[3]{-28.86u*^3 + 98.96\kappa\sigma w*^3} & \text{for } \sigma < \epsilon \\ \kappa sqrt[3]{-28.86u*^3 + 98.96\kappa\epsilon w*^3} & \text{for } \sigma \geq \epsilon \end{cases}$$

where σ is the nondimensional vertical coordinate in the boundary layer (0 at the surface and 1 at the base).

4.6.2.3 K profile

For $K_T = h_{bl} w_S(\sigma) G(\sigma)$, $G(\sigma)$ is a cubic polynomial, such that

- $G(0) = 0$, $K = 0$ at the surface;
- $(\delta G(0)/\delta\sigma) = 1$, linear reduction of flux with distance in the surface layer;
- $G(1) = (K_T(h_{bl})/h_{bl} w_S(1))$, match of boundary layer and interior diffusivities at h_{bl}; and
- $(\delta G(1)/\delta\sigma) = (\delta/\delta\sigma)[K(h_{bl}/h_{bl} w(1)]$, match of boundary layer and interior derivatives at h_{bl}.

Chapter 5

Ocean feedback to tropical cyclones: climatology and processes

Contents

5.1 Introduction 123
5.2 Models and Methods 124
5.2.1 Atmospheric model 124
5.2.2 Ocean model 126
5.2.3 Coupling procedure 127
5.2.4 Forced simulation setup 128
5.2.5 Tracking methodology 129
5.2.6 Compositing methodology 130
5.3 Environmental conditions 131
5.3.1 The ocean-atmosphere interface 131
5.3.2 SPCZ and cyclogenesis index 133
5.4 TC structure 134
5.5 Coupling effect on cyclonic activity 138
5.5.1 Cyclogenesis geography 138
5.5.2 Intensity distribution 139
5.6 Coupling effect on air-sea fluxes 140
5.6.1 SST cooling 140
5.6.2 Specific humidity 142
5.6.3 Air-sea fluxes 142
5.7 The role of ocean dynamics 143
5.7.1 Geography of storm-induced cooling 143

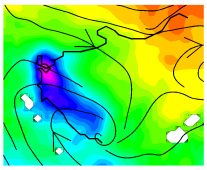

5.7.2 Storm sensitivity to SST 144
5.7.3 Mixed layer depth 145
5.7.4 Barrier layers 146
5.7.5 Ocean eddies 147
5.8 TC INTENSIFICATION **149**
5.9 SUMMARY AND DISCUSSION **153**

Abstract

This study presents the first multidecadal and coupled regional simulation of cyclonic activity in the South Pacific. The long-term integration of state-of the art models provides reliable statistics, missing in event studies, of air-sea coupling processes controlling tropical cyclone (TC) intensity. The coupling effect is analyzed through comparison of the coupled model with a companion forced experiment. Cyclogenesis patterns in the coupled model are closer to observations with reduced cyclogenesis in the Coral Sea. This provides novel evidence of air-sea coupling impacting not only intensity but also spatial cyclogenesis distribution. Storm-induced cooling and consequent negative feedback is stronger for regions of shallow mixed layers and thin or absent barrier layers as in the Coral Sea. The statistical effect of oceanic mesoscale eddies on TC intensity (crossing over them 20% of the time) is also evidenced. Anticyclonic eddies provide an insulating effect against storm-induced upwelling and mixing and appear to reduce SST cooling. Cyclonic eddies on the contrary tend to promote strong cooling, particularly through storm-induced upwelling. Air-sea coupling is shown to have a significant role on the intensification process but the sensitivity of TCs to SST cooling is nonlinear and generally lower than predicted by thermodynamic theories: about 15 rather than over 30 hPa/°C and only for strong cooling. The reason is that the cooling effect is not instantaneous but accumulated over time within the TC inner-core. These results thus contradict the classical *evaporation-wind feedback* process as being essential to intensification and rather emphasize the role of macro-scale dynamics.

Accepted, *Climate Dynamics*, 2014

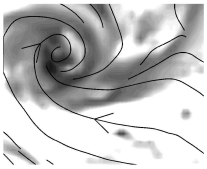

5.1 Introduction

Tropical cyclones (TCs) are strongly coupled systems. They intensify by extracting heat energy from the ocean [Emanuel, 1986; Rotunno and Emanuel, 1987; Holland, 1997] and, in turn, provide oceanic momentum expressed as strong upwelling and asymmetric mixing that result in sea surface temperature (SST) cooling under the eye and eyewall [*e.g.*, Price, 1981; Shay et al., 1989; Jullien et al., 2012]. The main objective of this study is to improve our understanding of coupling processes controlling TC intensity. The SST feedback effect, *i.e.*, the sensitivity of TC intensity to TC-induced cooling is generally investigated and discussed from theoretical and case studies. Thermodynamic arguments [Holland, 1997; Schade, 2000] suggest a large negative SST feedback on storm intensity, reducing the cyclone's maximum potential intensity (MPI) by 21 to 45 hPa/°C. This sensitivity is much higher than that of storm intensity to the ambient (large-scale) SST estimated from thermodynamic theory (Emanuel, 1988: 10 hPa/°C) or observations (*e.g.*, Demaria and Kaplan, 1994: 10-20 hPa/°C). However, sensitivity to SST cooling is lower in modeled case studies than theoretical predictions with values of about 10 hPa/°C or less [Bender et al., 1993; Bender and Ginis, 2000]. Table 5.1 provides a short summary of the SST feedback effect from various studies.

Table 5.1 - Negative SST feedback effect on TC central pressure from various sources and models. ΔSST is storm-induced SST cooling in °C and ΔP the difference of TC central pressure between forced and coupled models in hPa. The sensitivity of storm intensity to SST cooling is given in hPa/°C.

Reference	Data type	ΔSST (°C)	ΔP (hPa)	ΔP/°C (hPa/°C)
Holland [1997]	static theory			33
Schade [2000]	dynamic theory			21-45
Bender et al. [1993]	idealized static storm model	5.6	16.4	2.9
Bender et al. [1993]	idealized moving storm ($7.5 m/s$) model	2.6-3	7.3	2.6
Bender and Ginis [2000]	model of realistic events	3	10-40	3-13
this study	20-yr realistic model	0-6	0-30	0-15

Numerous factors may affect storm-induced SST cooling and feedback. Slow translation speed and shallow ocean mixed layer depth (MLD) appear to favor stronger SST cooling and negative feedback [Sutyrin and Khain, 1984; Schade and Emanuel, 1999]. Schade and Emanuel [1999] from a simple coupled model propose a range of 10-60 % decrease of storm intensity depending on their motion speed. Other subsurface oceanic features such as thermocline stratification or fine scales associated with fronts and eddies also have potential to affect storm intensity [Schade and Emanuel, 1999; Bao et al., 2000; Wu et al., 2007; Vincent et al., 2012b]. The deepened mixed layer of warm-core eddies for example are known to promote TC intensification [*e.g.*, Chang and Anthes, 1978; Sutyrin and

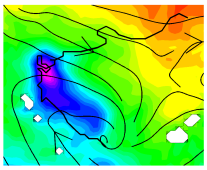

Khain, 1984; Bao et al., 2000]. However, no statistical characterization of ocean eddy effect has been proposed for a whole cyclogenesis basin.

Independently from the cooling process, the feedback effect invoked by thermodynamic theories may also be overestimated. Paradigms for TC intensification based on thermodynamic considerations generally assume that surface moisture fluxes in the core region have a direct control on the growth rate of storms by a linear instability mechanism between evaporation and tangential wind speed (the WISHE mechanism of Emanuel, 1986). Other paradigms attempt to include more explicitly the role of intra-eyewall dynamics [Schubert et al., 1999; Yang et al., 2007; Montgomery et al., 2009; Wang and Wu, 2004], and that of the TC secondary circulation, *i.e.*, radial advection driving humidity convergence [Charney and Eliassen, 1964; Ooyama, 1969] and absolute angular momentum [Smith et al., 2009]. If radial convergence is an essential process of intensification, then the local effect of SST feedback on air-sea fluxes must be integrated in a macro-scale dynamical framework.
In addition to its effect on TC intensity, idealized model experiments suggests that ocean coupling has some impact on the number of cyclogenesis [Schade and Emanuel, 1999], storm translation speed and storm tracks [Bender et al., 1993; Bender and Ginis, 2000], the latter owing to alteration of the beta drift.

Comparative forecasts of TCs with operational uncoupled and equivalent coupled models show that coupling substantially improves the forecast of TC intensity [Bender and Ginis, 2000; Sandery et al., 2010]. Three-dimensional oceanic features (MLD, eddies, stratification...) are of primary relevance in these experiments and suggest that the use of simple mixed layer models is not adequate to assess the effect of coupling. However, realistic coupled model applications have been limited to either short-time storm events or coarse resolution climate studies that only produce cyclone-like vortices [Scoccimarro et al., 2011]. The present study is based on a regional, mesoscale coupled model to provide a climatology of tropical cyclone-ocean interactions in the present climate. 20 years of simulation and about 160 tropical cyclones provide some statistical reliability that is generally missing in event studies. This approach has already been used with success to study the South Pacific climatology of tropical cyclones [Jourdain et al., 2011] and its oceanic response [Jullien et al., 2012] in non coupled modes (forced atmosphere or forced ocean). Here, we pursue the same approach, adding the coupling effect. First, the impact of coupling on TC distributions is assessed by comparing forced and coupled simulations. Then, the processes at play in the control of TC intensity by the ocean are investigated.

5.2 Models and Methods

5.2.1 Atmospheric model

In this study, the Weather Research and Forecasting (WRF) model version 3.3.1 is used with the Advanced Research WRF (ARW) dynamic solver [Skamarock and

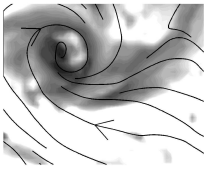

Klemp, 2008]. ARW was specially designed with high-order numerical schemes to enhance the model's effective resolution of mesoscale dynamics [Skamarock, 2004]. The configuration and choice of parametrization is very similar to that of Jourdain et al. [2011] and was selected to realistically represent the large-scale environment and related tropical cyclone activity in the Southwest Pacific. Physical parametrizations include the Betts-Miller-Janjic (BMJ) convective scheme; the Yonsei University (YSU) planetary boundary layer (PBL) with Monin-Obukhov surface layer parameterization; the WRF single-moment three-class microphysics scheme (WSM3); the Dudhia shortwave radiation scheme; and the Rapid Radiation Transfer Model (RRTM) for longwave radiation. The surface drag coefficient is given by the classical Charnock relation. The model simulations use 31 terrain-following vertical levels with refinement in the PBL. Horizontal refinement is provided through a two-way nesting procedure. The coarser grid with 105 km resolution encompasses the Indo-Pacific region [89.8°-240.2°E, 41.2°S-21.6°N] and the inner grid with 35 km resolution encompasses the South Pacific Convergence Zone (SPCZ) region [139.6°-200.0°E, 31.4°-1.6°S]. Boundary and surface forcing for the coarser grid are from the 6-hourly National Centers for Environmental Prediction Reanalysis 2 [NCEP-2 reanalysis; Kanamitsu et al., 2002].

A detailed sensitivity study to model parameterizations is presented in Jourdain et al. [2011]. A similar investigation was repeated here [our WRF version was upgraded from that used by Jourdain et al., 2011] but rather focusing on air-sea interactions. The usual difficulty of coupled models, even at regional scales is the added freedom of SST and air-sea fluxes to drift away from the observed state, indicating a loss of the initial surface heat balance.This loss can largely be attributed to inaccurate physics parametrizations and our selection in this respect proved satisfactory in preventing important drift.

The largest coupled model sensitivity is found on the choice of shortwave radiation parametrization. Specifically, we dismissed the Goddard radiative scheme implemented in WRF that produced excessive surface heat flux resulting in warmer surface temperatures than observed (over land and ocean). In turn, the associated change in surface pressure produced overly-strong winds converging from the north to the SPCZ. Accurate wind observations provided by the QuikSCAT scatterometer proved useful as a proxy for assessing the surface heat flux consistency with dynamical balance.

Surface drag is another key feature of air-sea interactions as it represents the ocean-wave-atmosphere interface. If the Charnock relation [Charnock, 1955] is generally considered valid for intermediate wind speed and mature waves, measurements in extreme wind conditions suggest an increase of the drag coefficient due to the presence of young seas [as theorized by Janssen, 1989] but at the same time some form of saturation due to various possible wind-wave decoupling mechanisms [Powell et al., 2003; Donelan et al., 2004]. In WRF, the Donelan relation which causes drag saturation at high wind speed was made available for hurricane studies but our sensitivity experiments showed that it worsens the regional wind

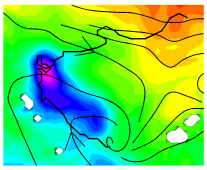

and SST climatology (and TC climatology as well). This appears to result from a drag reduction in the Donelan compared with Charnock relation even at intermediate and low wind speeds. Drag saturation (if confirmed) is only expected for extreme winds, which are very rarely attained with our 35-km grid resolution (maximum wind speed is rarely up to 35 m/s in the model). We thus consider our study in the range of validity of the Charnock relation.

The parameterization of convection is less directly relevant to air-sea interactions but is crucial for both an accurate representation of the SPCZ and the cyclogenesis process; it was thoroughly tested by Jourdain et al. [2011] who found the best behavior with BMJ (also the simplest and cheapest option in WRF). With similar experiments, we could confirm their result in the coupled model [1].

WSM3 is a cheap and simple scheme for microphysics. Rain and snow are combined into a single variable, as are cloud water and ice. There is no representation of mixed phase microphysical processes: freezing occurs instantaneously and completely at the first level where the temperature is colder than 0°C, and melting occurs similarly one level below the freezing level. In a cloud resolving application of WRF, Stern and Nolan [2011] show a relatively weak sensitivity of microphysics schemes (including WSM3 and more complicated ones) on TC intensification. Microphysics in our mesoscale application is mostly involved in the maturing phase of TCs associated with strong grid-scale updrafts (precipitation is otherwise due to subgrid-scale convection). The neglect of mixed phase processes may affect the detailed process of diabatic heating at this point but with no large consequences [Stern and Nolan, 2011].

Finally, we also confirmed the good agreement between model and observations using the YSU closure scheme, a K profile parameterization with non-local mixing that is better suited to convective regimes than other local closure models implemented in WRF [see also Hill and Lackmann, 2009].

5.2.2 Ocean model

The ocean model used is the Regional Oceanic Modeling System [ROMS; Shchepetkin and McWilliams, 2005]. ROMS solves the primitive equations in an Earth-centered rotating environment, based on the Boussinesq approximation and hydrostatic vertical momentum balance. In this study, we use the ROMS-AGRIF version of the model that has a compact package for implementation of realistic configurations [Penven et al., 2006; Debreu et al., 2012]. It is a split-explicit,

[1] In BMJ, Janjić [1994] introduced a cloud efficiency parameter to improve the original Betts-Miller scheme. This allows a modulation of the precipitation response to a change of the environment by acting on the timescale of convective adjustment (set between 1 and 2 hours). A lower cloud efficiency gives longer adjustment timescale and weaker convective precipitation. Cloud efficiency has different values in various WRF releases and is higher in the 3.3 than in the 2.2 release used by Jourdain et al. [2011]. We kept the default V3.3 parameters, which generally provided more realistic precipitation patterns at the price of somewhat excessive summer rainfall. It generally improved the spatial distribution of cyclogenesis.

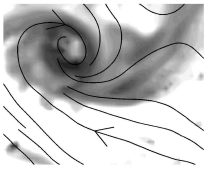

free-surface ocean model, discretized in terrain-following coordinates with high-order numerical methods for reduction of numerical dispersion and diffusion errors. Associated with a 3rd-order time stepping, a 3rd-order, upstream-biased advection scheme allows the generation of steep gradients, enhancing the model's effective resolution [Marchesiello et al., 2011]. Because of implicit diffusion in the advection scheme, explicit lateral viscosity is unnecessary, except in sponge layers near the open boundaries where it increases smoothly close to the lateral open boundaries. For tracers, a 3rd-order upstream-biased advection scheme is also implemented but the diffusion part is rotated along isopycnal surfaces to avoid spurious diapycnal mixing and loss of water masses [Marchesiello et al., 2009; Lemarie et al., 2012]. A non-local, K-profile planetary (KPP) boundary layer scheme [Large et al., 1994] parameterizes the unresolved physical vertical subgrid-scale processes at the surface, bottom and interior of the ocean. If a lateral boundary faces the open ocean, an active, implicit, upstream biased, radiation condition connects the model solution to the surroundings [Marchesiello et al., 2001]. The model was thus developed for regional applications and its computational methods allow for realistic, long-term integrations in a fine-mesh regional domain.

The oceanic configuration used in the coupled study is very similar to that described in Jullien et al. [2012] with few changes given in the following summary. The configuration was processed with ROMSTOOLS [Penven et al., 2008], a collection of global data sets and a series of Matlab programs collected in an integrated toolbox for generating the grid, initial conditions, and open boundary data. The vertical grid has 51 terrain-following levels with 2-5 m resolution in the first 50 m, 10-20 m resolution in the thermocline and 50-250 m in the deep ocean. The oceanic domain is the same as the inner atmospheric domain [139.6°-200.0°E, 31.4°-1.62°S] with the exact same grid and same 35 km horizontal resolution (no interpolation is needed to transfer data between the ocean and atmosphere). The interannual oceanic forcing is from the ORCA025-G70S global ocean simulation at a quarter degree resolution [Barnier et al., 2006] and applied at open boundaries with the mixed active/passive conditions described above. Initialization is also from ORCA025-G70S; the simulation starts in January 1979 with a model spin-up that ends well before the cyclonic season of 1979-1980 (the first considered in our analyzes).

5.2.3 Coupling procedure

Air-sea coupling is performed in the high-resolution SPCZ domain, *i.e.*, on the 35km grid shared by both oceanic and atmospheric models. The coupled simulation ran for 20 years over the present climate (1979-1999).

The oceanic and atmospheric models are coupled using a global in time Schwarz method within a simple Fortran coupler designed by Lemarié [2008]. The coupling frequency is 3 h, a multiple of the baroclinic time steps of the atmospheric model (5 min) and oceanic model (30 min). The coupling algorithm consists in three steps:

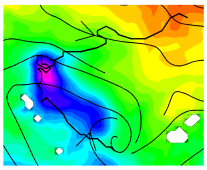

1 Advancing the atmospheric solution on a 3-h time window, using the ocean model SST of the last time window (or the initial SST field at initialization)

2 Averaging surface momentum, heat and fresh water fluxes from the atmospheric model over the 3-h time window

3 Advancing the ocean model for the same 3-h time window using surface fluxes computed at step 2.

This algorithm does not strictly ensure consistency of surface fluxes in the oceanic and atmospheric models because the oceanic model forcing is a function of SST computed on the previous time window. The original iterative procedure of the Schwarz method was designed to correct this problem and thereby suppress a form of coupling instability [Lemarié, 2008]. This would be particularly useful for climate studies using low frequency coupling but has an extra computational cost. Here, the relatively high coupling frequency of 3 hours appears to avoid the instability problem even without correction and the results are weakly sensitive to the converging procedure. At this frequency, the diurnal cycle and storm displacement are also properly resolved. On the other hand, very high coupling frequency should be avoided as bulk flux formulations are uncertain at time-scales of less than an hour [Large, 2006]. For this reason also, the use of time-averaged fluxes is preferable to instantaneous fluxes.

Note that the ocean model computes a bulk rather than skin SST that requires very fine surface resolution. The skin SST has a larger diurnal variability (particularly in the Pacific warm pool area) that directly impact air-sea fluxes. For more realism in the estimation of these fluxes in WRF, a sea surface skin temperature is computed from the scheme of Zeng and Beljaars [2005]. It consists of prognostic, one-dimensional heat transfer equations for the molecular sublayer (cool skin) and diurnal layer (warm skin) of the ocean. It provides the difference of temperature between the skin temperature at the top of the cool skin and the bulk temperature (given by the model SST) at the bottom of the warm layer. The ocean model bulk SST is here taken at 10 m depth for consistency with the scheme of Zeng and Beljaars [2005]. Our simulations show realistic 0.5-2°C diurnal variations of skin SST and a mean difference between bulk and skin SST of about 0.25°C. The skin SST is colder in average due to heat loss in the cool skin by long-wave radiation. As expected, a sensitivity test using bulk rather than skin SST for the computation of surface fluxes (not shown) revealed that the use of skin SST slightly reduces the surface heat and moisture fluxes to the atmosphere. However, the regional climate and cyclonic activity did not appear greatly affected by this choice.

5.2.4 Forced simulation setup

A twin uncoupled atmospheric simulation (hereafter called *forced simulation*) is performed in order to analyze the impact of coupling on tropical cyclones. The forced simulation is computed using exactly the same WRF configuration and SST fields from the coupled simulation, but the latter are reprocessed to remove

TC-induced cold wakes. Cold wake removal is done by a 90 day low-pass FFT filter applied at each location of TC occurrence over a 3 degree radius disk and from 1 day before occurrence (cyclones by their large size have an effect ahead of their core) to 20 days after. Then, the high-frequency ambient SST (which is filtered in the same time as the storm-induced cooling) is injected back in the cyclone track by interpolating fields from the sides of the TC track. As a result, the forced simulation has no ocean feedback from TC occurrence but keeps all other oceanic impact. An example of cold wake filtering is presented in Fig. 5.1.

It is important to note that even the small SST perturbations produced by the

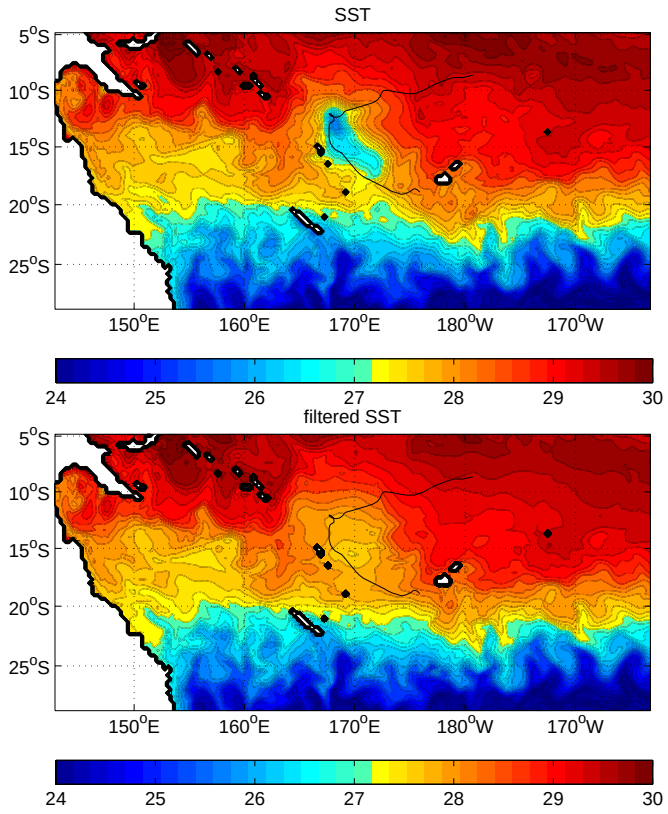

Figure 5.1 - Example of a TC cold wake event and its filtering procedure: (a) SST field from the coupled model (°C), (b) filtered SST field used in the forced model.

filtering method are enough to change the course of chaotic events in the present climate. Tropical cyclones in the forced simulation are independent events from the coupled cyclones. Their genesis time and trajectories are different and, therefore, rarely cross the filtered SST locations. Therefore, they are weakly affected by the choice of filtering methods. The downside is that the two simulations are only comparable at a statistical level, not for particular events.

5.2.5 Tracking methodology

The tracking method used in this work was developed by Chauvin et al. [2006] and used in Jourdain et al. [2011] with few modifications. Several criteria are used

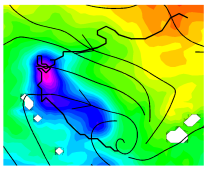

to distinguish tropical cyclones from intense mid-latitude systems at each time step:

- Mean sea level pressure is a local minimum
- 850 hPa vorticity > VOR
- maximum 850 hPa wind speed > WT
- Mean 700-300 hPa temperature anomaly > TT
- 300 hPa temperature anomaly > 850 hPa temperature anomaly
- 850 hPa tangential wind > 300 hPa tangential wind

where VOR, WT and TT are threshold parameters. Anomalies are defined as the difference between the system and its environment (defined using the radius of maximum radial pressure gradient; see Chauvin et al., 2006). The tracks are then constructed by an iterative process that links the points where the criteria are satisfied. As a final step, all criteria except "850 hPa vorticity > VOR" are relaxed so that the tracks are completed both backward and forward. This relaxation method prevents a cyclonic system whose intensity decreases and then increases again from being counted twice.

The WT threshold can be objectively determined following Walsh et al. [2007]. An empirical choice of the two other thresholds was made by testing different values of the criteria and verifying that the detected systems were actual tropical cyclones. The thresholds retained for this study are:

$$\text{VOR}=20.10^{-5}\ \text{s}^{-1}\ ,\ \text{WT}=17\ \text{m.s}^{-1}\ \text{and TT}=1\ \text{K}.$$

Since VOR and TT thresholds are empirical, the sensitivity of the tracking method to their choice was investigated as in Jourdain et al. [2011]. A positive TT criteria is important to detect warm core vortices, whereas excessive values fail to detect all tropical cyclones. The vorticity threshold has a significant role in filtering weaker mesoscale vortices.

5.2.6 Compositing methodology

As mentioned above, the direct comparison of particular events between forced and coupled simulations is impossible due to the chaotic nature of the simulations. However, we can construct composite cyclones in various ways in order to compare statistical quantities along cyclone tracks. The composite methodology of Jullien et al. [2012] was used again for its robustness. Three types of composites are presented here: an *Eulerian composite*, a *cross-track composite* and an *along-track Lagrangian composite*. As a first step, TC characteristics are extracted along the tracks of all simulated events.

Specifically, on each TC location where wind speed reaches at least 17 $m.s^{-1}$, a cross track section is extracted by interpolation of all fields on a finer cross-track

grid (10-km resolution). To avoid "smearing" the strong eyewall features during the compositing of all TCs, the interpolated fields are re-centered on the minimum wind location and normalized by their radius of maximum winds. After normalization, the composited TC track is rescaled by the mean radius of maximum winds. This procedure is efficient in constructing a smooth but realistic composite of tropical cyclones.

The Eulerian composite is built by looking at cross-track sections around the time of TC occurrence: from 10 days before to 30 days after passage. Eulerian composite analyses are thus presented as a function of time around occurrence, which we call 'lag'. It represents an Eulerian view: at any given location, the storm is shown to approach, pass through and get away.

Finally, an along-track Lagrangian composite is built by averaging TC variables over a 400-km cross track distance around the track center at the TC passage time. Each TC is then normalized by its duration and the final composite is rescaled by the mean duration. It creates an along-track composite that represents a Lagrangian view of a composited TC life cycle (intensification, mature phase and decay).

5.3 Environmental conditions

5.3.1 The ocean-atmosphere interface

Climatological 1979-1998 summer SST computed from the coupled simulation (Fig. 5.2) is presented here as an end product of surface oceanic conditions. The model SST is in good agreement with southwest Pacific observations and shows no drift over the 20-year simulation (not shown). This suggests a consistent representation of air-sea exchanges that validates our choice of physical parametrization, particularly the shortwave radiation scheme and turbulent exchange parameters.

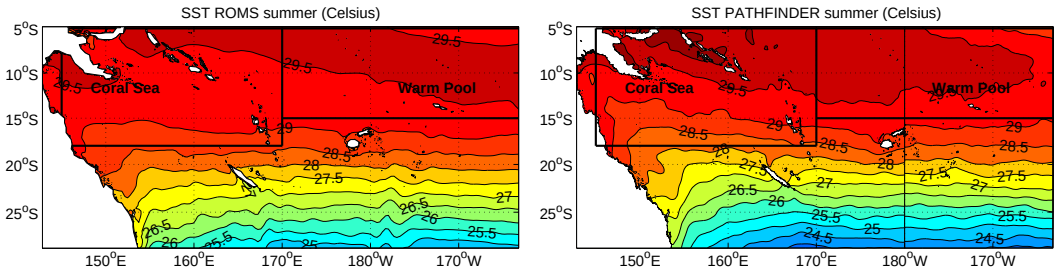

Figure 5.2 - Mean austral summer (January-March) SST (°C) from (a) the 1979-1998 coupled model, (b) Pathfinder climatological observations (dataset developed by the NASA Physical Oceanography Distributed Active Archive Center (PO.DAAC) and the NOAA National Oceanographic Data Center (NODC)).

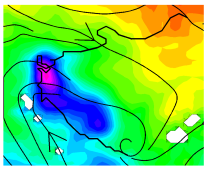

The net heat flux seasonal cycle (Fig. 5.3) is similar to observations, albeit with lower values, but the accuracy of heat flux observation is much lower than that of SST as illustrated by large discrepancies among observational products. A generally better accuracy is attributed to QuikSCAT surface scatterometer wind data (Fig. 5.3 and 5.4), validating the model representation of SPCZ circulation. We see the trade wind confluence in the east and convergence of trade winds and Australian monsoon winds in the west (monsoon winds are slightly overestimated). The correct representation of surface dynamics is an indirect validation of its surface thermodynamic forcing. In addition, the coupled model shows no drift or instability associated with the added degree of freedom.

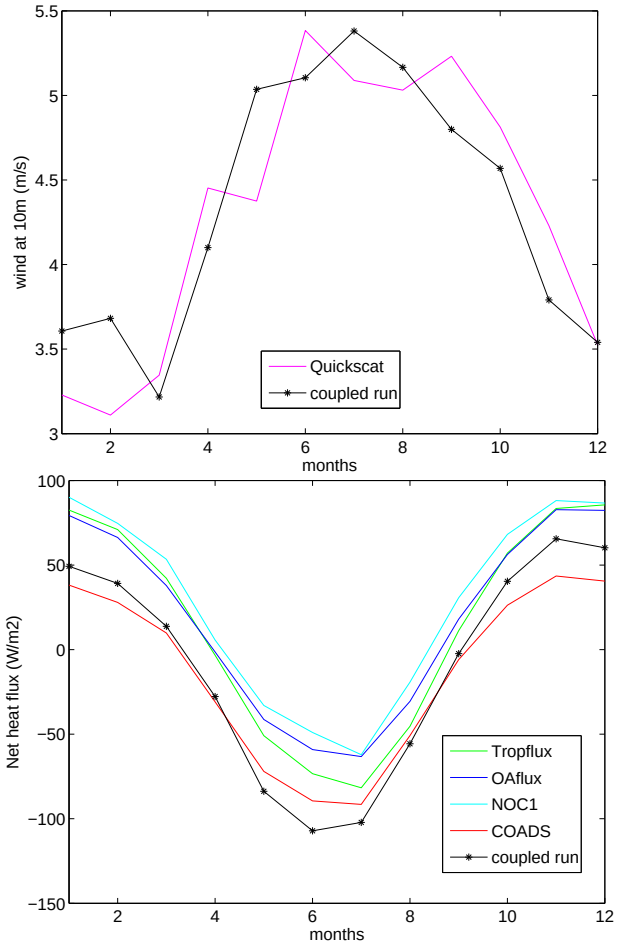

Figure 5.3 - Seasonal cycle of (a) 10-m wind speed ($m.s^{-1}$) and (b) surface net heat flux ($W.m^{-2}$) from the 1979-1998 coupled model (black line) and various observational datasets (colored lines): QuikSCAT 1999-2009 (purple line; http://cersat.ifremer.fr), TropFlux 1979-1998 (green line; http://www.locean-ipsl.upmc.fr/~tropflux/data), OAflux 1979-1998 (blue line; http://oaflux.whoi.edu), NOC1 climatology (cyan line; http://www.noc.soton.ac.uk/science-technology/earth-ocean-system/atmosphere-ocean/) and COADS climatology (red line; Comprehensive Ocean-Atmosphere Data Set [COADS; Slutz et al., 1985; da Silva et al., 1994]).

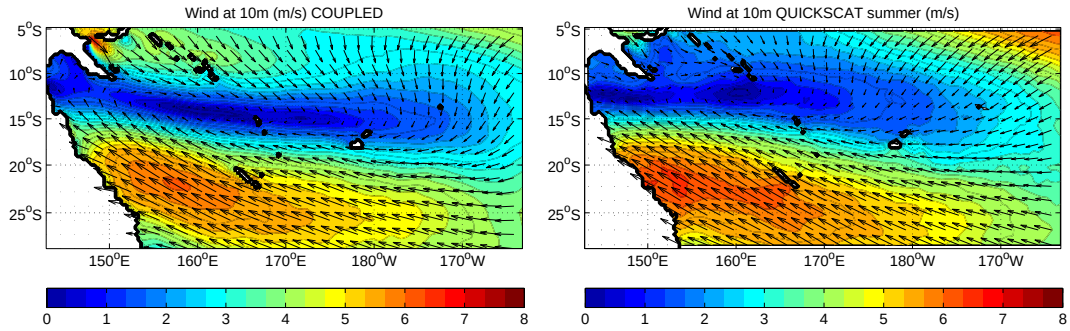

Figure 5.4 - Mean austral summer (January-March) 10-m wind speed ($m.s^{-1}$, shaded area) and vectors from (a) the 1979-1998 coupled model, (b) QuikSCAT observations.

In the SST map of Figure 5.2, we identify two important subregions: the Coral Sea [145°-170°E, 5°-18°S] and the warm pool region [170°-200°E, 5°-15°S]. The latter is a warm SST region with relatively deep oceanic mixed layer (Fig. 5.5 shows the model MLD, which favorably compares with estimations by Montegut et al., 2004). The Coral Sea is slightly cooler and features shallower mixed layer. The following sections will unveil a strong regional modulation of coupling strength pertaining to the dependence of SST on thermocline structure under mixing and upwelling conditions.

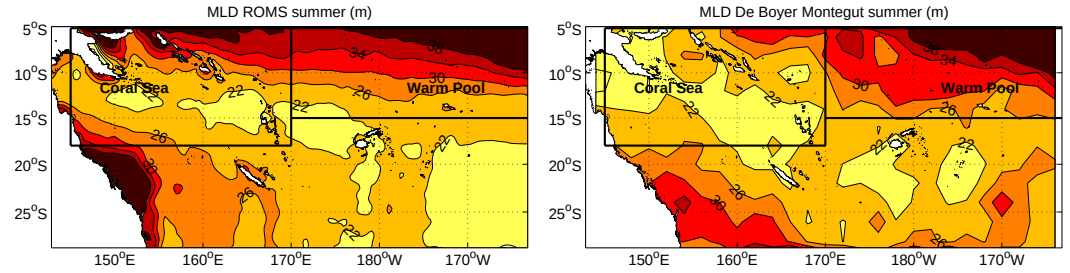

Figure 5.5 - Mean austral summer (January-March) mixed layer depth (m) from (a) the 1979-1998 coupled model, (b) observational climatology from Montegut et al. [2004] (http://www.ifremer.fr/cerweb/deboyer/mld) using a surface density+0.03 $kg.m^{-3}$ criterion.

5.3.2 SPCZ and cyclogenesis index

The environmental conditions of cyclogenesis are essentially related to convective potential, wind shear, mid-tropospheric humidity, and vorticity [Gray, 1975]. The localization of maximum convective potential is given by the SPCZ position (Fig. 5.6). It is computed as the meridional maximum precipitation in both observations [Tropical Rainfall Measuring Mission 3B-42 gridded product; Adler et al., 2000] and the coupled simulation. Model and observations are in very good agreement showing the same classical east-west tilt of maximum precipitation that is reminiscent of surface wind convergence patterns (Fig. 5.4). This result is not trivial as evidenced by the failure of climate models [Walsh, 2004; Jourdain et al., 2011;

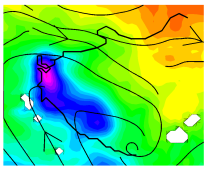

Brown et al., 2013].

Next, the combined effect of all atmospheric conditions favorable to cyclogenesis is represented by the Convective Yearly Genesis Potential Index [CYGP; Royer et al., 1998] computed as follows:

$$CYGP = \underbrace{|f| I_\xi I_S}_{dynamic} \underbrace{k(P_C - P_0)}_{thermal} \tag{5.1}$$

where f is the Coriolis parameter in 10^{-5}s $^{-1}$, $I_\xi = \xi_r \frac{f}{|f|} + 5$ with ξ_r the relative vorticity at 925 hPa in $10^{-6}s^{-1}$, $I_S = (|\frac{\delta V}{\delta P}| + 3)^{-1}$ with $\frac{\delta V}{\delta P}$ the vertical shear of the horizontal wind between 925 and 200 hPa in $m.s^{-1}/755hPa$, k is an arbitrary constant adjusted to produce the right number of cyclones, P_C is the convective precipitation in $mm.day^{-1}$ and P_0 is a threshold below which the convective potential is set to zero to avoid spurious cyclogenesis off the tropics. We chose to use this cyclogenesis index (with $P_0 = 3$) in agreement with Menkes et al. [2012b] for its good performances in the South Pacific. CYGP (Fig. 5.6) shows favorable conditions of cyclogenesis slightly south of the SPCZ position, i.e. near the maximum of vorticity. The region of highest potential cyclogenesis given by CYGP is the Coral Sea [145°-170°E, 5°-18°S] as in observations [see Vincent et al., 2011].

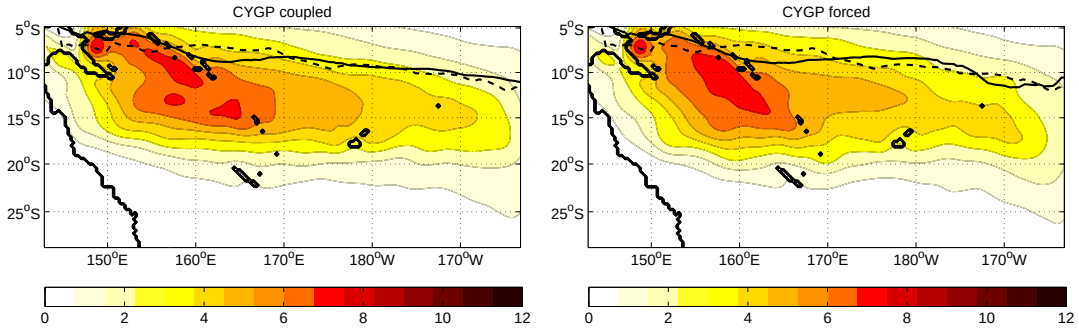

Figure 5.6 - Mean yearly CYGP index (in number of TCs per 5° and per 20 years and normalized to the observed number of TCs) for (a) the coupled model and (b) the forced model. The black solid line represents the summer SPCZ position in the model and the dashed line represents the summer SPCZ in TRMM 3B-42 gridded product observations [Adler et al., 2000].

5.4 TC STRUCTURE

The composited TC structure of the coupled model is presented in Figure 5.7 as a function of cross track distance from the cyclone eye (the right-hand side of the plot represents the left-hand side of the storm which is strongest in the southern hemisphere; we choose this convention for easier comparison with studies of the

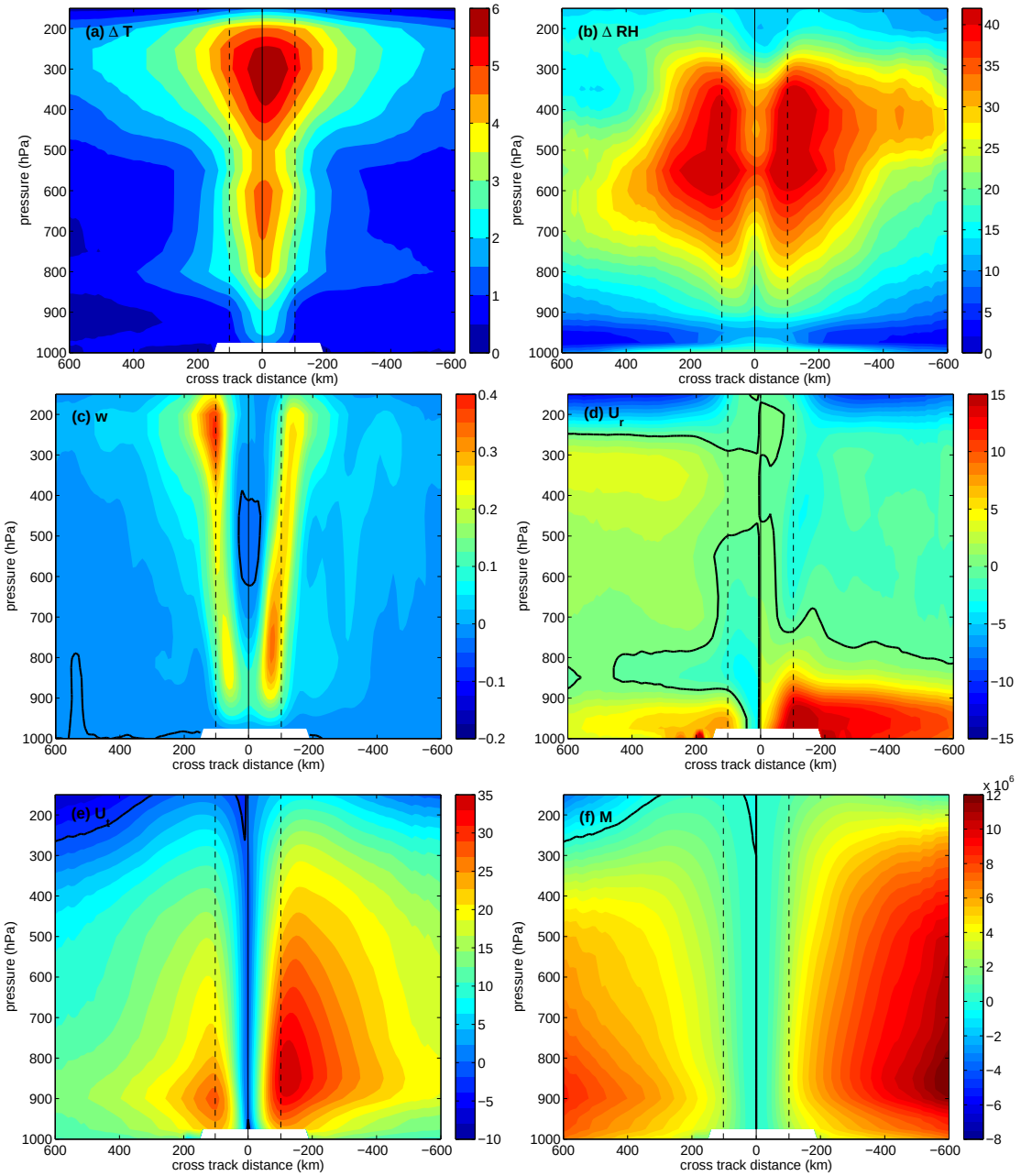

Figure 5.7 - Cross track sections of the coupled model composited TC, based on all events with wind speed greater than 27 $m.s^{-1}$. (a) Warm core anomaly (°C); (b) relative humidity anomaly (%); (c) vertical velocity ($m.s^{-1}$); (d) radial velocity ($m.s^{-1}$); (e) tangential velocity ($m.s^{-1}$); and (f) absolute angular momentum per unit mass ($m^2.s^{-1}$). The coordinates are the cross track distance (in km) and vertical pressure levels (in hPa). Ambient values of temperature and humidity (needed to construct anomalies) are pre-storm time-mean values between days −10 and −2. The vertical dashed lines represent the averaged radius of maximum winds; the vertical solid line shows the TC center; the solid bold lines in velocity plots represent zero values.

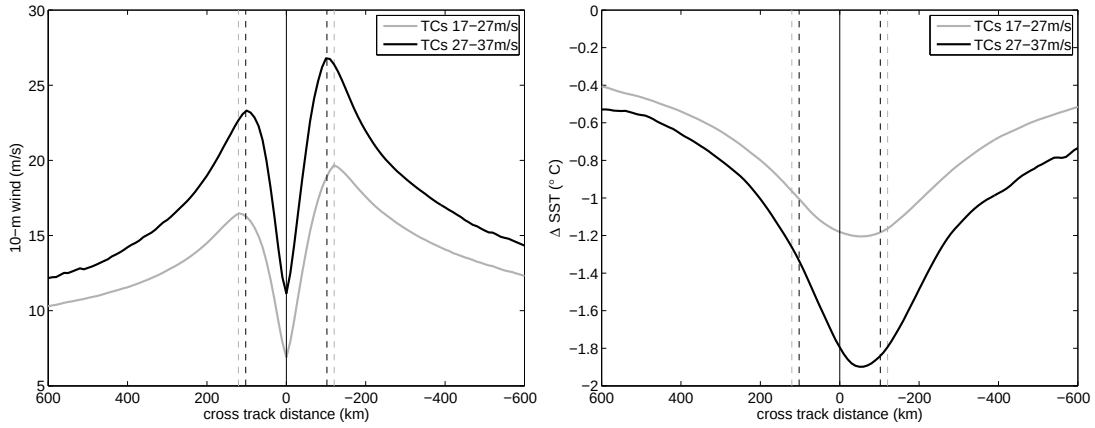

Figure 5.8 - Cross track composite of TC surface features: (a) 10-m wind speed ($m.s^{-1}$) at TC occurrence time; and (b) SST cooling (°C) at the time of maximum cooling. The results are presented for two TC wind categories: 17-27 $m.s^{-1}$ (gray lines) and 27-37 $m.s^{-1}$ (black lines). The vertical dashed lines represent the averaged radius of maximum winds for each category.

northern hemisphere) and pressure vertical levels. This analysis emphasizes the persistent properties of simulated cyclones and filters the anomalies of isolated events. It can thus be thought of as an archetypal phenomenon. Here, we selected TCs with wind speed higher than 27m/s. The composite computed from all weak and strong events is similar but with less amplitude and asymmetry.

The composited TC presents all features of observed cyclones [*e.g.*, Gentry and Lackmann, 2009; Stern and Nolan, 2011; Jourdain et al., 2011, for a selection of observations for model validation]. The warm core temperature (Fig. 5.7a) has the classical V-shape structure, with 6 K maximum anomaly (over 10 K for some individual events) located in the upper troposphere (200-400 hPa) and a ridge through the outflow layer. There is also a second midlevel maximum around 600 hPa. The warming of the core of tropical cyclones is one of its most emblematic attribute. It is supposedly due to a combination of diabatic heating in the eyewall updraft and dry adiabatic descent within the eye (a forced response to the eyewall heating in the Sawyer-Eliassen secondary circulation). However, the inner core temperature profiles, including the magnitude of upper- and mid-level maxima, are still debated [Stern and Nolan, 2011].

Relative humidity anomaly in the TC core relative to ambient humidity (Fig. 5.7b) shows a 40-45% increase in mid-troposphere (400-700 hPa) with larger values on the strong side.

Vertical velocities (Fig. 5.7c) present tilted and asymmetric updrafts along the eyewall with values of up to 0.4 m/s in the composite, although they can reach more than 1.5 m/s in individual TCs [2]. The eye structure is well represented by a minimum of vertical velocity and even some subsidence appearing in the compos-

[2]The sloping of the eyewall results from the action of centrifugal forces on ascending air parcels

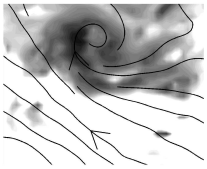

ite between 400 and 600 hPa (there is smoothing in the composite as individual events show subsidence variably extending to the top but the mid-level maximum seems the most robust feature).

Radial and tangential velocities present a very strong asymmetry (Fig. 5.7d-e). The main radial inflow is in the surface Ekman layer, it converts into eyewall updraft (maximum above the boundary layer) and the main outflow is at 150 hPa. Surface inflow is forced by tangential winds that are maximum in the eyewall in the upper boundary layer (suggesting supergradient winds in the inner-core; Smith and Montgomery, 2010) and decreases with height, consistent with gradient wind balance in a warm core system (note the anticyclonic flow aloft at larger radii). The radius of maximum winds is about 100 km, which is larger than the mean observed value of 50 km but expected from a mesoscale resolution model [Gentry and Lackmann, 2009]. The cyclone's secondary circulation is thus composed of a frictionally forced circulation added to the forced response to eyewall convection.

The absolute angular momentum (Fig. 5.7f; $M = rv + \frac{1}{2} f r^2$, with r, v and f the radial distance, tangential velocity and Coriolis frequency), as described in Smith et al. [2009], emphasizes the dynamical role of radial convergence in amplifying tangential winds above the boundary layer in the outer-core. The removal of M by friction counteracts its strong radial influx in the boundary layer but the patterns of M and v towards the inner-core suggest some boundary layer spin-up there as well (strong vorticity in the inner-core effectively increases the Coriolis parameter; see Smith et al., 2009).

Figure 5.8 presents cross-track profiles of surface properties for weak (17-27 m/s) and strong (27-37 m/s) TC categories. The 10-m wind speed profile features a clear cyclone eye with strong wind drop off in the center and asymmetric eye wall. Stronger winds appear on the storm's left-hand side because of the addition of TC translation speed on the left-hand side and subtraction on the right-hand side. Note that the decay of tangential winds away from the center is relatively mild. A leftward SST cooling asymmetry (Fig. 5.8) results from this TC wind pattern but also from wind-current resonance at near-inertial periods [Shay et al., 1989; Jullien et al., 2012; Vincent et al., 2012a]. SST cooling by the strong composited TC is almost twice as much as that of the weak TC, *i.e.*, 1.9°C at the maximum. This value for individual events can reach 6°C but maximum cooling generally lags maximum wind forcing and thus occurs in the cyclone wake, *i.e.*, outside the inner-core region. This remark is important for feedback effects that will be analyzed later in this paper.

as pressure gradient decreases. The slope is tightly related to the warm core and tangential wind structure and thereby dependent on grid resolution, steeper for coarser models (*e.g.*, Gentry and Lackmann, 2009)

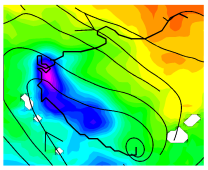

5.5 Coupling effect on cyclonic activity

5.5.1 Cyclogenesis geography

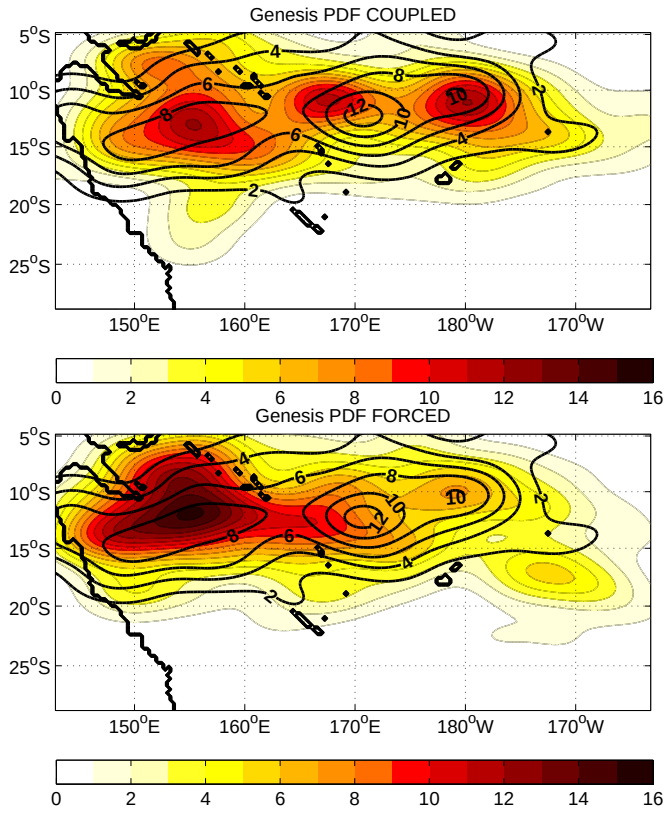

Figure 5.9 - PDF of cyclogenesis (in number of TCs per 5° and per 20 years, shaded area) for (a) the coupled and (b) the forced model. Black contours overlaid on the shaded plots present the PDF of cyclogenesis from SPEArTC observations.

The spatial distribution of cyclogenesis in the coupled and forced simulations and in observational data for the 20-year period 1979-1999 is represented by probability density functions (PDFs; Fig. 5.9), as in Jourdain et al. [2011]. The observations are given by the new South Pacific Enhanced Archive for Tropical Cyclones (SPEArTC) dataset from Diamond et al. [2012] that was built using data from the International Best Tracks for Climate Stewardship (IBTrACS) project information, historical data from numerous islands and a strict quality control of each track.

The coupled model cyclogenesis distribution appears in very good agreement with observations and outperforms the forced model showing excessive cyclogenesis in the Coral Sea and in southeastern SPCZ region. The average number of cyclogenesis per year (Table 5.2) is also slightly overestimated in the forced model with 8.7 TCs/year compared with the observed 7.4 TCs/year that is closer to the coupled model result of 7.9 TCs/year.

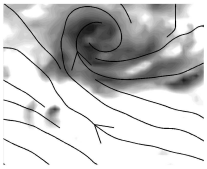

Table 5.2 - TC statistics from SPEArTC observations and from the forced and coupled models: annual mean and standard deviation of the number of cyclogenesis events; west/east distribution (*i.e.*, Coral Sea/Warm Pool) of the annual mean; and mean TC life time of weak (17-27 m/s) and strong (27-37 m/s) cyclone categories.

	Observations SPEArTC	Forced model	Coupled model
Number of TCs/year	7.4 ± 3.0	8.7 ± 3.1	7.9 ± 2.4
West/East distribution	4.5/2.9	5.7/2.9	4.8/3.1
Weak TC life time (days)	6.6	5.6	5.7
Strong TC life time (days)	8.2	8.8	7.8

To better quantify the PDF differences, we partitioned the cyclogenesis distribution between western and eastern SPCZ regions, *i.e.*, the Coral Sea and warmpool genesis areas, using the 170°E meridian as a separation line. Table 5.2 confirms the realistic east-west genesis distribution of the coupled model with 4.8 TCs/year in the Coral Sea and 3.1 TCs/year in the warmpool, very close to the observed 4.5 and 2.9 TCs/year respectively. The forced model produces about one more TC in the Coral Sea. This statistically significant difference (significant at 62%) cannot be related to the large-scale atmospheric conditions as the CYGP distribution (Fig. 5.6) is very similar in both simulations. It thus has to do with ocean-storm coupling whose mechanisms will be explored in Section 5.6.

5.5.2 Intensity distribution

The storm intensity distribution presented in Fig. 5.10 is the number of cyclone days per year as a function of central pressure. It shows that the coupled model succeeds in representing the intensity of intermediate-strength cyclones and poorly performs for the most intense ones. This is understandable considering the 35-km model resolution that smooths out the sharp eyewall structure of tangential winds; it also underestimates the strongest eyewall updrafts and compensating subsidence within the eye which contributes to the warming of the core region and hydrostatic reduction of central pressure [Gentry and Lackmann, 2009]. Nevertheless, the intensity distribution of the forced model shows an overestimation of cyclone days for TCs with 970-990 hPa intensity. This result can only be explain by the absence of negative SST feedback.

Interestingly, stronger TCs are more affected by the coupling process (Table 5.3). Towards the spectrum tail, TCs of category 4 are present in the forced model but absent in the coupled model. On the contrary, weaker cyclones are only weakly affected by coupling. For quantitative analysis, the classification based on 2 categories of cyclones is justified: a moderate category with wind speed between 17 and 27 $m.s^{-1}$ that features moderate coupling effects; and a category of strong TCs with winds over 27 $m.s^{-1}$ that shows the largest effect.

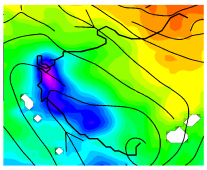

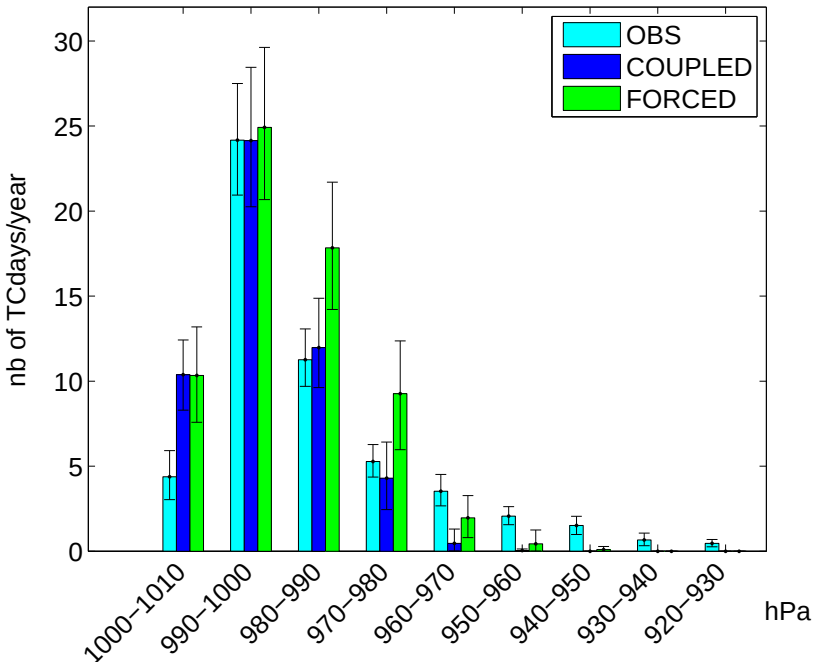

Figure 5.10 - Distribution of TC central pressure (in number of TC days per year) for the period 1979-1999 and from SPEArTC observations (cyan), the coupled model (blue) and the forced model (green). The 5-95 percentiles bootstrap error bars are also presented.

Table 5.3 - Percentage of the difference in TC days between forced and coupled models in various storm categories.

TC pressure category	Coupling effect on TC events
1000-1010 hPa	-25 %
990-1000 hPa	-24 %
980-990 hPa	18 %
970-980 hPa	36 %
960-970 hPa	67 %
950-960 hPa	90 %
940-950 hPa	100 %

5.6 Coupling effect on air-sea fluxes

5.6.1 SST cooling

The composited effect of TC occurrence on SST and air-sea fluxes is examined as a function of time relative to TC passage (lag) where a zero lag represents the occurrence time. As described in Section 5.2.6, this Eulerian composite is a 400-km cross-track average at each TC location. A comparable composite is constructed for microwave SST observations from the Tropical Rainfall Measuring Mission (TRMM) Microwave Imager (TMI) and Advanced Microwave Scanning Radiometer for Earth Observing System (AMSR-E; http://www.ssmi.com/sst). Microwave SSTs

are taken from 1998 to 2007 along the observed cyclone tracks. Cooling is defined as the difference between local SST and and pre-storm (ambient) SST. Ambient SST is computed as the averaged value between days −10 and −2 as in Jullien et al. [2012]. For both model and observations, the seasonal SST cycle is removed by subtracting the daily climatology.
The mean Eulerian representation of TC-induced cooling is shown in Figure 5.11a for the coupled model and TMI-AMSR-E observations. The coupled model shows a realistic depiction of cooling intensity and timing. The cooling is not maximum under the cyclone eye but 2 days after its passage because of the time needed by upwelling and near-inertial mixing to impact surface temperatures, as described in Jullien et al. [2012].

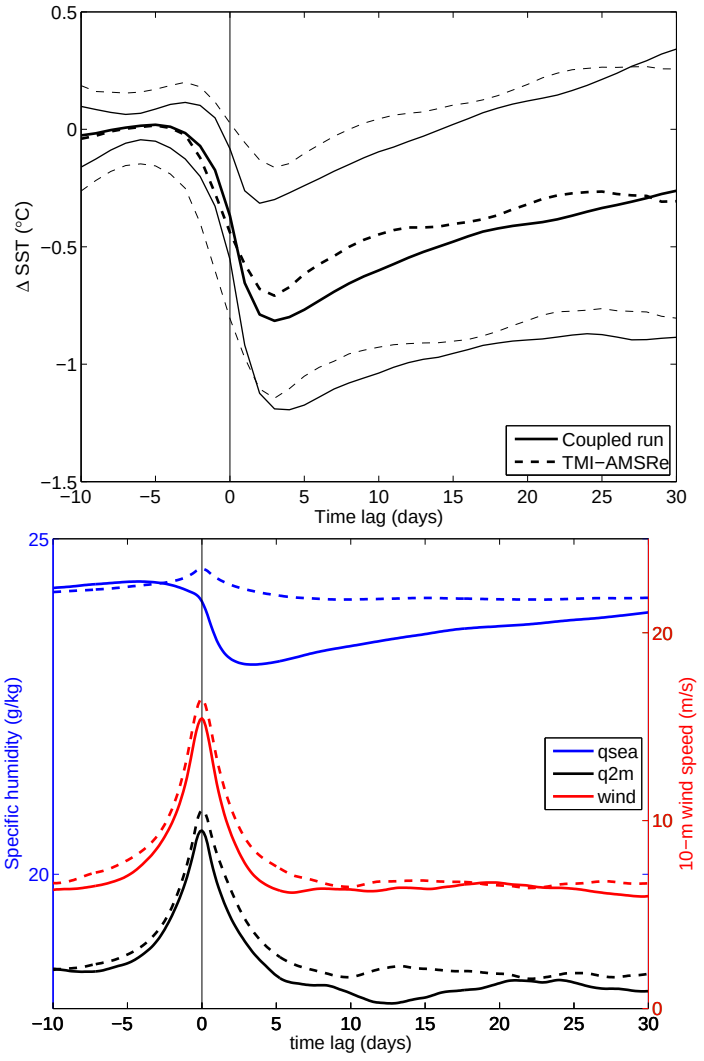

Figure 5.11 - Cyclone wake composites as a function of time from TC occurrence (lag in days). (a) SST cooling (°C, bold lines) and its standard deviation (thin lines) for the coupled model (solid lines) and TMI-AMSRe observations (dashed lines); (b) 10-m wind speed ($m.s^{-1}$, red lines) and specific humidity ($g.kg^{-1}$) at 2 m (black lines) and at sea level (blue lines) in the coupled model (solid lines) and forced model (dashed lines).

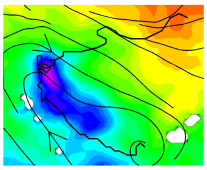

5.6.2 Specific humidity

The evolution of 2-m specific humidity (Fig. 5.11b, black curves) shows little differences between coupled and forced simulations with, in both cases, an increase of humidity during cyclone occurrence. The storm impact is noted from days −5 to +5 because of its very large spatial extent. The difference between the two runs can be attributed to a small difference in large-scale conditions and in storm intensity associated with a few stronger (Fig. 5.11b, red curves) and moister TCs in the forced simulation.

Sea level specific humidity (Fig. 5.11b, blue curves), on the other hand, is significantly different between the two simulations because it is tightly related to SST. In the forced run, there is no cooling feedback and sea-level humidity only slightly increases during cyclone occurrence because of the warm core low pressure anomaly. The reduction of surface pressure is one known process that affects surface fluxes by increasing the saturation mixing ratio [*e.g.*, Schade, 2000]. In the coupled simulation however, humidity changes are opposite and much larger than those created by pressure changes. Sea level specific humidity follows the evolution of surface cooling with a maximum decrease 2 days after TC passage. This leads to a reduction of air-sea moisture difference, *i.e.*, the thermodynamic disequilibrium at the sea surface that weakens the latent heat flux.

5.6.3 Air-sea fluxes

The evolution of air-sea fluxes as the cyclone passes are presented in Figure 5.12a. Short-wave radiation to the ocean decreases during TC occurrence because of TC clouds that limit the penetration of downward solar fluxes in the troposphere. On the contrary, downward long-wave radiation increases because of TC clouds, but at a lower rate. Sensible and latent heat fluxes from the ocean to the atmosphere both increase when storm winds extract heat and moisture from the ocean, the latent heat flux being largely dominant.

The difference between forced and coupled simulations is also most important for the latent heat flux (Fig. 5.12a and 5.12b). There is a milder effect on the sensible and upward long-wave radiation. The latter is directly affected by SST cooling and thus follows the same evolution pattern with a maximum decrease of 5 $W.m^{-2}$ 2 days after TC passage. The decrease in sensible heat flux of 10 $W.m^{-2}$ can be attributed to both SST cooling and a decrease in wind intensity in the coupled simulation. More importantly, the latent heat flux is 70 $W.m^{-2}$ lower in the TCs of the coupled simulation following cyclone occurrence. This can be attributed to some extent to the presence of weaker cyclones in the coupled run but the time evolution of changes with a peak 2 days after TC passage rather suggests a major effect of SST cooling through its control of sea-level specific humidity.

The mean effect of ocean-hurricane coupling is thus an SST cooling of 0.6°C (Fig. 5.11a) that leads to a latent heat flux reduction of 70 $W.m^{-2}$ and a lesser reduction in sensible heat flux of 10 $W.m^{-2}$.

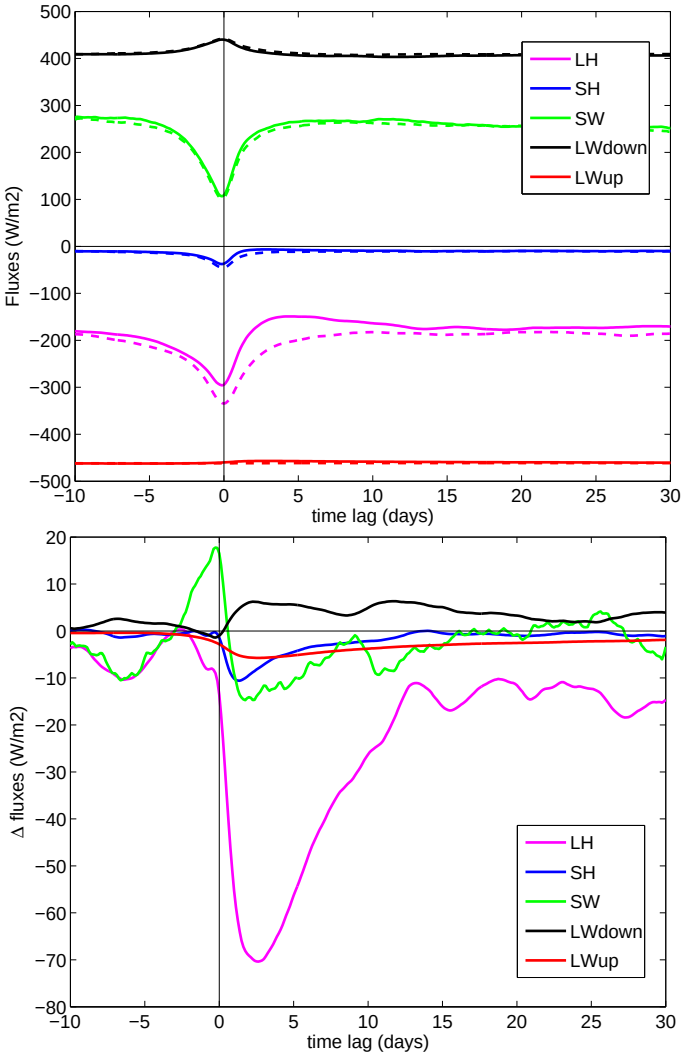

Figure 5.12 - Cyclone wake composites as a function of time from TC passage (lag in days) of surface heat fluxes for (a) the coupled model (solid lines) and forced model (dashed lines); and (b) the difference between forced and coupled models. Latent heat flux is in purple, sensible heat flux in blue, shortwave radiation in green, longwave downward radiation in black and longwave upward radiation in red.

5.7 The role of ocean dynamics

5.7.1 Geography of storm-induced cooling

Ambient SST and TC-induced SST cooling are both related to the ocean stratification, which is structured by ocean dynamics. At the regional scale, stratification in the Coral Sea is strongly affected by negative winter heat fluxes and downwelling associated with the gyre-scale anticyclonic circulation [Marchesiello et al., 2010a]. The winter mixed layer is deep and relatively cold, contrasting with the warm pool region characterized by a thick layer of warm water piled up by equatorial currents. Summer stratification in the Coral Sea then produces a shallow layer of warm water above the cool water generated in winter. The potential for storm-

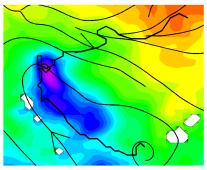

induced SST cooling is thus particularly high in the Coral Sea and low in the warm pool.

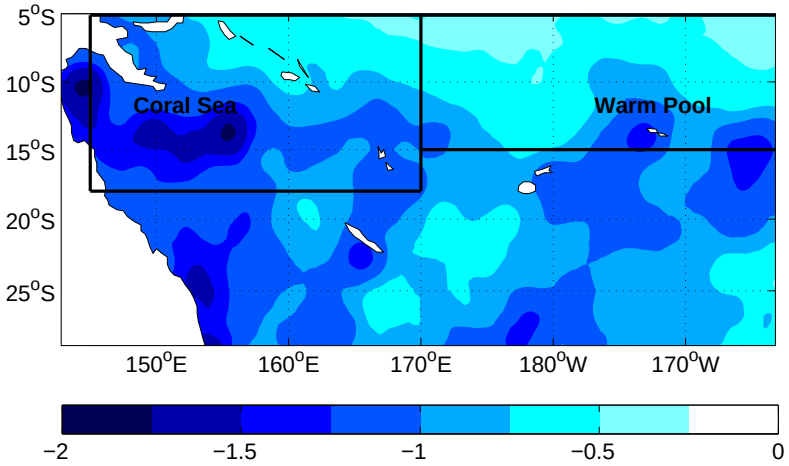

Figure 5.13 - Composite map of storm-induced SST cooling (°C). In the construction of this map, if two TC tracks overlap, the coolings are averaged.

This is confirmed by our experiments. A map representing the combined SST cooling of all TCs over the 20 years of coupled simulation is presented in Figure 5.13. It is computed by mapping all SST cooling events along TC tracks and taking the average value of 2 events if there tracks happen to cross each other. This map provides a distribution of TC-induced cooling in the southwest Pacific that confirms strong cooling in the Coral Sea where the oceanic mixed layer is relatively shallow (Fig. 5.5). On the contrary, very weak cooling appears in the warm pool.

5.7.2 Storm sensitivity to SST

To isolate the SST feedback effect in the relation between central pressure and SST, we now present (Fig. 5.14) the TC intensity difference between forced and coupled runs as a function of ambient SST and SST cooling [3]. Here, SST cooling is not defined as the maximum found in the TC area but as the mean inner-core value (averaged over 400km cross track), which should be more relevant to the feedback effect. Large negative values of pressure difference (red color in Fig. 5.14) indicates strong coupling effect (SST feedback). A maximum reduction of 15hPa in central pressure occurs for SST cooling of 2°C and ambient SST of more than 28°C. Figure 5.14 shows that storm intensity is affected by both SST effects but is more sensitive to TC-induced cooling than to ambient SST. Interestingly, the maximum possible SST cooling calculated by Schade [2000, cooling that results in the cancellation of radial gradient of moist entropy in the boundary layer] is also

[3] To generate the SST cooling associated with TCs of the forced atmospheric simulation, we ran the ocean model alone driven by surface fluxes from the forced atmospheric model. This forced oceanic simulation (without SST feedback to the atmosphere) gives the oceanic response to the forced atmospheric model, which can be compared to the fully coupled model response.

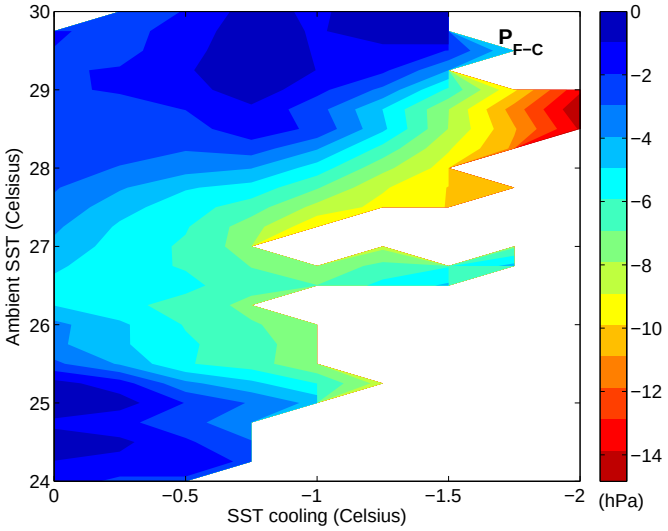

Figure 5.14 - TC central pressure difference between forced and coupled models as a function of SST cooling and ambient SST.

present in our modeling results and increases with the ambient SST as predicted (see the white area of Fig. 5.14 where TCs would be suppressed by excess cooling).

An indication of coupling sensitivity to SST cooling alone can be obtained by averaging the previous functions for all ambient SST categories (Fig. 5.15a). It shows that the feedback effect on storm intensity is highly nonlinear. It is weak for coolings below 1-1.5°C but then increases steadily at a rate of about 15 hPa/°C. Even for strong cooling, the intensity feedback is less than half the theoretical range given by Holland [1997] and Schade [2000] but closer to that of idealized and test case experiments (Table 5.1).

5.7.3 Mixed layer depth

Instead of SST cooling, Wu et al. [2007] have used the ambient mixed layer depth as a parameter of oceanic feedback. It provides a more easily measurable quantity for prediction of storm intensity. In our realistic experimental setting, the variability of storm intensity for any given MLD value (due to the variability of atmospheric conditions or intrinsic processes) renders the comparison between forced and coupled models quite sensitive. By entering SST cooling as a second parameter, we reduce the risk that coupled and forced TCs are incomparable in the parameter space. The averaging of all SST cooling categories provides a sensitivity value to ambient MLD alone (Fig. 5.15b). This estimation has again a nonlinear behavior: it is low for deep MLD but for shallower MLD it reaches 5 hPa increase of TC central pressure for every 10 m increase of MLD (compare with a constant value of 4.7 hPa/10m given by the simple model of Wu et al., 2007). There are uncertainties associated with the methodology but our results are consistent with the expectation that entrainment of cold subsurface water should be weakly sensitive to deep mixed layers (at least for depths deeper than

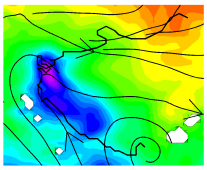

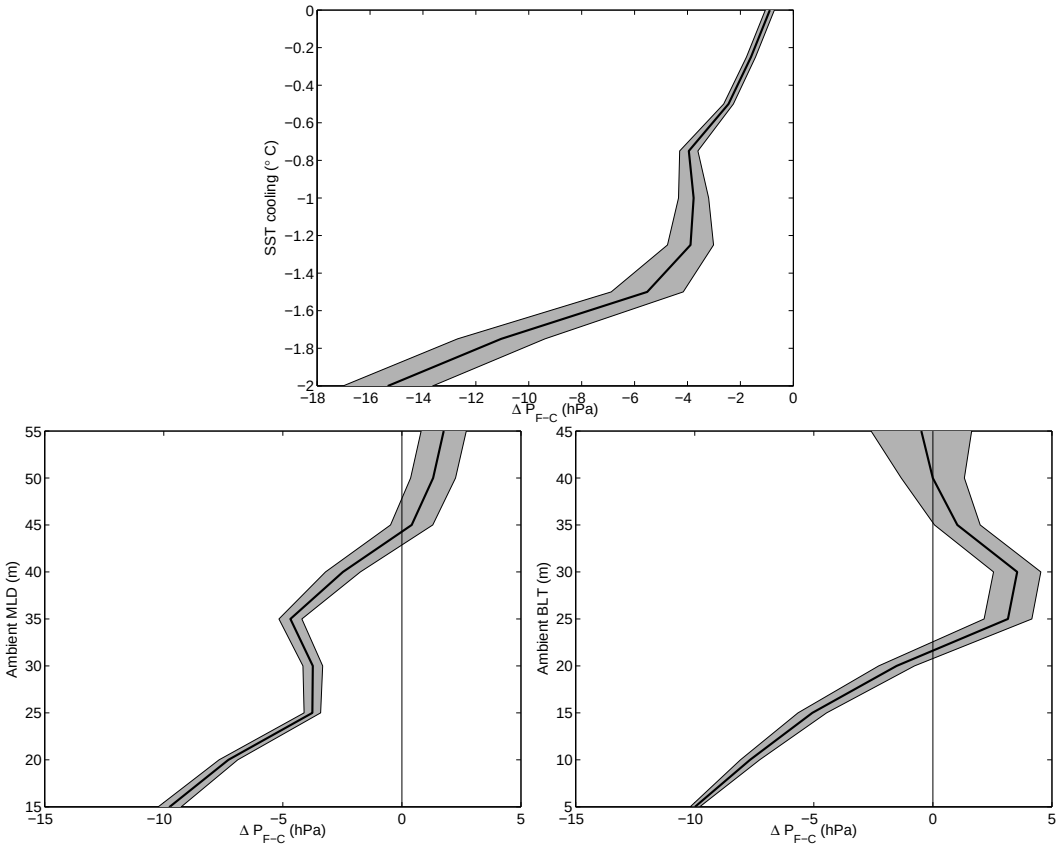

Figure 5.15 - TC central pressure difference (hPa) between forced and coupled models as a function of (a) SST cooling; (b) ambient MLD; and (c) ambient BLT. The standard error of the mean (at 90% confidence) is presented in shades of grey.

the mixing length due to extreme winds). The analysis is also consistent with our previous observation that variations of MLD between the Coral Sea and warm pool regions are correlated with the differences in SST cooling and negative feedback effects.

5.7.4 Barrier layers

Balaguru et al. [2012] and Neetu et al. [2012] recently suggested that the salinity barrier layer of tropical oceans may be another key player in the SST cooling process that impacts storm intensity. A barrier layer between the oceanic mixed layer and the underlying thermocline occurs when enough fresh water pours into the ocean from strong tropical precipitation (subduction of salty water from eastern equatorial regions is another contributor). Depending on its thickness, it can insulate the surface from subsurface colder waters. The model and observed summer climatological distribution of barrier layer thickness (BLT) are presented in Figure 5.16. It shows that a barrier layer is only present in the SPCZ and warm pool regions but large thickness values are characteristic of the warm pool. The fact that thick barrier layers tend to be also located in areas of deep mixed layers weakens arguments based on the correlation between storm intensity and BLT

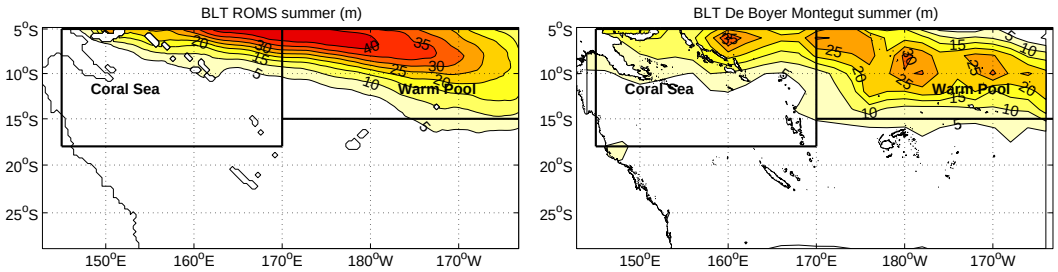

Figure 5.16 - Mean austral summer (January-March) barrier layer thickness (BLT) from (a) the 1979-1998 coupled model, (b) observational climatology from Montegut et al. [2004] (http://www.ifremer.fr/cerweb/deboyer/mld). The BLT is computed as the thickness of the layer between the mixed layer depth and the depth of the isotherm SST-0.2°C.

[as in Balaguru et al., 2012]. Nevertheless, Figure 5.15c indicates that a critical thickness exists (around 25 m) beyond which storm-induced cooling and feedback are prevented. Below 25 m thickness, storm intensity is sensitive to BLT at a rate of about 5 hPa increase of TC central pressure for every 10 m increase of BLT.

5.7.5 Ocean eddies

The effect of mesoscale eddies in the feedback mechanism of storm intensity has been mostly studied in the Gulf of Mexico [*e.g.*, Bao et al., 2000] or in the North Pacific [Wu et al., 2007; Zheng et al., 2010] where loop currents frequently release large eddies, sometimes along cyclone tracks. As yet, no reported attempt has been made to provide global statistical estimations of ocean eddies effect on storm intensity. Our experimental design allows us to provide basin-scale estimates.

We tracked all ocean mesoscale eddies of the computational domain using the tracker methodology described in Chaigneau et al. [2008, 2009] and constructed composite plots of coupling effect on TCs crossing cyclonic or anticyclonic eddies. The cyclonic (anticyclonic) eddy detection algorithm consists in locating eddy centers associated with local minima (maxima) of sea level anomaly (SLA) in a moving window of 6 x 6 grid points. Then, for each possible eddy center, the algorithm searches for the outermost closed SLA contour, which corresponds to the eddy edge. For each identified eddy, the apparent eddy radius corresponds to that of an equivalent circular vortex of the same area.

Mesoscale eddies in the southwest Pacific are associated with zonal jets driven by particularly numerous islands and ridges of this part of the world [Couvelard et al., 2008]. The eddy field can be separated in two large families located to the north and south of New Caledonia (Fig. 5.17). In the North, eddies are mostly confined to the Coral Sea and are generated by barotropic instability of the North Caledonia and Vanuatu jets. In subtropical latitudes between 20-30°S, there is a zonal band of numerous strong eddies associated with baroclinic instability of the South Pacific Subtropical Countercurrent Qiu et al. [2008]. A number of eddy generation are also associated with western boundary currents (East Australian

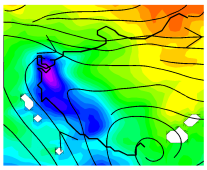

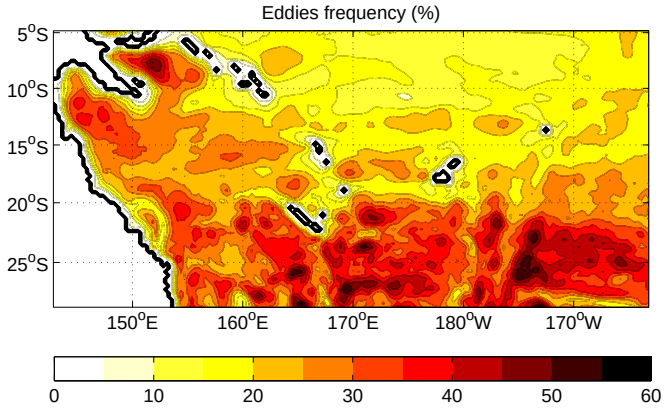

Figure 5.17 - Eddy frequency as the percentage of eddy presence in the 1979-1998 coupled model.

and North Queensland currents) closer to Australia. On the contrary, the warm pool region is a desert in terms of mesoscale eddies.

Figure 5.18 presents a cross-track composite (Sec. 5.2.6) of SST cooling and associated central pressure difference between forced and coupled runs for TCs positioned over pre-existing cyclonic or anticyclonic ocean eddies. The same analysis is given for TCs positioned over a neutral area (no underlying eddies, which represents the most frequent condition: 80 % of the time) and for all TCs combined. TCs cross over cyclonic eddies more frequently (11 % of the time) than anticyclonic eddies (9 % of the time) because there are simply more cyclonic eddies. Anticyclonic eddies are characterized by a deepened mixed layer and clearly appear to limit SST cooling compared to the general case by providing an insulating effect against storm-induced upwelling and mixing. Cyclonic eddies on the other hand are characterized by shallower mixed layer and tend to promote particularly strong cooling.

An interesting feature is that cooling over cyclonic eddies is less asymmetric, due to a larger part played by upwelling compared to mixing, as indicated by the surface heat budget analysis presented in Table 5.4 (see Jullien et al., 2012 for the exact definition of all terms). TC-induced upwelling is a deep process that occurs under the cyclone eye and produces vertical advection towards the mixed layer base [Jullien et al., 2012]. TC-induced mixing is a relay process of upwelling as it brings subsurface water up to the surface, but it is asymmetric with respect to the cyclone eye. In the case of anticyclonic eddies, the asymmetric effect is increased because the relay is rendered more difficult by mixed layer deepening (upwelling is limited to deeper levels). On the contrary for cyclonic eddies, the relay is almost as efficient in the cyclone eye as on the strong cyclone side because upwelling reaches shallower levels. Overall, eddies slightly increase storm-induced cooling compared to the neutral case (albeit not significantly so), because cyclonic eddies are slightly more frequent than anticyclonic eddies and also because the cooling tendency of cyclonic eddies is larger than its limitation by anticyclonic eddies.

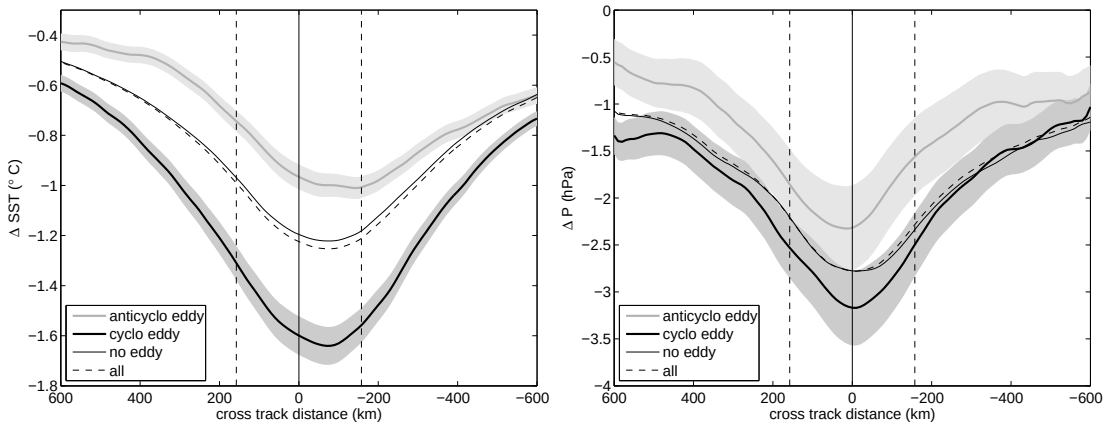

Figure 5.18 - Cross track composites of (a) SST cooling (°C) in the coupled model and (b) TC central pressure differences (hPa) between forced and coupled models. The results are given for all TCs (dashed line); TCs located over a cyclonic eddy (bold black solid line); TCs located over an anticyclonic eddy (bold gray solid line); TCs located over a neutral ocean (neither a cyclonic nor anticyclonic eddy; thin black solid line). The standard error of the mean (at 90% confidence) is presented in shades of grey.

Table 5.4 - Ocean mixed layer heat budget (integrated from day -10 to the time of maximum cooling) under TCs as they cross over cyclonic and anticyclonic eddies (°C). The budget terms are: the time rate of change (Rate); vertical mixing (Vmix); vertical advection (Vadv); horizontal advection (Hadv); surface forcing (Forc); Horizontal mixing (Hmix) and entrainment (Entr).

	Rate	Vmix	Vadv	Hadv	Forc	Hmix	Entr
Cyclonic eddies	-1.55	-0.23	-1.03	0.18	-0.72	-0.02	0.26
Anticyclonic eddies	-0.85	-0.06	-0.45	0.11	-0.69	-0.01	0.26

The eddy feedback effect on storm intensity is consistent with the cooling patterns, showing a significant decrease (increase) of central pressure for TCs crossing over anticyclonic (cyclonic) eddies. The amplitude of central pressure anomalies is relatively small (about 2hPa/°C). Recall that the largest sensitivity of storm intensity to SST cooling is highly nonlinear showing significant values only for strong coolings associated with strong TCs (15hPa/°C). Here, the sensitivity to eddy effects is given for all combined TCs, which are considerably more numerous in the weak categories. The sensitivity for stronger TCs is thus expected to be much larger but the signal to noise ratio decreases for extreme events.

5.8 TC INTENSIFICATION

Finally, we investigate the evolution of TCs along their track, *i.e.*, their life cycle of initialization, intensification, maturity and decay phases. For simplicity, we

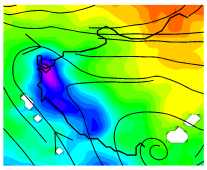

only consider strong TCs ($> 27\ m.s^{-1}$), and two regions of interest: the Coral Sea region in the west characterized by shallow oceanic mixed layer and the warm pool region in the northeast with warmer SST and deeper oceanic mixed layer. The life cycle of moderate cyclones is similar in the coupled and forced simulations and in both regions. However for strong TCs, there is a clear regional modulation. Note that coupled TCs have a shorter lifetime in average (strong TCs) than forced ones: 7.8 days instead of 8.8 days compared with 8.2 days in the observations (see Table 5.2). In Figure 5.19, the lifetime of forced and coupled TC composites are re-scaled according to their respective mean values.

The composite cyclone evolution along its track (Sec. 5.2.6) is first illustrated by its central pressure in Figure 5.19a. In the Coral Sea, the forced composited cyclone can reach higher intensity, while in the warm pool region, forced and coupled models experience similar TC evolution.

SST evolution (Fig. 5.19b) shows continuous cooling along the composite cyclone tracks, illustrating the general southward storm migration where ambient water becomes increasingly cold. In the Coral Sea, cooling by strong TCs adds up to the change of ambient SST, limiting the intensification process in the coupled model. In the warm pool region, coupled cyclogenesis occurs on warmer waters and the along-track cooling rate is weaker during the intensification phase than in the Coral Sea. These two features lead to a greater supply of latent heat to the intensifying cyclone (Fig. 5.19c) and thus act as a natural selection process for maintaining the presence of strong coupled cyclones. Note that the latent heat supply rapidly falls down because of TC migration to colder waters and TC-induced SST cooling (Fig. 5.19b-c). These results are indicative of the factors that control the rate of intensification. Clearly, even in the forced simulation, the general evolution of TC intensity from intensification to mature and decaying phases is uncorrelated with SST and surface heat flux, indicating that tropical cyclones are not adjusted to the inner core surface fluxes, contrarily to the assumption made in thermodynamic paradigms of TC intensification.

This result is consistent with the idealized experiment presented by Montgomery et al. [2009]. Using both mesoscale and cloud-scale atmospheric models, the sensitivity of vortex intensification is investigated by capping the wind speed effect on latent and sensible heat fluxes in the bulk aerodynamic formulae (*i.e.*, surface fluxes are unaffected by wind speed past a certain threshold). In this case, the WISHE instability mechanisms involving mutual feedback between surface fluxes and tangential velocity in the core region is shut down. Yet, final storm intensity is only weakly modified and the characteristics of vortex evolution are otherwise unaffected. Smith et al. [2009] in a companion paper show that vortex spin-up is largely controlled by frictional convergence that has the dual role of moistening the core region (providing latent heat to the warm core aloft) and increasing tangential winds by conserving absolute angular momentum (the dynamical role of the boundary layer). They conclude that surface fluxes affect the final storm intensity but are unessential to the instability mechanism. In our case

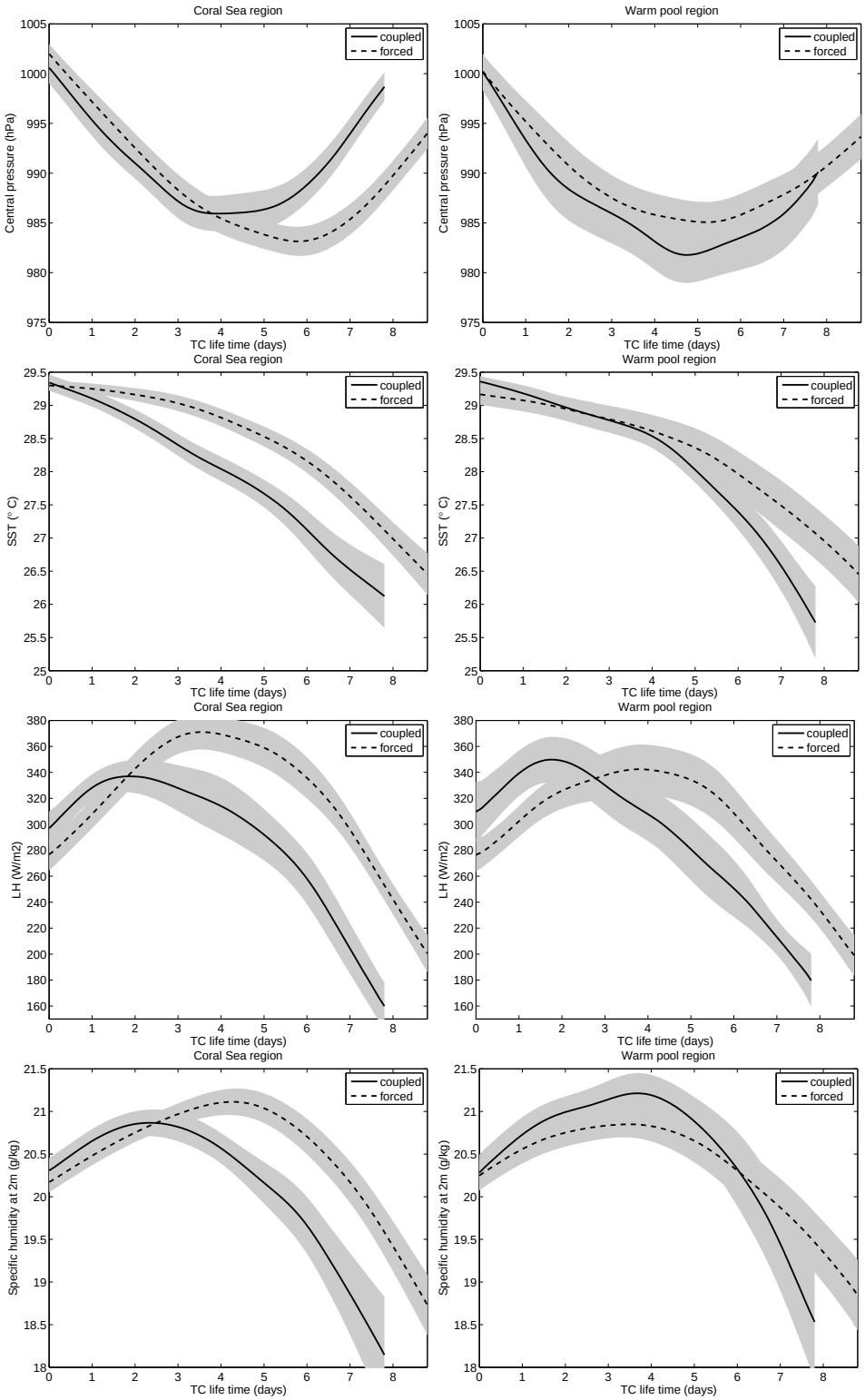

Figure 5.19 - TC life cycle composite constructed from 400-km cross-track averages of TC characteristics in the forced and coupled models. Only strong TCs with wind speed larger than 27 m/s are considered. (a-b) TC central pressure (hPa); (c-d) SST (°C); (e-f) latent heat flux ($W.m^{-2}$); (g-h) specific humidity at 2 meters ($g.kg^{-1}$). The results are for the Coral Sea region on the left and warm pool region on the right. Dashed (solid) curves are for the forced (coupled) model. The standard error of the mean (at 90% confidence) is presented in shades of grey.

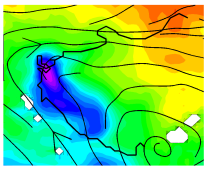

also, the along-track decrease of ambient SST and storm-induced cooling reduce the final storm intensity but poorly affect its evolution pattern. On the contrary, both inner-core surface humidity (Fig. 5.19d) and humidity convergence (not shown) are correlated with storm intensity.

Following Wada [2009], we computed the time accumulation of surface heat fluxes (Fig. 5.20), a measure of the accumulated upper-ocean heat content transported in the eyewall and released in the adiabatic heating process. It shows a much better relation with the timing of coupling effect. The cut-off point where the coupled model accumulated heat flux is lower than that of the forced model corresponds to a change in storm intensity between the two simulations. In the Coral Sea, this point is between day 2 and 3 and nearly coincides with the moment when intensification shows the effect of coupling; in the warm pool, it lies in the decaying phase at day 6. In all cases, coupled cyclones decay faster than forced ones (explaining the mean difference in life duration) but the secondary circulation appears as a mediator of storm reaction to changes in surface fluxes.

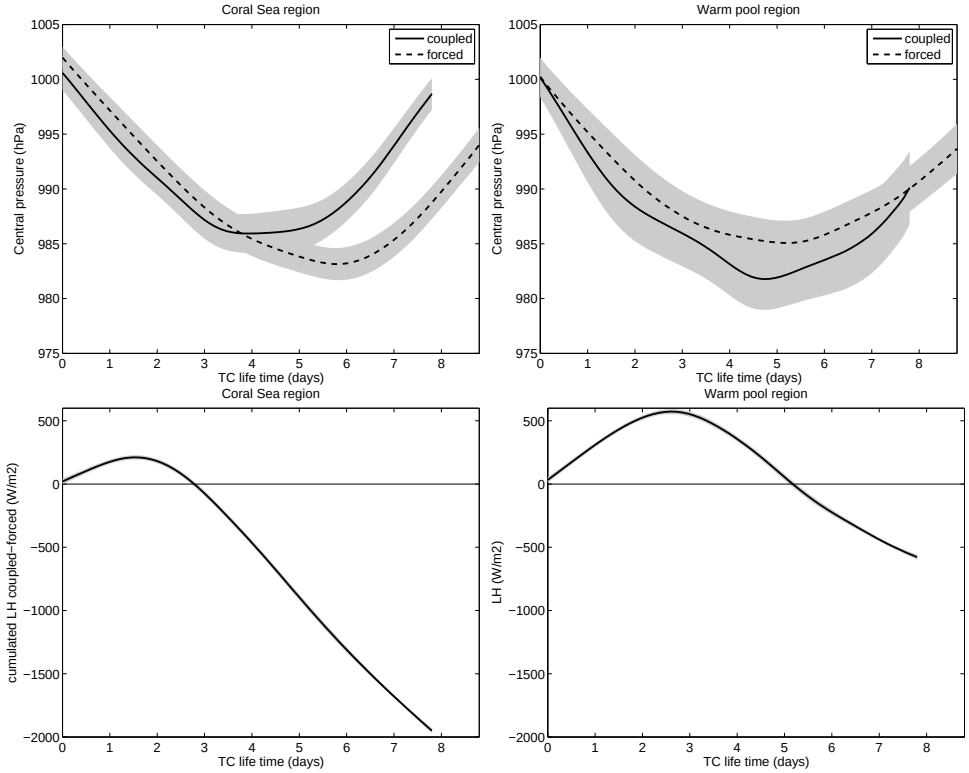

Figure 5.20 - Same as Fig. 5.19 for (a-b) TC central pressure (hPa); (c-d) cumulated latent heat flux difference ($W.m^{-2}$) between coupled and forced models.

All that supports the notion that the evaporation-wind feedback process is not essential to intensification, implying delayed SST effect on storm intensity. It would explain that realistic model applications tend to produce lower SST feedback effects than predicted from thermodynamic and gradient-wind balance assumptions alone.

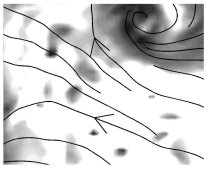

5.9 Summary and Discussion

In this study, we present and analyze the first long-term, regional coupled simulation of the South Pacific cyclonic activity. The coupled modeling system is state-of-the-art and applied for mesoscale resolution (35 km grid mesh size). 20 years of simulation and about 160 tropical cyclones provide some statistical reliability that is generally missing in event studies. The modeled cyclonic activity is characterized by its environmental conditions, by the structure of TCs, their spatial and intensity distributions, and air-sea exchanges that control their intensity.

We first checked the model skills in reproducing the observed regional atmospheric and oceanic climate, in particular the SPCZ position generally poorly represented in global models. The model was also shown to produce realistic tropical cyclones and magnitude of storm-induced surface cooling. This validation stage allowed us to proceed with the statistical analysis of TC-ocean interaction in the South Pacific.

The environmental conditions of cyclogenesis evaluated with the CYGP genesis index gives a stronger probability of cyclogenesis in the Coral Sea region. Cyclogenesis distribution in the forced simulation closely follows the CYGP pattern but the coupled model solution is closer to the observed distribution where cyclogenesis spreads further eastward in the warm pool area. This is the first reported evidence of air-sea coupling impact on cyclogenesis spatial distribution. It indicates that cyclogenesis indices must account for subsurface ocean features (not only SST) for proper prediction. The intensity distribution and average number of TCs is also better represented in the coupled than in the forced model arguing again for a significant role played by oceanic feedback on cyclonic activity. This feedback effect increases with storm intensity.

The composite study of coupling mechanisms revealed that storm-induced SST cooling leads to a mean decrease in air-sea fluxes of 70 $W.m^{-2}$ for the latent heat flux, 10 $W.m^{-2}$ for the sensible heat flux and 5 $W.m^{-2}$ for long-wave upward radiation. Ocean dynamics at multiple scales are able to modulate these numbers by their control of surface stratification. The shallow mixed layer depth of the Coral Sea associated with the regional anticyclonic gyre circulation is favorable to strong SST cooling and negative feedback effect on storm intensity. On the other hand, the thickness of salinity barrier layers in the warm pool is a limiting factor of storm-induced SST cooling and thus promote TC intensification. Even mesoscale ocean eddies that are mostly generated in the Coral Sea (as opposed to the warm pool) may have a residual negative effect that would accentuate the regional differences between the two regions. These environmental factors all contribute to spread the cyclogenesis distribution eastward by limiting the recruitment of TCs in the Coral Sea (from the large pool of mesoscale vortices) and to restrict intensification of the strongest storms.

Our results quantify the sensitivity of storm intensity to SST cooling. It is

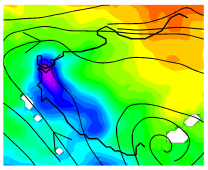

highly nonlinear, *i.e.*, weak for weak SST cooling and about 15 hPa/°C for strong cooling above 1°C. These numbers are in the range of previous realistic case studies [Table 5.1; Bender et al., 1993; Bender and Ginis, 2000], but much lower than theoretical estimations [Table 5.1; Holland, 1997; Schade, 2000]. The difference may be understood through the paradigms proposed for TC intensification. The underlying paradigm behind theoretical estimations of SST feedback effects is the evaporation-wind feedback process (WISHE; Emanuel, 1986). WISHE requires that storm intensity be directly restricted by the magnitude of surface heat and moisture fluxes in the core region [Craig and Gray, 1996]. The axisymmetric model of Emanuel [1986] assumed gradient-wind and hydrostatic balance everywhere, thus precluding unbalanced dynamics such as radial convergence in the lower troposphere and boundary layer (predicted by the Sawyer-Eliassen equation of secondary circulation). Our results contradict this paradigm by showing a lack of correlation between storm intensification and surface fluxes. This is similar to the experiment of vortex evolution with capped fluxes [Montgomery et al., 2009]. The effect of SST is thus not instantaneous but accumulated over time within the inner core of the cyclone. Macro-scale processes, particularly the role of radial advection in the boundary layer and lower free troposphere must be accounted for [Smith et al., 2009].

Radial convergence has a dual role in moistening the core region and increasing its tangential speed through absolute angular momentum conservation (Fig. 5.7f). Surface friction provides both an intense radial flow that fuels the storm engine and a competing dissipation mechanism. Further studies should thus focus more importantly in the parametrization of surface momentum fluxes and boundary layer dynamics (as also discussed in Nolan et al., 2009).

It is generally argued [see Craig and Gray, 1996] that the choice of convection scheme in mesoscale models would determine the time scale of convection and thus the instability mechanisms for storm intensification. In our model, cumulus convection appears more affected by coupling than macro-scale circulation (Fig. 5.21).This is consistent with the work of Wada [2009] using a cloud-resolving model coupled with a slab mixed-layer ocean model. In cloud-resolving models, cumulus convection during the early intensification phase is organized as intense eyewall mesovortices. They play a crucial role in the vertical transfer of heat and moisture before merger and axisymmetrisation result in an annular ring of vorticity. Similarity to our findings, SST feedback in Wada [2009] is essentially effective against mesovortices (represented as sub-grid scale convective processes in our case) but has a poor effect on macro-scale dynamics. The author concludes that coupling effects are different at various stages of intensification Interestingly, it is also the accumulation of upper-ocean heat content, not instantaneous surface fluxes, that affects TC intensity in this coupled cloud-resolving experiment.

In mesoscale models, it is conceivable that convection schemes with faster adjustment leading to more efficient adiabatic heating would increase the response of intensification rate to surface heat fluxes. We tested the Kain-Fritsch scheme (see

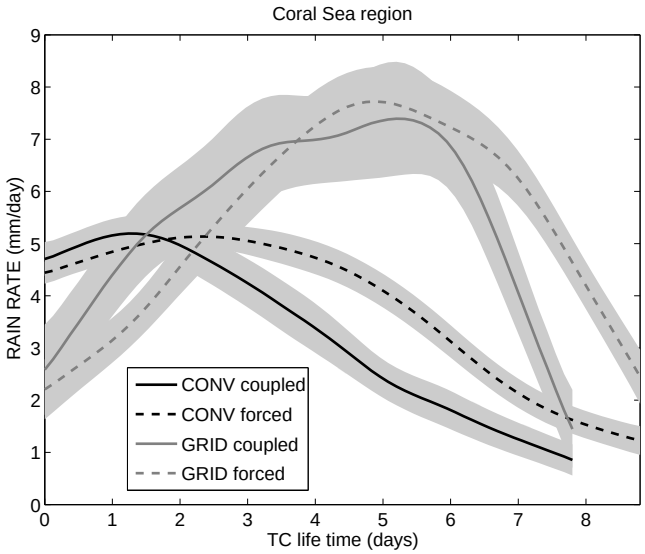

Figure 5.21 - TC life cycle composite for subgrid-scale (CONV) and grid-scale (GRID) precipitations (mm/day) in the coupled and forced models and in the Coral Sea for TCs with wind speed larger than 27 m/s. The standard error of the mean (at 90% confidence) is presented in shades of grey.

Jourdain et al., 2011), which increases the ratio of subgrid- to grid-scale precipitation during TC intensification. We found a general degradation of model results for both the large-scale conditions (SPCZ dynamics) and TC activity (largely overestimated cyclogenesis number). We thus believe that our original modeling setup provides the most realistic results.

Even though our model suggests a lower range of SST feedback effect than predicted by theory, this effect remains significant on the statistics of cyclonic activity. It confirm the suggestions made from idealized model or case studies that the negative feedback appears stronger for regions where intensity potential is larger, MLD is smaller, barrier layers are thiner or absent. Vincent et al. [2012b] propose a Cooling Inhibition index (CI) based on these multiple quantities. It is intended for evaluating the potential coupling impact on TC intensity, genesis and intensification rate. However, beyond the known effect on TC intensity, we show that coupling has also an effect on the yearly cyclogenesis number as more TCs are produced in the forced model. Schade and Emanuel [1999] found similar results from idealized sensitivity experiments. We suggest that among the large pool of mesoscale vortices generated during the cyclonic season in the SPCZ, even a small effect of SST feedback would impact the recruitment of named TCs.

Other characteristics of cyclonic activity appear less affected by SST feedback. The effect on storm tracks suggested by Bender et al. [1993] as a result of alteration of the beta drift (due to weakening of the tangential flow) is not apparent in our results. Specific analysis may be required to extract this information. There is a clear coupling effect, however, on the TC life time of strong events which is shorter in average in the coupled model and closer to observations (Table 5.2). On the

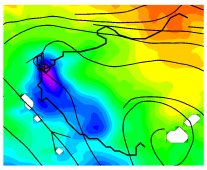

effect of translation speed, as pointed out in Jullien et al. [2012], South Pacific TCs are generally fast moving storms with Froude numbers (ratio of TC translation speed to the first baroclinic mode phase speed of near-inertial oscillations) usually greater than 1 (about 2 in the mean, corresponding to a mean TC translation speed of about 4 m/s). Low Fr numbers are accidental along cyclone tracks and their effect are embedded in the composites. The general effect of storm translation is to reduce SST cooling in the inner-core by about half its maximum value in the outer region. Therefore, the high maximum values of SST cooling (up to 5-6 °C) in TC wakes sometimes observed in satellite images (and reproduced in our model) are spectacular but generally not relevant to the TC-ocean coupling problem.

Finally, we have neglected the role of surface gravity waves. In case studies, age wave factors have shown to exert a sensitivity to storm intensity of order 5 hPa [Doyle, 2002], which is in the lower range of the SST feedback effect on strong cyclones. The representation of the bulk effect of sea spray on the fluxes of heat and moisture is also of particular interest [Bao et al., 2000] but will require higher model resolution to represent extreme wind conditions.

Ackowledgments The simulations of this study were conducted with HPC resources from the Computing Center of Region Midi-Pyrénées (CALMIP, Toulouse, France; grants 2011,2012,2013 - project 1044). We also thanks Alexis Chaigneau for his help on the ocean eddy tracking procedure.

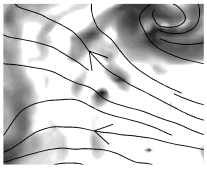

Chapter 6

Conclusions and Perspectives

Contents

6.1 Conclusions 158
6.1.1 Development of a mesoscale resolution regional coupled model 159
6.1.2 Oceanic response to TCs 160
6.1.3 Ocean feedback effect on tropical cyclones 162
6.2 Directions for future work 164
6.2.1 Increasing resolution 164
6.2.2 Improving the air-sea interface 165
6.2.3 Short and long-term variability of cyclonic activity . . . 168
6.2.4 Marine ecosystems and coastal impacts 169

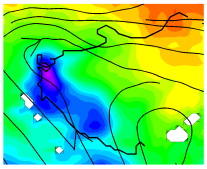

6.1 Conclusions

During the course of my thesis, I studied the relationship between tropical cyclones and the ocean in the South Pacific region. This work provided a statistically robust estimation of the oceanic response to TCs and feedback. The main objectives were to understand the coupled cyclone-scale processes and characterize the robustness and climatic impact of such processes on a great number of events and seasons, filling a gap between case studies and coarse resolution climatic studies.

Much work has been reported on isolated TC events particularly for the North Atlantic and North Pacific. It usually uses high-resolution or idealized models for process-oriented investigation of specific aspects of TC evolution (*e.g.*, extratropical transitions off the U.S. East coast; intensification affected by oceanic eddies released by the Loop Current of the Gulf of Mexico...). However, case studies are not representative of all events even if attention is given to select so-called "representative events". Their structure and effects have a high degree of variability, so that the climatological representation of TCs and their effects may be very different from any small number combination. Our approach based on 20-year long simulations of realistic cyclonic activity (except for the very strong but rare events) offers by contrast some statistically reliability. It also allows the study of interannual variability and climatic residual effects of TC passage. For meaningful analyses, we developed a specific methodology with twin simulations to isolate cyclone effects and feedback. First, twin ocean simulations were conducted with and without extreme TC wind forcing to asses the oceanic response to TCs. Second, twin atmospheric simulations were conducted with and without ocean coupling to study the ocean feedback to TCs. Statistical distributions and composites were then built to describe the processes at play, at least those sufficiently robust to mark the climatological fields.

The setting and analysis of long-term coupled regional simulations is a very demanding task. It requires performant models in their full complexity (including a well-posed coupling procedure), computer power, disk space management, powerful pre- and post-processing tools. It also requires a team with expertise in regional climate dynamics and modeling at multiple scales. The complexity of the task would explain that the present work is the first of its kind. An important help comes from the availability of new generation regional models, which are community models with fast growing capability. They have efficient and accurate kernels composing the dynamic core of the system and constantly evolving sets of parameterizations for various applications. As they are mesoscale and sometimes cloud resolving models, regional models offer clear advantages over more cumbersome and costly global models. There is no doubt that regional climate modeling will have a major role in the future, particularly concerning extreme events, and we hope that our positive experience will contribute to opening the way.

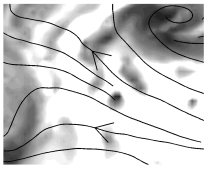

6.1.1 Development of a mesoscale resolution regional coupled model

The first task of this thesis was to develop a regional coupled model for interannual simulations. The coupled system is composed of ROMS and WRF for oceanic and atmospheric models, and a Fortran coupler that computes and exchanges time mean fluxes between the models every 3 hours. High-frequency coupling was needed to avoid synchronization issues between models and maintain consistent oceanic and atmospheric solutions. A sensitivity study on the coupler's iterative scheme to ensure synchronicity of surface fluxes confirmed that our coupling procedure performed satisfactorily. It avoids in particular a numerical instability identified by Lemarie et al. [2013] and associated with loss of synchronicity.

The testing of various atmospheric parameterizations attributed the largest sensitivity of the coupled system to the short-wave incoming radiation, as it dominates the balance of surface fluxes that also drives wind convergence patterns. The surface drag parameterization is also important for its major effect on surface momentum fluxes. We found that the Donelan parameterization, newly implemented in WRF for tropical cyclone studies, failed to accurately represent air-sea exchanges because of its lowering of surface roughness (compared with the Charnock relation) even at moderate wind speeds. Regional wind convergence patterns and associated cyclogenesis location were consequently badly represented. Future studies should rather consider increasing the complexity of the interfacial problem, using a wave-model.

Our study of the convection parametrization is consistent with that of Jourdain et al. [2011] as the Betts-Miller-Janjic scheme confirmed its relevance to long-term mesoscale simulations of tropical dynamics. Nevertheless, we extended the parameter study to the cloud efficiency parameter of the scheme and showed its control of precipitation rates. Another point of concern is the convection scheme effect on cloud fraction. In WRF implementation of BMJ, cloud formation is left to the microphysical parametrization, which relies on grid-scale circulation. Future improvement could be devoted to the parametrization of cloud fraction by the convection scheme (as in the Eta model).

We successfully tested the SST skin model of Zeng and Beljaars [2005] in long-term simulations of a coupled system. It performed according to observations by generally lowering skin temperatures compared with the bulk SST (by 0.5°) and permitted a diurnal cycle of up to 2-3° in the surface ocean. The use of SST skin improved the realism of the surface heat balance, although the overall effect on TC activity did not seem substantial. Finer analyses should be conducted on the matter.

The coupled model with our selection of parameterizations shows good skills for regional climate modeling. In particular, it is successful in representing the SPCZ position, which relies on the delicate balance between surface fluxes,

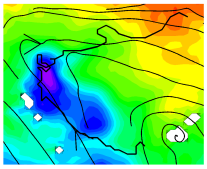

subgrid-scale convection and large-scale atmospheric circulation. The vertical structure in the atmosphere and the ocean is also realistic. The most noticeable bias is a too strong amount of precipitation in the convergence zone that produces excessively fresh water. This bias can be corrected by a more accurate tuning of the cloud efficiency as already mentioned.

As for cyclonic activity, the structure and distribution of events are accurately represented by the coupled model. The seasonal and interannual variability (associated with ENSO) are realistic with a northeast/southwest dipole pattern of cyclonic activity between El Niño and La Niña years. Integrated over the whole region, we found as in Jourdain et al. [2011] that most of the interannual variability is stochastic. The forced variability by environmental conditions is evaluated using the CYGP cyclogenesis index and appears very low as previously shown by Menkes et al. [2012b]. The question raised at this point is the ability of cyclogenesis indices to reproduce the actual environmental forcing of cyclogenesis. In our experiments, the coupled model gives a better account of cyclogenesis location than the forced model even though the latter is in better agreement with CYGP. It suggests that cyclogenesis indices such as CYGP fail to account for oceanic pre-conditions to storm-induced cooling. Some progress can be made in that direction that may also improve the indices' ability to reproduce the interannual variability of TC counts. In any case, we do not expect stochasticity variability to be weak in the South Pacific.

The intensity distribution of cyclones in the model is good for weak and moderate TCs but stronger TCs are missing. This is due to the limited 35-km model resolution that prevents extreme wind speed at the eye-wall scale. However, we show that very strong TCs are rare in the region (less than 1 TC per year) and do not have a significant impact on the statistics of cyclonic activity. On the other hand, coupling effects are stronger and more statistically significant in stronger events, implying that the difference between forced and coupled models can only increase with finer model resolution.

6.1.2 Oceanic response to TCs

The ocean response to TCs is first investigated and provides new results in contradiction with simple theoretical models [Emanuel, 2001; Sriver and Huber, 2007]. We used a 25-year ocean simulation forced by surface winds from the atmospheric simulation of Jourdain et al. [2011]. Storm-induced cooling, frequently observed in TC wakes, presents the classical asymmetry with stronger cooling on the cyclone's *strong side* (left hand side in the Southern Hemisphere). Cooling asymmetry is due in part to asymmetric wind forcing, *i.e.*, the addition of cyclonic winds and translation speed, and also to near-inertial resonance (between winds and oceanic near-inertial currents) that promote oceanic mixing. The degree of asymmetry increases with the translation speed. Below the mixed layer, wind-induced mixing between surface and subsurface layers presents the counterpart warm asymmetry. Under the cyclone eye, strong upwelling is produced by the wind curl, which

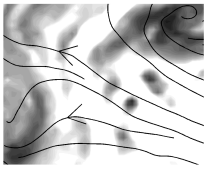

brings cold water from deeper layers. The ratio between the cyclone translation speed and the first baroclinic mode phase speed of near-inertial oscillations (this ratio is the Froude number) reveals that most cyclones along their tacks have supercritical translation speeds. This confirms the ubiquity of near-inertial oscillations that are prone to vertical shear instability. However at some occasions, TCs can be more static (subcritical) and induce very strong upwelling. This is usually where ocean cooling is the strongest, but even in the supercritical regime, upwelling effects remain significant.

Upwelling has been largely underestimated in previous studies. In the surface heat budget, both mixing and upwelling processes appear as important. Our understanding is that mixing is a relay process to upwelling in cooling surface waters (upwelling is maximum at the base of the mixing layer and vanishes above). In the same time, these two processes are competing in the subsurface. Consequently, previous estimates that assumes a subsurface heat gain equivalent to the surface heat loss [called *ocean heat uptake*; Emanuel, 2001; Sriver and Huber, 2007] are wrong. We find that subsurface warming actually represents only a fifth of surface cooling. At large scale, storm-induced Ekman pumping is usually considered to have no effect as it redistributes heat reversibly (with upwelling under the eye and downwelling on the sides). We find that there is however a large-scale reorganization of temperature anomalies owing to the geography of TC distribution. Climatological anomalies are most noticeable in the thermocline between 150-400 m and show cooling around 18°S in the center of TC distribution and warming towards the meridional limits (north of 10°S and south of 24°S). Lateral transports then act in spreading anomalies away from the cyclonic area.

The transport of heat content anomalies due to tropical cyclones has recently been a subject of debate. Our study shows that 60% of the heat accumulated in subsurface by TC activity is actually lost to the atmosphere at seasonal timescale by winter entrainment inducing a re-emergence of warm anomalies to the surface. This reduces again the previous estimate of *ocean heat uptake* by TCs. The remaining heat input under the mixed layer is transported by the flow outside the cyclogenesis region with interannual variability. This meridional heat transport is necessarily much weaker than suggested in previous studies [Emanuel, 2001; Vincent et al., 2012c].

Note that our study so far only considered the cyclonic wind effects on the ocean, omitting the role of storm-induced changes of humidity and air temperature on the turbulent heat fluxes. In the coupled model (described below), we re-visited the ocean response to TCs. Coupling improved further the realism of composited induced cooling, which became very close to the observations. The mixed layer heat budget shows that latent heat fluxes have a significant role in SST cooling especially for weak and moderate storms and away from the center, *i.e.*, in areas where mixing and upwelling are of lesser magnitude. Therefore, storm-induced changes of humidity is a significant contributor to storm-induced SST cooling through its part in turbulent fluxes.

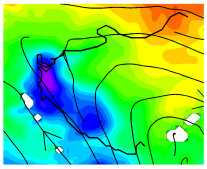

The impact of TCs on the ocean has also been investigated at the global scale in a companion study by Vincent et al. [2012a], to which I contributed as co-author. The methodology was different with an alternative choice of cyclonic forcing (analytical vortices following observed tracks). Nevertheless, the results are very similar to those of the present study highlighting their robustness. In addition, it shows that TC-induced heat flux effect on the ocean is significant but only for weak TCs. This effect becomes of lower importance compared with mixing for moderate to stronger TCs.

The effect of heavy cyclonic rainfall is investigated in another dedicated work which I co-authored [Jourdain et al., 2013]. It uses observations, GLORYS reanalyses and an analytical model hypothesizing that SST cooling is only due to mixing. The stabilizing effect of rainfall is found to have little impact on the average cold wake formation (7% reduction of SST cooling) but it could be important for particular events or regions where stratification is already strong. On the other hand, rain temperature has negligible effect. Finally, the rainfall effect on salt budget is also relatively weak as mixing with saltier waters overwhelms freshwater input. These results were later confirmed by our coupled model that includes all processes (not shown).

6.1.3 Ocean feedback effect on tropical cyclones

The analysis of the ocean response to TCs allowed us next to investigate the feedback effect of the ocean. Theoretical models [Holland, 1997; Schade, 2000] show that TC cold wakes lower the ocean energy source for TC intensification. Our objective was to test the theoretical concepts by analyzing and quantifying the coupled mechanisms at work in the present regional climate. Again, the force of our approach is realism and statistical reliability.

The 20-year long twin experiments in forced and coupled modes present realistic cyclonic activity. Interesting differences appear between the forced and coupled model that bring up novel results. First, the coupled model produces less cyclones than the forced model (one cyclone per year) and is in better agreement with the observations. Second, the spatial cyclogenesis distribution in the coupled model is also closer to observations as it extends further east than the forced model. The latter is more consistent with predictions by the CYGP genesis index, which ignores the pre-conditions to SST-cooling. The intensity distribution of weak and moderate cyclones is also better represented in the coupled model while the forced model overestimates TC counts in these categories. All this suggests that coupled phenomena play an important role in shaping TC distributions. But are coupling effects as strong as predicted by theory ? A clear novel result is the influence of coupling on the regional distribution of cyclogenesis, which was never anticipated (K. Emanuel, personal communication).

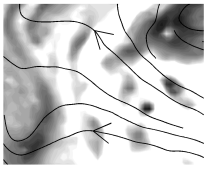

The expected *negative SST feedback* is confirmed in our experiments. SST cooling affects the heat supply to TCs, reducing the latent heat flux by 60 $W.m^{-2}$, sensible heat flux by 10 $W.m^{-2}$ and long-wave upward radiation by 5 $W.m^{-2}$ in average for all modeled TCs. The limitation of heat supply tends to decrease the average TC intensity. However, the coupling effect differs in sub-regions of cyclonic area. SST cooling is in average stronger where the mixed layer depth is shallow, *i.e.*, in the Coral Sea and south of 16°S. Consequently, SST feedback effect on TC intensity is also stronger in these locations. This is of course particularly true for the Coral Sea where many cyclones are produced.

On the contrary in the warm pool, SST feedback effects are very weak. This can be directly linked to the structure and dynamics of the warm pool characterized by a convergence of warm water forming a deep surface layer. Mixing in this region is inefficient as shown in the study of the oceanic response to TCs; it fails to reach cooler subsurface waters. Another characteristics of the warm pool is the presence of a barrier layer. The salinity barrier that forms in the warm pool is due to large rainfall that increases surface buoyancy, thereby acting against the production of shear-flow instabilities. It thus contributes to reducing mixing and thus storm-induced cooling. We found that barrier layers thicker than 25 m are strong enough to prevent any negative SST feedback on TC intensity. Mixed layer depth deeper than 45 m also prevents any significant coupling effect. Both conditions are found in the warm pool region and explain the regional pattern of SST cooling and feedback that we see in our southwest Pacific model.

The role of ocean mesoscale eddies was next investigated. Anticyclonic eddies characterized by deeper mixed layer tended to damp the oceanic response while cyclonic eddies have an opposite effect. An interesting result is the increased symmetry (asymmetry) of SST cooling in cyclonic (anticyclonic) eddies. An analysis of the surface heat budget indicates that the contribution of vertical advection (*i.e.*, upwelling) to cooling is higher (lower) in cyclonic (anticyclonic) eddies. Therefore in anticyclonic eddies, upwelling is confined to deeper levels and the relay process with mixing is altered. As a result, the asymmetric mixing pattern dominates the pattern of SST cooling. In cyclonic eddies, the relay of processes is promoted and cold subsurface waters are easily reached: SST cooling is more symmetric. Because cyclonic eddies are more frequent than anticyclonic eddies in the region, mesoscale activity has in average a positive effect on SST cooling. Therefore, the strong regional pattern of mesoscale activity, with almost no eddy activity in the warm pool, tends to enhance regional differences in coupling effects.

Regional oceanography has thus a large impact on the coupling intensity between tropical cyclones and the ocean surface. The coupling is stronger in the Coral Sea that has shallow mixed layer and numerous eddies but is extremely weak in the warm pool that has deep mixed layer, thick barrier layer and no mesoscale activity. These pre-conditions to SST cooling have a clear impact on the spatial distributions of TCs and could even impact the global TC counts by affecting the recruitment of TCs from the growth of tropical storms.

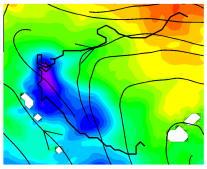

The sensitivity of TC intensity to SST cooling in our model is 5-15 hPa/°C, which is in the range of previous realistic case studies [Bender et al., 1993; Bender and Ginis, 2000]. However, it is much lower than theoretical estimations [Holland, 1997; Schade, 2000]. The difference may be understood through the mechanisms that are proposed to control the rate of intensification, *i.e.*, the CISK and WISHE mechanisms. In the CISK mechanism, the growth rate is limited by frictional convergence driving a storm-scale secondary circulation and is not as strongly restricted by the magnitude of surface heat and moisture fluxes as in the WISHE mechanism [Craig and Gray, 1996]. Our results are thus inconsistent with WISHE (and more consistent with CISK) as they show a lack of correlation along tracks between storm intensity and latent heat flux. Surface friction has a dual role: it acts to dissipate kinetic energy and is an important factor of the decay process of extreme winds, but it also supplies latent heat energy to the system through frictional convergence in the intensification phase. If this process evolves at a lower rate than the others (surface fluxes and vortex adjustment to gradient balance) then it is a major rate-limiting process for intensification. In this case, rapid changes in SST conditions are less effective than assumed in theoretical models to affect storm intensity. In other words, SST feedback has a significant effect but not as large as expected from thermodynamic arguments alone.

Overall, this thesis brings greater understanding of extreme ocean-atmosphere interactions. The study of the oceanic response to TCs and feedback highlighted the role of oceanic and atmospheric dynamics and tends to contradict extreme estimates from oversimplified theoretical models. It shows that the impact of TCs on the climate is probably overestimated in studies that neglect advection processes and winter redistribution. Negative SST feedback is also overestimated because of strong hypotheses made on the scales involved in the TC intensification process. Similarly, the large-scale and mesoscales oceanic structure is often neglected (*e.g.*, in cyclogenesis indices) but they strongly modulated coupling mechanisms. Finally, the use of mesoscale models and long-term simulations with great number of events is essential to separate a robust feature from anecdotal evidence. Yet, our approach presents a few weaknesses, which we try to expose in the next section together with possible directions for future work.

6.2 Directions for future work

6.2.1 Increasing resolution

Gentry and Lackmann [2009] suggested that a resolution of 2 km or less is required to simulate the large radial gradient of vorticity and the physical processes, such as updraft and downdraft motions, that are needed for capturing the eye-wall structure and hence the maximum storm intensity. A resolution of 35-km appears insufficient in this respect and limits the intensification of the strongest cyclones. Even though very strong events are rare, it leaves a level of uncertainty in our

calculations that is difficult to estimate.

The computational cost of regional coupled models is high. Even with supercomputing facility, increasing the resolution over the entire domain would be out of our reach for the present time. Alternatively, we can use WRF's moving nest with automatic vortex tracking for a local and selective increase of resolution. The automatic moving nest uses a mid-level vortex following algorithm to detect TCs and refine the grid around the detected system. The algorithm would probably need adjustment in a long-term simulations were vortices are not as easily detected as in case studies. If it works, we anticipate a better simulation of strong TC categories and possibly a finer representation of coupling processes in all TCs. The expected results would be a greater impact of TCs on the ocean (in the Coral Sea) and greater SST feedback. Again, very strong events are rare and our analysis of SST observations showed that they would not change the climatological impact of TCs on the ocean. It is not even certain that they would extend the range of cooling effect on TCs because this range maybe limited to about 5°C as suggested by the theoretical work of Craig and Gray [1996]. This would be however interesting to confirm.

6.2.2 Improving the air-sea interface

Air-sea exchanges in the model are dependent on the coupling frequency and parameterization of turbulent transfer coefficients. A 3-hour coupling frequency appeared satisfactory, at least with averaged fluxes in the coupler's windowing procedure. This aspect seems important as instantaneous fields presented subsampling issues. However, high-frequency changes of surface fluxes remains a challenge. Further study of the coupling algorithm and parameters would be useful and could be performed with the OASIS coupler (increasing the coupling frequency in the present Fortran coupler would be computationally expensive).

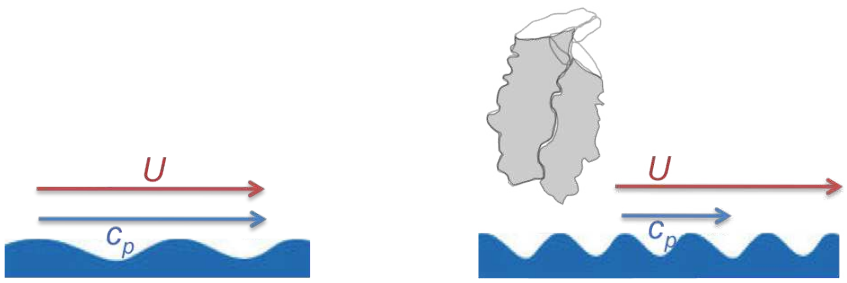

Figure 6.1 - Schematic representation of the wind-wave relationship depending on wave age: (a) mature seas, (b) young seas.

More importantly, a clear improvement should come from better inclusion of wave dynamics in the air-sea interface. It would require to couple a wave model with the atmospheric and oceanic models. Wave dynamics under tropical cyclones are particularly complex, combining young an mature seas, cross swells, sea-spray

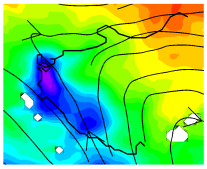

and foam layers. But essentially, the wave model produces a surface wave spectra in response to wind forcing and computes a roughness length associated with wave form drag.
The Charnock formulation of surface drag that was used in our work is expressed as follows:

$$C_D = \left(\frac{\kappa}{ln(z/z_0)} \right)^2 \qquad \text{with} \qquad z_0 = \alpha \frac{u_*^2}{g} \tag{6.1}$$

where z_0 is the surface roughness length, z the altitude, u_* the friction velocity, g the gravity constant, κ the von Karman constant and α the Charnock parameter which equals 0.0185 in our model. α can however be modify to account for wave age, *i.e.*, the ratio of wind to wave phase speed c_P. For instance, an empirical relationship were proposed by Smith et al. [1992]:

$$\alpha = 0.01 \frac{U}{c_P} \tag{6.2}$$

here, α is directly proportional to the wave age. Fig. 6.1 illustrates how the wave age can modify surface roughness: if the wave speed is the same as the wind speed (as for mature seas), the wind feels no drag from the waves; on the contrary, if the wave speed is slower than the wind speed (as for young seas), it exerts a drag on the wind that can be thought of as added surface roughness (in addition to the effect of viscous drag).

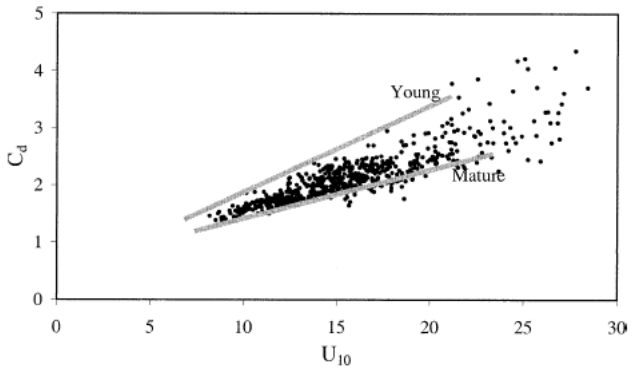

Figure 6.2 - Surface drag as a function of 10-m wind speed for different wave conditions. Figure from Doyle [2002].

Some studies have investigated the effect of waves on observed tropical cyclones using wave-atmosphere coupled models [*e.g.*, Doyle, 2002; Bao et al., 2000]. They reported on the important impact of wave age on the surface drag (Fig. 6.2). Wind-wave coupling in Doyle [2002] produces an increase of surface drag that lowers storm intensity with negative feedback on wave height (Fig. 6.3). On the contrary, Bao et al. [2000] found an increase of storm intensity in the coupled system (Fig. 6.4b) because they assumed that the effect of sea-spray dominates over all others for extreme winds (Fig. 6.4a). Different wave-cyclone coupling parametrizations in these two studies have opposite effects without obvious way of assessing their

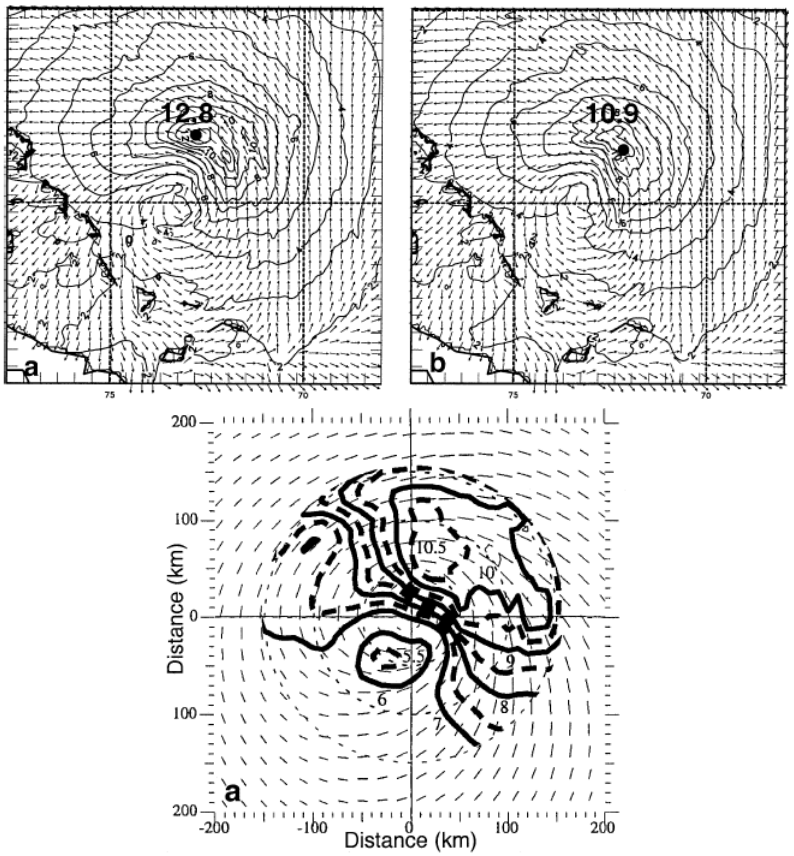

Figure 6.3 - Wave significant height field for the case of (a) cyclone model, (b) cyclone-wave coupled models and (c) aircraft *in situ* measurements. Figure from Doyle [2002].

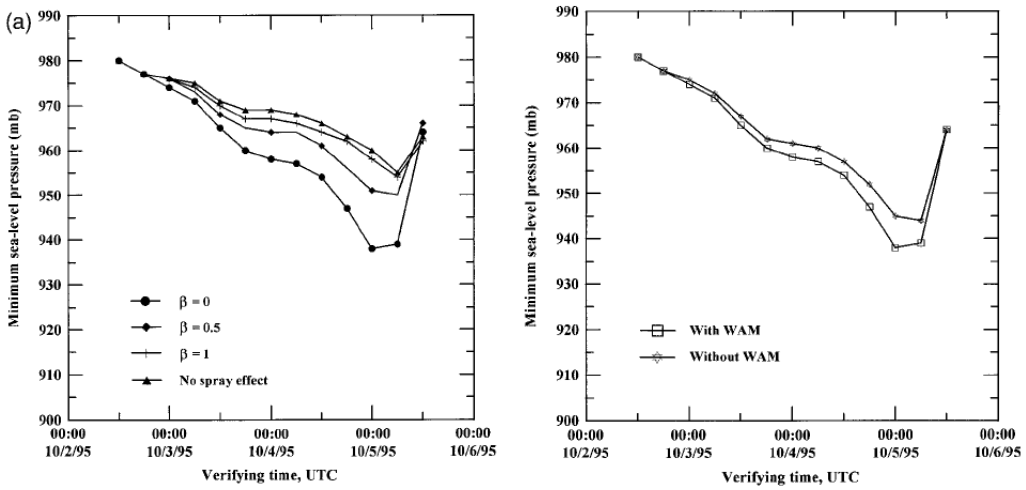

Figure 6.4 - Time series of minimum sea level pressure (in hPa) sampled every 6 h for the numerical experiments (a) on sea-spray sensitivity, (b) with and without coupling with WAM providing a wave-age effect. Figures from Bao et al. [2000].

results. A statistical approach based on a great number of cyclones could provide

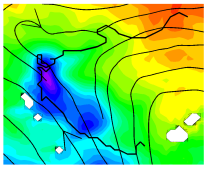

further insight.

6.2.3 Short and long-term variability of cyclonic activity

6.2.3.1 Intra-seasonal MJO variability

During this thesis, we have shown the model ability to represent spatial patterns, seasonal and interannual variability of cyclonic activity. However, we ignored the role of intra-seasonal phenomena like the Madden-Julian Oscillation (MJO). Jourdain et al. [2011] reported that their atmospheric model was not able to properly transmit the MJO signal forced at the lateral boundaries by NCEP-2 data. This advocates for using a parent domain encompassing the whole region of MJO formation, including the Indian Ocean. Studies using reanalyses and observed TC tracks [*e.g.*, Hall et al., 2001] have shown a modulation of cyclonic activity by MJO. They also found a combined effect of MJO and ENSO. Intra-seasonal and interannual variability could be assessed by our coupled model, extending the computational domain over the Indian and Pacific basins or, better, the whole tropical channel. Configurations of this kind are presently developed by our colleagues (thesis project of S. Thibaut; PULSATION project of S. Masson) and will be available for cyclonic studies.

6.2.3.2 Climate change

This thesis work concerned the present climate. The future evolution of TC activity poses another challenge. It was met at many occasions (see Walsh et al., 2012, for South Pacific projections) but without reaching consensus. A common issue is the difficulty of climate models to reproduce environmental conditions for cyclogenesis even in the present climate [Codron and Marchesiello, 2011]. Bador et al. [2012] used an approach that consists of downscaling ensemble-mean climate conditions using WRF in the South Pacific (forced mode). Again, the ensemble-mean present climate did not prove good enough to support realistic cyclogenesis. Therefore, only the climate change anomalies were used added to a present climate reanalysis. This is presently the state of the art methodology for regional climate change studies. It relies on the assumption that climatic changes are more robust (as it present less dispersion among the various climate models) than present climate simulations. Confidence in the results is of course of limited extent. Anyhow, within this assumption, Bador et al. [2012] predict a slight increase of TC intensity but a decrease in TC counts in a warmer climate (Fig. 6.5). A logical continuation of this work could be the use of a coupled model that would account for the changed structure of the regional ocean. However, enhancing the degree of confidence of the results will heavily rely on climate model improvements.

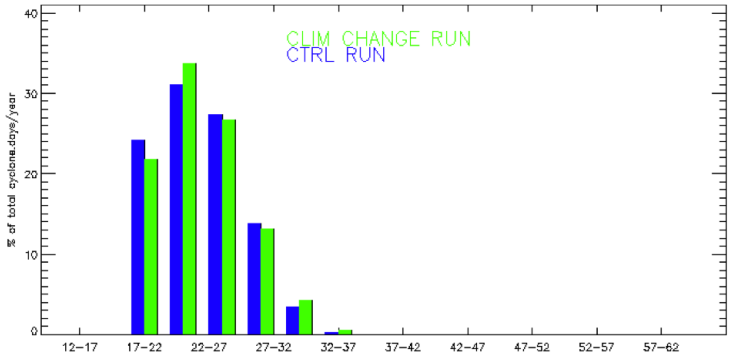

Figure 6.5 - 20-year mean wind-speed (m/s) TC distribution in percent of the total number of cyclone.days/year, for the control run (blue) and climate change simulation (green). Figure from Bador et al. [2012].

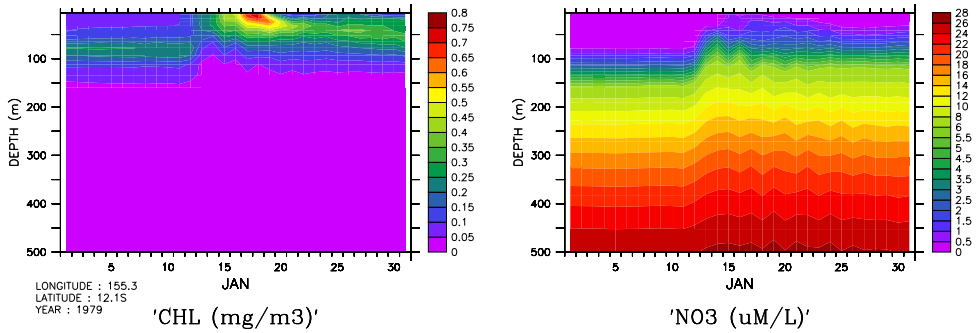

Figure 6.6 - Time-evolution of the vertical (a) chlorophyl concentration ($mg.m^{-3}$) and (b) nitrates concentration ($\mu mol.L^{-1}$) at a model location reached by a TC on January 13.

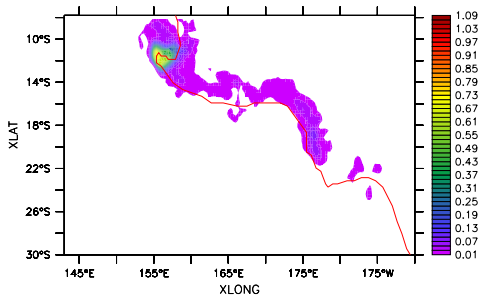

Figure 6.7 - Chlorophyl concentration anomaly ($mg.m^{-3}$) between a simulation with and without cyclone forcing along a cyclone track 4 days after its passage.

6.2.4 Marine ecosystems and coastal impacts

6.2.4.1 Marine ecosystems

The South Pacific is an oligotrophic region with low nutrient supply to the surface layer. The region is thus characterized by a deep maximum of primary production and poor surface waters. During a cyclonic event, we expect from our previous analysis that a large amount of nutrients would be transported to the surface (by

upwelling and mixing) and cause phytoplankton blooms [McPhaden et al., 2009]. A preliminary study of biogeochemical impacts of TCs was conducted during my master's thesis based on the coupling of ROMS with the geochemical model PISCES. Fig. 6.6 confirms the storm effect of providing nutrients to the euphotic layer with the subsequent occurrence of algal blooms (increase in chlorophyl concentration) that feeds the trophic chain. Interestingly, the blooms are not appearing all along the TC track (Fig. 6.7), but particularly where the storm is subcritical, *i.e.*, where upwelling is very strong. Blooms can be observed on satellite images and compared with model results [Menkes et al., 2012a]. The biogeochemical model still needs further tuning to fit the available climatologies; then, a statistical estimate of storm-induced primary production will be possible. A similar study focused on the impact of air-sea CO_2 fluxes was performed by Levy et al. [2012] and resulted in a very small fraction at the global scale. However, the impact of algal blooms on the trophic chain may reveal different results, especially in the South Pacific where fisheries, an important part of the islands' economy, are sensitive to changes of a relatively poor environment.

6.2.4.2 Island vulnerability

Finally, the most important perspective of applications of my work concerns the impact of TCs on the coastal zones of South Pacific islands. the South Pacific is dotted with numerous poor islands which are particularly vulnerable to TC activity. The connection between our coupled model and coastal dynamics requires the addition of wave-currents interaction. This capability is currently implemented and tested in ROMS. It will provide access to both processes of wind and wave-driven coastal sea level changes associated with extreme events, which can be used to draw maps of vulnerability.

Conclusion générale

Au cours de ma thèse, j'ai étudié la relation entre les cyclones tropicaux et l'océan dans la région du Pacifique Sud. Ce travail a fourni une estimation statistiquement fiable de la réponse océanique aux cyclones et de sa rétroaction sur leur intensité et leur distribution spatiale. Les principaux objectifs étaient de comprendre les processus couplés à l'échelle du cyclone et de caractériser leur robustesse et leur impact climatique sur un grand nombre d'événements et de saisons cycloniques.

Notre approche basée sur des simulations longues (20 ans) et réalistes de l'activité cyclonique a également permis d'étudier la variabilité interannuelle et les effets résiduels du passage des cyclones à l'échelle climatique. J'ai pour cela développé une méthodologie spécifique utilisant des simulations jumelles afin d'isoler uniquement l'effet des cyclones sur l'océan et l'effet du couplage sur les cyclones. Tout d'abord, des simulations océaniques jumelles avec et sans forçage par les vents extrêmes des cyclones ont été réalisées permettant ainsi d'évaluer la réponse océanique aux cyclones. Ensuite, des simulations atmosphériques jumelles avec et sans couplage avec l'océan ont permis d'étudier la rétroaction de l'océan sur les cyclones. Des distributions statistiques et des composites ont alors été construits et analysés afin de décrire les processus en jeu, et de déterminer ceux suffisamment robustes pour marquer les champs climatologiques.

La mise en place et l'analyse de simulations régionales couplées longues ne sont pas tâche facile. Cela nécessite l'utilisation de modèles complexes, une procédure de couplage bien posée, de la puissance de calcul, la gestion de très gros volumes d'espace disque et l'utilisation d'outils de pré et post-traitement. Cela exige aussi une expertise en dynamique et modélisation à des échelles climatiques et régionales. C'est certainement pour toutes ces raisons que le travail exposé ici est le premier de la sorte. La disponibilité de nouveaux modèles régionaux, qui sont des modèles communautaires avec une capacité d'évolution de plus en plus rapide et qui possèdent des noyaux performants et de nombreuses paramétrisations disponibles, offre des avantages évidents par rapport aux modèles globaux plus lourds et plus coûteux. Une résolution méso-échelle voire une résolution assez fine pour résoudre la dynamique nuageuse est également atteignable avec de tels modèles. Il ne fait aucun doute que la modélisation régionale du climat aura un rôle important à l'avenir, en particulier en ce qui concerne les événements extrêmes, et nous espérons que notre expérience positive contribuera à ouvrir une voie en ce sens.

Réponse océanique aux cyclones

Tout d'abord, la réponse de l'océan aux cyclones tropicaux a été abordée. Les résultats mettent en évidence le rôle souvent négligé de la dynamique océanique tridimensionnelle, en particulier l'importance de l'upwelling induit par le passage du cyclone modérant ainsi les estimations extrêmes données par les modèles théoriques simplifiés. Le bilan de chaleur océanique de surface est dominé par

le mélange qui ramène en surface des eaux froides remontées par l'upwelling sous la couche mélangée. En sub-surface, ces deux processus sont au contraire en concurrence. Par conséquent, les estimations antérieures négligeant le processus d'upwelling surestiment la quantité de chaleur absorbée par l'océan. Par ailleurs, 60 % de cette chaleur est reperdue vers l'atmosphère en hiver lorsque la couche mélangée s'approfondit et ramène les anomalies chaudes en surface. Le pompage d'Ekman produit par les vents cycloniques engendre également une réorganisation à grande échelle des anomalies de température du fait de la distribution géographique des cyclones. Des anomalies de chaleur climatologiques sont alors visibles dans la thermocline entre 150 m et 400 m et sont transportées à l'extérieur de la région de cyclogenèse avec une variabilité interannuelle.

Rétroaction de l'océan sur les cyclones

La rétroaction de cette réponse océanique sur les cyclones est ensuite étudiée en comparant des expériences forcée et couplée. Celles-ci ne diffèrent que par le champ de température de surface de la mer qui ne comporte pas de sillage froid dû aux cyclones dans la configuration forcée. L'activité cyclonique est simulée de manière réaliste, le modèle couplé étant plus proche des observations quelles que soient les estimations statistiques considérées. Le modèle forcé surestime le nombre de cyclones, particulièrement dans la mer de Corail. La distribution en intensité des cyclones est significativement affectée par le couplage. Cependant, la rétroaction du sillage froid sur l'intensité des cyclones est moins importante que celle prévue par les modèles théoriques basés sur des arguments thermodynamiques. Nos analyses ne sont pas en accord avec un contrôle thermodynamique direct de l'intensification du cyclone par les flux d'humidité de surface mais penchent plutôt en faveur d'un contrôle dynamique de l'intensification à l'échelle du cyclone. De plus, l'océanographie régionale a un impact important sur les interactions air-mer. Les structures océaniques de grande et de moyenne échelle modulent fortement les mécanismes de refroidissement. Le couplage est plus important dans la mer de Corail où la couche de mélange est peu profonde et où de nombreux tourbillons sont présents alors qu'il est particulièrement faible dans la warm pool où la couche de mélange est profonde, où des couches barrière de sel épaisses peuvent se former et où l'activité méso-échelle est absente. Toutes ces conditions modulent le refroidissement et ont un impact évident sur les distributions spatiales de cyclones. Comme ces conditions affectent le recrutement des cyclones dès leur stade de croissance, elles pourraient même avoir un impact sur le nombre de cyclones global.

Bibliography

Adler R., Kummerow C., Bolvin D., Curtis S., and Kidd C. Status of trmm monthly estimates of tropical precipitation. *Meteorological Monographs*, 29(51):223–223, 2003.

Adler R. F., Huffman G. J., Bolvin D. T., Curtis S., and Nelkin E. J. Tropical rainfall distributions determined using trmm combined with other satellite and rain gauge information. *Journal of Applied Meteorology*, 39(12):2007–2023, 2000.

Andersson E., Bauer P., Beljaars A., Chevallier F., Holm E., Janiskova M., Kallberg P., Kelly G., Lopez P., McNally A., AP, Moreau E., Simmons A., Thépaut J., and Tompkins A. Assimilation and modeling of the atmospheric hydrological cycle in the ecmwf forecasting system. *Bull. Amer. Meteor. Soc.*, 86(387–402), 2005.

Bador M., Menkes C., Lengaigne M., and Lefevre J. Impact of climate change on the spcz and tropical cyclone activity. Master's thesis, University of Toulouse, 2012.

Baik J. J., Demaria M., and Raman S. Tropical cyclone simulations with the betts convective adjustment scheme .1. model description and control simulation. *Monthly Weather Review*, 118(3):513–528, 1990.

Balaguru K., Chang P., Saravanan R., Leung L. R., Xu Z., Li M., and Hsieh J.-S. Ocean barrier layers' effect on tropical cyclone intensification. *Proceedings of the National Academy of Sciences of the United States of America*, 109(36):14343–14347, 2012.

Bao J. W., Wilczak J. M., Choi J. K., and Kantha L. H. Numerical simulations of air-sea interaction under high wind conditions using a coupled model: A study of hurricane development. *Monthly Weather Review*, 128(7):2190–2210, 2000.

Barnier B., Madec G., Penduff T., Molines J.-M., Treguier A.-M., Le Sommer J., Beckmann A., Biastoch A., Boening C., Dengg J., Derval C., Durand E., Gulev S., Remy E., Talandier C., Theetten S., Maltrud M., McClean J., and De Cuevas B. Impact of partial steps and momentum advection schemes in a global ocean circulation model at eddy-permitting resolution. *Ocean Dynamics*, 56(5-6):543–567, 2006.

Bender M. A. and Ginis I. Real-case simulations of hurricane-ocean interaction using a high-resolution coupled model: Effects on hurricane intensity. *Monthly Weather Review*, 128(4):917–946, 2000.

Bender M. A., Ginis I., and Kurihara Y. Numerical simulations of tropical cyclone-ocean interaction with a high-resolution coupled model. *Journal of Geophysical Research-Atmospheres*, 98(D12):23245–23263, 1993.

Bengtsson L., Botzet M., and Esch M. Hurricane-type vortices in a general circulation model. *Tellus A*, 47(2):175–196, 1995.

Black P. G., D'Asaro E. A., Drennan W. M., French J. R., Niiler P. P., Sanford T. B., Terrill E. J., Walsh E. J., and Zhang J. A. Air-sea exchange in hurricanes - synthesis of observations from the coupled boundary layer air-sea transfer experiment. *Bulletin of the American Meteorological Society*, 88 (3):357–+, 2007.

Boccaletti G., Ferrari R., and Fox-Kemper B. Mixed layer instabilities and restratification. *Journal of Physical Oceanography*, 37 (9):2228–2250, 2007.

Bretherton C. S. and Park S. A new moist turbulence parameterization in the community atmosphere model. *Journal of Climate*, 22(12):3422–3448, 2009.

Brown J., Moise A., and Colman R. The south pacific convergence zone in cmip5 simulations of historical and future climate. *Climate Dynamics*, accepted, 2013.

Bryan F. O., Kauffman B. G., Large W. G., and Gent P. R. *The NCAR CSM flux coupler*. NCAR, 1998.

Caballero R. Hadley cell bias in climate models linked to extratropical eddy stress. *Geophysical Research Letters*, 35(L18709), 2008.

Camargo S. J., Barnston A. G., and Zebiak S. E. A statistical assessment of tropical cyclone activity in atmospheric general circulation models. *Tellus A*, 57(4):589–604, 2005.

Camargo S. J., Emanuel K. A., and Sobel A. H. Use of a genesis potential index to diagnose enso effects on tropical cyclone genesis. *Journal of Climate*, 20:4819–4834, 2007.

Camargo S. J., Wheeler M. C., and Sobel A. H. Diagnosis of the mjo modulation of tropical cyclogenesis using an empirical index. *Journal of the Atmospheric Sciences*, 66 (10):3061–3074, 2009.

Chaigneau A., Gizolme A., and Grados C. Mesoscale eddies off peru in altimeter records: Identification algorithms and eddy spatio-temporal patterns. *Progress in Oceanography*, 79(2-4):106–119, 2008.

Chaigneau A., Eldin G., and Dewitte B. Eddy activity in the four major upwrelling systems from satellite altimetry (1992-2007). *Progress in Oceanography*, 83(1-4): 117–123, 2009.

Chand S. S. and Walsh K. J. E. Tropical cyclone activity in the fiji region: Spatial patterns and relationship to large-scale circulation. *Journal of Climate*, 22(14):3877–3893, 2009.

Chand S. S., L. McBride J., Tory K. J., Wheeler M. C., and Walsh K. J. Impact of different enso regimes on southwest pacific tropical cyclones. *Journal of Climate*, 26(2):600–608, 2013.

Chang S. W. and Anthes R. A. Numerical simulations of oceans non-linear, baroclinic response to translating hurricanes. *Journal of Physical Oceanography*, 8(3):468–480, 1978.

Chang S. W. and Anthes R. A. Mutual response of the tropical cyclone and the ocean. *Journal of Physical Oceanography*, 9 (1):128–135, 1979.

Charney J. G. and Eliassen A. On the growth of the hurricane depression. *Journal of the Atmospheric Sciences*, 21(1):68–75, 1964.

Charnock M. Wind stress on a water surface. *Quarterly Journal of the Royal Meteorological Society*, 81:639–640, 1955.

Chauvin F., Royer J. F., and Deque M. Response of hurricane-type vortices to global warming as simulated by arpege-climat at high resolution. *Climate Dynamics*, 27(4): 377–399, 2006.

Chelton D. B., Schlax M. G., and Samelson R. M. Global observations of nonlinear mesoscale eddies. *Progress in Oceanography*, 91(2):167–216, 2011.

Codron F. and Marchesiello P. La modélisation du climat: reproduction du climat actuel (part v, chap. 13). In Jeandel C. and Mosseri R., editors, *Le climat à découvert. Outils et méthodes en recherche climatique*. CNRS, 2011.

Couvelard X., Marchesiello P., Gourdeau L., and Lefevre J. Barotropic zonal jets induced by islands in the southwest pacific. *Journal of Physical Oceanography*, 38(10): 2185–2204, 2008.

Craig G. C. and Gray S. L. Cisk or wishe as the mechanism for tropical cyclone intensification. *Journal of the Atmospheric Sciences*, 53(23):3528–3540, 1996.

da Silva A., Young A. C., and Levitus S. Atlas of surface marine data 1994, volume 1: Algorithms and procedures. Tech. Rep. 6, U.S. Department of Commerce, NOAA, NESDIS, 1994.

D'Asaro E. A. The ocean boundary layer below hurricane dennis. *Journal of Physical Oceanography*, 33(3):561–579, 2003.

D'Asaro E. A., Sanford T. B., Niiler P. P., and Terrill E. J. Cold wake of hurricane frances. *Geophysical Research Letters*, 34 (15), 2007.

Debreu L., Marchesiello P., Penven P., and Cambon G. Two-way nesting in split-explicit ocean models: Algorithms, implementation and validation. *Ocean Modelling*, 49-50:1–21, 2012.

Dee D., Uppala S., Simmons A., Berrisford P., Poli P., Kobayashi S., Andrae U., Balmaseda M., Balsamo G., Bauer P., et al. The era-interim reanalysis: Configuration and performance of the data assimilation system. *Quarterly Journal of the Royal Meteorological Society*, 137(656):553–597, 2011.

Demaria M. and Kaplan J. Sea-surface temperature and the maximum intensity of atlantic tropical cyclones. *Journal of Climate*, 7(9):1324–1334, 1994.

Diamond H. J., Lorrey A. M., Knapp K. R., and Levinson D. H. Development of an enhanced tropical cyclone tracks database for the southwest pacific from 1840 to 2010. *International Journal of Climatology*, 32(14): 2240–2250, 2012.

Donelan M., Haus B., Reul N., Plant W., Stiassnie M., Graber H., Brown O., and Saltzman E. On the limiting aerodynamic roughness of the ocean in very strong winds. *Geophysical Research Letter*, 31: 4539–4542, 2004.

Doyle J. D. Coupled atmosphere-ocean wave simulations under high wind conditions. *Monthly Weather Review*, 130(12): 3087–3099, 2002.

Dritschel D. G. A general theory for two-dimensional vortex interactions. *Journal of Fluid Mechanics*, 293:269–303, 1995.

Dudhia J. Numerical Study of Convection Observed during the Winter Monsoon Experiment Using a Mesoscale Two-Dimensional Model. *Journal of the Atmospheric Sciences*, 46(20):3077–3107, 1989.

Emanuel K. Contribution of tropical cyclones to meridional heat transport by the oceans. *Journal of Geophysical Research-Atmospheres*, 106(D14):14771–14781, 2001.

Emanuel K. A. An air sea interaction theory for tropical cyclones .1. steady-state maintenance. *Journal of the Atmospheric Sciences*, 43(6):585–604, 1986.

Emanuel K. A. The maximum intensity of hurricanes. *Journal of the Atmospheric Sciences*, 45(7):1143–1155, 1988.

Emanuel K. A. Sensitivity of tropical cyclones to surface exchange coefficients and a revised steady-state model incorporating

eye dynamics. *Journal of the Atmospheric Sciences*, 52(22):3969–3976, 1995.

Emanuel K. A. Thermodynamic control of hurricane intensity. *Nature*, 401(6754): 665–669, 1999.

Emanuel K. A., David Neelin J., and Bretherton C. S. On large-scale circulations in convecting atmospheres. *Quarterly Journal of the Royal Meteorological Society*, 120(519):1111–1143, 1994.

Errico R. M. Spectra Computed from a Limited Area Grid. *Monthly Weather Review*, 113:1554–1562, 1985.

Evans J., Ekstrom M., and Ji F. Evaluating the performance of a wrf physics ensemble over south-east australia. *Climate Dynamics*, 39:1241–1258, 2012.

Evans J. L. and Allan R. J. El niño/southern oscillation modification to the structure of the monsoon and tropical cyclone activity in the australasian region. *International Journal of Climatology*, 12(6):611–623, 1992.

Fairall C., Bradley E. F., Hare J., Grachev A., and Edson J. Bulk parameterization of air-sea fluxes: Updates and verification for the coare algorithm. *Journal of Climate*, 16 (4):571–591, 2003.

Folland C., Renwick J., Salinger M., and Mullan A. Relative influences of the interdecadal pacific oscillation and enso on the south pacific convergence zone. *Geophysical Research Letters*, 29(13):1643, 2002.

Garratt J. Review of drag coefficients over the oceans and continents. *Monthly Weather Review*, 105:915–929, 1977.

Gentry M. S. and Lackmann G. M. Sensitivity of simulated tropical cyclone structure and intensity to horizontal resolution. *Monthly Weather Review*, 138(3):688–704, 2013/09/11 2009.

Gray W. and Emanuel K. *Introduction to tropical meteorology*, chapter 8. Tropical Cyclones. COMET® Website at http://meted.ucar.edu of the University Corporation for Atmospheric Research (UCAR), 2010.

Gray W. M. Global view of the origin of tropical disturbances and storms. *Monthly Weather Review*, 96(10):669–700, 1968.

Gray W. M. Global view of tropical cyclone genesis. *Bulletin of the American Meteorological Society*, 56(2):322–322, 1975.

Gray W. M. The formation of tropical cyclones. *Meteorology and Atmospheric Physics*, 67(1-4):37–69, 1998.

Greatbatch R. J. On the response of the ocean to a moving storm - the non-linear dynamics. *Journal of Physical Oceanography*, 13(3):357–367, 1983.

Grell G. and Devenyi D. A generalized approach to parameterizing convection combining ensemble and data assimilation techniques. *Geophysical Research Letters*, 29 (14):1693, 2002.

Guinn T. A. and Schubert W. H. Hurricane spiral bands. *Journal of Atmospheric Science*, 50:3380–3403, 1993.

Gutzler D. Uncertainties in climatological tropical humidity profiles: some implications for estimating the greenhouse effect. *Journal of Climate*, 6(978-982), 1993.

Hall J. D., Matthews A. J., and Karoly D. J. The modulation of tropical cyclone activity in the australian region by the madden-julian oscillation. *Monthly Weather Review*, 129(12):2970–2982, 2001.

Halliwell J., G. R., Shay L. K., Brewster J. K., and Teague W. J. Evaluation and sensitivity analysis of an ocean model response to hurricane ivan. *Monthly Weather Review*, 139(3):921–945, 2011.

Hill K. A. and Lackmann G. M. Analysis of idealized tropical cyclone simulations using the weather research and forecasting model: Sensitivity to turbulence parameterization and grid spacing. *Monthly Weather Review*, 137(2):745–765, 2009.

Holland G. J. The maximum potential intensity of tropical cyclones. *Journal of the Atmospheric Sciences*, 54(21):2519–2541, 1997.

Holton J. *An Introduction to Dynamic Meteorology, Volume 88, Fourth Edition (International Geophysics)*. Academic Press, 4 edition, 2004. ISBN 0123540151.

Huang P. S., Sanford T. B., and Imberger J. Heat and turbulent kinetic energy budgets for surface layer cooling induced by the passage of hurricane frances (2004). *Journal of Geophysical Research-Oceans*, 114, 2009.

Huffman G. J. Estimates of root-mean-square random error for finite samples of estimated precipitation. *Journal of Applied Meteorology*, 36(9):1191–1201, 1997.

Jacob S. D. and Shay L. K. The role of oceanic mesoscale features on the tropical cyclone-induced mixed layer response: A case study. *Journal of Physical Oceanography*, 33(4):649–676, 2003.

Jacob S. D., Shay L. K., Mariano A. J., and Black P. G. The 3d oceanic mixed layer response to hurricane gilbert. *Journal of Physical Oceanography*, 30(6):1407–1429, 2000.

Jaimes B. and Shay L. K. Mixed layer cooling in mesoscale oceanic eddies during hurricanes katrina and rita. *Monthly Weather Review*, 137(12):4188–4207, 2009.

Jaimes B. and Shay L. K. Near-inertial wave wake of hurricanes katrina and rita over mesoscale oceanic eddies. *Journal of Physical Oceanography*, 40(6):1320–1337, 2010.

Janjić Z. The Step-Mountain Eta Coordinate Model: Further Developments of the Convection, Viscous Sublayer, and Turbulence Closure Schemes. *Monthly Weather Review*, 122(5):927–945, 1994.

Jansen M. F., Ferrari R., and Mooring T. A. Seasonal versus permanent thermocline warming by tropical cyclones. *Geophysical Research Letters*, 37, 2010.

Janssen P. Wave-induced stress and the drag of air-flow over sea waves. *Journal of Physical Oceanography*, 19(6):745–754, 1989.

Jourdain N. C., Marchesiello P., Menkes C. E., Lefevre J., Vincent E. M., Lengaigne M., and Chauvin F. Mesoscale simulation of tropical cyclones in the south pacific: Climatology and interannual variability. *Journal of Climate*, 24(1):3–25, 2011.

Jourdain N. C., Lengaigne M., Vialard J., Madec G., Menkes C. E., Vincent E. M., Jullien S., and Barnier B. Observation-based estimates of surface cooling inhibition by heavy rainfall under tropical cyclones. *Journal of Physical Oceanography*, 43(1):205–221, 2013.

Jullien S., Menkes C. E., Marchesiello P., Jourdain N. C., Lengaigne M., Koch-Larrouy A., Lefevre J., Vincent E. M., and Faure V. Impact of tropical cyclones on the heat budget of the south pacific ocean. *Journal of Physical Oceanography*, 42(11): 1882–1906, 2012.

Kain J. S. The kain-fritsch convective parameterization: An update. *Journal of Applied Meteorology*, 43(1):170–181, 2004.

Kanamitsu M., Ebisuzaki W., Woollen J., Yang S. K., Hnilo J. J., Fiorino M., and Potter G. L. Ncep-doe amip-ii reanalysis (r-2). *Bulletin of the American Meteorological Society*, 83(11):1631–1643, 2002.

Kuleshov Y., Ming F., Qi L., Chouaibou I., Hoareau C., and Roux F. Tropical cyclone genesis in the southern hemisphere and its relationship with the enso. *Annals of Geophysics*, 27:2523–2538, 2009.

Kumar B. P., Vialard J., Lengaigne M., Murty V., and McPhaden M. Tropflux: air-sea fluxes for the global tropical oceans—description and evaluation. *Climate dynamics*, 38(7-8):1521–1543, 2012.

Kunze E. Near-inertial wave-propagation in geostrophic shear. *Journal of Physical Oceanography*, 15(5):544–565, 1985.

Kuo H., Chen G., and C.H. L. Merger of tropical cyclones zeb and alex. *Monthly Weather Review*, 128:2967–2975, 2000.

Large W. G. *Large, W. G., 2006: Surface fluxes for practitioners of global ocean data assimilation. An Integrated View of Oceanography: Ocean Weather Forecasting in the 21st Century*, chapter 9. Springer, 2006.

Large W. G., McWilliams J. C., and Doney S. C. Oceanic vertical mixing - a review and a model with a nonlocal boundary-layer parameterization. *Reviews of Geophysics*, 32 (4):363–403, 1994.

Leipper D. Observed ocean conditions and hurricane hilda. *Journal of Atmospheric Science*, 24:182–196, 1967.

Lemarié F. *Algorithmes de Schwarz et couplage océan-atmosphère*. PhD thesis, Université Joseph-Fourier - Grenoble I, 11 2008.

Lemarie F., Debreu L., Shchepetkin A. F., and McWilliams J. C. On the stability and accuracy of the harmonic and biharmonic isoneutral mixing operators in ocean models. *Ocean Modelling*, 52-53:9–35, 2012.

Lemarie F., Marchesiello P., and Debreu L. Sensitivity of an ocean-atmosphere coupled model to the coupling method : a study of the tropical cyclone erica. *Ocean Modelling*, Submitted, 2013.

Leroy A. and Wheeler M. C. Statistical prediction of weekly tropical cyclone activity in the southern hemisphere. *Monthly Weather Review*, 136(10):3637–3654, 2008.

Levy M., Lengaigne M., Bopp L., Vincent E. M., Madec G., Ethe C., Kumar D., and Sarma V. V. S. S. Contribution of tropical cyclones to the air-sea co2 flux: A global view. *Global Biogeochemical Cycles*, 26, 2012.

Lloyd I. D. and Vecchi G. A. Observational evidence for oceanic controls on hurricane intensity. *Journal of Climate*, 24(4):1138–1153, 2011.

Luo Z., Kley D., Johnson R., and Smit H. Ten years of measurements of tropical upper-tropospheric water vapor by mozaic. part i: Climatology, variability, transport, and relation to deep convection. *Journal of Climate*, 20(3):418, 2007.

Manucharyan G., Brierley C., and Fedorov A. Climate impacts of intermittent upper ocean mixing induced by tropical cyclones. *Journal of Geophysical Research: Oceans (1978–2012)*, 116(C11), 2011.

Marchesiello P., McWilliams J. C., and Shchepetkin A. Open boundary conditions for long-term integration of regional oceanic models. *Ocean Modelling*, 3(1-2): 1–20, 2001.

Marchesiello P., Debreu L., and Couvelard X. Spurious diapycnal mixing in terrain-following coordinate models: The problem and a solution. *Ocean Modelling*, 26(3-4): 156–169, 2009.

Marchesiello P., Lefèvre J., Vega A., Couvelard X., and Menkes C. Coastal upwelling, circulation and heat balance around new caledonia's barrier reef. *Marine Pollution Bulletin*, 61(7-12):432–448, 2010a. ISSN 0025326X. doi: 10.1016/j.marpolbul.2010.06.043.

Marchesiello P., Lefevre J., Vega A., Couvelard X., and Menkes C. Coastal upwelling, circulation and heat balance around new caledonia's barrier reef. *Marine Pollution Bulletin*, 61(7-12):432–448, 2010b.

Marchesiello P., Capet X., Menkes C., and Kennan S. C. Submesoscale dynamics in tropical instability waves. *Ocean Modelling*, 39(1-2):31–46, 2011.

McPhaden M., Foltz G., Lee T., Murty V., Ravichandran M., Vecchi G., Vialard J., Wiggert J., and Yu L. Ocean-atmosphere interactions during cyclone nargis. *EOS*, 90(7):53–54, 2009.

McWilliams J. *Fundamentals of Geophysical Fluid Dynamics*. Cambridge University Press, 2006. ISBN 052185637X.

Menkes C., Levy M., Lengaigne M., Bopp L., Vincent E., Ethe C., Madec G., and Jullien S. Global impact of tropical cyclone onto primary production. *10th International Conference on Southern Hemisphere Meteorology and Oceanography*, 2012a.

Menkes C. E., Lengaigne M., Marchesiello P., Jourdain N. C., Vincent E. M., Lefevre J., Chauvin F., and Royer J.-F. Comparison of tropical cyclogenesis indices on seasonal to interannual timescales. *Climate Dynamics*, 38(1-2):301–321, 2012b.

Menkes C. E. R., Vialard J. G., Kennan S. C., Boulanger J. P., and Madec G. V. A modeling study of the impact of tropical instability waves on the heat budget of the eastern equatorial pacific. *Journal of Physical Oceanography*, 36(5):847–865, 2006.

Montegut C. D., Madec G., Fischer A. S., Lazar A., and Iudicone D. Mixed layer depth over the global ocean: An examination of profile data and a profile-based climatology. *Journal of Geophysical Research-Oceans*, 109(C12), 2004.

Montgomery M., Sang N., R.K. S., and Persing J. Do tropical cyclones intensify by wishe. *Quaterly Journal of the Royal Meteorological Society*, 135:1697–1714, 2009.

Moon I., Ginis I., and Hara T. Effect of surface waves on charnock coefficient under tropical cyclones. *Geophysical Research Letters*, 31:L20302, 2004.

Neetu S., Lengaigne M., Vincent E. M., Vialard J., Madec G., Samson G., Kumar M. R. R., and Durand F. Influence of upper-ocean stratification on tropical cyclone-induced surface cooling in the bay of bengal. *Journal of Geophysical Research-Oceans*, 117, 2012.

Noh Y., Cheon W., Hong S., and Raasch S. Improvement of the k-profile model for the planetary boundary layer based on large eddy simulation data. *Boundary-Layer Meteorology*, 107(2):401–427, 2003.

Nolan D. S., Stern D. P., and Zhang J. A. Evaluation of planetary boundary layer parameterizations in tropical cyclones by comparison of in situ observations and high-resolution simulations of hurricane isabel (2003). part ii: Inner-core boundary layer and eyewall structure. *Monthly Weather Review*, 137(11): 3675–3698, 2013/11/06 2009. doi: 10.1175/2009MWR2786.1.

Ooyama K. Numerical simulation of the life cycle of tropical cyclones. *Journal of the Atmospheric Sciences*, 26:3–40, 1969.

Paltridge G., Arking A., and Pook M. Trends in middle- and upper-level tropospheric humidity from ncep reanalysis data. *Theoretical and Applied Climatology*, 98(3):351–359, 2009.

Pasquero C. and Emanuel K. Tropical cyclones and transient upper-ocean warming. *Journal of Climate*, 21(1):149–162, 2008.

Penven P., Debreu L., Marchesiello P., and McWilliams J. C. Evaluation and application of the roms 1-way embedding procedure to the central california upwelling system. *Ocean Modelling*, 12(1-2):157–187, 2006.

Penven P., Marchesiello P., Debreu L., and Lefevre J. Software tools for pre- and post-processing of oceanic regional simulations. *Environmental Modelling & Software*, 23(5): 660–662, 2008.

Perlin N., Skyllingstad E. D., Samelson R. M., and Barbour P. L. Numerical simulation of air-sea coupling during coastal upwelling. *Journal of Physical Oceanography*, 37(8):2081–2093, 2007.

Powell M. D., Vickery P. J., and Reinhold T. A. Reduced drag coefficient for high wind speeds in tropical cyclones. *Nature*, 422(6929):279–283, 2003.

Price J. F. Upper ocean response to a hurricane. *Journal of Physical Oceanography*, 11 (2):153–175, 1981.

Price J. F., Sanford T. B., and Forristall G. Z. Forced stage response to a moving hurricane. *Journal of Physical Oceanography*, 24 (2):233–260, 1994.

Price J. F., Morzel J., and Niiler P. P. Warming of sst in the cool wake of a moving hurricane. *Journal of Geophysical Research-Oceans*, 113(C7), 2008.

Pudov V. D. Influence of heat-content of the upper ocean upon typhoon trajectories. *Okeanologiya*, 19(6):1002–1007, 1979.

Qiu B., Scott R. B., and Chen S. Length scales of eddy generation and nonlinear evolution of the seasonally modulated south pacific subtropical countercurrent. *Journal of Physical Oceanography*, 38(7): 1515–1528, 2008.

Ramsay H. A., Leslie L. M., Lamb P. J., Richman M. B., and Leplastrier M. Interannual variability of tropical cyclones in the australian region: Role of large-scale environment. *Journal of Climate*, 21(5):1083–1103, 2008.

Rotunno R. and Emanuel K. A. An air-sea interaction theory for tropical cyclones .2. evolutionary study using a nonhydrostatic axisymmetrical numerical-model. *Journal of the Atmospheric Sciences*, 44(3):542–561, 1987.

Royer J. F., Chauvin F., Timbal B., Araspin P., and Grimal D. A gcm study of the impact of greenhouse gas increase on the frequency of occurrence of tropical cyclones. *Climatic Change*, 38(3):307–343, 1998.

Samson G., Giordani H., Caniaux G., and Roux F. Numerical investigation of an oceanic resonant regime induced by hurricane winds. *Ocean Dynamics*, 59(4):565–586, 2009.

Samson G., Masson S., Keerthi M., Lengaigne M., Vialard J., Pous S., Madec G., Jourdain N., Menkes C., Jullien S., and Marchesiello P. Coupled regional modeling of te tropical indian ocean: simulated climate variability and tropical cyclone activity. *in prep.*, 2013.

Sandery P. A., Brassington G. B., Craig A., and Pugh T. Impacts of ocean-atmosphere coupling on tropical cyclone intensity change and ocean prediction in the australian region. *Monthly Weather Review*, 138(6):2074–2091, 2010.

Sanford T. B., Price J. F., Girton J. B., and Webb D. C. Highly resolved observations and simulations of the ocean response to a hurricane. *Geophysical Research Letters*, 34 (13), 2007.

Schade L. R. Tropical cyclone intensity and sea surface temperature. *Journal of the Atmospheric Sciences*, 57(18):3122–3130, 2000.

Schade L. R. and Emanuel K. A. The ocean's effect on the intensity of tropical cyclones: Results from a simple coupled atmosphere-ocean model. *Journal of the Atmospheric Sciences*, 56(4):642–651, 1999.

Schubert W. H., Montgomery M. T., Taft R. K., Guinn T. A., Fulton S. R., Kossin J. P., and Edwards J. P. Polygonal eyewalls, asymmetric eye contraction, and potential vorticity mixing in hurricanes. *Journal of the Atmospheric Sciences*, 56(9):1197–1223, 2013/10/30 1999. doi: 10.1175/1520-0469(1999)056<1197:PEAECA>2.0.CO;2.

Scoccimarro E., Gualdi S., Bellucci A., Sanna A., Fogli P. G., Manzini E., Vichi M., Oddo P., and Navarra A. Effects of tropical cyclones on ocean heat transport in a high-resolution coupled general circulation model. *Journal of Climate*, 24(16): 4368–4384, 2011.

Shay L. K. and Uhlhorn E. W. Loop current response to hurricanes isidore and lili. *Monthly Weather Review*, 136(9):3248–3274, 2008.

Shay L. K., Elsberry R. L., and Black P. G. Vertical structure of the ocean current response to a hurricane. *Journal of Physical Oceanography*, 19(5):649–669, 1989.

Shay L. K., Black P. G., Mariano A. J., Hawkins J. D., and Elsberry R. L. Upper ocean response to hurricane gilbert. *Journal of Geophysical Research-Oceans*, 97 (C12):20227–20248, 1992.

Shay L. K., Goni G. J., and Black P. G. Effects of a warm oceanic feature on hurricane opal. *Monthly Weather Review*, 128(5): 1366–1383, 2000.

Shchepetkin A. F. and McWilliams J. C. The regional oceanic modeling system (roms): a split-explicit, free-surface, topography-following-coordinate oceanic model. *Ocean Modelling*, 9(4):347–404, 2005.

Skamarock W. C. Evaluating mesoscale nwp models using kinetic energy spectra. *Monthly Weather Review*, 132(12):3019–3032, 2004.

Skamarock W. C. and Klemp J. B. A time-split nonhydrostatic atmospheric model for weather research and forecasting applications. *Journal of Computational Physics*, 227(7):3465–3485, 2008.

Slutz R. J., Lubker S. J., Hiscox J. D., Woodruff S., Jenne R., Joseph D., Steurer P., and Elms J. Comprehensive ocean-atmosphere data set: Release 1. *I: Climate Research Program, ERL/NOAA, Boulder, CO*, 1985.

Smith R. and Montgomery M. Hurricane boundary-layer theory. *Quaterly Journal of the Royal Meteorological Society*, 136:1–6, 2010.

Smith R., Montgomery M., and S.V. N. Tropical cyclone spin-up revisited. *Quaterly Journal of the Royal Meteorological Society*, 135:1321–1335, 2009.

Smith S. D., Anderson R. J., Oost W. A., Kraan C., Maat N., De Cosmo J., Katsaros K. B., Davidson K. L., Bumke K., Hasse L., et al. Sea surface wind stress and drag coefficients: The hexos results. *Boundary-Layer Meteorology*, 60(1-2):109–142, 1992.

Sriver R. L. Climate change tropical cyclones in the mix. *Nature*, 463(7284):1032–1033, 2010.

Sriver R. L. and Huber M. Observational evidence for an ocean heat pump induced by tropical cyclones. *Nature*, 447(7144): 577–580, 2007.

Sriver R. L., Huber M., and Nusbaumer J. Investigating tropical cyclone-climate feedbacks using the trmm microwave imager and the quick scatterometer. *Geochemistry Geophysics Geosystems*, 9, 2008.

Stern D. P. and Nolan D. S. On the height of the warm core in tropical cyclones. *Journal of the Atmospheric Sciences*, 69(5):1657–1680, 2013/10/02 2011. doi: 10.1175/JAS-D-11-010.1.

Sugi M., Noda A., and Sato N. Influence of the global warming on tropical cyclone climatology: An experiment with the jma global model. *Journal of the Meteorological Society of Japan*, 80(2):249–272, 2002.

Sutyrin G. G. Energetics of a stratified ocean under a stationary tropical cyclone. *Izvestiya Akademii Nauk Sssr Fizika Atmosfery I Okeana*, 15(10):1076–1083, 1979.

Sutyrin G. G. and Khain A. P. The influence of the ocean-atmosphere interaction on the intensity of moving tropical cy-

clones. *Izvestiya Akademii Nauk Sssr Fizika Atmosfery I Okeana*, 20(9):787–794, 1984.

Vincent E. M., Lengaigne M., Menkes C. E., Jourdain N. C., Marchesiello P., and Madec G. Interannual variability of the south pacific convergence zone and implications for tropical cyclone genesis. *Climate Dynamics*, 36(9-10):1881–1896, 2011.

Vincent E. M., Lengaigne M., Madec G., Vialard J., Samson G., Jourdain N. C., Menkes C. E., and Jullien S. Processes setting the characteristics of sea surface cooling induced by tropical cyclones. *Journal of Geophysical Research-Oceans*, 117:18, 2012a.

Vincent E. M., Lengaigne M., Vialard J., Madec G., Jourdain N. C., and Masson S. Assessing the oceanic control on the amplitude of sea surface cooling induced by tropical cyclones. *Journal of Geophysical Research-Oceans*, 117, 2012b.

Vincent E. M., Madec G., Lengaigne M., Vialard J., and Koch-Larrouy A. Influence of tropical cyclones on sea surface temperature seasonal cycle and ocean heat transport. *Climate Dynamics*, pages 1–20, 2012c.

Wada A. Idealized numerical experiments associated with the intensity and rapid intensification of stationary tropical-cyclone-like vortex and its relation to initial sea-surface temperature and vortex-induced sea-surface cooling. *Journal of Geophysical Research: Atmospheres*, 114(D18):n/a–n/a, 2009. ISSN 2156-2202. doi: 10.1029/2009JD011993.

Walsh K. Tropical cyclones and climate change: unresolved issues. *Climate Research*, 27(1):77–83, 2004.

Walsh K. J. E. and Watterson I. Tropical Cyclone-like Vortices in a Limited Area Model: Comparison with Observed Climatology. *Journal of Climate*, 10(9):2240–2259, 1997.

Walsh K. J. E., Nguyen K. C., and McGregor J. L. Fine-resolution regional climate model simulations of the impact of climate change on tropical cyclones near australia. *Climate Dynamics*, 22(1):47–56, 2004.

Walsh K. J. E., Fiorino M., Landsea C. W., and McInnes K. L. Objectively determined resolution-dependent threshold criteria for the detection of tropical cyclones in climate models and reanalyses. *Journal of Climate*, 20(10):2307–2314, 2007.

Walsh K. J. E., McInnes K. L., and McBride J. L. Climate change impacts on tropical cyclones and extreme sea levels in the south pacific - a regional assessment. *Global and Planetary Change*, 80-81:149–164, 2012.

Wang Y. and Wu C.-C. Current understanding of tropical cyclone structure and intensity changes – a review. *Meteorology and Atmospheric Physics*, 87(4):257–278, 2004. ISSN 0177-7971. doi: 10.1007/s00703-003-0055-6.

Webb D. J. Evidence for shallow zonal jets in the south equatorial current region of the southwest pacific. *Journal of physical oceanography*, 30(4):706–720, 2000.

Withee G. and Johnson A. Buoy observations during hurricane eloise (september 19 to october 11, 1975). Technical report, U.S. Department of Commerce NOAA/NSTL Station Data Report, 1976.

Wu C.-C., Lee C.-Y., and Lin I. I. The effect of the ocean eddy on tropical cyclone intensity. *Journal of the Atmospheric Sciences*, 64(10):3562–3578, 2007.

Xie P. and Arkin P. A. Global precipitation: A 17-year monthly analysis based on gauge observations, satellite estimates, and numerical model outputs. *Bulletin of the American Meteorological Society*, 78(11):2539–2558, 1997.

Yang B., Wang Y., and Wang B. The effect of internally generated inner-core asymmetries on tropical cyclone potential intensity*. *Journal of the Atmospheric Sciences*,

64(4):1165–1188, 2013/10/30 2007. doi: 10.1175/JAS3971.1.

Yu L. and Rienecker M. Xin, j., and ra weller, 2008: Multidecade global flux datasets from the objectively analyzed air-sea fluxes (oaflux) project: Latent and sensible heat fluxes, ocean evaporation, and related surface meteorological variables. Technical Report OA-2008-01, OAFlux Project Tech. Rep., Woods Hole. Massachusetts, 2008.

Zeng X. B. and Beljaars A. A prognostic scheme of sea surface skin temperature for modeling and data assimilation. *Geophysical Research Letters*, 32(14), 2005.

Zhao M., Held I. M., Lin S. J., and Vecchi G. A. Simulations of global hurricane climatology, interannual variability, and response to global warming using a 50-km resolution gcm. *Journal of Climate*, 22(24): 6653–6678, 2009.

Zheng Z.-W., Ho C.-R., Zheng Q., Lo Y.-T., Kuo N.-J., and Gopalakrishnan G. Effects of preexisting cyclonic eddies on upper ocean responses to category 5 typhoons in the western north pacific. *Journal of Geophysical Research: Oceans (1978–2012)*, 115 (C9), 2010.

Appendix A

Description of WRF namelist variables

Description of namelist variables

For WRF-NMM users, please see Chapter 5 of the WRF-NMM User's Guide for
information on NMM specific settings (http://www.dtcenter.org/wrf-nmm/users)

Note: variables followed by (max_dom) indicate that this variable needs to
be defined for the nests when max_dom > 1.

&time_control
run_days = 1, ; run time in days
run_hours = 0, ; run time in hours
Note: if it is more than 1 day, one may use both run_days and run_hours
or just run_hours. e.g. if the total run length is 36 hrs, you may
set run_days = 1, and run_hours = 12, or run_days = 0, and run_hours = 36
run_minutes = 0, ; run time in minutes
run_seconds = 0, ; run time in seconds
start_year (max_dom) = 2001, ; four digit year of starting time
start_month (max_dom) = 06, ; two digit month of starting time
start_day (max_dom) = 11, ; two digit day of starting time
start_hour (max_dom) = 12, ; two digit hour of starting time
start_minute (max_dom) = 00, ; two digit minute of starting time
start_second (max_dom) = 00, ; two digit second of starting time
Note: the start time is used to name the first wrfout file.
It also controls the start time for nest domains, and the time to restart
tstart (max_dom) = 00, ; FOR NMM: starting hour of the forecast
end_year (max_dom) = 2001, ; four digit year of ending time
end_month (max_dom) = 06, ; two digit month of ending time
end_day (max_dom) = 12, ; two digit day of ending time
end_hour (max_dom) = 12, ; two digit hour of ending time
end_minute (max_dom) = 00, ; two digit minute of ending time
end_second (max_dom) = 00, ; two digit second of ending time
It also controls when the nest domain integrations end
All start and end times are used by real.exe.

Note that one may use either run_days/run_hours etc. or
end_year/month/day/hour etc. to control the length of
model integration. But run_days/run_hours
takes precedence over the end times.
Program real.exe uses start and end times only.

interval_seconds = 10800, ; time interval between incoming real data, which will be the interval
between the lateral boundary condition file
input_from_file (max_dom) = T, ; whether nested run will have input files for domains other than 1
fine_input_stream (max_dom) = 0, ; field selection from nest input for its initialization
0: all fields are used; 2: only static and time-varying, masked land
surface fields are used. In V3.2, this requires the use of
io_form_auxinput2
history_interval (max_dom) = 60, ; history output file interval in minutes
frames_per_outfile (max_dom) = 1, ; number of output times per history output file,
used to split output into multiple files
into smaller pieces
restart = F, ; whether this run is a restart run
cycling = F, ; whether this run is a cycling run, if so, initializes look-up table for Thompson
schemes only
restart_interval = 1440, ; restart output file interval in minutes
reset_simulation_start = F, ; whether to overwrite simulation_start_date with forecast start time
io_form_history = 2, ; 2 = netCDF
io_form_restart = 2, ; 2 = netCDF
io_form_input = 2, ; 2 = netCDF
io_form_boundary = 2, ; netCDF format
= 4, ; PHD5 format
= 5, ; GRIB1 format

```
                    = 10,      ; GRIB2 format
                    = 11,      ; pnetCDF format
 frames_per_emissfile          = 12,      ; number of times in each chemistry emission file.
 io_style_emiss              = 1,       ; style to use for the chemistry emission files.
                               ; 0 = Do not read emissions from files.
                               ; 1 = Cycle between two 12 hour files (set frames_per_emissfile=12)
                               ; 2 = Dated files with length set by frames_per_emissfile
 debug_level                 = 0,     ; 50,100,200,300 values give increasing prints
 diag_print                  = 0,       ; print out time series of model diagnostics
                               ; 0 = no print
                               ; 1 = no print
 all_ic_times                = .false., ; whether to write out wrfinput for all processing times
 adjust_output_times           = .false., ; adjust output times to the nearest hour

To choose between SI and WPS input to real for EM core:
 auxinput1_inname              = "met_em.d<domain>.<date>"           ; Input to real from WPS (default since 3.0)
                    = "wrf_real_input_em.d<domain>.<date>"  ; Input to real from SI

To choose between SI and WPS input to real for NMM core:
 auxinput1_inname              = "met_nm.d<domain>.<date>"           ; Input to real from WPS
                    = "wrf_real_input_nm.d<domain>.<date>"  ; Input to real from SI

Other output options:

 auxhist2_outname              = "rainfall" ; file name for extra output; if not specified,
                               auxhist2_d<domain>_<date> will be used
                               also note that to write variables in output other
                               than the history file requires Registry.EM file change
 auxhist2_interval (max_dom)       = 10,      ; interval in minutes
 io_form_auxhist2              = 2,       ; output in netCDF
 frames_per_auxhist2           = 1000,    ; number of output times in this file

For SST updating (used only with sst_update=1):

 auxinput4_inname              = "wrflowinp_d<domain>"
 auxinput4_interval            = 360      ; minutes generally matches time given by interval_seconds
 io_form_auxinput4             = 2        ; IO format, required in V3.2

For additional regional climate surface fields

 output_diagnostics            = 1        ; adds 36 surface diagnostic arrays (max/min/mean/std)
 auxhist3_outname              = 'wrfxtrm_d<domain>_<date>' ; file name for added diagnostics
 io_form_auxhist3              = 2        ; netcdf
 auxhist3_interval             = 1440     ; minutes between outputs (1440 gives daily max/min)
 frames_per_auxhist3           = 1        ; output times per file

For observation nudging:
 auxinput11_interval           = 10       ; interval in minutes for observation data. It should be
                               set as or more frequently as obs_ionf (with unit of
                               coarse domain time step).
 auxinput11_end_h              = 6        ; end of observation time in hours.

Options for run-time IO:

 iofields_filename (max_dom)       = "my_iofields_list.txt",
                           (example: +:h:21:rainc, rainnc, rthcuten)
 ignore_iofields_warning         = .true.,  ; what to do when encountering an error in the user-specified files
                           .false., : abort when encountering an error in iofields_filename file

Additional settings when running WRFVAR:

 write_input                 = t,       ; write input-formatted data as output
 inputout_interval             = 180,     ; interval in minutes when writing input-formatted data
```

```
 input_outname                 = 'wrfinput_d<domain>_<date>' ; you may change the output file name
 inputout_begin_y              = 0
 inputout_begin_mo             = 0
 inputout_begin_d              = 0
 inputout_begin_h              = 3
 inputout_begin_m              = 0
 inputout_begin_s              = 0
 inputout_end_y                = 0
 inputout_end_mo               = 0
 inputout_end_d                = 0
 inputout_end_h                = 12
 inputout_end_m                = 0
 inputout_end_s                = 0       ; the above shows that the input-formatted data are output
                                 starting from hour 3 to hour 12 in 180 min interval.

 &domains
 time_step                   = 60,     ; time step for integration in integer seconds
                                 recommend 6*dx (in km) for typical real-data cases
 time_step_fract_num           = 0,            ; numerator for fractional time step
 time_step_fract_den           = 1,            ; denominator for fractional time step
                                 Example, if you want to use 60.3 sec as your time step,
                                 set time_step = 60, time_step_fract_num = 3, and
                                 time_step_fract_den = 10
 time_step_dfi                 = 60,  ; time step for DFI, may be different from regular time_step
 max_dom                       = 1,    ; number of domains - set it to > 1 if it is a nested run
 s_we (max_dom)                = 1,            ; start index in x (west-east) direction (leave as is)
 e_we (max_dom)                = 91,           ; end index in x (west-east) direction (staggered dimension)
 s_sn (max_dom)                = 1, ; start index in y (south-north) direction (leave as is)
 e_sn (max_dom)                = 82,           ; end index in y (south-north) direction (staggered dimension)
 s_vert (max_dom)              = 1,; start index in z (vertical) direction (leave as is)
 e_vert (max_dom)              = 28,           ; end index in z (vertical) direction (staggered dimension)
                                 Note: this refers to full levels including surface and top
                                 vertical dimensions need to be the same for all nests
                                 Note: most variables are unstaggered (= staggered dim - 1)
 dx (max_dom)                  = 10000,        ; grid length in x direction; ARW: unit in meters, NMM: unit in degrees
(e.g. 0.667)
 dy (max_dom)                  = 10000,        ; grid length in y direction; ARW: unit in meters, NMM: unit in degrees
(e.g. 0.0658)
 ztop (max_dom)                = 19000.        ; used in mass model for idealized cases
 grid_id (max_dom)             = 1,            ; domain identifier
 parent_id (max_dom)           = 0,      ; id of the parent domain
 i_parent_start (max_dom)      = 0,      ; starting LLC I-indices from the parent domain
 j_parent_start (max_dom)      = 0,      ; starting LLC J-indices from the parent domain
 parent_grid_ratio (max_dom)   = 1,      ; parent-to-nest domain grid size ratio: for real-data cases
                                 the ratio has to be odd; for idealized cases,
                                 the ratio can be even if feedback is set to 0. (NMM: must be 3)
 parent_time_step_ratio (max_dom)  = 1,      ; parent-to-nest time step ratio; it can be different
                                 from the parent_grid_ratio (NMM: must be 3)
 feedback                    = 1,      ; feedback from nest to its parent domain; 0 = no feedback
 smooth_option                 = 0       ; smoothing option for parent domain, used only with feedback
                                 option on. 0: no smoothing; 1: 1-2-1 smoothing; 2: smoothing-desmoothing
```

Namelist variables specifically for the WPS input for real:

```
 num_metgrid_soil_levels       = 4       ; number of vertical soil levels or layers input
                               ; from WPS metgrid program
 num_metgrid_levels            = 27      ; number of vertical levels of 3d meteorological fields coming
                               ; from WPS metgrid program
 interp_type                   = 2       ; vertical interpolation
                               ; 1 = linear in pressure
                               ; 2 = linear in log(pressure)
 extrap_type                   = 2       ; vertical extrapolation of non-temperature fields
                               ; 1 = extrapolate using the two lowest levels
```

```
                          ; 2 = use lowest level as constant below ground
t_extrap_type              = 2       ; vertical extrapolation for potential temperature
                          ; 1 = isothermal
                          ; 2 = -6.5 K/km lapse rate for temperature
                          ; 3 = constant theta
use_levels_below_ground          = .true.   ; in vertical interpolation, use levels below input surface level
                          ; T = use input isobaric levels below input surface
                          ; F = extrapolate when WRF location is below input surface value
use_surface               = .true.   ; use the input surface level data in the vertical interp and extrap
                          ; T = use the input surface data
                          ; F = do not use the input surface data
lagrange_order             = 1       ; vertical interpolation order
                          ; 1 = linear
                          ; 2 = quadratic
zap_close_levels           = 500     ; ignore isobaric level above surface if delta p (Pa) < zap_close_levels
lowest_lev_from_sfc          = .false.  ; place the surface value into the lowest eta location
                          ; T = use surface value as lowest eta (u,v,t,q)
                          ; F = use traditional interpolation
force_sfc_in_vinterp         = 1       ; use the surface level as the lower boundary when interpolating
                          ; through this many eta levels
                          ; 0 = perform traditional trapping interpolation
                          ; n = first n eta levels directly use surface level
sfcp_to_sfcp              = .false.  ; Optional method to compute model's surface pressure when incoming
                          ; data only has surface pressure and terrain, but not SLP
smooth_cg_topo             = .false.  ; Smooth the outer rows and columns of domain 1's topography w.r.t.
                          ; the input data
use_tavg_for_tsk           = .false.  ; whether to use diurnally averaged surface temp as skin temp. The
                            diurnall averaged surface temp can be computed using WPS utility
                            avg_tsfc.exe. May use this option when SKINTEMP is not present.
aggregate_lu              = .false.  ; whetger to aggregate the grass, shrubs, trees in dominant landuse;
                            default is false.
rh2qv_wrt_liquid           = .true.,  ; whether to compute RH with respect to water (true) or ice (false)
rh2qv_method               = 1,       ; which methed to use to computer mixing ratio from RH:
                            default is option 1, the old MM5 method; option 2 uses a WMO
                            recommended method (WMO-No. 49, corrigendum, August 2000) -
                            there is a difference between the two methods though small
p_top_requested            = 5000     ; p_top (Pa) to use in the model
ptsgm                     = 42000.   ; FOR NMM:  defines the pressure interface dividing
                          ;          the terrain following portion of the hybrid vertical
                          ;          coordinate (p > ptsgm) and the purely
                          ;          isobaric portion of the vertical coordinate (p < ptsgm)
vert_refine_fact           = 1       ; vertical refinement factor for ndown
```

Users may explicitly define full eta levels. Given are two distributions for 28 and 35 levels. The number of levels must agree with the number of eta surfaces allocated (e_vert). Users may alternatively request only the number of levels (with e_vert), and the real program will compute values. The computation assumes a known first several layers, then generates equi-height spaced levels up to the top of the model.

```
eta_levels                 = 1.000, 0.990, 0.978, 0.964, 0.946,
                           0.922, 0.894, 0.860, 0.817, 0.766,
                           0.707, 0.644, 0.576, 0.507, 0.444,
                           0.380, 0.324, 0.273, 0.228, 0.188,
                           0.152, 0.121, 0.093, 0.069, 0.048,
                           0.029, 0.014, 0.000,
eta_levels                 = 1.000, 0.993, 0.983, 0.970, 0.954,
                           0.934, 0.909, 0.880, 0.845, 0.807,
                           0.765, 0.719, 0.672, 0.622, 0.571,
                           0.520, 0.468, 0.420, 0.376, 0.335,
                           0.298, 0.263, 0.231, 0.202, 0.175,
                           0.150, 0.127, 0.106, 0.088, 0.070,
                           0.055, 0.040, 0.026, 0.013, 0.000
```

Namelist variables for controling the specified moving nest:

Note that this moving nest option needs to be activated at the compile time by adding -DMOVE_NESTS
to the ARCHFLAGS. The maximum number of moves, max_moves, is set to 50
but can be modified in source code file frame/module_driver_constants.F.

num_moves = 4 ; total number of moves
move_id(max_moves) = 2,2,2,2, ; a list of nest domain id's, one per move
move_interval(max_moves) = 60,120,150,180, ; time in minutes since the start of this domain
move_cd_x(max_moves) = 1,1,0,-1,; the number of parent domain grid cells to move in i direction
move_cd_y(max_moves) = 1,0,-1,1,; the number of parent domain grid cells to move in j direction
positive is to move in increasing i and j direction, and
negative is to move in decreasing i and j direction.
0 means no move. The limitation now is to move only 1 grid cell
at each move.

Namelist variables for controling the automatic moving nest:

Note that this moving nest option needs to be activated at the compile time by adding -DMOVE_NESTS
and -DVORTEX_CENTER to the ARCHFLAGS. This option uses an mid-level vortex following algorthm
to
determine the nest move. This option is experimental.

vortex_interval(max_dom) = 15 ; how often the new vortex position is computed
max_vortex_speed(max_dom) = 40 ; used to compute the search radius for the new vortex position
corral_dist(max_dom) = 8 ; how many coarse grid cells the moving nest is allowed to get
near the mother domain boundary
track_level = 50000 ; pressure value in Pa where the vortex is tracked
time_to_move(max_dom) = 0. ; time (in minutes) to start the moving nests

tile_sz_x = 0, ; number of points in tile x direction
tile_sz_y = 0, ; number of points in tile y direction
can be determined automatically
numtiles = 1, ; number of tiles per patch (alternative to above two items)
nproc_x = -1, ; number of processors in x for decomposition
nproc_y = -1, ; number of processors in y for decomposition
-1: code will do automatic decomposition
>1: for both: will be used for decomposition

Namelist variables for controlling the adaptive time step option:

These options are only valid for the ARW core.

use_adaptive_time_step = .false. ; T/F use adaptive time stepping, ARW only
step_to_output_time = .true. ; if adaptive time stepping, T/F modify the
time steps so that the exact history time is reached
target_cfl(max_dom) = 1.2,1.2 ; vertical and horizontal CFL <= to this value implies
no reason to reduce the time step, and to increase it
target_hcfl(max_dom) = .84,.84 ; horizontal CFL <= to this value implies
max_step_increase_pct(max_dom) = 5,51 ; percentage of previous time step to increase, if the
max(vert cfl, horiz cfl) <= target_cfl, then the time
will increase by max_step_increase_pct. Use something
large for nests (51% suggested)
starting_time_step(max_dom) = -1,-1 ; flag = -1 implies use 6 * dx (defined in start_em),
starting_time_step = 100 means the starting time step
for the coarse grid is 100 s
max_time_step(max_dom) = -1,-1 ; flag = -1 implies max time step is 3 * starting_time_step,
max_time_step = 100 means that the time step will not
exceed 100 s
min_time_step(max_dom) = -1,-1 ; flag = -1 implies max time step is 0.5 * starting_time_step,
min_time_step = 100 means that the time step will not
be less than 100 s
adaptation_domain = 1 ; default, all fine grid domains adaptive dt driven by coarse-grid
; 2 = Fine grid domain #2 determines the fundamental adaptive dt.

&physics

Note: even the physics options can be different in different nest domains,
caution must be used as what options are sensible to use

chem_opt = 0, ; chemistry option - use WRF-Chem
mp_physics (max_dom) microphysics option
= 0, no microphysics
= 1, Kessler scheme
= 2, Lin et al. scheme
= 3, WSM 3-class simple ice scheme
= 4, WSM 5-class scheme
= 5, Ferrier (new Eta) microphysics
= 6, WSM 6-class graupel scheme
= 7, Goddard GCE scheme (also uses gsfcgce_hail, gsfcgce_2ice)
= 8, Thompson scheme (new for V3.1)
= 9, Milbrandt-Yau 2-moment scheme (new for V3.2)
= 10, Morrison (2 moments)
= 13, SBU_YLIN scheme
= 14, WDM 5-class scheme
= 16, WDM 6-class scheme

For non-zero mp_physics options, to keep Qv .GE. 0, and to set the other moisture
fields .LT. a critcal value to zero

mp_zero_out = 0, ; no action taken, no adjustment to any moist field
= 1, ; except for Qv, all other moist arrays are set to zero
; if they fall below a critical value
= 2, ; Qv is .GE. 0, all other moist arrays are set to zero
; if they fall below a critical value
mp_zero_out_thresh = 1.e-8 ; critical value for moist array threshold, below which
; moist arrays (except for Qv) are set to zero (kg/kg)

gsfcgce_hail = 0 ; for running gsfcgce microphysics with graupel
= 1 ; for running gsfcgce microphysics with hail
default value = 0
gsfcgce_2ice = 0 ; for running with snow, ice and graupel/hail
= 1 ; for running with only ice and snow
= 2 ; for running with only ice and graupel
(only used in very extreme situation)
default value = 0
gsfcgce_hail is ignored if gsfcgce_2ice is set to 1 or 2.

no_mp_heating = 0 ; normal
= 1 ; turn off latent heating from a microphysics scheme

ra_lw_physics (max_dom) longwave radiation option
= 0, no longwave radiation
= 1, rrtm scheme
= 3, cam scheme
also must set levsiz, paerlev, cam_abs_dim1/2 (see below)
= 4, rrtmg scheme
= 5, Goddard longwave scheme
= 31, Earth Held-Suarez forcing
= 99, GFDL (Eta) longwave (semi-supported)
also must use co2tf = 1 for ARW

ra_sw_physics (max_dom) shortwave radiation option
= 0, no shortwave radiation
= 1, Dudhia scheme
= 2, Goddard short wave
= 3, cam scheme
also must set levsiz, paerlev, cam_abs_dim1/2 (see below)
= 5, Goddard shortwave scheme
= 4, rrtmg scheme
= 99, GFDL (Eta) longwave (semi-supported)
also must use co2tf = 1 for ARW

radt (max_dom) = 30, ; minutes between radiation physics calls
recommend 1 min per km of dx (e.g. 10 for 10 km)

nrads (max_dom) = FOR NMM: number of fundamental timesteps between
calls to shortwave radiation; the value
is set in Registry.NMM but is overridden
by namelist value; radt will be computed
from this.

nradl (max_dom) = FOR NMM: number of fundamental timesteps between
calls to longwave radiation; the value
is set in Registry.NMM but is overridden
by namelist value.

co2tf CO2 transmission function flag only for GFDL radiation
= 0, read CO2 function data from pre-generated file
= 1, generate CO2 functions internally in the forecast

ra_call_offset radiation call offset
= 0 (no offset), =-1 (old offset)

cam_abs_freq_s = 21600 CAM clearsky longwave absorption calculation frequency
(recommended minimum value to speed scheme up)
levsiz = 59 for CAM radiation input ozone levels
paerlev = 29 for CAM radiation input aerosol levels
cam_abs_dim1 = 4 for CAM absorption save array
cam_abs_dim2 = value of e_vert for CAM 2nd absorption save array

sf_sfclay_physics (max_dom) surface-layer option (old bl_sfclay_physics option)
= 0, no surface-layer
= 1, Monin-Obukhov scheme
= 2, Monin-Obukhov (Janjic) scheme
= 3, NCEP Global Forecast System scheme (NMM only)
= 4, QNSE surface layer
= 5, MYNN surface layer
= 7, Pleim-Xiu surface layer (ARW only)
= 10, TEMF surface layer (ARW only)

sf_surface_physics (max_dom) land-surface option (old bl_surface_physics option)
= 0, no surface temp prediction
= 1, thermal diffusion scheme
= 2, Unified Noah land-surface model
= 3, RUC land-surface model
= 7, Pleim-Xiu LSM (ARW)

sf_urban_physics(max_dom) = 0, ; activate urban canopy model (in Noah LSM only)
= 0: no
= 1: Single-layer, UCM
= 2: Multi-layer, Building Environment Parameterization (BEP) scheme
(works only with MYJ and BouLac PBL)
= 3: Multi-layer, Building Environment Model (BEM) scheme
(works only with MYJ and BouLac PBL)

bl_pbl_physics (max_dom) boundary-layer option
= 0, no boundary-layer
= 1, YSU scheme
= 2, Mellor-Yamada-Janjic TKE scheme
= 3, NCEP Global Forecast System scheme (NMM only)
= 4, Quasi-Normal Scale Elimination PBL
= 5, MYNN 2.5 level TKE scheme, works with
sf_sfclay_physics=1 or 2 as well as 5
= 6, MYNN 3rd level TKE scheme, works only
MYNNSFC (sf_sfclay_physics = 5)

= 7, ACM2 (Pleim) PBL (ARW)
= 8, Bougeault and Lacarrere (BouLac) PBL
= 9, UW boundary layer scheme from CAM5 (CESM 1_0_1)
= 10, TEMF (Total Energy Mass Flux) scheme (ARW only)
= 99, MRF scheme

bldt (max_dom) = 0, ; minutes between boundary-layer physics calls

grav_settling = 0, ; MYNN PBL only; gravitational settling of fog/cloud droplets (1=yes)
nphs (max_dom) = FOR NMM: number of fundamental timesteps between calls to turbulence and microphysics; the value is set in Registry.NMM but is overridden by namelist value; bldt will be computed from this.

cu_physics (max_dom) cumulus option
= 0, no cumulus
= 1, Kain-Fritsch (new Eta) scheme
= 2, Betts-Miller-Janjic scheme
= 3, Grell-Devenyi ensemble scheme
= 4, Simplified Arakawa-Schubert scheme
= 5, Grell 3D ensemble scheme
= 6, Modifed Tiedtke scheme (ARW only)
= 7, Zhang-McFarlane scheme from CAM5 (CESM 1_0_1)
= 14, New GFS simplified Arakawa-Schubert scheme from YSU (ARW only)
= 99, previous Kain-Fritsch scheme

shcu_physics (max_dom) independent shallow cumulus option (not tied to deep convection)
= 0, no independent shallow cumulus
= 1, Grell 3D ensemble scheme (use with cu_physics=5) (PLACEHOLDER: SWITCH NOT YET IMPLEMENTED--use ishallow)
= 2, Park and Bretherton shallow cumulus from CAM5 (CESM 1_0_1)

ishallow = 1, Shallow convection used with Grell 3D ensemble scheme (cu_physics = 5)
clos_choice = 0, closure choice (place holder only)

cu_diag = 0, additional t-averaged stuff for cu physics (GD and G3 only)
convtrans_avglen_m = 30, averaging time for convective transport output variables (minutes) (GD and G3 only)

cudt = 0, ; minutes between cumulus physics calls

kfeta_trigger KF trigger option (cu_physics=1 only):
= 1, default option
= 2, moisture-advection based trigger (Ma and Tan [2009]) - ARW only
= 3, RH-dependent additional perturbation to option 1 (JMA)

cugd_avedx ; number of grid boxes over which subsidence is spread.
= 1, default, for large grid distances
= 3, for small grid distances (DX < 5 km)

ncnvc (max_dom) = FOR NMM: number of fundamental timesteps between calls to convection; the value is set in Registry.NMM but is overridden by namelist value; cudt will be computed from this.

tprec (max_dom) = FOR NMM: number of hours in precipitation bucket
theat (max_dom) = FOR NMM: number of hours in latent heating bucket
tclod (max_dom) = FOR NMM: number of hours in cloud fraction average
trdsw (max_dom) = FOR NMM: number of hours in short wave buckets
trdlw (max_dom) = FOR NMM: number of hours in long wave buckets
tsrfc (max_dom) = FOR NMM: number of hours in surface flux buckets
pcpflg (max_dom) = FOR NMM: logical switch for precipitation assimilation

```
isfflx                          = 1,          ; heat and moisture fluxes from the surface
                                  (only works for sf_sfclay_physics = 1)
                                  1 = with fluxes from the surface
                                  0 = no flux from the surface
                                     with bl_pbl_physics=0 this uses tke_drag_coefficient
                                     and tke_heat_flux in vertical diffusion
                                  2 = use drag from sf_sfclay_physics and heat flux from
                                     tke_heat_flux with bl_pbl_physics=0
ifsnow                          = 0,        ; snow-cover effects
                                  (only works for sf_surface_physics = 1)
                                  1 = with snow-cover effect
                                  0 = without snow-cover effect
icloud                          = 1,        ; cloud effect to the optical depth in radiation
                                  (only works for ra_sw_physics = 1 and ra_lw_physics = 1)
                                  1 = with cloud effect
                                  0 = without cloud effect
swrad_scat                      = 1.        ; scattering tuning parameter (default 1. is 1.e-5 m2/kg)
surface_input_source            = 1,            ; where landuse and soil category data come from:
                                  1 = WPS/geogrid but with dominant categories recomputed
                                  2 = GRIB data from another model (only possible
                                     (VEGCAT/SOILCAT are in met_em files from WPS)
                                  3 = use dominant land and soil categories from WPS/geogrid

num_soil_layers                 = 5,  ; number of soil layers in land surface model
                                  = 5: thermal diffusion scheme
                                  = 4: Noah landsurface model
                                  = 6: RUC landsurface model
                                  = 2: Pleim-Xu landsurface model
num_land_cat                    = 24,       ; number of land categories in input data.
                                  24 - for USGS (default); 20 for MODIS
                                  28 - for USGS if including lake category
                                  21 - for MODIS if including lake category
num_soil_cat                    = 16,       ; number of soil categories in input data

pxlsm_smois_init(max_dom)       = 1         ; PXLSM Soil moisture initialization option
                                  0 - From analysis, 1 - From MAVAIL

maxiens                         = 1,        ; Grell-Devenyi only
maxens                          = 3,        ; G-D only
maxens2                         = 3,        ; G-D only
maxens3                         = 16        ; G-D only
ensdim                          = 144       ; G-D only
                                  These are recommended numbers. If you would like to use
                                  any other number, consult the code, know what you are doing.
seaice_threshold                = 271       ; tsk < seaice_threshold, if water point and 5-layer slab
                                  ; scheme, set to land point and permanent ice; if water point
                                  ; and Noah scheme, set to land point, permanent ice, set temps
                                  ; from 3 m to surface, and set smois and sh2o
sst_update                      = 0         ; time-varying sea-surface temp (0=no, 1=yes). If selected real
                                  ; puts SST, XICE, ALBEDO and VEGFRA in wrflowinp_d01 file, and wrf updates
                                  ; these from it at same interval as boundary file. Also requires
                                  ; namelists in &time_control: auxinput4_interval, auxinput4_end_h,
                                  ; auxinput4_inname = "wrflowinp_d<domain>",
                                  ; and in V3.2 io_form_auxinput4
usemonalb                       = .true.    ; use monthly albedo map instead of table value
                                  ; (must be used for NMM and recommended for sst_update=1)
rdmaxalb                        = .true.    ; use snow albedo from geogrid; false means using values from table
rdlai2d                         = .false.   ; use LAI from input; false means using values from table
bucket_mm                       = -1.       ; bucket reset value for water accumulations (value in mm, -1.=inactive)
bucket_J                        = -1.       ; bucket reset value for energy accumulations (value in J, -1.=inactive)
tmn_update                      = 0         ; update deep soil temperature (1, yes; 0, no)
lagday                          = 150       ; days over which tmn is computed using skin temperature
```

```
 sst_skin                  = 0       ; calculate skin SST
 slope_rad (max_dom)       = 0       ; slope effects for solar radiation (1=on, 0=off)
 topo_shading (max_dom)    = 0       ; neighboring-point shadow effects for solar radiation (1=on, 0=off)
 shadlen                   = 25000.  ; max shadow length in meters for topo_shading=1
 omlcall                   = 0       ; activate simple ocean mixed layer model (0=no, 1=yes); works with
                                       sf_surface_physics = 1 only
 oml_hml0                  = 50      ; oml model can be initialized with a constant depth everywhere (m)
 oml_gamma                 = 0.14    ; oml deep water lapse rate (K m-1)
 isftcflx                  = 0       ; alternative Ck, Cd formulation for tropical storm application (0=default, 1=new,
2=Garratt)
 fractional_seaice         = 0       ; treat sea-ice as fractional field (1) or ice/no-ice flag (0)
 tice2tsk_if2cold          = .false. ; set Tice to Tsk to avoid unrealistically low sea ice temperatures
 iz0tlnd                   = 0       ; thermal roughness length for sfclay and myjsfc (0 - old, 1 - veg dependent Czil)
 mp_tend_lim               = 10.,    ; limit on temp tendency from mp latent heating from radar data assimilation
 prec_acc_dt (max_dom)     = 0.,     ; number of minutes in precipitation bucket (ARW only) - will add three
                                       new 2d output fields: prec_acc_c, prec_acc_nc and snow_acc_nc
```

Options for wind turbine drag parameterization:

```
 td_turbgridid             = -1      ; which grid id has turbines in it
 td_hubheight              = 100.    ; hub height (m)
 td_diameter               = 60.     ; turbine diameter (m)
 td_stdthrcoef             = .158    ; standing thrust coefficient
 td_cutinspeed             = 4.      ; cut-in speed (m/s)
 td_cutoutspeed            = 27.     ; cut-out speed (m/s)
 td_power                  = 2.      ; turbine power (MW)
 td_turbpercell            = 1.      ; number of turbines per cell
 td_ewfx                   = 0       ; extent of wind farm in x-cells
 td_ewfy                   = 0       ; extent of wind farm in y-cells
 td_pwfx                   = 1       ; southwest corner of wind farm in x-cells
 td_pwfy                   = 1       ; southwest corner of wind farm in y-cells
```

Options for stochastic kinetic-energy backscatter scheme:

```
 stoch_force_opt (max_dom)       = 0,      : No stochastic parameterization
                                   1,      : Stochastic kinetic-energy backscatter scheme (SKEB)
 stoch_vertstruc_opt (max_dom)   = 0,      : Constant vertical structure of random pattern generator
                                   1,      : Random phase vertical structure random pattern generator
 tot_backscat_psi          = 115200, ; Controls amplitude of rotational wind perturbations
 tot_backscat_t            = 2.E-6   ; Controls amplitude of potential temperature perturbations
 nens                      = 1       ; an integer that controls the random number stream which will then
                                       change the run. When running an ensemble, this can be
                                       ensemble member number, so that each ensemble member gets a
                                       different random number stream, hence a different perturbed run.
```

```
 &dynamics
 rk_ord                    = 3,      ; time-integration scheme option:
                                       2 = Runge-Kutta 2nd order
                                       3 = Runge-Kutta 3rd order
 diff_opt                  = 0,      ; turbulence and mixing option:
                                       0 = no turbulence or explicit
                                          spatial numerical filters (km_opt IS IGNORED).
                                       1 = evaluates 2nd order
                                          diffusion term on coordinate surfaces.
                                          uses kvdif for vertical diff unless PBL option
                                          is used. may be used with km_opt = 1 and 4.
                                          (= 1, recommended for real-data cases)
                                       2 = evaluates mixing terms in
                                          physical space (stress form) (x,y,z).
                                          turbulence parameterization is chosen
                                          by specifying km_opt.
 km_opt                    = 1,      ; eddy coefficient option
```

```
                                1 = constant (use khdif kvdif)
                                2 = 1.5 order TKE closure (3D)
                                3 = Smagorinsky first order closure (3D)
                                   Note: option 2 and 3 are not recommended for DX > 2 km
                                4 = horizontal Smagorinsky first order closure
                                   (recommended for real-data cases)
 damp_opt                  = 0,     ; upper level damping flag
                                0 = without damping
                                1 = with diffusive damping, maybe used for real-data cases
                                   (dampcoef nondimensional ~0.01-0.1)
                                2 = with Rayleigh  damping (dampcoef inverse time scale [1/s] e.g. .003; idealized case
only
                                   not for real-data cases)
                                3 = with w-Rayleigh damping (dampcoef inverse time scale [1/s] e.g. .05;
                                   for real-data cases)
 diff_6th_opt              = 0,      ; 6th-order numerical diffusion
                                0 = no 6th-order diffusion (default)
                                1 = 6th-order numerical diffusion (not recommended)
                                2 = 6th-order numerical diffusion but prohibit up-gradient diffusion
 diff_6th_factor           = 0.12,   ; 6th-order numerical diffusion non-dimensional rate (max value 1.0
                                   corresponds to complete removal of 2dx wave in one timestep)
 dampcoef (max_dom)          = 0.,        ; damping coefficient (see above)
 zdamp (max_dom)           = 5000.,     ; damping depth (m) from model top
 w_damping                 = 0,      ; vertical velocity damping flag (for operational use)
                                0 = without damping
                                1 = with    damping
 base_temp                 = 290.,    ; real-data, em ONLY, base sea-level temp (K)
 base_pres                 = 10^5     ; real-data, em ONLY, base sea-level pres (Pa), DO NOT CHANGE
 base_lapse                = 50.,     ; real-data, em ONLY, lapse rate (K), DO NOT CHANGE
 iso_temp                  = 0.,      ; real-data, em ONLY, reference temp in stratosphere
 use_baseparam_fr_nml        = .f.,     ; whether to use base state parameters from the namelist
 khdif (max_dom)             = 0,; horizontal diffusion constant (m^2/s)
 kvdif (max_dom)             = 0,; vertical diffusion constant (m^2/s)
 smdiv (max_dom)             = 0.1,       ; divergence damping (0.1 is typical)
 emdiv (max_dom)             = 0.01,      ; external-mode filter coef for mass coordinate model
                               (0.01 is typical for real-data cases)
 epssm (max_dom)             = .1,        ; time off-centering for vertical sound waves
 non_hydrostatic (max_dom)       = .true., ; whether running the model in hydrostatic or non-hydro mode
 pert_coriolis (max_dom)       = .false.,   ; Coriolis only acts on wind perturbation (idealized)
 top_lid (max_dom)           = .false., ; Zero vertical motion at top of domain
 mix_full_fields(max_dom)        = .true.,  ; used with diff_opt = 2; value of ".true." is recommended, except for
                               highly idealized numerical tests; damp_opt must not be 1 if ".true."
                               is chosen. .false. means subtract 1-d base-state profile before mixing
 mix_isotropic(max_dom)          = 0       ; 0=anistropic vertical/horizontal diffusion coeffs, 1=isotropic
 mix_upper_bound(max_dom)        = 0.1     ; non-dimensional upper limit for diffusion coeffs
 tke_drag_coefficient(max_dom)   = 0.,     ; surface drag coefficient (Cd, dimensionless) for diff_opt=2 only
 tke_heat_flux(max_dom)          = 0.,     ; surface thermal flux (H/(rho*cp), K m/s) for diff_opt=2 only
 h_mom_adv_order (max_dom)       = 5,      ; horizontal momentum advection order (5=5th, etc.)
 v_mom_adv_order (max_dom)       = 3,      ; vertical momentum advection order
 h_sca_adv_order (max_dom)       = 5,      ; horizontal scalar advection order
 v_sca_adv_order (max_dom)       = 3,      ; vertical scalar advection order

                              ; advection options for scalar variables: 0=simple, 1=positive definite, 2=monotonic
 moist_adv_opt (max_dom)         = 1       ; for moisture
 scalar_adv_opt (max_dom)        = 1       ; for scalars
 chem_adv_opt (max_dom)          = 1       ; for chem variables
 tracer_adv_opt (max_dom)        = 1       ; for tracer variables (WRF-Chem activated)
 tke_adv_opt (max_dom)           = 1       ; for tke

 time_step_sound (max_dom)       = 4 /     ; number of sound steps per time-step (0=set automatically)
                               (if using a time_step much larger than 6*dx (in km),
                               proportionally increase number of sound steps - also
                               best to use even numbers)
```

```
 do_avgflx_em (max_dom)              = 0,      ; whether to output time-averaged mass-coupled advective velocities
                                     0 = no (default)
                                     1 = yes
 do_avgflx_cugd (max_dom)            = 0,      ; whether to output time-averaged convective mass-fluxes from Grell-
Devenyi ensemble scheme
                                     0 = no (default)
                                     1 = yes (only takes effect if do_avgflx_em=1 and cu_physics= 3
 do_coriolis (max_dom)               = .true.,    ; whether to do Coriolis calculations (idealized) (inactive)
 do_curvature (max_dom)              = .true.,  ; whether to do curvature calculations (idealized) (inactive)
 do_gradp (max_dom)                  = .true.,    ; whether to do horizontal pressure gradient calculations (idealized)
(inactive)
 fft_filter_lat                  = 45.     ; the latitude above which the polar filter is turned on

 gwd_opt                         = 0      ; for running without gravity wave drag
                                 = 1      ; for running the WRF-ARW with its gravity wave drag
                                 = 2      ; for running the WRF-NMM with its gravity wave drag
 sfs_opt (max_dom)                 = 0      ; nonlinear backscatter and anisotropy (NBA) off
                                 = 1      ; NBA1 using diagnostic stress terms (km_opt=2,3 for scalars)
                                 = 2      ; NBA2 using tke-based stress terms (km_opt=2 needed)
 m_opt (max_dom)                   = 0      ; no added output
                                 = 1      ; adds output of Mij stress terms when NBA is not used
 tracer_opt(max_dom)               = 0      ;

&bdy_control
 spec_bdy_width                  = 5,      ; total number of rows for specified boundary value nudging
 spec_zone                       = 1,      ; number of points in specified zone (spec b.c. option)
 relax_zone                      = 4,      ; number of points in relaxation zone (spec b.c. option)
 specified (max_dom)               = .false., ; specified boundary conditions (only can be used for domain 1)
                                    the above 4 are used for real-data runs
 spec_exp                        = 0.      ; exponential multiplier for relaxation zone ramp for specified=.t.
                                    (0.=linear ramp default, e.g. 0.33=~3*dx exp decay factor)
 constant_bc                     = .false.  ; constant boundary condition used with DFI

 periodic_x (max_dom)              = .false., ; periodic boundary conditions in x direction
 symmetric_xs (max_dom)              = .false., ; symmetric boundary conditions at x start (west)
 symmetric_xe (max_dom)              = .false., ; symmetric boundary conditions at x end (east)
 open_xs (max_dom)                 = .false., ; open boundary conditions at x start (west)
 open_xe (max_dom)                 = .false., ; open boundary conditions at x end (east)
 periodic_y (max_dom)              = .false., ; periodic boundary conditions in y direction
 symmetric_ys (max_dom)              = .false., ; symmetric boundary conditions at y start (south)
 symmetric_ye (max_dom)              = .false., ; symmetric boundary conditions at y end (north)
 open_ys (max_dom)                 = .false., ; open boundary conditions at y start (south)
 open_ye (max_dom)                 = .false., ; open boundary conditions at y end (north)
 nested (max_dom)                  = .false., ; nested boundary conditions (must be used for nests)
 polar                           = .false., ; polar boundary condition
                                    (v=0 at polarward-most v-point)
 euler_adv                       = .false., ; conservative Eulerian passive advection (NMM only)
 idtadt                          = 1,      ; fundamental timesteps between calls to Euler advection, dynamics (NMM only)
 idtadc                          = 1       ; fundamental timesteps between calls to Euler advection, chemistry (NMM only)


&tc                                ; controls for tc_em.exe ONLY, no impact on real, ndown, or model

 insert_bogus_storm                = .false.  ; T/F for inserting a bogus tropical storm (TC)
 remove_storm                    = .false.  ; T/F for only removing the original TC
 num_storm                       = 1        ; Number of bogus TC
 latc_loc                        = -999.    ; center latitude of the bogus TC
 lonc_loc                        = -999.    ; center longitude of the bogus TC
 vmax_meters_per_second(max_bogus)   = -999.    ; vmax of bogus storm in meters per second
 rmax                            = -999.    ; maximum radius outward from storm center
 vmax_ratio(max_bogus)             = -999.    ; ratio for representative maximum winds, 0.75 for 45 km grid, and
                                    0.9 for 15 km grid.
```

rankine_lid = -999. ; top pressure limit for the tc bogus scheme

&namelist_quilt This namelist record controls asynchronized I/O for MPI applications.

nio_tasks_per_group = 0, default value is 0: no quilting; > 0 quilting I/O
nio_groups = 1, default 1, don't change

&grib2:
background_proc_id = 255, ; Background generating process identifier, typically defined by the originating center to identify the background data that was used in creating the data. This is octet 13 of Section 4 in the grib2 message
forecast_proc_id = 255, ; Analysis or generating forecast process identifier, typically defined by the originating center to identify the forecast process that was used to generate the data. This is octet 14 of Section 4 in the grib2 message
production_status = 255, ; Production status of processed data in the grib2 message. See Code Table 1.3 of the grib2 manual. This is octet 20 of Section 1 in the grib2 record
compression = 40, ; The compression method to encode the output grib2 message. Only 40 for jpeg2000 or 41 for PNG are supported

Appendix B

WRF namelist used for coupled and forced experiments

Namelist used for coupled and forced experiments

```
&time_control
 run_days                  = 0,
 run_hours                 = RUNHOURS,
 run_minutes               = 0,
 run_seconds               = 0,
 start_year                = STARTYEAR,STARTYEAR,
 start_month               = STARTMONTH,STARTMONTH,
 start_day                 = STARTDAY,STARTDAY,
 start_hour                = STARTHOUR,STARTHOUR,
 start_minute              = 00,00,
 start_second              = 00,00,
 end_year                  = ENDYEAR,ENDYEAR,
 end_month                 = ENDMONTH,ENDMONTH,
 end_day                   = ENDDAY,ENDDAY,
 end_hour                  = ENDHOUR,ENDHOUR,
 end_minute                = 00,00,
 end_second                = 00,00,
 interval_seconds          = 10800
 input_from_file           = .TRUE.,.TRUE.,
 history_interval          = 30,30,
 frames_per_outfile        = 150,150,
 restart                   = IFRESTART,
 restart_interval          = RSTARTH,
 io_form_history           = 2,
 io_form_restart           = 2,
 io_form_input             = 2,
 io_form_boundary          = 2,
 debug_level               = 0,
 auxinput4_inname          = "wrflowinp_d<domain>",
 auxinput4_interval        = 180,180,180,
 auxinput4_end_h           = RUNHOURS
 io_form_auxinput4         = 2
 iofields_filename         = "myoutfields.txt", "myoutfields.txt"
 ignore_iofields_warning   = .true.,
 override_restart_timers   = .true.,
/

 &domains
 time_step                 = 300,
 time_step_fract_num       = 0,
 time_step_fract_den       = 1,
 max_dom                   = 2,
 s_we                      = 1,1,
 e_we                      = 158,190,1,
 s_sn                      = 1,1,
 e_sn                      = 72,100,1,
 s_vert                    = 1,1,
 e_vert                    = 31,31,
 num_metgrid_levels        = 18
 dx                        = 105000., 35000., 1,
 dy                        = 105000., 35000., 1,
 grid_id                   = 1,2,3,
 parent_id                 = 0,1,2,
 i_parent_start            = 0,53,30
 j_parent_start            = 0,14,21
 parent_grid_ratio         = 1,3,6,
```

```
parent_time_step_ratio              = 1,3,6,
feedback                            = 1,
smooth_option                       = 2
/

&physics
mp_physics                          = 3,3,
ra_lw_physics                       = 1,1,
ra_sw_physics                       = 1,1,
radt                                = 30,30,
sf_sfclay_physics                   = 1,1,
sf_surface_physics                  = 2,2,
bl_pbl_physics                      = 1,1,
bldt                                = 0,0,
cu_physics                          = 2,2,
cudt                                = 0,0,
isfflx                              = 1,
ifsnow                              = 0,
icloud                              = 1,
surface_input_source                = 1,
sst_update                          = 1,
isftcflx                            = 2,
tmn_update                          = 1,
sst_skin                            = 1,
num_soil_layers                     = 4,
maxiens                             = 1,
maxens                              = 3,
maxens2                             = 3,
maxens3                             = 16,
ensdim                              = 144,
/

&dynamics
dyn_opt                             = 2,
rk_ord                              = 3,
damp_opt                            = 0,
zdamp                               = 5000.,5000.,
dampcoef                            = 0.01,0.1,
w_damping                           = 1,
diff_opt                            = 1,
km_opt                              = 4,
khdif                               = 0,0,
kvdif                               = 0,0,
smdiv                               = 0.1,0.1,
emdiv                               = 0.01,0.01,
epssm                               = 0.1,0.1,
non_hydrostatic                     = .true.,.true.,
time_step_sound                     = 4,4,
h_mom_adv_order                     = 5,5,
v_mom_adv_order                     = 3,3,
h_sca_adv_order                     = 5,5,
v_sca_adv_order                     = 3,3,
moist_adv_opt                       = 1,1,
gwd_opt                             = 1,
/

&bdy_control
spec_bdy_width                      = 10,
spec_zone                           = 1,
relax_zone                          = 9,
```

```
spec_exp                 = 0.33,
specified                = .true., .false.,
periodic_x               = .false., .false.,
symmetric_xs             = .false., .false.,
symmetric_xe             = .false., .false.,
open_xs                  = .false., .false.,
open_xe                  = .false., .false.,
periodic_y               = .false., .false.,
symmetric_ys             = .false., .false.,
symmetric_ye             = .false., .false.,
open_ys                  = .false., .false.,
open_ye                  = .false., .false.,
nested                   = .false., .true.,
/

&namelist_quilt
nio_tasks_per_group      = 0,
nio_groups               = 1,
/

&fdda
/

&grib2
/
```

Appendix C

Statistical tables

Tables statistiques

1 Fonction de répartition de la loi normale centrée réduite

Si U suit la loi normale centrée réduite, pour $x \geq 0$, la table donne la valeur $\phi(x) = P(U \leq x)$ avec $x = x_1 + x_2$ où x_1 et x_2 sont indiqués en marge. Pour $x < 0$, on utilise $\phi(x) = 1 - \phi(-x)$.

	x_1									
x_2	**0.00**	**0.01**	**0.02**	**0.03**	**0.04**	**0.05**	**0.06**	**0.07**	**0.08**	**0.09**
0.0	0.5000	0.5040	0.5080	0.5120	0.5160	0.5199	0.5239	0.5279	0.5319	0.5359
0.1	0.5398	0.5438	0.5478	0.5517	0.5557	0.5596	0.5636	0.5675	0.5714	0.5753
0.2	0.5793	0.5832	0.5871	0.5910	0.5948	0.5987	0.6026	0.6064	0.6103	0.6141
0.3	0.6179	0.6217	0.6255	0.6293	0.6331	0.6368	0.6406	0.6443	0.6480	0.6517
0.4	0.6554	0.6591	0.6628	0.6664	0.6700	0.6736	0.6772	0.6808	0.6844	0.6879
0.5	0.6915	0.6950	0.6985	0.7019	0.7054	0.7088	0.7123	0.7157	0.7190	0.7224
0.6	0.7257	0.7291	0.7324	0.7357	0.7389	0.7422	0.7454	0.7486	0.7517	0.7549
0.7	0.7580	0.7611	0.7642	0.7673	0.7704	0.7734	0.7764	0.7794	0.7823	0.7852
0.8	0.7881	0.7910	0.7939	0.7967	0.7995	0.8023	0.8051	0.8078	0.8106	0.8133
0.9	0.8159	0.8186	0.8212	0.8238	0.8264	0.8289	0.8315	0.8340	0.8365	0.8389
1.0	0.8413	0.8438	0.8461	0.8485	0.8508	0.8531	0.8554	0.8577	0.8599	0.8621
1.1	0.8643	0.8665	0.8686	0.8708	0.8729	0.8749	0.8770	0.8790	0.8810	0.8830
1.2	0.8849	0.8869	0.8888	0.8907	0.8925	0.8944	0.8962	0.8980	0.8997	0.9015
1.3	0.9032	0.9049	0.9066	0.9082	0.9099	0.9115	0.9131	0.9147	0.9162	0.9177
1.4	0.9192	0.9207	0.9222	0.9236	0.9251	0.9265	0.9279	0.9292	0.9306	0.9319
1.5	0.9332	0.9345	0.9357	0.9370	0.9382	0.9394	0.9406	0.9418	0.9429	0.9441
1.6	0.9452	0.9463	0.9474	0.9484	0.9495	0.9505	0.9515	0.9525	0.9535	0.9545
1.7	0.9554	0.9564	0.9573	0.9582	0.9591	0.9599	0.9608	0.9616	0.9625	0.9633
1.8	0.9641	0.9649	0.9656	0.9664	0.9671	0.9678	0.9686	0.9693	0.9699	0.9706
1.9	0.9713	0.9719	0.9726	0.9732	0.9738	0.9744	0.9750	0.9756	0.9761	0.9767
2.0	0.9772	0.9778	0.9783	0.9788	0.9793	0.9798	0.9803	0.9808	0.9812	0.9817
2.1	0.9821	0.9826	0.9830	0.9834	0.9838	0.9842	0.9846	0.9850	0.9854	0.9857
2.2	0.9861	0.9864	0.9868	0.9871	0.9875	0.9878	0.9881	0.9884	0.9887	0.9890
2.3	0.9893	0.9896	0.9898	0.9901	0.9904	0.9906	0.9909	0.9911	0.9913	0.9916
2.4	0.9918	0.9920	0.9922	0.9925	0.9927	0.9929	0.9931	0.9932	0.9934	0.9936
2.5	0.9938	0.9940	0.9941	0.9943	0.9945	0.9946	0.9948	0.9949	0.9951	0.9952
2.6	0.9953	0.9955	0.9956	0.9957	0.9959	0.9960	0.9961	0.9962	0.9963	0.9964
2.7	0.9965	0.9966	0.9967	0.9968	0.9969	0.9970	0.9971	0.9972	0.9973	0.9974
2.8	0.9974	0.9975	0.9976	0.9977	0.9977	0.9978	0.9979	0.9979	0.9980	0.9981
2.9	0.9981	0.9982	0.9982	0.9983	0.9984	0.9984	0.9985	0.9985	0.9986	0.9986
3.0	0.9987	0.9987	0.9987	0.9988	0.9988	0.9989	0.9989	0.9989	0.9990	0.9990
3.1	0.9990	0.9991	0.9991	0.9991	0.9992	0.9992	0.9992	0.9992	0.9993	0.9993
3.2	0.9993	0.9993	0.9994	0.9994	0.9994	0.9994	0.9994	0.9995	0.9995	0.9995
3.3	0.9995	0.9995	0.9995	0.9996	0.9996	0.9996	0.9996	0.9996	0.9996	0.9997
3.4	0.9997	0.9997	0.9997	0.9997	0.9997	0.9997	0.9997	0.9997	0.9997	0.9998
3.5	0.9998	0.9998	0.9998	0.9998	0.9998	0.9998	0.9998	0.9998	0.9998	0.9998
3.6	0.9998	0.9998	0.9999	0.9999	0.9999	0.9999	0.9999	0.9999	0.9999	0.9999
3.7	0.9999	0.9999	0.9999	0.9999	0.9999	0.9999	0.9999	0.9999	0.9999	0.9999
3.8	0.9999	0.9999	0.9999	0.9999	0.9999	0.9999	0.9999	0.9999	0.9999	0.9999
3.9	1.0000	1.0000	1.0000	1.0000	1.0000	1.0000	1.0000	1.0000	1.0000	1.0000

2 Fractiles de la loi normale centrée réduite

u_p est le fractile d'ordre p de la loi normale centrée réduite. Donc $\phi(u_p) = p$.
La table donne la valeur u_p pour $p = p_1 + p_2$ avec p_1 et p_2 indiqués en marge.
Pour les valeurs $p < 0,5$, on utilise la relation $u_p = -u_{1-p}$.

	p_1									
p_2	**0.000**	**0.001**	**0.002**	**0.003**	**0.004**	**0.005**	**0.006**	**0.007**	**0.008**	**0.009**
0.50	0.0000	0.0025	0.0050	0.0075	0.0100	0.0125	0.0150	0.0175	0.0201	0.0226
0.51	0.0251	0.0276	0.0301	0.0326	0.0351	0.0376	0.0401	0.0426	0.0451	0.0476
0.52	0.0502	0.0527	0.0552	0.0577	0.0602	0.0627	0.0652	0.0677	0.0702	0.0728
0.53	0.0753	0.0778	0.0803	0.0828	0.0853	0.0878	0.0904	0.0929	0.0954	0.0979
0.54	0.1004	0.1030	0.1055	0.1080	0.1105	0.1130	0.1156	0.1181	0.1206	0.1231
0.55	0.1257	0.1282	0.1307	0.1332	0.1358	0.1383	0.1408	0.1434	0.1459	0.1484
0.56	0.1510	0.1535	0.1560	0.1586	0.1611	0.1637	0.1662	0.1687	0.1713	0.1738
0.57	0.1764	0.1789	0.1815	0.1840	0.1866	0.1891	0.1917	0.1942	0.1968	0.1993
0.58	0.2019	0.2045	0.2070	0.2096	0.2121	0.2147	0.2173	0.2198	0.2224	0.2250
0.59	0.2275	0.2301	0.2327	0.2353	0.2378	0.2404	0.2430	0.2456	0.2482	0.2508
0.60	0.2533	0.2559	0.2585	0.2611	0.2637	0.2663	0.2689	0.2715	0.2741	0.2767
0.61	0.2793	0.2819	0.2845	0.2871	0.2898	0.2924	0.2950	0.2976	0.3002	0.3029
0.62	0.3055	0.3081	0.3107	0.3134	0.3160	0.3186	0.3213	0.3239	0.3266	0.3292
0.63	0.3319	0.3345	0.3372	0.3398	0.3425	0.3451	0.3478	0.3505	0.3531	0.3558
0.64	0.3585	0.3611	0.3638	0.3665	0.3692	0.3719	0.3745	0.3772	0.3799	0.3826
0.65	0.3853	0.3880	0.3907	0.3934	0.3961	0.3989	0.4016	0.4043	0.4070	0.4097
0.66	0.4125	0.4152	0.4179	0.4207	0.4234	0.4261	0.4289	0.4316	0.4344	0.4372
0.67	0.4399	0.4427	0.4454	0.4482	0.4510	0.4538	0.4565	0.4593	0.4621	0.4649
0.68	0.4677	0.4705	0.4733	0.4761	0.4789	0.4817	0.4845	0.4874	0.4902	0.4930
0.69	0.4959	0.4987	0.5015	0.5044	0.5072	0.5101	0.5129	0.5158	0.5187	0.5215
0.70	0.5244	0.5273	0.5302	0.5330	0.5359	0.5388	0.5417	0.5446	0.5476	0.5505
0.71	0.5534	0.5563	0.5592	0.5622	0.5651	0.5681	0.5710	0.5740	0.5769	0.5799
0.72	0.5828	0.5858	0.5888	0.5918	0.5948	0.5978	0.6008	0.6038	0.6068	0.6098
0.73	0.6128	0.6158	0.6189	0.6219	0.6250	0.6280	0.6311	0.6341	0.6372	0.6403
0.74	0.6433	0.6464	0.6495	0.6526	0.6557	0.6588	0.6620	0.6651	0.6682	0.6713
0.75	0.6745	0.6776	0.6808	0.6840	0.6871	0.6903	0.6935	0.6967	0.6999	0.7031
0.76	0.7063	0.7095	0.7128	0.7160	0.7192	0.7225	0.7257	0.7290	0.7323	0.7356
0.77	0.7388	0.7421	0.7454	0.7488	0.7521	0.7554	0.7588	0.7621	0.7655	0.7688
0.78	0.7722	0.7756	0.7790	0.7824	0.7858	0.7892	0.7926	0.7961	0.7995	0.8030
0.79	0.8064	0.8099	0.8134	0.8169	0.8204	0.8239	0.8274	0.8310	0.8345	0.8381
0.80	0.8416	0.8452	0.8488	0.8524	0.8560	0.8596	0.8633	0.8669	0.8705	0.8742
0.81	0.8779	0.8816	0.8853	0.8890	0.8927	0.8965	0.9002	0.9040	0.9078	0.9116
0.82	0.9154	0.9192	0.9230	0.9269	0.9307	0.9346	0.9385	0.9424	0.9463	0.9502
0.83	0.9542	0.9581	0.9621	0.9661	0.9701	0.9741	0.9782	0.9822	0.9863	0.9904
0.84	0.9945	0.9986	1.0027	1.0069	1.0110	1.0152	1.0194	1.0237	1.0279	1.0322
0.85	1.0364	1.0407	1.0450	1.0494	1.0537	1.0581	1.0625	1.0669	1.0714	1.0758
0.86	1.0803	1.0848	1.0893	1.0939	1.0985	1.1031	1.1077	1.1123	1.1170	1.1217
0.87	1.1264	1.1311	1.1359	1.1407	1.1455	1.1503	1.1552	1.1601	1.1650	1.1700
0.88	1.1750	1.1800	1.1850	1.1901	1.1952	1.2004	1.2055	1.2107	1.2160	1.2212
0.89	1.2265	1.2319	1.2372	1.2426	1.2481	1.2536	1.2591	1.2646	1.2702	1.2759
0.90	1.2816	1.2873	1.2930	1.2988	1.3047	1.3106	1.3165	1.3225	1.3285	1.3346
0.91	1.3408	1.3469	1.3532	1.3595	1.3658	1.3722	1.3787	1.3852	1.3917	1.3984
0.92	1.4051	1.4118	1.4187	1.4255	1.4325	1.4395	1.4466	1.4538	1.4611	1.4684
0.93	1.4758	1.4833	1.4909	1.4985	1.5063	1.5141	1.5220	1.5301	1.5382	1.5464
0.94	1.5548	1.5632	1.5718	1.5805	1.5893	1.5982	1.6072	1.6164	1.6258	1.6352
0.95	1.6449	1.6546	1.6646	1.6747	1.6849	1.6954	1.7060	1.7169	1.7279	1.7392
0.96	1.7507	1.7624	1.7744	1.7866	1.7991	1.8119	1.8250	1.8384	1.8522	1.8663
0.97	1.8808	1.8957	1.9110	1.9268	1.9431	1.9600	1.9774	1.9954	2.0141	2.0335
0.98	2.0537	2.0749	2.0969	2.1201	2.1444	2.1701	2.1973	2.2262	2.2571	2.2904
0.99	2.3263	2.3656	2.4089	2.4573	2.5121	2.5758	2.6521	2.7478	2.8782	3.0902

3 Fractiles de la loi de Student

$t_{\nu,p}$ est le fractile d'ordre p de la loi de Student à ν degrés de liberté.
Pour les valeurs de $p \leq 0,5$, on utilise la relation $t_{\nu,p} = -t_{\nu,1-p}$.
Lorsque $\nu > 50$, on utilise l'approximation de la loi de Student par la loi normale $\mathcal{N}(0,1)$, ce qui revient à : $t_{\nu,p} \approx u_p$.

						p				
ν	**0.60**	**0.70**	**0.80**	**0.90**	**0.95**	**0.9750**	**0.9900**	**0.9950**	**0.9990**	**0.9995**
1	0.325	0.727	1.376	3.078	6.314	12.706	31.821	63.657	318.309	636.619
2	0.289	0.617	1.061	1.886	2.920	4.303	6.965	9.925	22.327	31.599
3	0.277	0.584	0.978	1.638	2.353	3.182	4.541	5.841	10.215	12.924
4	0.271	0.569	0.941	1.533	2.132	2.776	3.747	4.604	7.173	8.610
5	0.267	0.559	0.920	1.476	2.015	2.571	3.365	4.032	5.893	6.869
6	0.265	0.553	0.906	1.440	1.943	2.447	3.143	3.707	5.208	5.959
7	0.263	0.549	0.896	1.415	1.895	2.365	2.998	3.499	4.785	5.408
8	0.262	0.546	0.889	1.397	1.860	2.306	2.896	3.355	4.501	5.041
9	0.261	0.543	0.883	1.383	1.833	2.262	2.821	3.250	4.297	4.781
10	0.260	0.542	0.879	1.372	1.812	2.228	2.764	3.169	4.144	4.587
11	0.260	0.540	0.876	1.363	1.796	2.201	2.718	3.106	4.025	4.437
12	0.259	0.539	0.873	1.356	1.782	2.179	2.681	3.055	3.930	4.318
13	0.259	0.538	0.870	1.350	1.771	2.160	2.650	3.012	3.852	4.221
14	0.258	0.537	0.868	1.345	1.761	2.145	2.624	2.977	3.787	4.140
15	0.258	0.536	0.866	1.341	1.753	2.131	2.602	2.947	3.733	4.073
16	0.258	0.535	0.865	1.337	1.746	2.120	2.583	2.921	3.686	4.015
17	0.257	0.534	0.863	1.333	1.740	2.110	2.567	2.898	3.646	3.965
18	0.257	0.534	0.862	1.330	1.734	2.101	2.552	2.878	3.610	3.922
19	0.257	0.533	0.861	1.328	1.729	2.093	2.539	2.861	3.579	3.883
20	0.257	0.533	0.860	1.325	1.725	2.086	2.528	2.845	3.552	3.850
21	0.257	0.532	0.859	1.323	1.721	2.080	2.518	2.831	3.527	3.819
22	0.256	0.532	0.858	1.321	1.717	2.074	2.508	2.819	3.505	3.792
23	0.256	0.532	0.858	1.319	1.714	2.069	2.500	2.807	3.485	3.768
24	0.256	0.531	0.857	1.318	1.711	2.064	2.492	2.797	3.467	3.745
25	0.256	0.531	0.856	1.316	1.708	2.060	2.485	2.787	3.450	3.725
26	0.256	0.531	0.856	1.315	1.706	2.056	2.479	2.779	3.435	3.707
27	0.256	0.531	0.855	1.314	1.703	2.052	2.473	2.771	3.421	3.690
28	0.256	0.530	0.855	1.313	1.701	2.048	2.467	2.763	3.408	3.674
29	0.256	0.530	0.854	1.311	1.699	2.045	2.462	2.756	3.396	3.659
30	0.256	0.530	0.854	1.310	1.697	2.042	2.457	2.750	3.385	3.646
31	0.256	0.530	0.853	1.309	1.696	2.040	2.453	2.744	3.375	3.633
32	0.255	0.530	0.853	1.309	1.694	2.037	2.449	2.738	3.365	3.622
33	0.255	0.530	0.853	1.308	1.692	2.035	2.445	2.733	3.356	3.611
34	0.255	0.529	0.852	1.307	1.691	2.032	2.441	2.728	3.348	3.601
35	0.255	0.529	0.852	1.306	1.690	2.030	2.438	2.724	3.340	3.591
36	0.255	0.529	0.852	1.306	1.688	2.028	2.434	2.719	3.333	3.582
37	0.255	0.529	0.851	1.305	1.687	2.026	2.431	2.715	3.326	3.574
38	0.255	0.529	0.851	1.304	1.686	2.024	2.429	2.712	3.319	3.566
39	0.255	0.529	0.851	1.304	1.685	2.023	2.426	2.708	3.313	3.558
40	0.255	0.529	0.851	1.303	1.684	2.021	2.423	2.704	3.307	3.551
41	0.255	0.529	0.850	1.303	1.683	2.020	2.421	2.701	3.301	3.544
42	0.255	0.528	0.850	1.302	1.682	2.018	2.418	2.698	3.296	3.538
43	0.255	0.528	0.850	1.302	1.681	2.017	2.416	2.695	3.291	3.532
44	0.255	0.528	0.850	1.301	1.680	2.015	2.414	2.692	3.286	3.526
45	0.255	0.528	0.850	1.301	1.679	2.014	2.412	2.690	3.281	3.520
46	0.255	0.528	0.850	1.300	1.679	2.013	2.410	2.687	3.277	3.515
47	0.255	0.528	0.849	1.300	1.678	2.012	2.408	2.685	3.273	3.510
48	0.255	0.528	0.849	1.299	1.677	2.011	2.407	2.682	3.269	3.505
49	0.255	0.528	0.849	1.299	1.677	2.010	2.405	2.680	3.265	3.500
50	0.255	0.528	0.849	1.299	1.676	2.009	2.403	2.678	3.261	3.496

4 Fractiles de la loi du χ^2

$\chi^2_{\nu,p}$ est le fractile d'ordre p de la loi du χ^2.

Pour les valeurs de $\nu > 50$, on utilise l'approximation $\chi^2_{\nu,p} \approx \dfrac{(u_p + \sqrt{2\nu - 1})^2}{2}$

	p												
ν	**0.001**	**0.005**	**0.010**	**0.025**	**0.05**	**0.1000**	**0.5000**	**0.9000**	**0.9500**	**0.9750**	**0.9900**	**0.9950**	**0.9990**
1	0.000	0.000	0.000	0.001	0.004	0.016	0.455	2.706	3.841	5.024	6.635	7.879	10.828
2	0.002	0.010	0.020	0.051	0.103	0.211	1.386	4.605	5.991	7.378	9.210	10.597	13.816
3	0.024	0.072	0.115	0.216	0.352	0.584	2.366	6.251	7.815	9.348	11.345	12.838	16.266
4	0.091	0.207	0.297	0.484	0.711	1.064	3.357	7.779	9.488	11.143	13.277	14.860	18.467
5	0.210	0.412	0.554	0.831	1.145	1.610	4.351	9.236	11.070	12.833	15.086	16.750	20.515
6	0.381	0.676	0.872	1.237	1.635	2.204	5.348	10.645	12.592	14.449	16.812	18.548	22.458
7	0.598	0.989	1.239	1.690	2.167	2.833	6.346	12.017	14.067	16.013	18.475	20.278	24.322
8	0.857	1.344	1.646	2.180	2.733	3.490	7.344	13.362	15.507	17.535	20.090	21.955	26.124
9	1.152	1.735	2.088	2.700	3.325	4.168	8.343	14.684	16.919	19.023	21.666	23.589	27.877
10	1.479	2.156	2.558	3.247	3.940	4.865	9.342	15.987	18.307	20.483	23.209	25.188	29.588
11	1.834	2.603	3.053	3.816	4.575	5.578	10.341	17.275	19.675	21.920	24.725	26.757	31.264
12	2.214	3.074	3.571	4.404	5.226	6.304	11.340	18.549	21.026	23.337	26.217	28.300	32.909
13	2.617	3.565	4.107	5.009	5.892	7.042	12.340	19.812	22.362	24.736	27.688	29.819	34.528
14	3.041	4.075	4.660	5.629	6.571	7.790	13.339	21.064	23.685	26.119	29.141	31.319	36.123
15	3.483	4.601	5.229	6.262	7.261	8.547	14.339	22.307	24.996	27.488	30.578	32.801	37.697
16	3.942	5.142	5.812	6.908	7.962	9.312	15.338	23.542	26.296	28.845	32.000	34.267	39.252
17	4.416	5.697	6.408	7.564	8.672	10.085	16.338	24.769	27.587	30.191	33.409	35.718	40.790
18	4.905	6.265	7.015	8.231	9.390	10.865	17.338	25.989	28.869	31.526	34.805	37.156	42.312
19	5.407	6.844	7.633	8.907	10.117	11.651	18.338	27.204	30.144	32.852	36.191	38.582	43.820
20	5.921	7.434	8.260	9.591	10.851	12.443	19.337	28.412	31.410	34.170	37.566	39.997	45.315
21	6.447	8.034	8.897	10.283	11.591	13.240	20.337	29.615	32.671	35.479	38.932	41.401	46.797
22	6.983	8.643	9.542	10.982	12.338	14.041	21.337	30.813	33.924	36.781	40.289	42.796	48.268
23	7.529	9.260	10.196	11.689	13.091	14.848	22.337	32.007	35.172	38.076	41.638	44.181	49.728
24	8.085	9.886	10.856	12.401	13.848	15.659	23.337	33.196	36.415	39.364	42.980	45.559	51.179
25	8.649	10.520	11.524	13.120	14.611	16.473	24.337	34.382	37.652	40.646	44.314	46.928	52.620
26	9.222	11.160	12.198	13.844	15.379	17.292	25.336	35.563	38.885	41.923	45.642	48.290	54.052
27	9.803	11.808	12.879	14.573	16.151	18.114	26.336	36.741	40.113	43.195	46.963	49.645	55.476
28	10.391	12.461	13.565	15.308	16.928	18.939	27.336	37.916	41.337	44.461	48.278	50.993	56.892
29	10.986	13.121	14.256	16.047	17.708	19.768	28.336	39.087	42.557	45.722	49.588	52.336	58.301
30	11.588	13.787	14.953	16.791	18.493	20.599	29.336	40.256	43.773	46.979	50.892	53.672	59.703
31	12.196	14.458	15.655	17.539	19.281	21.434	30.336	41.422	44.985	48.232	52.191	55.003	61.098
32	12.811	15.134	16.362	18.291	20.072	22.271	31.336	42.585	46.194	49.480	53.486	56.328	62.487
33	13.431	15.815	17.074	19.047	20.867	23.110	32.336	43.745	47.400	50.725	54.776	57.648	63.870
34	14.057	16.501	17.789	19.806	21.664	23.952	33.336	44.903	48.602	51.966	56.061	58.964	65.247
35	14.688	17.192	18.509	20.569	22.465	24.797	34.336	46.059	49.802	53.203	57.342	60.275	66.619
36	15.324	17.887	19.233	21.336	23.269	25.643	35.336	47.212	50.998	54.437	58.619	61.581	67.985
37	15.965	18.586	19.960	22.106	24.075	26.492	36.336	48.363	52.192	55.668	59.893	62.883	69.346
38	16.611	19.289	20.691	22.878	24.884	27.343	37.335	49.513	53.384	56.896	61.162	64.181	70.703
39	17.262	19.996	21.426	23.654	25.695	28.196	38.335	50.660	54.572	58.120	62.428	65.476	72.055
40	17.916	20.707	22.164	24.433	26.509	29.051	39.335	51.805	55.758	59.342	63.691	66.766	73.402
41	18.575	21.421	22.906	25.215	27.326	29.907	40.335	52.949	56.942	60.561	64.950	68.053	74.745
42	19.239	22.138	23.650	25.999	28.144	30.765	41.335	54.090	58.124	61.777	66.206	69.336	76.084
43	19.906	22.859	24.398	26.785	28.965	31.625	42.335	55.230	59.304	62.990	67.459	70.616	77.419
44	20.576	23.584	25.148	27.575	29.787	32.487	43.335	56.369	60.481	64.201	68.710	71.893	78.750
45	21.251	24.311	25.901	28.366	30.612	33.350	44.335	57.505	61.656	65.410	69.957	73.166	80.077
46	21.929	25.041	26.657	29.160	31.439	34.215	45.335	58.641	62.830	66.617	71.201	74.437	81.400
47	22.610	25.775	27.416	29.956	32.268	35.081	46.335	59.774	64.001	67.821	72.443	75.704	82.720
48	23.295	26.511	28.177	30.755	33.098	35.949	47.335	60.907	65.171	69.023	73.683	76.969	84.037
49	23.983	27.249	28.941	31.555	33.930	36.818	48.335	62.038	66.339	70.222	74.919	78.231	85.351
50	24.674	27.991	29.707	32.357	34.764	37.689	49.335	63.167	67.505	71.420	76.154	79.490	86.661

5 Fractiles de la loi de Fisher-Snédécor

$f_{\nu_1,\nu_2,p}$ est le fractile d'ordre p de la loi de Fisher-Snédécor à ν_1 et ν_2 degrés de liberté.
Les tables statistiques qui suivent donnent les valeurs de $f_{\nu_1,\nu_2,p}$ pour $p \in \{0,90; 0,95; 0,975; 0,99\}$.
Pour $p \in \{0,01; 0,025; 0,05; 0,10\}$, on utilise la relation $f_{\nu_1,\nu_2,p} = 1/f_{\nu_2,\nu_1,1-p}$.

ν_2	$\nu_1 \rightarrow$	2	3	4	5	6	7	8	10	12	15	20	30	50	∞
$\downarrow$	p														
1	0.900	49.5	53.6	55.8	57.2	58.2	59.1	59.7	60.5	61.0	61.5	62.0	62.6	63.0	63.3
	0.950	199.	216.	225.	230.	234.	237.	239.	242.	244.	246.	248.	250.	252.	254.
	0.975	800.	864.	900.	922.	937.	948.	957.	969.	977.	985.	993.			
	0.990														
	0.999														
2	0.900	9.00	9.16	9.24	9.29	9.33	9.35	9.37	9.39	9.41	9.43	9.44	9.46	9.47	9.49
	0.950	19.0	19.2	19.2	19.3	19.3	19.4	19.4	19.4	19.4	19.4	19.4	19.5	19.5	19.5
	0.975	39.0	39.2	39.2	39.3	39.3	39.4	39.4	39.4	39.4	39.4	39.4	39.5	39.5	39.5
	0.990	99.0	99.2	99.2	99.3	99.3	99.4	100.	100.	100.	100.	100.	100.	100.	99.5
	0.999	999.	999.												
3	0.900	5.46	5.39	5.34	5.31	5.28	5.27	5.25	5.23	5.22	5.20	5.18	5.17	5.15	5.13
	0.950	9.55	9.28	9.12	9.01	8.94	8.89	8.85	8.79	8.74	8.70	8.66	8.62	8.58	8.53
	0.975	16.0	15.4	15.1	14.9	14.7	14.6	14.5	14.4	14.3	14.3	14.2	14.1	14.0	13.9
	0.990	30.8	29.5	28.7	28.2	27.9	27.7	27.5	27.2	27.1	26.9	26.7	26.5	26.4	26.1
	0.999	149.	141.	137.	135.	133.	132.	131.	129.	128.	127.	126.	125.	125.	123.
4	0.900	4.32	4.19	4.11	4.05	4.01	3.98	3.95	3.92	3.90	3.87	3.84	3.82	3.79	3.76
	0.950	6.94	6.59	6.39	6.26	6.16	6.09	6.04	5.96	5.91	5.86	5.80	5.75	5.70	5.63
	0.975	10.6	9.98	9.60	9.36	9.20	9.07	8.98	8.84	8.75	8.66	8.56	8.46	8.38	8.26
	0.990	18.0	16.7	16.0	15.5	15.2	15.0	14.8	14.5	14.4	14.2	14.0	13.8	13.7	13.5
	0.999	61.2	56.2	53.4	51.7	50.5	49.7	49.0	48.0	47.4	46.8	46.1	45.4	44.9	44.1
5	0.900	3.78	3.62	3.52	3.45	3.40	3.37	3.34	3.30	3.27	3.24	3.21	3.17	3.15	3.10
	0.950	5.79	5.41	5.19	5.05	4.95	4.88	4.82	4.74	4.68	4.62	4.56	4.50	4.44	4.36
	0.975	8.43	7.76	7.39	7.15	6.98	6.85	6.76	6.62	6.52	6.43	6.33	6.23	6.14	6.02
	0.990	13.3	12.1	11.4	11.0	10.7	10.5	10.3	10.1	9.89	9.72	9.55	9.38	9.24	9.02
	0.999	37.1	33.2	31.1	29.8	28.8	28.2	27.6	26.9	26.4	25.9	25.4	24.9	24.4	23.8
6	0.900	3.46	3.29	3.18	3.11	3.05	3.01	2.98	2.94	2.90	2.87	2.84	2.80	2.77	2.72
	0.950	5.14	4.76	4.53	4.39	4.28	4.21	4.15	4.06	4.00	3.94	3.87	3.81	3.75	3.67
	0.975	7.26	6.60	6.23	5.99	5.82	5.70	5.60	5.46	5.37	5.27	5.17	5.07	4.98	4.85
	0.990	10.9	9.78	9.15	8.75	8.47	8.26	8.10	7.87	7.72	7.56	7.40	7.23	7.09	6.88
	0.999	27.0	23.7	21.9	20.8	20.0	19.5	19.0	18.4	18.0	17.6	17.1	16.7	16.3	15.7
7	0.900	3.26	3.07	2.96	2.88	2.83	2.78	2.75	2.70	2.67	2.63	2.59	2.56	2.52	2.47
	0.950	4.74	4.35	4.12	3.97	3.87	3.79	3.73	3.64	3.57	3.51	3.44	3.38	3.32	3.23
	0.975	6.54	5.89	5.52	5.29	5.12	4.99	4.90	4.76	4.67	4.57	4.47	4.36	4.28	4.14
	0.990	9.55	8.45	7.85	7.46	7.19	6.99	6.84	6.62	6.47	6.31	6.16	5.99	5.86	5.65
	0.999	21.7	18.8	17.2	16.2	15.5	15.0	14.6	14.1	13.7	13.3	12.9	12.5	12.2	11.7
8	0.900	3.11	2.92	2.81	2.73	2.67	2.62	2.59	2.54	2.50	2.46	2.42	2.38	2.35	2.29
	0.950	4.46	4.07	3.84	3.69	3.58	3.50	3.44	3.35	3.28	3.22	3.15	3.08	3.02	2.93
	0.975	6.06	5.42	5.05	4.82	4.65	4.53	4.43	4.29	4.20	4.10	4.00	3.89	3.81	3.67
	0.990	8.65	7.59	7.01	6.63	6.37	6.18	6.03	5.81	5.67	5.52	5.36	5.20	5.07	4.86
	0.999	18.5	15.8	14.4	13.5	12.9	12.4	12.0	11.5	11.2	10.8	10.5	10.1	9.80	9.33

Fractiles $f_{\nu_1,\nu_2,p}$ de la loi de Fisher-Snédécor

ν_2	$\nu_1 \rightarrow$	2	3	4	5	6	7	8	10	12	15	20	30	50	∞
$\downarrow$	p														
9	0.900	3.01	2.81	2.69	2.61	2.55	2.51	2.47	2.42	2.38	2.34	2.30	2.25	2.22	2.16
	0.950	4.26	3.86	3.63	3.48	3.37	3.29	3.23	3.14	3.07	3.01	2.94	2.86	2.80	2.71
	0.975	5.71	5.08	4.72	4.48	4.32	4.20	4.10	3.96	3.87	3.77	3.67	3.56	3.47	3.33
	0.990	8.02	6.99	6.42	6.06	5.80	5.61	5.47	5.26	5.11	4.96	4.81	4.65	4.52	4.31
	0.999	16.4	13.9	12.6	11.7	11.1	10.7	10.4	9.89	9.57	9.24	8.90	8.55	8.26	7.81
10	0.900	2.92	2.73	2.61	2.52	2.46	2.41	2.38	2.32	2.28	2.24	2.20	2.16	2.12	2.06
	0.950	4.10	3.71	3.48	3.33	3.22	3.14	3.07	2.98	2.91	2.84	2.77	2.70	2.64	2.54
	0.975	5.46	4.83	4.47	4.24	4.07	3.95	3.85	3.72	3.62	3.52	3.42	3.31	3.22	3.08
	0.990	7.56	6.55	5.99	5.64	5.39	5.20	5.06	4.85	4.71	4.56	4.41	4.25	4.11	3.91
	0.999	14.9	12.6	11.3	10.5	9.93	9.52	9.20	8.75	8.45	8.13	7.80	7.47	7.19	6.76
11	0.900	2.86	2.66	2.54	2.45	2.39	2.34	2.30	2.25	2.21	2.17	2.12	2.08	2.04	1.97
	0.950	3.98	3.59	3.36	3.20	3.09	3.01	2.95	2.85	2.79	2.72	2.65	2.57	2.51	2.40
	0.975	5.26	4.63	4.28	4.04	3.88	3.76	3.66	3.53	3.43	3.33	3.23	3.12	3.03	2.88
	0.990	7.21	6.22	5.67	5.32	5.07	4.89	4.74	4.54	4.40	4.25	4.10	3.94	3.81	3.60
	0.999	13.8	11.6	10.3	9.58	9.05	8.66	8.35	7.92	7.63	7.32	7.01	6.68	6.42	6.00
12	0.900	2.81	2.61	2.48	2.39	2.33	2.28	2.24	2.19	2.15	2.10	2.06	2.01	1.97	1.90
	0.950	3.89	3.49	3.26	3.11	3.00	2.91	2.85	2.75	2.69	2.62	2.54	2.47	2.40	2.30
	0.975	5.10	4.47	4.12	3.89	3.73	3.61	3.51	3.37	3.28	3.18	3.07	2.96	2.87	2.72
	0.990	6.93	5.95	5.41	5.06	4.82	4.64	4.50	4.30	4.16	4.01	3.86	3.70	3.57	3.36
	0.999	13.0	10.8	9.63	8.89	8.38	8.00	7.71	7.29	7.00	6.71	6.40	6.09	5.83	5.42
13	0.900	2.76	2.56	2.43	2.35	2.28	2.23	2.20	2.14	2.10	2.05	2.01	1.96	1.92	1.85
	0.950	3.81	3.41	3.18	3.03	2.92	2.83	2.77	2.67	2.60	2.53	2.46	2.38	2.31	2.21
	0.975	4.97	4.35	4.00	3.77	3.60	3.48	3.39	3.25	3.15	3.05	2.95	2.84	2.74	2.60
	0.990	6.70	5.74	5.21	4.86	4.62	4.44	4.30	4.10	3.96	3.82	3.66	3.51	3.37	3.17
	0.999	12.3	10.2	9.07	8.35	7.86	7.49	7.21	6.80	6.52	6.23	5.93	5.63	5.37	4.97
14	0.900	2.73	2.52	2.39	2.31	2.24	2.19	2.15	2.10	2.05	2.01	1.96	1.91	1.87	1.80
	0.950	3.74	3.34	3.11	2.96	2.85	2.76	2.70	2.60	2.53	2.46	2.39	2.31	2.24	2.13
	0.975	4.86	4.24	3.89	3.66	3.50	3.38	3.29	3.15	3.05	2.95	2.84	2.73	2.64	2.49
	0.990	6.51	5.56	5.04	4.69	4.46	4.28	4.14	3.94	3.80	3.66	3.51	3.35	3.22	3.00
	0.999	11.8	9.73	8.62	7.92	7.44	7.08	6.80	6.40	6.13	5.85	5.56	5.25	5.00	4.60
15	0.900	2.70	2.49	2.36	2.27	2.21	2.16	2.12	2.06	2.02	1.97	1.92	1.87	1.83	1.76
	0.950	3.68	3.29	3.06	2.90	2.79	2.71	2.64	2.54	2.48	2.40	2.33	2.25	2.18	2.07
	0.975	4.77	4.15	3.80	3.58	3.41	3.29	3.20	3.06	2.96	2.86	2.76	2.64	2.55	2.40
	0.990	6.36	5.42	4.89	4.56	4.32	4.14	4.00	3.80	3.67	3.52	3.37	3.21	3.08	2.87
	0.999	11.3	9.34	8.25	7.57	7.09	6.74	6.47	6.08	5.81	5.53	5.25	4.95	4.70	4.31
16	0.900	2.67	2.46	2.33	2.24	2.18	2.13	2.09	2.03	1.99	1.94	1.89	1.84	1.79	1.72
	0.950	3.63	3.24	3.01	2.85	2.74	2.66	2.59	2.49	2.42	2.35	2.28	2.19	2.12	2.01
	0.975	4.69	4.08	3.73	3.50	3.34	3.22	3.12	2.99	2.89	2.79	2.68	2.57	2.47	2.32
	0.990	6.23	5.29	4.77	4.44	4.20	4.03	3.89	3.69	3.55	3.41	3.26	3.10	2.97	2.75
	0.999	11.0	9.01	7.94	7.27	6.80	6.46	6.19	5.81	5.55	5.27	4.99	4.70	4.45	4.06
17	0.900	2.64	2.44	2.31	2.22	2.15	2.10	2.06	2.00	1.96	1.91	1.86	1.81	1.76	1.69
	0.950	3.59	3.20	2.96	2.81	2.70	2.61	2.55	2.45	2.38	2.31	2.23	2.15	2.08	1.96
	0.975	4.62	4.01	3.66	3.44	3.28	3.16	3.06	2.92	2.82	2.72	2.62	2.50	2.41	2.25
	0.990	6.11	5.18	4.67	4.34	4.10	3.93	3.79	3.59	3.46	3.31	3.16	3.00	2.87	2.65
	0.999	10.7	8.73	7.68	7.02	6.56	6.22	5.96	5.58	5.32	5.05	4.77	4.48	4.24	3.85

Fractiles $f_{\nu_1,\nu_2,p}$ de la loi de Fisher-Snédécor

ν_2	$\nu_1 \rightarrow$	2	3	4	5	6	7	8	10	12	15	20	30	50	∞
$\downarrow$	p														
18	0.900	2.62	2.42	2.29	2.20	2.13	2.08	2.04	1.98	1.93	1.89	1.84	1.78	1.74	1.66
	0.950	3.55	3.16	2.93	2.77	2.66	2.58	2.51	2.41	2.34	2.27	2.19	2.11	2.04	1.92
	0.975	4.56	3.95	3.61	3.38	3.22	3.10	3.01	2.87	2.77	2.67	2.56	2.44	2.35	2.19
	0.990	6.01	5.09	4.58	4.25	4.01	3.84	3.71	3.51	3.37	3.23	3.08	2.92	2.78	2.57
	0.999	10.4	8.49	7.46	6.81	6.35	6.02	5.76	5.39	5.13	4.87	4.59	4.30	4.06	3.67
19	0.900	2.61	2.40	2.27	2.18	2.11	2.06	2.02	1.96	1.91	1.86	1.81	1.76	1.71	1.63
	0.950	3.52	3.13	2.90	2.74	2.63	2.54	2.48	2.38	2.31	2.23	2.16	2.07	2.00	1.88
	0.975	4.51	3.90	3.56	3.33	3.17	3.05	2.96	2.82	2.72	2.62	2.51	2.39	2.30	2.13
	0.990	5.93	5.01	4.50	4.17	3.94	3.77	3.63	3.43	3.30	3.15	3.00	2.84	2.71	2.49
	0.999	10.2	8.28	7.27	6.62	6.18	5.85	5.59	5.22	4.97	4.70	4.43	4.14	3.90	3.51
20	0.900	2.59	2.38	2.25	2.16	2.09	2.04	2.00	1.94	1.89	1.84	1.79	1.74	1.69	1.61
	0.950	3.49	3.10	2.87	2.71	2.60	2.51	2.45	2.35	2.28	2.20	2.12	2.04	1.97	1.84
	0.975	4.46	3.86	3.51	3.29	3.13	3.01	2.91	2.77	2.68	2.57	2.46	2.35	2.25	2.09
	0.990	5.85	4.94	4.43	4.10	3.87	3.70	3.56	3.37	3.23	3.09	2.94	2.78	2.64	2.42
	0.999	9.95	8.10	7.10	6.46	6.02	5.69	5.44	5.08	4.82	4.56	4.29	4.00	3.76	3.38
21	0.900	2.57	2.36	2.23	2.14	2.08	2.02	1.98	1.92	1.87	1.83	1.78	1.72	1.67	1.59
	0.950	3.47	3.07	2.84	2.68	2.57	2.49	2.42	2.32	2.25	2.18	2.10	2.01	1.94	1.81
	0.975	4.42	3.82	3.48	3.25	3.09	2.97	2.87	2.73	2.64	2.53	2.42	2.31	2.21	2.04
	0.990	5.78	4.87	4.37	4.04	3.81	3.64	3.51	3.31	3.17	3.03	2.88	2.72	2.58	2.36
	0.999	9.77	7.94	6.95	6.32	5.88	5.56	5.31	4.95	4.70	4.44	4.17	3.88	3.64	3.26
22	0.900	2.56	2.35	2.22	2.13	2.06	2.01	1.97	1.90	1.86	1.81	1.76	1.70	1.65	1.57
	0.950	3.44	3.05	2.82	2.66	2.55	2.46	2.40	2.30	2.23	2.15	2.07	1.98	1.91	1.78
	0.975	4.38	3.78	3.44	3.22	3.05	2.93	2.84	2.70	2.60	2.50	2.39	2.27	2.17	2.00
	0.990	5.72	4.82	4.31	3.99	3.76	3.59	3.45	3.26	3.12	2.98	2.83	2.67	2.53	2.31
	0.999	9.61	7.80	6.81	6.19	5.76	5.44	5.19	4.83	4.58	4.33	4.06	3.78	3.54	3.15
23	0.900	2.55	2.34	2.21	2.11	2.05	1.99	1.95	1.89	1.84	1.80	1.74	1.69	1.64	1.55
	0.950	3.42	3.03	2.80	2.64	2.53	2.44	2.37	2.27	2.20	2.13	2.05	1.96	1.88	1.76
	0.975	4.35	3.75	3.41	3.18	3.02	2.90	2.81	2.67	2.57	2.47	2.36	2.24	2.14	1.97
	0.990	5.66	4.76	4.26	3.94	3.71	3.54	3.41	3.21	3.07	2.93	2.78	2.62	2.48	2.26
	0.999	9.47	7.67	6.70	6.08	5.65	5.33	5.09	4.73	4.48	4.23	3.96	3.68	3.44	3.05
24	0.900	2.54	2.33	2.19	2.10	2.04	1.98	1.94	1.88	1.83	1.78	1.73	1.67	1.62	1.53
	0.950	3.40	3.01	2.78	2.62	2.51	2.42	2.36	2.25	2.18	2.11	2.03	1.94	1.86	1.73
	0.975	4.32	3.72	3.38	3.15	2.99	2.87	2.78	2.64	2.54	2.44	2.33	2.21	2.11	1.94
	0.990	5.61	4.72	4.22	3.90	3.67	3.50	3.36	3.17	3.03	2.89	2.74	2.58	2.44	2.21
	0.999	9.34	7.55	6.59	5.98	5.55	5.23	4.99	4.64	4.39	4.14	3.87	3.59	3.36	2.97
25	0.900	2.53	2.32	2.18	2.09	2.02	1.97	1.93	1.87	1.82	1.77	1.72	1.66	1.61	1.52
	0.950	3.39	2.99	2.76	2.60	2.49	2.40	2.34	2.24	2.16	2.09	2.01	1.92	1.84	1.71
	0.975	4.29	3.69	3.35	3.13	2.97	2.85	2.75	2.61	2.51	2.41	2.30	2.18	2.08	1.91
	0.990	5.57	4.68	4.18	3.85	3.63	3.46	3.32	3.13	2.99	2.85	2.70	2.54	2.40	2.17
	0.999	9.22	7.45	6.49	5.89	5.46	5.15	4.91	4.56	4.31	4.06	3.79	3.52	3.28	2.89
26	0.900	2.52	2.31	2.17	2.08	2.01	1.96	1.92	1.86	1.81	1.76	1.71	1.65	1.59	1.50
	0.950	3.37	2.98	2.74	2.59	2.47	2.39	2.32	2.22	2.15	2.07	1.99	1.90	1.82	1.69
	0.975	4.27	3.67	3.33	3.10	2.94	2.82	2.73	2.59	2.49	2.39	2.28	2.16	2.05	1.88
	0.990	5.53	4.64	4.14	3.82	3.59	3.42	3.29	3.09	2.96	2.81	2.66	2.50	2.36	2.13
	0.999	9.12	7.36	6.41	5.80	5.38	5.07	4.83	4.48	4.24	3.99	3.72	3.44	3.21	2.82

Fractiles $f_{\nu_1,\nu_2,p}$ de la loi de Fisher-Snédécor

ν_2	$\nu_1 \rightarrow$	2	3	4	5	6	7	8	10	12	15	20	30	50	∞
$\downarrow$	p														
27	0.900	2.51	2.30	2.17	2.07	2.00	1.95	1.91	1.85	1.80	1.75	1.70	1.64	1.58	1.49
	0.950	3.35	2.96	2.73	2.57	2.46	2.37	2.31	2.20	2.13	2.06	1.97	1.88	1.81	1.67
	0.975	4.24	3.65	3.31	3.08	2.92	2.80	2.71	2.57	2.47	2.36	2.25	2.13	2.03	1.85
	0.990	5.49	4.60	4.11	3.78	3.56	3.39	3.26	3.06	2.93	2.78	2.63	2.47	2.33	2.10
	0.999	9.02	7.27	6.33	5.73	5.31	5.00	4.76	4.41	4.17	3.92	3.66	3.38	3.14	2.75
28	0.900	2.50	2.29	2.16	2.06	2.00	1.94	1.90	1.84	1.79	1.74	1.69	1.63	1.57	1.48
	0.950	3.34	2.95	2.71	2.56	2.45	2.36	2.29	2.19	2.12	2.04	1.96	1.87	1.79	1.65
	0.975	4.22	3.63	3.29	3.06	2.90	2.78	2.69	2.55	2.45	2.34	2.23	2.11	2.01	1.83
	0.990	5.45	4.57	4.07	3.75	3.53	3.36	3.23	3.03	2.90	2.75	2.60	2.44	2.30	2.06
	0.999	8.93	7.19	6.25	5.66	5.24	4.93	4.69	4.35	4.11	3.86	3.60	3.32	3.09	2.69
29	0.900	2.50	2.28	2.15	2.06	1.99	1.93	1.89	1.83	1.78	1.73	1.68	1.62	1.56	1.47
	0.950	3.33	2.93	2.70	2.55	2.43	2.35	2.28	2.18	2.10	2.03	1.94	1.85	1.77	1.64
	0.975	4.20	3.61	3.27	3.04	2.88	2.76	2.67	2.53	2.43	2.32	2.21	2.09	1.99	1.81
	0.990	5.42	4.54	4.04	3.73	3.50	3.33	3.20	3.00	2.87	2.73	2.57	2.41	2.27	2.03
	0.999	8.85	7.12	6.19	5.59	5.18	4.87	4.64	4.29	4.05	3.80	3.54	3.27	3.03	2.64
30	0.900	2.49	2.28	2.14	2.05	1.98	1.93	1.88	1.82	1.77	1.72	1.67	1.61	1.55	1.46
	0.950	3.32	2.92	2.69	2.53	2.42	2.33	2.27	2.16	2.09	2.01	1.93	1.84	1.76	1.62
	0.975	4.18	3.59	3.25	3.03	2.87	2.75	2.65	2.51	2.41	2.31	2.20	2.07	1.97	1.79
	0.990	5.39	4.51	4.02	3.70	3.47	3.30	3.17	2.98	2.84	2.70	2.55	2.39	2.25	2.01
	0.999	8.77	7.05	6.12	5.53	5.12	4.82	4.58	4.24	4.00	3.75	3.49	3.22	2.98	2.59
60	0.900	2.39	2.18	2.04	1.95	1.87	1.82	1.77	1.71	1.66	1.60	1.54	1.48	1.41	1.29
	0.950	3.15	2.76	2.53	2.37	2.25	2.17	2.10	1.99	1.92	1.84	1.75	1.65	1.56	1.39
	0.975	3.93	3.34	3.01	2.79	2.63	2.51	2.41	2.27	2.17	2.06	1.94	1.82	1.70	1.48
	0.990	4.98	4.13	3.65	3.34	3.12	2.95	2.82	2.63	2.50	2.35	2.20	2.03	1.88	1.60
	0.999	7.77	6.17	5.31	4.76	4.37	4.09	3.86	3.54	3.32	3.08	2.83	2.55	2.32	1.89
80	0.900	2.37	2.15	2.02	1.92	1.85	1.79	1.75	1.68	1.63	1.57	1.51	1.44	1.38	1.24
	0.950	3.11	2.72	2.49	2.33	2.21	2.13	2.06	1.95	1.88	1.79	1.70	1.60	1.51	1.32
	0.975	3.86	3.28	2.95	2.73	2.57	2.45	2.35	2.21	2.11	2.00	1.88	1.75	1.63	1.40
	0.990	4.88	4.04	3.56	3.26	3.04	2.87	2.74	2.55	2.42	2.27	2.12	1.94	1.79	1.49
	0.999	7.54	5.97	5.12	4.58	4.20	3.92	3.70	3.39	3.16	2.93	2.68	2.41	2.16	1.72
100	0.900	2.36	2.14	2.00	1.91	1.83	1.78	1.73	1.66	1.61	1.56	1.49	1.42	1.35	1.21
	0.950	3.09	2.70	2.46	2.31	2.19	2.10	2.03	1.93	1.85	1.77	1.68	1.57	1.48	1.28
	0.975	3.83	3.25	2.92	2.70	2.54	2.42	2.32	2.18	2.08	1.97	1.85	1.71	1.59	1.35
	0.990	4.82	3.98	3.51	3.21	2.99	2.82	2.69	2.50	2.37	2.22	2.07	1.89	1.74	1.43
	0.999	7.41	5.86	5.02	4.48	4.11	3.83	3.61	3.30	3.07	2.84	2.59	2.32	2.08	1.62
120	0.900	2.35	2.13	1.99	1.90	1.82	1.77	1.72	1.65	1.60	1.54	1.48	1.41	1.34	1.19
	0.950	3.07	2.68	2.45	2.29	2.18	2.09	2.02	1.91	1.83	1.75	1.66	1.55	1.46	1.25
	0.975	3.80	3.23	2.89	2.67	2.52	2.39	2.30	2.16	2.05	1.94	1.82	1.69	1.56	1.31
	0.990	4.79	3.95	3.48	3.17	2.96	2.79	2.66	2.47	2.34	2.19	2.03	1.86	1.70	1.38
	0.999	7.32	5.78	4.95	4.42	4.04	3.77	3.55	3.24	3.02	2.78	2.53	2.26	2.02	1.54
∞	0.900	2.30	2.08	1.94	1.85	1.77	1.72	1.67	1.60	1.55	1.49	1.42	1.34	1.26	1.00
	0.950	3.00	2.60	2.37	2.21	2.10	2.01	1.94	1.83	1.75	1.67	1.57	1.46	1.35	1.00
	0.975	3.69	3.12	2.79	2.57	2.41	2.29	2.19	2.05	1.94	1.83	1.71	1.57	1.43	1.00
	0.990	4.61	3.78	3.32	3.02	2.80	2.64	2.51	2.32	2.18	2.04	1.88	1.70	1.52	1.00
	0.999	6.91	5.42	4.62	4.10	3.74	3.47	3.27	2.96	2.74	2.51	2.27	1.99	1.73	1.00

TABLE DU CHI-DEUX : $\chi^2(n)$

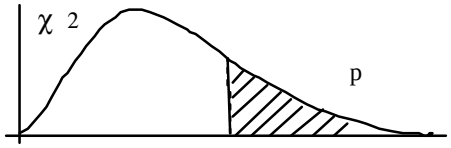

n p	0.90	0.80	0.70	0.50	0.30	0.20	0.10	0.05	0.02	0.01
1	0,0158	0,0642	0,148	0,455	1,074	1,642	2,706	3,841	5,412	6,635
2	0,211	0,446	0,713	1,386	2,408	3,219	4,605	5,991	7,824	9,210
3	0,584	1,005	1,424	2,366	3,665	4,642	6,251	7,815	9,837	11,341
4	1,064	1,649	2,195	3,357	4,878	5,989	7,779	9,488	11,668	13,277
5	1,610	2,343	3,000	4,351	6,064	7,289	9,236	11,070	13,388	15,086
6	2,204	3,070	3,828	5,348	7,231	8,558	10,645	12,592	15,033	16,812
7	2,833	3,822	4,671	6,346	8,383	9,803	12,017	14,067	16,622	18,475
8	3,490	4,594	5,527	7,344	9,524	11,030	13,362	15,507	18,168	20,090
9	4,168	5,380	6,393	8,343	10,656	12,242	14,684	16,919	19,679	21,666
10	4,865	6,179	7,267	9,342	11,781	13,442	15,987	18,307	21,161	23,209
11	5,578	6,989	8,148	10,341	12,899	14,631	17,275	19,675	22,618	24,725
12	6,304	7,807	9,034	11,340	14,011	15,812	18,549	21,026	24,054	26,217
13	7,042	8,634	9,926	12,340	15,119	16,985	19,812	22,362	25,472	27,688
14	7,790	9,467	10,821	13,339	16,222	18,151	21,064	23,685	26,873	29,141
15	8,547	10,307	11,721	14,339	17,322	19,311	22,307	24,996	28,259	30,578
16	9,312	11,152	12,624	15,338	18,418	20,465	23,542	26,296	29,633	32,000
17	10,085	12,002	13,531	16,338	19,511	21,615	24,769	27,587	30,995	33,409
18	10,865	12,857	14,440	17,338	20,601	22,760	25,989	28,869	32,346	34,805
19	11,651	13,716	15,352	18,338	21,689	23,900	27,204	30,144	33,687	36,191
20	12,443	14,578	16,266	19,337	22,775	25,038	28,412	31,410	35,020	37,566
21	13,240	15,445	17,182	20,337	23,858	26,171	29,615	32,671	36,343	38,932
22	14,041	16,314	18,101	21,337	24,939	27,301	30,813	33,924	37,659	40,289
23	14,848	17,187	19,021	22,337	26,018	28,429	32,007	35,172	38,968	41,638
24	15,659	18,062	19,943	23,337	27,096	29,553	33,196	36,415	40,270	42,980
25	16,473	18,940	20,867	24,337	28,172	30,675	34,382	37,652	41,566	44,314
26	17,292	19,820	21,792	25,336	29,246	31,795	35,563	38,885	42,856	45,642
27	18,114	20,703	22,719	26,336	30,319	32,912	36,741	40,113	44,140	46,963
28	18,939	21,588	23,647	27,336	31,391	34,027	37,916	41,337	45,419	48,278
29	19,768	22,475	24,577	28,336	32,461	35,139	39,087	42,557	46,693	49,588
30	20,599	23,364	25,508	29,336	33,530	36,250	40,256	43,773	47,962	50,892

Pour n > 30, on peut admettre que $\sqrt{2\chi^2} - \sqrt{2n-1} \approx N(0,1)$

Extended summary

Tropical cyclone-ocean interactions are essential for cyclone formation and evolution. The ocean heat content is the fuel of tropical cyclones. In return, extreme winds inject mechanical energy into the ocean and modify its structure. Surface cooling is generally observed in the cyclone wake and is expected to exert a negative feedback to the storm intensity. The main objectives of the thesis were to provide a climatology of the ocean response and feedback to tropical cyclones and understand the mechanisms at work. To that end, a coupled regional model of the southwest Pacific was developed for present climate simulations at mesoscale resolution. This approach provides statistically robust experiments that fills a gap between coarse-resolution and short-term studies.

The ocean response to tropical cyclones is first addressed. The results highlight the neglected role of three-dimensional oceanic dynamics, particularly cyclone-induced upwelling, that moderates the usually extreme estimates given by over-simplified theoretical models. In the surface heat budget, mixing is a relay process to upwelling in the cooling of surface waters. In the subsurface, these two processes are competing. Therefore, previous estimates that neglect the upwelling process overestimate the local heat uptake by the ocean. In addition, 60% of this uptake is actually lost to the atmosphere through winter entrainment that drives warm anomalies back to the surface. Cyclonic Ekman pumping also produces a large-scale reorganization of temperature anomalies owing to the geography of TC distribution. Climatological anomalies are most noticeable in the thermocline between 150-400 m and are transported by the flow outside the cyclogenesis region with interannual variability.

The feedback of the ocean response is then investigated by comparing forced and coupled experiments that only differ by the SST fields: there is no cold wake in the forced model. The simulated cyclonic activity is realistic, the coupled model being closer to observations in all statistical estimations. The forced model overestimates the number of cyclones, which are also too strongly concentrated in the Coral Sea. The intensity distribution is also significantly affected but the feedback of SST cooling to storm intensity is of moderate amplitude, compared with theoretical models based on thermodynamic arguments. Actually, our analyses contradict the direct thermodynamic control of TC intensification by surface moisture fluxes in favor of a storm-scale dynamic control. In addition, regional oceanography has a large impact on air-sea interactions. The large-scale and mesoscales oceanic structures strongly modulate the cooling mechanisms. Coupling is stronger in the Coral Sea that has shallow mixed layer and numerous eddies but is extremely weak in the warm pool that has deep mixed layer, thick barrier layer and no mesoscale activity. These pre-conditions to SST cooling have a clear impact on the spatial distributions of TCs and could even impact the global TC counts by affecting the recruitment of TCs from the growth of tropical storms.

Abstract

Tropical cyclone (TC)-ocean interactions are essential for cyclone formation and evolution. Surface cooling is observed in the cyclone wake and is expected to exert a negative feedback to the storm intensity. This thesis provide a quantification of the ocean response and its feedback using a coupled regional model of the south-west Pacific developed for present climate long-term simulations at mesoscale resolution which are requested to separate robust features from anecdotic effects. The results highlight the neglected role of three-dimensional dynamics in the ocean and the atmosphere and tend to contradict the extreme estimations made from simple theoretical models. Previous estimates that neglect the upwelling process and ocean warm anomaly re-emergence by winter entrainment overestimate the local heat uptake by the ocean. The intensity distribution of TCs is significantly affected by the cold wake but the feedback of SST cooling to storm intensity is of moderate amplitude, compared with theoretical models based on thermodynamic arguments. Actually, our analyses contradict the direct thermodynamic control of TC intensification by surface moisture fluxes in favor of a storm-scale dynamic control. In addition, regional oceanography has a large impact on coupling. It is stronger in the Coral Sea that has shallow mixed layer and numerous eddies but extremely weak in the warm pool that has deep mixed layer, thick barrier layer and no mesoscale activity.

Key words: Tropical cyclones, air-sea interactions, coupling, modeling, mesoscale

Résumé

Cette thèse apporte une meilleure compréhension des interactions océan-atmosphère au sein d'évènements extrêmes que sont les cyclones tropicaux. L'étude de la réponse océanique aux cyclones et de sa rétroaction a permis de souligner l'importance de la dynamique océanique et atmosphérique et tend à contredire les estimations extrêmes faites précédemment à partir de modèles théoriques simplifiés. L'impact des cyclones sur le climat est probablement surestimé dans les études qui négligent les processus d'advection et la réémergence d'anomalies océaniques en surface durant l'hiver. La rétroaction négative du refroidissement de surface induit par les cyclones est également surestimée dans les études théoriques en raison des fortes hypothèses faites sur les échelles de temps impliquées dans le processus d'intensification des cyclones. De même, la structure océanique à grande et moyenne échelle est souvent négligée (par exemple dans les indices de cyclogenèse), alors qu'elle module fortement les mécanismes de couplage. Enfin, l'utilisation de modèles à méso-échelle et de simulations à long terme produisant un grand nombre d'événements est essentielle afin de séparer un mécanisme robuste d'effets anecdotiques.

Mots-clés: Cyclones tropicaux, interactions air-mer, couplage, modélisation, méso-échelle